UNIVERSITY OF CALIFORNIA

Santa Barbara

The Thermal Evolution of Lower Continental Crust

A dissertation submitted in partial satisfaction of the

requirements for the degree Doctor of Philosophy

in Earth Science

by

Francisco Emmanuel Apen

Committee in charge:

Professor Roberta L. Rudnick, Co-Chair

Professor John M. Cottle, Co-Chair

Professor Zachary C. Eilon

September 2022

The dissertation of Francisco Emmanuel Apen is approved.

_____
Zachary C. Eilon

_____
John M. Cottle, Committee Co-Chair

_____
Roberta L. Rudnick, Committee Co-Chair

July 2022

ACKNOWLEDGEMENTS

The work presented here was only possible with the support and guidance of many, many people. First and foremost, my doctoral advisors, Roberta Rudnick and John Cottle. I cannot imagine having greater advisors. Roberta is an infinite source of wisdom and a powerhouse, constantly pushing me to formulate well founded questions and think about the big picture. Roberta is also a trusted life mentor and friend, always taking the time to talk about life and provide sage career advice. From the start John has treated me like a colleague and not just a student. He has given me the freedom to explore different ideas and learn from my various failures, for which I am thankful. It has been a true privilege to have worked with you both, and I very much look forward to continuing collaborations.

I also owe a great deal to Brad Hacker. Brad has been an invaluable tertiary advisor, providing keen criticism and insight (both in doing science and in navigating my career), and inspires me to be a more critical, practical, and well-rounded scientist. In the lab, Gareth Seward and Andrew Kylander-Clark have provided exceptional analytical support and fun music discussions (Dio > Ozzy); thank you for sharing your wisdom and granting me unfettered access to world-class lab spaces. I also benefited greatly from interactions with various UCSB faculty, namely Zach Eilon, Francis Macdonald, Matt Rioux, Matt Jackson, and Susannah Porter.

Many students and friends have also made my time at UCSB. In particular, Elizabeth Erickson, Ryan Stoner, Amy Moser, and Pengyuan Han. Several undergraduates research assistants helped progress my studies: Khalil Droubi, Jack Rager, Aran Mazariegos, Odalys Callejas, and Alaina Rosenthal. And of course Murphy, thank you for being you!

I must also acknowledge my mentors before my time at UCSB. I am indebted to Howard Day for taking me on as an undergraduate lab assistant at UC Davis all those years ago and for introducing me to scientific research. I would not have started on this journey were it not for him. Sujoy Mukhopadhyay welcomed me into his research group as a junior specialist (also at UC Davis). He fostered my scientific curiosity and let me get my hands dirty in the lab. I am immensely appreciative of his continued mentorship.

Thanks also go to my collaborators for providing samples and productive discussions: Madalyn Blondes, Phil Piccoli, Dmitri Ionov, Jean-François Moyen, Alexander Golovin, Corey Wall, Mark Schmitz, Frank Dudas, Thomas Stachel, Volker Schenk, Harald Fritz, Christoph Hauzenberger, Kyle Larson, and many others. Further thanks to the department staff (Yann Ricard, Yvette Howze, Jaima Ortega, Patricia Machuca, and Tim Cuellar) for logistical support.

I owe everything to my parents, Guadalupe and Luis, and sisters, Maria and Mildred. Their unwavering support and love through it all means the world to me. Although I went down an uncharted (left hand?) path, the lessons imparted into me by my family—to work diligently and to see things through to the end—have served me in life far better than any class I have taken.

Lastly, I dedicate this to the memory of my friend Alex Johnson. Thank you for all of those times talking science, joking around, waxing quixotic about the esoteric, and driving around and exploring the world. More than anything else, I wish that you were still with us to share these moments.

VITA OF FRANCISCO EMMANUEL APEN

August 2022

EDUCATION

2017–2022	Ph.D. Earth Science, University of California, Santa Barbara
2012–2015	B.Sc. Geology with Highest Honors, University of California, Davis

APPOINTMENTS

2017–2022	Graduate Teaching and Research Assistant, UC Santa Barbara
2015–2017	Junior Research Specialist, UC Davis
2014–2015	Undergraduate Research Assistant, UC Davis

AWARDS & HONORS

2022	Presidential Postdoctoral Research Fellowship, Princeton University
2017–2022	Graduate Research Fellowship, National Science Foundation
2021	IGNITE - Future Faculty Development Program, College of William & Mary
2021	Alex Johnson Memorial Scholarship for undergrad mentoring, UC Santa Barbara
2021	Exploring and Preparing for the Professoriate Summer Institute, UC Santa Barbara
2020, 2021	Student Research Grant, Geological Society of America
2020	Richard V. Fisher Scholarship, UC Santa Barbara
2019	AGeS2 Award, Geological Society of America
2019	Alumni Graduate Award for Research Excellence, UC Santa Barbara
2017–2018	Regents in Earth Science Fellowship, UC Santa Barbara
2016	On to the Future Scholarship, Geological Society of America
2015	Citation for Outstanding Performance, UC Davis
2014–2015	Everett Dale Jackson Memorial Scholarship, UC Davis

SERVICE

2020–2022	Diversity, Equity, and Inclusion committee, Geochemical Society
2019–2020	Graduate student liaison to Earth Science faculty, UC Santa Barbara
2018–2020	Earth Science Department lecture series organizer, UC Santa Barbara

TEACHING & MENTORING EXPERIENCE:

Senior thesis co-supervisor (w/ Roberta Rudnick), Aran Mazariegos, UC Santa Barbara, 2021–2022
Senior thesis co-supervisor (w/ Roberta Rudnick), Odalys Callejas, UC Santa Barbara, 2020–2022
Senior thesis co-supervisor (w/ Roberta Rudnick), Jackson Rager, UC Santa Barbara, 2020–2021

Senior thesis co-supervisor (w/ Roberta Rudnick), Khalil Droubi, UC Santa Barbara, 2018–2020
Senior thesis co-supervisor (w/ Roberta Rudnick and Yongsheng Liu), Yuan Zhou, CUG Wuhan, 2020
Senior thesis co-supervisor (w/ John Wakabayashi), Lance Rodriguez, CSU Fresno, 2019
Undergrad research co-supervisor (w/ Roberta Rudnick), Ranpeng Li, UC Santa Barbara, 2019–2020
Teaching assistant, Earth 18: Introduction to Field Studies (Instructors: Susannah Porter and Tanya Atwater), UC Santa Barbara, 2022
Teaching assistant, Earth 18: Introduction to Field Studies (Instructor: Bradley Hacker), UC Santa Barbara, 2021
Teaching assistant, Earth 102C: Metamorphic Petrology (Instructor: Bradley Hacker), UC Santa Barbara, 2019
Teaching assistant, Earth 115: Analytical Methods in Geomaterials (Instructor: Matthew Rioux), UC Santa Barbara, 2018

PUBLICATIONS

Apen, F.E., Rudnick, R.L., Ionov, D., Cottle, J.M., Moyen, J.-F., Golovin, A., and Koreskov, A., Heat production and transfer in cratonic continental crust: Petrochronology of xenoliths from the Udachnaya kimberlite (Siberian Craton). *in revision for G-Cubed.*

Therriault, I., Larson, K.P., Steenkamp, H., **Apen, F.E.**, Graziani, R., Soret, M., Guilmette, C. and Cottle, J.M., Characterization of the Wager shear zone, Nunavut, Canada: Insights from microstructures and geochronology. *Canadian Journal of Earth Sciences.*

Apen, F.E., Wall, C.J., Cottle, J.M., Schmitz, M.D., Kylander-Clark, A.R.C. and Seward, G.G.E., 2022, Apatites for destruction: reference apatites from Morocco and Brazil for U-Pb petrochronology and Nd and Sr isotope geochemistry. *Chemical Geology*, 590, p.120689.

Apen, F.E., Wakabayashi, J., Day, H.W., Roeske, S.M., Souders, A.K. and Dumitru, T.A., 2021, Regional-scale correlations of accreted units in the Franciscan Complex, California: a record of long-lived, episodic subduction accretion, in Wakabayashi, J., and Dilek, Y., eds., *Plate Tectonics, Ophiolites, and Societal Significance of Geology: A Celebration of the Career of Eldridge Moores: Geological Society of America Special Paper 552*, p. 233–255.

Sun, J., Mitchell, R.N., Kostrovitsky, S.I. and **Apen, F.E.,** 2021. Siberia's largest pulse of kimberlites: U-Pb geochronology of perovskite and rutile from the Obnazhennaya kimberlite and its xenoliths, Siberia craton. *International Geology Review*, pp.1-12.

Swanson-Hysell, N.L., Avery, M.S., Zhang, Y., Hodgin, E.B., Sherwood, R.J., **Apen, F.E.,** Boerboom, T.J., Keller, C.B. and Cottle, J.M., 2021. The paleogeography of Laurentia in its early years: new constraints from the Paleoproterozoic East-Central Minnesota batholith. *Tectonics*, p. e2021TC006751.

Apen, F.E., Rudnick, R.L., Cottle, J.M., Kylander-Clark, A.R.C., Blondes, M.S., Piccoli, P.M. and Seward, G., 2020. Four-dimensional thermal evolution of the East African Orogen: accessory phase petrochronology of crustal profiles through the Tanzanian Craton and

Mozambique Belt, northeastern Tanzania. *Contributions to Mineralogy and Petrology*, 175(11), pp.1-30.

Larson, K.P., Graziani, R., Cottle, J.M., **Apen, F.**, Corthouts, T. and Lageson, D., 2020. The structural evolution of the Qomolangma Formation, Mount Everest, Nepal. *Journal of Structural Geology*, 138, p.104123.

ABSTRACT

The Thermal Evolution of Lower Continental Crust

by

Francisco Emmanuel Apen

Temperatures of the lower crust and Moho are critical boundary conditions for models of heat transfer and production in the lithosphere, as well as models of the bulk composition of the continental crust, yet they remain uncertain. This dissertation focuses on xenoliths—fragments of *in situ* deep crust transported rapidly to the surface by volcanism—and accessory phase U-Pb and trace-element petrochronology in order to provide direct insights into the long-term thermal history of lower continental crust. Chapter I constitutes a study of xenoliths and basement outcrops from northern Tanzania aimed at unraveling crustal vs. mantle heat contributions to variable surface heat flow across the tectonically-stable craton and adjacent rifting crust. Lower-crustal xenoliths erupted on the craton edge contain rutile with U-Pb dates as old as 1000 Ma, whereas xenoliths from the rift have rutile and apatite with near-zero Ma U-Pb dates but significantly older titanite dates (up to 560 Ma). These and other data suggest that Moho temperatures beneath the craton margin are cooler than below the rifting crust, such that regional differences in surface heat flow reflect variable mantle heat flow. Chapter II focuses on kimberlite-borne xenoliths from the central Siberian craton. Rutile and apatite in garnet-granulite xenoliths preserve U-Pb dates between 1.8 Ga

and 360 Ma (the timing of kimberlite eruption). Such spreads in U-Pb dates have been interpreted previously to reflect partial Pb loss during slow cooling through the Pb closure temperatures of rutile/apatite, but could also result from brief heating pulses in the lower crust prior to eruption. Laser ablation depth profiling reveals that U-Pb age and elemental gradients in rutile are coupled, contrary to diffusive decoupling expected for thermally-mediated volume diffusion over billions of years. These data are instead best explained by multiple transient heating episodes during distinct thermotectonic events, including immediately prior to kimberlite eruption. Finally, Chapter III presents TIMS and LASS-ICP-MS data for potential reference apatites. Using microbeam methods to obtain precise and accurate U-Pb, Sm-Nd, Sr isotopes and elemental abundances from apatite—a petrologically diverse thermochronometer—requires well-characterized and matrix-matched reference materials, yet suitable reference apatites are scarce. The development of the reference apatite suite provides new benchmarks for *in situ* apatite isotopic analyses and inter-laboratory calibrations.

TABLE OF CONTENTS

INTRODUCTION

The heat within Earth that drives mantle convection, plate tectonics, and the geodynamo is a combination of remnant heat from planetary accretion, latent heat of crystallization of the inner core, and heat produced by the decay of radioactive elements (e.g., Sclater et al., 1980; Pollack et al., 1993; Korenaga, 2008). Significant portions of Earth's radioactive (heating-producing) elements—U, Th, and K—are sequestered within the continental crust. As a result, the crust is an important contributor to the planet's total heat budget, despite its relatively small mass (~0.5% of the silicate Earth). Crustal heat production is, however, uncertain, with current estimates ranging between 25–95% of the silicate Earth's heat budget (e.g., Weaver and Tarney, 1984; Taylor and McLennan, 1985; 1995; 2009; Shaw et al., 1986; Christensen and Mooney, 1995; McDonough and Sun, 1995; Rudnick and Fountain, 1995; Wedepohl, 1995; Gao et al., 1998; Condie and Selverstone, 1999; Huang et al., 2013; Turcotte and Schubert, 2014; Rudnick and Gao, 2004; 2014; Jaupart and Mareschal, 2014; Hacker et al., 2011; 2015; Sammon and McDonough, 2021).

Temperatures of the lower crust and Moho are important boundary conditions for models of heat transfer and production in Earth's interior, information that also impacts models of the bulk composition of the continental crust (e.g., Rudnick et al., 1998; Sandiford and McLaren, 2002; Jaupart and Mareschal, 2014; Hacker et al., 2015). Surface heat flow measurements reveal the total amount of heat exiting the lithosphere, a combination of mantle heat flow entering the base of the lithosphere and heat production within the crust and mantle lithosphere (Roy et al., 1968; Perry et al., 2010). Measurements across the globe (albeit with uneven coverage) show that surface heat flow varies with crustal of ages (Fig. 1): Archean, Proterozoic, and Paleozoic continental crust have surface heat fluxes of 41 ± 11

mW/m^2, 48 ± 16 mW/m^2, and 58 ± 22 mW/m^2, respectively (values are the mean and standard deviation of the distribution; see Jaupart and Mareschal, 2014, and references therein). Surface heat flow measurements are relatively well-known, but heat fluxes across the Moho are much more uncertain, making it difficult to deconvolve the contributions of the mantle and crust to the total heat budget of the lithosphere. Given a known surface heat flow, basic heat transfer equations couple the values of Moho heat flow and crustal heat production (e.g., Jaupart et al., 2016). For example, a surface heat flow value of 50 mW/m^2 with a mantle heat flux of 17 mW/m^2 corresponds to a bulk crustal heat production of ~0.8 $\mu W/m^3$ (Rudnick and Gao, 2004; 2014; Huang et al., 2013); if mantle heat flux were lower (e.g., 11 mW/m^2), the crust must accordingly be more radioactive (bulk crustal heat production of ~1.1 $\mu W/m^3$; Hacker et al., 2015). Independent constraints on mantle heat flow and Moho temperatures can be obtained from seismic wavespeeds and other geophysical observations (e.g., Schutt et al., 2018; Goes et al., 2020) as well as from xenoliths—accidental fragments of the lithosphere transported rapidly to the surface by volcanic eruptions. If they sample *in situ* deep crust, xenoliths can uniquely offer direct constraints on the pressure-temperature evolution of the deep lithosphere, which in turn inform models of heat transfer across the Moho and crustal heat production (e.g., Rudnick et al., 1998; Hasterok and Chapman, 2011).

Thermobarometry of xenoliths can, in principle, be used to establish temperatures at the depth at which they equilibrated. However, a long recognized problem with this approach—most notably in stable cratonic regions—is that different lithologies record distinct temperature gradients through the lithosphere (e.g., Semprich and Simon, 2014). Pressure-temperature (P-T) arrays for cratonic mantle xenoliths define relatively cool geothermal

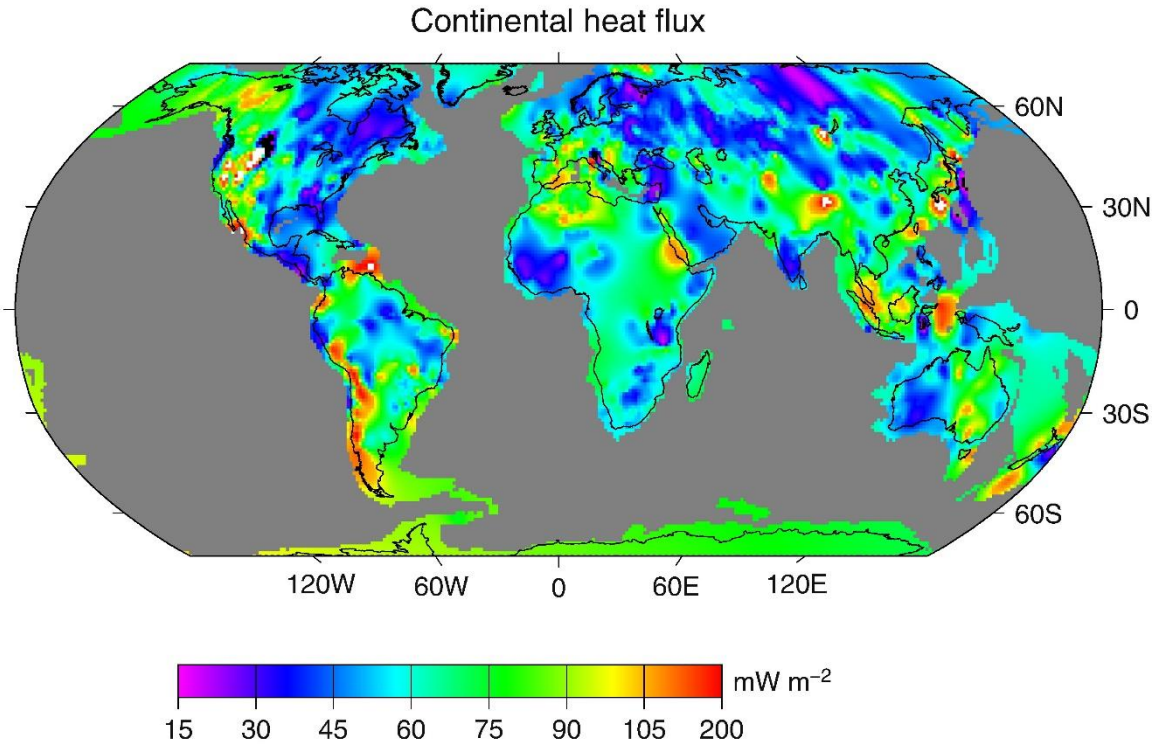

Figure 1. Map of continental heat flow (from Jaupart et al., 2016). Note that areas undergoing active tectonism and magmatism have higher surface heat flux compared to stable cratonic areas (<50 mW/m^2). Stable cratons are regions where conductive heat flow is likely to dominant, such that surface heat flow reflects crustal heat production and mantle heat flux (with little to no contributions from advective heat sources).

gradients (30–45 mW/m^2 geotherms) and projections of these gradients to the Moho suggests temperatures of 400–600°C (Hasterok and Chapman, 2011; Garber et al., 2018). Mantle xenoliths, however, only provide indirect constraints on Moho temperatures because robust thermobarometric calibrations are restricted to lithologies that equilibrated within the high-pressure garnet stability field (e.g., Brey and Köhler, 1990). Granulite xenolith derived from the lower crust could provide direct constraints on the thermal state of Moho, yet thermobarometry of granulite xenoliths often suggests geothermal gradients higher than peridotite xenoliths from the same sites (e.g., >60 mW/m^2; Jones et al., 1983; Semprich and Simon, 2014). This issue arises because most granulite xenoliths are refractory and

anhydrous, and thus fail to react and equilibrate beyond peak metamorphic conditions (e.g., Frost and Chacko, 1989; Pattison and Begin, 1990; Pattison, 2003).

The U-Pb isotope system holds much promise for extracting long-term thermal histories of the lower crust from xenoliths (Davis, 1997; Davis et al. 2003; Schmitz and Bowring, 2003; Blackburn et al., 2011; 2012; Edwards and Blackburn, 2018; O'Sullivan et al., 2021). U-Pb thermochronology exploits both the radioactive decay of U to Pb and the temperature-dependent retention (closure) of Pb in different accessory minerals (e.g., zircon, titanite, rutile, apatite). At temperatures above Pb closure, Pb will diffuse out of a crystal, precluding buildup of radiogenic Pb. At temperatures below Pb closure, Pb will be retained and the U-Pb ratios will evolve (Dodson, 1973). For zircon, Pb closure temperatures are >900 °C, for titanite >800 °C, for rutile ~500–600 °C, and apatite ~350–450 °C (all assuming a 50–500-µm-radius sphere and 0.01–0.1 °C/Myr cooling rates; Cherniak, 2010; Smye et al., 2018). These phases are thus expected to experience different degrees of Pb diffusion due to residence near or above their respective Pb closure temperatures in the lower crust (Schmitz and Bowring, 2003; Blackburn et al., 2011). For example, at 500 °C Pb diffusion in zircon, titanite, and rutile should be minor and the U-Pb system in these phases should exhibit closed-system behavior such that dates older than magmatic entrainment can be retained. At the same temperature, Pb diffusion in apatite would be significant (open-system behavior), resulting in U-Pb dates that overlap the timing of eruption, reflecting rapid cooling upon eruption. The ensuing chapters exploit multi-accessory U-Pb thermochronology in xenoliths to understand evolving heat fluxes throughout the lithosphere.

Chapter I constitutes a study of xenoliths and basement outcrops in northern Tanzania aimed at understanding how lower-crustal temperatures vary between the tectonically-stable

Archean craton and adjacent rifting crust. The average surface heat flow in the former is 38 mW/m^2 and in the latter is 47 mW/m^2. Rifting in this region is recent (<8 Ma; Dawson, 1991). Lower-crustal xenoliths from the craton margin have rutile have U-Pb dates that mostly fall into a 600–30 Ma age range and are interpreted to reflect residence at or below the Pb closure temperature of rutile. By contrast, rutile and apatite in Archean lower crustal xenoliths from the rifting crust yield near-zero age U-Pb isochrons, indicating residence at temperatures above rutile and apatite Pb closure prior to eruption. Rare titanite in on-rift lower-crustal granulite xenoliths preserve U-Pb dates related to decompression of the crust following orogenesis ca. 550 Ma. In tandem, these data suggest that Moho temperatures beneath the craton margin are cooler than below the rift, indicating that variable surface heat flow across northern Tanzania reflects changes in mantle heat flux. In concert with one-dimensional conductive geotherm models, I conclude that heat production across the area is uniformly low and consistent with previous estimates of crustal heat production in Archean provinces.

Chapter II focuses on kimberlite-borne xenoliths from the central Siberian craton. Rutile and apatite U-Pb dates in lower-crustal garnet granulite xenoliths range from 1.8 Ga to 360 Ma (the timing of kimberlite eruption). This contrasts with upper-crustal tonalite and amphibolite xenoliths that contain solely Paleoproterozoic apatite. Depth profiling of rutile from the lower-crustal xenoliths show that U-Pb dates increase gradually from rim to core over μm-scale distances, with Al, Zr, and Fe increasing in concentration across similar length-scales. The U-Pb and trace element gradients in rutile are incompatible with partial Pb loss during slow cooling in the lower crust and instead require depth-dependent heating of the crust for <1 Myr prior to eruption. A critical implication of these data is that Moho

temperatures were cooler than the Pb closure temperatures of rutile and probably apatite (<400°C) prior to entrainment at 360 Ma. The lower-crustal temperature bounds from these data are consistent with pressure-temperature arrays of Udachnaya peridotite xenoliths that suggest relatively cool geothermal gradients. Combined, the xenolith data conform to low geothermal gradients at the central Siberian craton (30–40 mW/m^2) and, consequently, low crustal heat production (~0.3 $\mu W/m^3$).

Chapter III of this thesis presents new ID-TIMS and LA-ICP-MS data for a suite of natural reference apatites. Apatite is a ubiquitous accessory mineral in igneous, metamorphic, and sedimentary rocks (Piccoli and Candela, 2002; Spear and Pyle, 2002; McCubbin and Jones, 2015). Because it takes in U, Sr, Nd, and other incompatible trace elements, petrochronological studies apatite studies have diverse applications, including but not limited to: thermo/petrochronology, provenance studies, and studying igneous and metamorphic petrogenesis processes (Spear and Pyle, 2002; Prowatke and Klemme, 2006; McFarlane and McCulloch, 2007; Horstwood et al., 2008; Chew et al., 2011; Henrichs et al., 2018). Despite the rising use of apatite petrochronology and geochemistry, suitable apatite reference materials (RMs) available for inter-laboratory comparisons (homogeneous, well-characterized, and accessible) are scarce. To ameliorate this issue, I determined the U-Pb, Sm-Nd, and Sr isotopic and elemental compositions of a suite of prospective apatite RMs, from Morocco and Brazil, using ID-TIMS and LA-ICP-MS. The data indicate that Morocco apatite may serve well as a U-Pb, Sm-Nd, and Sr RM, whereas Brazil apatite has the most potential as a Sm-Nd RM. These potential RMs provide new benchmarks for *in situ* apatite chemical analyses and inter-laboratory calibrations.

Chapter I. Four-dimensional thermal evolution of the East African Orogen: Accessory phase petrochronology of crustal profiles through the Tanzanian craton and Mozambique Belt, northeastern Tanzania

As published in Contributions to Mineralogy and Petrology in 2020

With co-authors Roberta L. Rudnick[1], John M. Cottle[1], Andrew R. C. Kylander-Clark[1], Madalyn S. Blondes[2], Philip M. Piccoli[3], and Gareth G.E. Seward[1]

[1]Department of Earth Science, University of California, Santa Barbara, CA 93106, USA

[2]United States Geological Survey, Reston, VA, 20192, USA

[3]Department of Geology, University of Maryland, College Park, MD, 20742, USA

ABSTRACT

Deep crustal xenoliths and basement outcrops across northeastern Tanzania provide insight into the thermal evolution of the Tanzanian craton and Mozambique Belt from Archean crust formation to Neoproterozoic orogenesis to Neogene rifting. At the craton margin, 2.8–2.5 Ga zircon, rutile, and apatite in granite and amphibolite xenoliths document thermal quiescence since the Archean. By contrast, lower crustal xenoliths from the same site record thermal pulses associated with Neoarchean ultra-high temperature metamorphism (ca. 2.64 Ga, >900°C zircon), the East African and Malagasy orogens (600–500 Ma rutile), and fluid influx during rifting (<5 Ma apatite). Rutile in garnet granulite xenoliths exhibit partial Pb loss that could be related to slow cooling of the lower crust after the orogeny. If so, this suggest residence at 500–600°C prior to entrainment; if partial Pb loss is instead a result of recent rifting, long-term ambient lower crustal temperatures could have been cooler. In contrast to the craton, the entire crust of the Mozambique Belt underwent differential cooling following the Proterozoic orogenies. Both the upper and middle crust record metamorphism from 640–560 Ma (zircon, monazite, and titanite) and rapid exhumation at 510–440 Ma (rutile and apatite). Lower crustal xenoliths from within the belt contain Archean zircon, but near-zero age rutile and apatite, indicating residence above their respective Pb closure temperatures at the time of eruption. Zoned titanite records growth during cooling of the lower crust at 550 Ma, followed by fluid influx during slow cooling and exhumation (0.1–1°C/Myr after 450 Ma). Permissible lower-crustal temperatures for the craton and orogen suggest variable mantle heat flow into the crust, reflecting differences in mantle lithosphere thickness rather than advective heating from rifting.

1.1 INTRODUCTION

Xenoliths carried rapidly to the surface by alkali basalts and kimberlites offer unique insights into the processes that operate at depth during lithosphere formation and evolution (Downes, 1993; Rudnick and Fountain, 1995). Of prime importance, xenoliths can yield direct constraints on the pressure-temperature evolution of the deep lithosphere, which in turn bear on models of heat transfer between the crust and mantle, the thermal evolution of orogens, and the distribution of heat-producing elements in the crust (Pollack and Chapman, 1977; Rudnick et al., 1998; Jaupart and Mareschal, 2014; Hacker et al., 2015).

Decrypting the rich record of lithosphere evolution contained within xenoliths, especially in high-grade granulites, is difficult with conventional petrological methods (e.g., major-element exchange thermobarometry and phase equilibria modeling) because many deep crustal xenolith suites are dominated by refractory and anhydrous lithologies that are effectively unreactive during retrogression (e.g., Frost and Chacko, 1989; Pattison and Begin, 1990). As a consequence, pressure-temperature (P-T) conditions during peak metamorphism are well-preserved, but conditions following metamorphism until volcanic eruption are much more uncertain. Geo- and thermochronometers in crustal xenoliths are sensitive to thermal histories that may be overlooked by petrological methods, providing an avenue to reconstruct the evolution of continental crust (e.g., Spencer et al., 2013; Garber et al., 2017). The U-Pb systematics of phases with different Pb closure temperatures—zircon, titanite, rutile, and apatite—commonly found in crustal lithologies provide bounds on the timing, duration, and rate of deep crustal heating and cooling (e.g., Davis, 1997; Davis et al., 2003; Schmitz and Bowring, 2003a, b; Blackburn et al., 2011). This is because the length-scales of U-Pb zonation in each of these minerals varies with temperature and duration of

thermal events, with length scales increasing with greater intensities and/or longer durations of heating (e.g., Kooijman et al., 2010; Blackburn et al., 2011; Smye et al., 2018). Thermal histories extracted from U-Pb data can be further tested and refined when they are combined with trace element data from the same phases: the length scales of trace elements should vary with the extent of heating according to their diffusivity (Crank, 1975). Further, trace-element data provide complementary information on thermal histories, such as crystallization temperatures or evidence for equilibration with metamorphic index minerals like garnet (e.g., Zack et al., 2004; Ferry and Watson, 2007; Hayden et al., 2008).

Here we report U-Pb and trace-element data for multiple accessory phases from crustal xenoliths erupted in young rift basalts (<1 Ma) on the Archean Tanzanian craton and adjacent Proterozoic Mozambique Belt in northeastern Tanzania, as well as outcrops of the Mozambique Belt. The xenoliths derive from variable crustal depths and, together with the outcrops, form composite sections through the crust. Data from zircon, monazite, titanite, rutile, and apatite data unravel a complex tectonic history in the area. In northeast Tanzania, key geologic events include crust formation and metamorphism in the Archean, continental collision during the Neoproterozoic–Cambrian East African and Malagasy orogenies, and present-day rifting. We use our data to address how orogenesis and recent rifting affected the long-term thermal state of the deep crust and to document lateral variations in the present-day thermal structure of the crust.

1.2 GEOLOGIC SETTING

The Archean Tanzanian Craton and the Mozambique Belt comprise the main basement units in northeastern Tanzania (Fig. 1) (Stern, 1994; Fritz et al., 2009). The latter consists of Archean–Mesoproterozoic crust that was metamorphosed to high grades during the

Neoproterozoic East African and Ediacaran–Cambrian Malagasy orogenies (e.g., Fritz et al., 2013), and is presently undergoing rifting. Each of these geological distinct regions and events are described below.

The Tanzanian Craton is an assemblage of granite-greenstone belts that formed from 2.8–2.5 Ga (e.g., Möller et al., 1998; Maboko, 2000; Manya et al., 2006; Sanislav et al., 2014; Thomas et al., 2016). Large granitic bodies were dominantly emplaced across the northern craton 2.7–2.5 Ga. Distinctive from other granitic assemblages are undeformed, ca. 2.6–2.5 Ga high-K granites which, due to their evolved geochemical compositions, are believed to have been produced by partial melting of pre-exiting crust in a continental collision zone (Manya and Maboko, 2003; Maboko et al., 2006) or a continental arc (Sanislav et al., 2018). Both seismic (Ritsema et al., 1998; Weeraratne et al., 2003) and xenolith studies (Lee and Rudnick, 1999; Chesley et al., 1999; Burton et al., 2000) suggest that the craton is underlain by a relatively thick (≥150 km), refractory, and Archean lithospheric mantle keel. Rayleigh wave tomography also reveals the presence of a thermal anomaly beneath the craton, which some have interpreted as evidence for a plume (e.g., Ritsema et al., 1998; Weeraratne et al., 2003). Indeed, mantle xenoliths from the deepest lithosphere bear evidence of heating and metasomatism (Lee and Rudnick, 1999; Chesley et al., 1999; Aulbach et al., 2008) consistent with the influence of a plume. Yet, surface heat flow on the craton margin is generally low (average of 38 mW/m^2; Nyblade et al., 1990; Nyblade, 1997), suggesting that any thermal perturbation below or within the mantle lithosphere is not yet manifested at the surface (Nyblade and Brazier, 2002; Weeraratne et al., 2003; Julià et al., 2005).

Outboard of the Tanzanian Craton is the Mozambique Belt (Fig. 1), a polymetamorphic orogen that underwent metamorphism during the East African (ca. 640–620 Ma) and Malagasy (ca. 560–540 Ma) orogenies (Fritz et al., 2013). Rocks recording the older Paleoproterozoic Usagaran orogeny dominantly crop out along the southeastern margin of the Tanzania Craton and are generally absent in the north (Fig. 1). Most of the Mozambique Belt in northern Tanzania was metamorphosed in the Cryogenian–Cambrian during periods of island arc accretion and subsequent continental collision (Stern, 1994; Fritz et al., 2013; Goscombe et al., 2019). The Mozambique Belt is generally divided into the Western Granulites and the Eastern Granulites. Both are lithologically similar and extensively deformed, but they generally record different metamorphic ages, metamorphic P-T paths, and protolith ages (Maboko, 1997; Appel et al., 1998; Möller et al., 1998; 2000; Maboko, 2001; Maboko and Nakamura, 2002; Johnson et al., 2003; Sommer et al., 2003; 2005; Fritz et al., 2005; 2009; Tenczer et al., 2013).

The Eastern Granulites are divided into a basement and cover. The basement is found primarily as uplifted blocks in the eastern Tanazania and is dominated by mafic–felsic orthogneisses with subordinate anorthosite, metapelite, and calcsilicates (Fig. 1) (Appel et al., 1998; Fritz et al., 2005 Tenczer et al., 2006; 2013). The cover consists of granitic orthogneisses, marbles, and metapelitic lithologies that occupy the lowlands to the west of the uplift basement (Fig. 1) (Tenczer et al., 2006; 2013). Whole-rock Sm-Nd model ages and zircon core U-Pb ages from the basement and cover are Meso- to Neoproterozoic (1500–700 Ma; Möller et al., 1998; Sommer et al., 2005; Hauzenberger et al., 2007; Tenczer et al., 2006; 2011; Mole et al., 2018; Mtabazi et al., 2019). The Proterozoic dates overlap in age with arc rocks distributed from the Arabian-Nubian Shield to Madagascar (e.g., Fritz et al.,

2013, and references therein) suggesting that the protoliths of the Eastern Granulites ultimately derive from a terrane outboard of the Tanzanian craton (e.g., Möller et al., 1998; Maboko and Nakamura, 2002; Mole et al., 2018). Detailed petrologic and thermobarometric studies of metapelites from the basement suggest similar P-T paths across strike the Eastern Granulites. The metapelites contain relict sillimanite inclusions in garnet and kyanite in the matrix, which are in turn rimmed by sillimanite (Appel et al., 1998); endmember equilibria thermobarometry indicate counter-clockwise P-T paths that attained peak metamorphism at 0.9–1.1 GPa and 750–850°C, followed by near isobaric cooling at 0.8–1.0 GPa before undergoing final exhumation (Coolen et al., 1982; Muhongo and Tuisku, 1996; Appel et al., 1998; Muhongo et al., 1999). These P-T paths have been interpreted to reflect metamorphism by magmatic underplating and loading at the base of a continental margin (as opposed to crustal thickening by continental collision; e.g., Bohlen and Mezger, 1989; Appel et al., 1998). Metamorphic monazite and zircon rims in the Eastern Granulites basement yield ca. 640–610 Ma dates (Möller et al., 1998, 2000; Tenczer et al., 2006; 2013; Thomas et al., 2016) and have been linked to episodes of underplating/loading during arc assembly (i.e., the East African Orogen; Möller et al., 2000; Cutten et al., 2006; Tenczer et al., 2006). Multi-grain U-Pb thermal ionization mass spectrometry (TIMS) dates of titanite from calcsilicates and orthogneisses and rutile from metapelites are 620–610 Ma and 550–500 Ma, respectively, and have been interpreted to correspond to slow exhumation and cooling (Möller et al., 2000).

The Western Granulites consist of Archean and Paleoproterozoic protoliths metamorphosed at amphibolite–granulite facies ca. 550 Ma (e.g., Möller et al., 1998; Vogt et al., 2006; Tenczer et al., 2013; Sommer et al., 2003; 2017). Detailed P-T data for the

Western Granulites are limited to studies of rare whiteschists at Mautia Hill (Jöns and Schenk, 2004; Cutten et al., 2006) and metapelites along the Ruaha river (Sommer et al., 2003; 2017). The whiteschists have polymetamorphic mineral assemblages that record metamorphism along clockwise P-T paths with peak metamorphism at 1.2–1.4 GPa and 700–850°C followed by isothermal decompression (Jöns and Schenk, 2004; Cutten et al., 2006). Metamorphic zircon rims from the whiteschist give imprecise 549 ± 41 Ma dates (Cutten et al., 2006). At Kidatu, along the Ruaha river, Sommer et al. (2003; 2017) also report clockwise P-T paths (see also Fritz et al., 2013), though peak metamorphism is dated at ca. 640 Ma, significantly older than most metamorphic dates for the Western Granulites. Whole-rock Sm-Nd model ages and zircon U-Pb core dates range from 2.7–2.5 Ga and 2.0–1.8 Ga (Möller et al., 1998; Johnson et al., 2003; Tenczer et al., 2013; Thomas et al., 2016). Metamorphic monazite and zircon rims are ca. 560–540 Ma and indicate that the Western Granulites protoliths were metamorphosed later than the Eastern Granulites (Johnson et al., 2003; Sommer et al., 2003; Cutten et al., 2006; Tenczer et al., 2013). The 560–540 Ma dates represent the timing of collision between east and west Gondwana and this event is referred the Kuunga or Malagasy orogeny (e.g., Meert, 1995; 2003; Collins and Pisarevsky, 2003; Goscombe et al., 2020). During this period, the Tanzanian craton margin (west Gondwana) was buried beneath the collage of exotic arc terranes and attending continental masses (east Gondwana) (e.g., Fritz et al., 2011; Tenczer et al., 2013).

The broad structure of the Mozambique Belt is constrained by geophysical and xenolith studies. The crust is estimated to be 38–42 km thick based on S-wave receiver functions (Julià et al., 2005), but thermobarometry of lower crustal xenolith indicates that the crust was at least 60 km thick in the past (Mansur et al., 2014). Zircon U-Pb dates of lower crustal

xenoliths from within the Mozambique Belt are exclusively Archean (Mansur et al., 2014). These data are consistent with Archean crust—along with the Western Granulites—forming the lower plate of the orogen, whereas the Eastern Granulites comprise the upper plate (Fig. 1; Cutten et al., 2006; Tenczer et al., 2013).

Rayleigh wave tomography indicates that the mantle lithosphere beneath the orogen is thinner compared to the craton, but there are significant uncertainties in lithosphere thickness based on this method (Weeraratne et al., 2003). Thermobarometry on garnet-bearing peridotite xenoliths from Lashaine suggest a minimum thickness of ~165 km (Rudnick et al., 1994), though garnet-bearing mantle xenoliths are rare elsewhere in the area (Cohen et al., 1984; Dawson and Smith, 1988; Aulbach et al., 2011). Compared to the craton, surface heat flow in the orogen is higher and more variable (40–60 mW/m^2, average 47 mW/m^2; Nyblade, 1997).

The East African rift system initiated in Ethiopia at ca. 40–30 Ma and propagated southward, reaching northern Tanzania by 8 Ma (Ebinger, 1989; Dawson, 1992; Foster et al., 1997). Where the rift impinges against the Tanzanian Craton, it widens and diverges into a western and eastern branch (inset in Fig. 1). The western branch forms a series of segmented normal faults (e.g., Ebinger, 1989), whereas the eastern branch is more magmatically active and forms numerous rift valleys that lie along older structures between the craton and orogenic belt and along sutures within the orogen (Dawson, 1992; Nyblade and Brazier, 2002; Le Gall et al., 2004; 2008). From 4.5 Ma to <0.5 Ma, rifting along the eastern branch led to the eruption of numerous tuff cones (Dawson, 1992; Le Gall et al., 2008), some of which bear xenoliths.

1.3 SAMPLES

The xenoliths investigated in this study come from young (<1 Ma) rift basalts erupted on the Tanzanian Craton and Mozambique Belt (Fig. 1). Mantle lithologies—garnet and spinel peridotites, pyroxenites, dunites, and glimmerites—have been widely investigated for their petrology, geochemistry, and physical properties (e.g., Dawson et al., 1970; Dawson and Smith, 1988; 1992; Dawson, 2002; Rudnick et al., 1993; Rudnick et al., 1994; Canil et al., 1994; Lee and Rudnick, 1999; Chesley et al., 1999; Burton et al., 2000; Vauchez et al., 2005; Aulbach et al., 2011; Chin, 2018; Xu et al., 2019), whereas previous work on crustal xenoliths is more limited (Dawson et al., 1970; Jones et al., 1983; Cohen et al., 1984; Bellucci et al., 2011; Mansur et al., 2014).

We analyzed accessory phases from 32 crustal xenoliths and seven surface samples using laser-ablation split-stream inductively coupled plasma mass spectrometry (LASS) (Table 1). Xenoliths come from three main regions: at the craton margin (Labait), within the Western Granulites (Natron area), and within the Eastern Granulites cover (Arusha area) (Fig. 1). Individual petrographic descriptions are presented in Appendix A.

1.3.1 Labait

The analyzed suite of Labait xenoliths consists of ten samples interpreted to sample the upper–lower crust samples—granite, schist, amphibolite, and granulites (Table 1). One granite xenolith is undoubtedly from the upper crust. In contrast, it is difficult to be certain of derivation depths of the schist and amphibolite xenoliths. Because the craton surface is dominated by granitoids, syenites, and orthogneisses, we infer that these xenolith lithologies are from mid-crustal depths, though this is not required. Additionally, pseudosection modeling for one amphibolite xenolith (sample LB04-89) indicates equilibration pressures

of <1 GPa and <450°C (Fig. S4), corroborating a mid-crustal origin. Six granulite xenoliths derive from lower-crustal depths. Thermobarometry and pseudosection modeling of two-pyroxene gabbroic granulite xenoliths indicate equilibration at >750°C and <1.0–1.2 GPa (Mansur et al., 2014). Garnet-orthopyroxene granulites equilibrated at higher pressures (1.0–1.6 GPa) and are interpreted to be derived from the lowermost crust of the craton (Mansur et al., 2014).

1.3.2 Natron area

We have analyzed ten xenoliths from Naibor Soito, Kisite, Pello Hill, and Eledoi (Fig. 1), which we refer to collectively as the Natron group. The Natron group xenoliths include orthogneisses, amphibolites, and granulites. As is the case for the Labait xenolith suite, the absence of key phases, like garnet, in the orthogneiss and amphibolite xenoliths and the occurrence of high-grade lithologies at the surface (Fig. 1) complicates interpretations of the derivation depths of these xenoliths. Pseudosection modeling of one amphibolite (sample LJ04-26) and one orthogneiss (sample OM04-13) indicates maximum pressures of 0.6–0.8 GPa (see Appendix A.).

Granulite xenoliths likely sample the *in situ* lower crust. Naibor Soito granulite xenoliths have variable mineral assemblages (Table 1), but thermobarometry and pseudosection modeling are all consistent with equilibration at >700°C and >1 GPa (Mansur et al., 2014). Mafic garnet granulites from Kisite and Pello Hill are similar to those from Naibor Soito and are thus also interpreted to be from the *in situ* lower crust.

1.3.3 Arusha area

We analyzed twelve xenoliths from Lashaine, Lemugur, Loljoro, and Olmani, referred to herein as the Arusha group. Rocks in the Arusha suite include orthogneisses, quartzites, schists, amphibolites, and garnet granulites. Like the Natron group xenoliths, we infer that the orthogneiss, quartzite, schist, and amphibolite xenoliths are from the middle crust (rather than the upper crust). Garnet granulite xenoliths from Lashaine are exclusively mafic (Table 1). Based on thermobarometry and pseudosection calculations and the presence of kyanite and garnet coronae, garnet granulites are inferred to have equilibrated at the base of a doubly-thickened crustal section (~800°C to >1200°C and 1.3 to >1.7 GPa; Jones et al., 1983; Mansur et al., 2014). Thermobarometry of biotite-garnet granulites suggest equilibration at temperatures and pressures lower than biotite-free garnet granulites (~600°C and <0.8 GPa; Mansur et al., 2014), indicating a shallower (likely mid-crustal) origin for these xenoliths (Table 1).

1.3.4 Basement outcrops

To obtain a more complete picture of the thermal history of the crust, we analyzed seven high-grade basement outcrops from the Western and Eastern Granulites. These include intermediate–mafic granulites and orthogneisses that were metamorphosed at mid–lower crustal depths during orogeny before being exhumed at the surface through post-orogenic uplift and erosion (e.g., Appel et al., 1998; Möller et al., 2000; Cutten et al., 2006).

Surface samples come from three areas in the Mozambique Belt: Loibor Serrit, Magugu, and Longido (Fig. 1). Loibor Serrit is situated within the Eastern Granulite cover (Tenczer et al. 2013). Samples from Loibor Serrit are orthogneisses containing clinopyroxene + plagioclase ± orthopyroxene ± quartz ± hornblende ± biotite ± garnet (some with

clinopyroxene rims) (Table 1). Samples from Longido and Magugu are situated within the Western Granulites. The Longido and Magugu samples are both foliated orthogneisses containing garnet + plagioclase + quartz + orthopyroxene ± hornblende ± biotite (Table 1).

1.4 METHODS

Accessory phases were separated at UCSB using standard crushing, magnetic and heavy liquid separation methods. LASS analyses utilized a Cetac Teledyne 193 nm excimer Analyte laser with a HelEx ablation cell coupled to two mass spectrometers: a multicollector (MC)-ICPMS for U-Pb dating and a quadrupole (Q)-ICPMS for simultaneous trace element determinations (following procedures modified from Kylander-Clark et al., 2013). A Nu Instruments Plasma HR-ES MC-ICP multicollector was used for data obtained in the first phase of the project, and a Nu Instruments Plasma 3D MC-ICP for later analyses. Trace elements were acquired using an Agilent 7700S Q-ICP. LASS analyses were done in two ways: conventional LASS spot analyses on polished crystal interiors or depth profiling of whole grains.

Laser ablation split-stream ICP-MS (LASS) analyses were done by conventional spot analyses on polished grains and by depth profiling on whole, unpolished grains. For spot analyses, laser spot sizes and fluences varied depending on the analyzed phases: 25 µm, 50% of 6 mJ for zircon; 8 µm, 50% of 6 mJ for monazite; 35 µm, 50% of 6 mJ for titanite; 50 µm, 100% of 9 mJ for rutile; and 50 µm, 50% of 6 mJ for apatite. The program Iolite (v. 2.5; Paton et al., 2011) was used to correct raw U-Pb and trace-element data for baselines, laser- and plasma-induced element fractionation, and instrument drift.

We employed matrix-matched primary and secondary standards throughout the analytical sessions to assess accuracy and precision. Zircon U-Pb analyses employed

reference material (RM) 91500 (1065 Ma, ID-TIMS; Wiedenbeck et al., 1995) as the primary bracketing standard with zircon RMs GJ1 (602 Ma, ID-TIMS; Jackson et al., 2004) and Plesovice (337 Ma, ID-TIMS; Sláma et al., 2008) analyzed as secondary standards. Monazite U-Pb analyses used RM 44069 (424 Ma, TIMS; Aleinikoff et al., 2006) as the primary standard with RMs Stern (512 Ma, ID-TIMS; Palin et al., 2013) and Treblicock (273 Ma, TIMS; Tomascak et al., 1996) as secondary standards. Titanite U-Pb analyses employed RM MKED1 (1518 Ma, ID-TIMS; Spandler et al., 2016) as the primary bracketing standard with titanite RMs BLR (1047 Ma, ID-TIMS; Aleinikoff et al., 2007) analyzed as the secondary standard. Rutile analyses employed rutile RM R10 (1091 Ma; Luvizotto et al., 2009) as the primary bracketing standard; rutile RMs Wodgina (2845 Ma; Ewing et al., 2015) and 9826J (382 Ma; Kylander-Clark et al., 2008) were analyzed as secondary standards. For apatite U-Pb analyses, RM MAD (479 Ma, ID-TIMS age; Apen et al., 2022) as the primary bracketing standard with apatite RMs McClure (524 Ma, ID-TIMS age; Schoene and Bowring, 2006) and OD306 (1597 Ma, ID-ICPMS age; 1545 Ma, LA-ICPMS age; Thompson et al., 2016) used as secondary standards.

We augmented the uncertainties of the baseline- and fractionation-corrected U-Pb data with the excess variance of secondary standards run throughout multiple analytical sessions; this typically introduced additional uncertainties of 1–4 % for $^{206}Pb/^{238}U$ and 1–2 % for $^{207}Pb/^{206}Pb$, which were added in quadrature. The U-Pb data were plotted on Tera-Wasserburg diagrams using the Isoplot plug-in for Excel (Ludwig, 2008). We refer to the weighted mean age and internal 2σ uncertainty of concordant analyses—>95% concordance between $^{238}U/^{206}Pb$ and $^{207}Pb/^{206}Pb$ ages—that comprise a single age population (Wendt and Carl, 1991). For phases that incorporate variable amounts of common Pb, like titanite and

apatite, we calculated isochron ages derived from multiple spot analyses. In the case where combined spot analyses do not enable a regression back to a common Pb composition, we utilized a model Pb composition at 2.6 Ga or 550 Ma (Stacey and Kramers, 1975) or the Pb composition of feldspars from the samples, where they exist (Bellucci, 2011; Bellucci et al., 2011), to correct the apparent $^{238}U/^{206}Pb$ date.

Trace-elements were also computed in Iolite. Analyses were corrected using internal-element standardization (Liu et al., 2008) with the standard glass BHVO for titanite, rutile, and apatite analyses, RM GJ-1 for zircon, and RM Stern for monazite. Internal elements used for standardization were: ^{90}Zr for apatite, ^{31}P for apatite, ^{44}Ca for titanite, ^{49}Ti for rutile, and ^{44}Ca for apatite (all assuming ideal stoichiometric values). The quoted uncertainties include only analytical uncertainties.

Depth profile analyses utilized similar procedures described above. We only analyzed grains that appeared to be intact, had a large enough surface for laser spot placement, and had appreciable amounts of U (>0.5 ppm). Several zircon, monazite, and titanite grains—where present—were depth profiled. Apatite and rutile in some samples were either too small (<40 μm) or were anhedral fragments, and thus were not depth profiled. We made no attempt to depth profile phases that were uniformly near-zero in age according to their spot analyses (i.e., apatite and rutile in most garnet granulites). In the case of rutile, these criteria severely limited our depth profile sampling: only samples LB04-36 and LJ04-08 had grains that were intact, of sufficient size, contained appreciable amounts of U-Pb, and yielded non-zero U-Pb dates.

Total ablation time for depth profiling was 75 secs (150 laser pulses at a repetition rate of 2 Hz) for zircon, titanite, rutile, and apatite. Monazite depth profiles utilized an 8-μm-

diameter spot size with a total ablation time of 25 secs (50 laser pulses at 2 Hz). Resulting pit depths were measured optically and were 10–13 μm deep for zircon, titanite, rutile, and apatite and 3–5 μm deep for monazite. The raw data for depth profiles were also processed using Iolite (see above). Whole profiles were exported from Iolite without formal uncertainties, and we approximated the uncertainty of each data point within a given profile using the 2RSD % of the primary standard (after Cottle et al., 2012).

1.5 RESULTS

Our dataset consists of depth profiles and spot analyses for a variety of accessory minerals. In most cases, spot analyses were able to date rims that were also sampled by depth profiling (see Fig. 2 for examples of zircon rims). Because spot analyses have lower uncertainties associated with both their U-Pb and trace-element compositions (Appendix A), we refer to them in our plots and discussion. Where depth profiling uniquely captured an age or compositional gradient, we present depth profile data separately from spot analyses.

1.5.1 Labait

Zircon, rutile, and apatite in upper–middle crustal xenoliths at Labait—one granite, one schist, and two amphibolites (Table 1)—record Archean dates. Zircon in the granite and schist is generally metamict and highly discordant (Appendix A), but in amphibolite xenoliths LB04-89 and LB04-92 zircon yields concordant dates of 2.68 ± 0.17 Ga and 2.65 ± 0.04 Ga, respectively (Table 2). Zircon has uniform trace-element compositions (Fig. 3) and records TiZ temperatures of ~680°C (Table 2). Rutile in one amphibolite xenolith (LB04-89) yields an Archean lower intercept date of 2.63 ± 0.03 Ga (Fig. 4) and exhibits ZiR temperatures between 520 and 730°C (Table 2). Apatite in these xenoliths lie along a 2.5 Ga reference isochron (Fig. 5A; see Table 2 for individual sample dates).

Zircon, rutile, and apatite in Labait granulite xenoliths yield variable U-Pb and trace elements data. Cathodoluminescence (CL) imaging of polished zircon grains from the granulite xenoliths reveals multiple growth domains in the form of thick overgrowths that mantle small (<40 μm), dark cores with strong sector zoning (Fig. 2A). In the three, two-pyroxene granulites, U-Pb zircon dates range from 2.8–2.6 Ga (Fig. 3A). Decreased Eu/Eu* and increased Ti contents—indicative of temperatures up to 940°C—correspond to younger dates (Fig. 3B, E). Zircon in three garnet-bearing granulites records dates that are slightly younger—mostly 2.76–2.54 Ga (Fig. 3A). Ti contents suggest temperatures that extend well into ultra-high temperatures (UHT; >900°C) at ca. 2.64 Ga (Fig. 3C). Zircon in the garnet granulites also documents elevated Gd/Yb_N and lower Lu/Hf across the same time interval, consistent with growth in the presence of garnet during this UHT event (Fig. 3B).

Rutile in Labait garnet-bearing granulites displays complex age and elemental patterns. Most rutile grains have low U (<1 ppm), making it difficult to extract dates from depth profiles (see Appendix A); we instead focus on spot analyses. Further complicating matters is that back-scattered electron (BSE) imaging and energy-dispersive X-ray spectroscopy (EDS) reveals networks of fine zircon exsolution lamellae in some grains (Fig. 2D). Spot analyses with elevated Si (>700 ppm) likely represent contamination from zircon exsolution lamellae and are filtered from the final rutile dataset (see Appendix A). A subset of analyses lies near concordia at 600–500 Ma (inset in Fig. 4B), though most are largely discordant (Fig. 4B). Common-Pb corrected dates from the filtered dataset range are 600 Ma to <20 Ma (Fig. 4B) with one datum at ca. 2.5 Ga and another at ca. 1.2 Ga. Concentrations of Zr vary by almost two orders of magnitude in the analyzed rutile grains (100–8000 ppm)

corresponding to temperatures between 500 and 900°C (Fig. 4C), but do not correlate with U-Pb date (Fig. 4D).

Apatite in two-pyroxene granulites show distinct U-Pb trends: in one sample (intermediate granulite LB04-36), the data lie along a 2.5 Ga reference isochron and diverge towards youngers dates (Fig. 5B), and in another sample (mafic granulite LB04-82), the data scatter about a 400 Ma reference isochron, but also show mixing with an older, Archean-age component (Fig. 5C). Depth profiles reveal the presence of discrete young (down to 10 Ma), <5 µm thick overprints on the edges of grains (Fig. 5D, E). Concomitant with changes in U-Pb dates are shifts in LREE and Sr contents. CL imaging of the dated grains reveals an intricate network of dark patches around grain rims and along cracks (Fig. 2E) typically observed in phases that have undergone partial dissolution/reprecipitation (e.g., Corfu et al., 2003; Harlov et al., 2005; Holder and Hacker, 2019).

1.5.2 Natron and Arusha

Crustal xenoliths from the Natron and Arusha areas contain accessory phases with a wide range of U-Pb and elemental compositions (Fig. 7). Given the large number of phases analyzed in the various xenoliths (see summary in Table 2), we focus on general trends in the data from middle (schists, amphibolites, orthogneisses, quartzites, etc.) and lower crustal (granulites) samples from the two xenolith regions (Natron and Arusha).

Zircon in three mid-crustal xenoliths from the Natron area and seven mid-crustal xenoliths from the Arusha area yield Neoproterozoic dates, Archean dates, or both (i.e., Neoproterozoic rims around Archean cores) (Table 2). There are general compositional differences between the Archean and Neoproterozoic age groups, including lower Th/U and Ti and higher Gd/Yb_N in the latter, but other than these, there are no clear temporal trends in

the zircon data (Appendix A). The Neoproterozoic dates in the mid-crustal xenoliths from both areas overlaps with those from the Western Granulites (Table 2), but the xenoliths show a much larger range of Archean dates, including much older populations at 3.0–2.6 Ga (Fig. S9).

Monazite is present in three mid-crustal xenoliths: Natron orthogneiss (EL04–01) and in an Arusha quartzite (LJ04-08) and schist (LG04-09; Fig. 7). Qualitative X-ray maps reveal core–rim differences in REEs and Y in different monazite grains (Fig. 2B). Spot analyses of monazite in Natron orthogneiss sample EL04-01 dominantly yield Archean cores that show minor mixing with a Neoproterozoic component; a Neoproterozoic rim is confirmed by depth profiling (546 ± 12 Ma; Table 2) and by chemical dates (Appendix A). In Arusha quartzite sample LJ04-08, spot analyses throughout different monazite grains yield a single age population (588 ± 2 Ma). In Arusha schist sample LG04-09, spot analyses of distinct compositional zones yield dates ranging from 605–567 Ma and show increasing Y and decreasing Gd/Yb_N with younger dates (Appendix A).

Titanite, rutile, and apatite in mid-crustal xenoliths from the Natron and Arusha groups are Neoproterozoic–Paleozoic in age. Titanite in a Natron amphibolite PH04-02 yields an age of 533 ± 7 Ma and an average ZiT temperature of ~760°C (Table 2). Titanite in Arusha orthogneisses LJ04-26 and OM04-13 (Table 1) yields 528 ± 9 and 514 ± 10 Ma dates, respectively, and a tight range of ZiT temperatures of 750–770°C (Table 2). Dates for titanite grains in Arusha amphibolite LG04-37 range between 540–480 Ma (Fig. 7) and have average ZiT temperatures of ~770°C (Table 2). Rutile in two Arusha schist and quartzite xenoliths (samples LG04-09 and LJ04-08) yields 500 ± 4 and 498 ± 3 Ma dates (Fig. 7) and both have overlapping 700–710°C ZiR temperatures (Table 2). Apatite dates are highly

variable among the Natron and Arusha mid-crustal xenoliths, but all are younger than coexisting titanite and rutile (Fig. 7); in Natron samples, apatite dates range from 515–470 Ma and in the Arusha samples 480–440 Ma (Table 2).

Accessory phase dates in granulite xenoliths are distinctive from those recorded in upper- and mid-crustal xenoliths. Zircon is only found in Natron mafic–intermediate granulite xenoliths, and is exclusively Archean (2.8–2.5 Ga) and has TiZ temperatures of 760–820°C (Table 2). Titanite in one mafic Natron garnet granulite and two mafic Arusha garnet granulites yields Neoproterozoic–Mesozoic dates, which are discussed separately below. Granulite xenoliths in both the Natron and Arusha groups all contain near-zero rutile and apatite dates (Fig. 7; Table 2); in Natron granulites where quartz and zircon are present, ZiR temperatures are 690 and 770°C (Table 2).

The presence of titanite overgrowths on rutile in the Natron and Arusha granulite xenoliths is given particular attention because they are retrogression features that can be linked to exhumation history of the lower crust (e.g., Manning and Bohlen, 1991; Ernst and Liu, 1998; Frost et al., 2001). Spot analyses of titanite in the two Arusha samples (samples 89-729 and 89-731) yield 550–260 Ma dates; depth profile data show a gradual decrease in age toward the rims (Fig. 8D, E). Trace elements with distinct diffusivities—like Sr, Nd, Nb, and Zr (e.g., Holder et al., 2019)—show similar variability across the depth profiles in the two samples. By contrast, spot analyses of titanite in a Natron granulite (sample KS04-10) vary between 550 and 440 Ma, but depth profiling does not show a rim-core relationship like that observed in the Natron granulites (Fig. 8D, F).

1.5.3 Mozambique Belt

Zircon from five samples of the Eastern Granulite cover locality at Loibor Serrit records concordant U-Pb dates ranging from 920–640 Ma (Fig. 6A). Zircon in garnet-absent two-pyroxene granulites and orthogneisses shows relatively constant Gd/Yb_N, Ti, and Th/U, but lower Eu/Eu* at 750–640 Ma. In garnet-bearing granulites, zircon records a spread of dates from 890–630 Ma and show greater variations in their trace elements (dark blue diamonds in Fig. 6B–E). Temperatures range from to 750°C to ~690°C from 780–610 Ma, Gd/Yb_N increases at 780–770 Ma, and Eu/Eu* decreases with decreasing age (Fig. 6B–E).

Titanite, rutile, and apatite in the Eastern Granulite cover are as young or younger than the youngest zircon dates (Fig. 7). Titanite and rutile in the same garnet-granulite (sample LS06-12) yield uniform U-Pb dates of 614 ± 3 and 568 ± 18 Ma, respectively. Application of the ZiR and ZiT thermometers in this sample yields overlapping temperatures of 860–900°C at 1.0–1.4 GPa. Apatite U-Pb dates in all samples significantly post-date those of titanite and rutile, and dominantly fall along a 527 Ma reference isochron (Fig. 7F; see Table 2 for individual sample dates).

Dates from two orthogneisses of the Western Granulites at Magugu and Longido are Archean and Neoproterozoic (Table 2). Concordant zircon rim dates are 613 ± 4 Ma and 630 ± 16 Ma (5–40 μm thick; Fig. 2A) and concordant zircon Archean cores dates are 2944 ± 20, 2522 ± 17 Ma, 2420 ± 6 Ma (Table 2). The rims record relatively low TiZ temperatures and Th/U compared to older cores (Fig. 6D). Titanite in sample LK06-02 has an age of 543 ± 13 Ma (Fig. 7) with a ZiT temperature of ~750°C (Table 2). Rutile in sample MG04-01 yields younger 515 ± 8 Ma dates (Fig. 7) and ZiR temperatures of ~680°C (Table 2). Apatite in

sample LK06-02 has an age of 457 ± 25, and apatite in sample MG04-01 has an age of 510 ± 9 Ma, which overlaps in age with rutile from the same rock (Fig. 7).

1.6 DISCUSSION

1.6.1 Diffusive length-scales

To distinguish Pb loss by thermally-mediated volume diffusion from non-diffusional processes (e.g., neocrystallization or recrystallization), we use the experimentally- and empirically-derived diffusivities of multiple elements. We assess characteristic length scales assuming diffusion through a sphere, described by the following relationship (Crank, 1975): $L= \sqrt{4Dt}$, where L is the characteristic diffusion length-scale, D is temperature-dependent diffusivity, and t is the duration of heating. If compositional variation in a mineral were driven by thermally-mediated volume diffusion, elements with different diffusivities should record different length-scales for a given temperature and duration of heating (Fig. 9). Additionally, where volume diffusion is inferred, this simple relationship enables distinction between diffusion caused by thermal events separated by significant time intervals. In our study, this could be recent heating related to rifting (<4 Myr; Dawson, 1992; Le Gall et al., 2008) versus long-term isothermal residence since orogeny (~600 Myr; Möller et al., 2000). Depth profiling is capable of resolving micron-scale near-rim variations—such as metamorphic rims or isotopic elemental gradients induced by thermally-mediated volume diffusion (e.g., Smye and Stockli, 2014; Stearns et al., 2016).

1.6.2 Multiple thermal imprints in the Tanzanian craton

1.6.2.1 Archean thermal histories

Zircon, rutile, and apatite from Labait granite, schist, and amphibolite xenoliths indicate that the upper–middle crust of the craton has not experienced significant thermal

overprinting since the Archean. Assuming that the upper and middle crust formed at similar times in the Archean, and integrating TiZ temperatures calculated for concordant zircon (~680°C at ~2.68 Ga in amphibolites; Table 2) and the ages and the nominal Pb closure temperatures of rutile and apatite (2.6 and 2.5 Ga over ~550–400°C), we calculate time-averaged cooling rates between 1 and 3°C/Ma from 2.6–2.5 Ga (Appendix A). The preservation of Neoarchean apatite dates further suggests that neither the Usagaran and East African orogenies, nor rifting have affected the upper–middle crust of the craton, even at its margin. Feldspar Pb isotope data from craton exposures near Dodoma (Fig. 1) do show resetting at 2.0 Ga (Möller et al., 1998), suggesting that the Usagaran Orogen only impacted the southern portion of the craton and does not extend to the Labait region (Fritz et al., 2005).

In contrast to upper–middle crustal xenoliths, lower crustal granulite xenoliths from Labait show evidence for thermal pulses during later Archean, Neoproterozoic, and recent events. Neoarchean UHT conditions are recorded in TiZ temperatures of ≥950°C at ca. 2.64 Ga in both the two-pyroxene and garnet granulites (Fig. 3E). UHT conditions were likely accompanied by partial melting (e.g., Yakymchuk and Brown, 2014) as indicated by the greater magnitude negative Eu anomalies in the hotter zircons (Fig. 3E). This trend reflects either buffered Eu^{3+}/Eu^{2+} ratios during feldspar crystallization (Kohn and Kelly, 2017) or changing redox state of the system (Hinton and Upton, 1991). Although the Eu^{3+}/Eu^{2+} ratio is redox-sensitive, this ratio is buffered by more dominant redox-sensitive elements (e.g., Fe), such that when feldspar removes Eu^{2+} during crystallization from a melt, some amount of Eu^{3+} is reduced to Eu^{2+} to maintain the Eu^{3+}/Eu^{2+} ratio (Kohn and Kelly, 2017). Because zircon preferentially incorporates Eu^{3+}, zircon that co-crystallizes with feldspar will have

increasing magnitudes of negative Eu anomalies over time, at constant fO_2 conditions (Kohn and Kelly, 2017). Were negative Eu anomalies related to lower oxygen fugacity, Ce anomalies in zircon should become more subdued (Trail et al., 2012; Kohn and Kelly, 2017), but only a weak trend between Ce anomalies and date is observed (Fig. S7). The same trend could reflect protracted zircon growth from a melt; zircon is the only phase present that preferentially sequesters and depletes Ce^{4+} in the system (Trail et al., 2012). Zircon geochemical signatures are best explained by protracted zircon crystallization from melt during Archean UHT metamorphism in the lower crust.

Ultra-high temperature metamorphism and partial melting of the lower crust of the Tanzanian Craton had previously been inferred on the basis of exsolved ternary feldspars in the two-pyroxene granulite xenoliths and significant whole-rock depletions of Cs, Rb, Th, and U (Mansur et al., 2014). Additional evidence for partial melting at this time is presence of 2.66–2.62 Ga high-K granites on the craton (Maboko et al., 2006; Sanislav et al., 2014; 2018) as well as U-depletion inferred from Pb isotopes in feldspars from Western Granulites (Möller et al., 1998). Zircon temperatures are highest at 2.62–2.60 Ga in the granulite xenoliths, providing a temporal link between deep crustal metamorphism and granite production.

1.6.2.2 Neoproterozoic and Neogene thermal overprinting

In addition to UHT metamorphism, the lower crust of the craton margin was affected by the East African Orogen and recent rifting. Previously, the only evidence for EAO-related events in the Labait lower crust was a garnet anorthosite containing plagioclase with Pb isotopic compositions plotting near a 550 Ma geochron (Mansur et al., 2014). Rutile in Labait garnet granulites dominantly yields Proterozoic and younger dates that point to a

complex thermal history in response to the East African and Malagasy orogenies. While there is evidence of an Archean phase of rutile growth—two data points at ca. 2.5 Ga and ca. 1.1 Ga (inset in Fig. 4B)—it is difficult to draw conclusions based on so few data. The two older rutile spot analyses exhibit modest temperatures of ~750°C (Fig. 4C), suggesting that the high ZiR temperatures recorded in the younger rutiles represent an additional high-T event after the Archean. Indeed, the most concordant rutile data at 600–500 Ma record elevated ZiR temperatures of ~820°C, yet most ZiR temperatures, however, do not correlate with date (Fig. 4D). Recrystallization and Pb loss during post-orogenic cooling and/or rift-related heating may explain the disparate U-Pb and trace-element patterns.

The range of ZiR temperatures may represent diffusive resetting, distinct thermal events, or variable $aSiO_2$ and/or $aZrSiO_4$ during rutile crystallization. The combined data suggest that variable $aZrSiO_4$ is the most likely scenario. The spread of ZiR temperatures is not likely to be related entirely to diffusive loss of Zr during rift-related heating. For 4 Myr at holding temperatures of 800°C (oldest rift magmatism in the area; Dawson, 1992), Zr diffusion would occur over length-scales of ~120 μm and the U-Pb system would be reset across the whole rutile grain (>200 μm; Fig. 9A) (Ewing et al., 2013; Pape et al., 2016), contrary to the preservation of Mesoproterozoic and older dates. Given the lack of any trend between ZiR temperature and U-Pb dates (Fig. 4D), it is also difficult to argue that the range of ZiR temperatures reflects mechanical mixing between discrete domains during ablation. By contrast, the absence of EAO-age zircon in all of the Labait granulite xenoliths is evidence that aZrSiO4 was not unity during Proterozoic rutile crystallization, and consequently, the range of ZiR temperatures may reflect variable $aZrSiO_4$ (plus $aSiO_2$). Several studies have observed that ZiR temperatures in high-grade rocks are highly variable

and have posited that maximum ZiR temperatures closely approximate peak temperatures (e.g., Kooijman et al., 2012; Kohn et al., 2016; Zack and Kooijman, 2018; Clark et al., 2019). The most cohesive explanation for our data is that rutile (re)crystallized during the EAO with variable $aZiSiO_4$ and/or $aSiO_2$ and underwent subsequent partial Pb loss.

Partial Pb loss in the rutile likely occurred during prolonged residence at elevated temperatures after the EAO. Characteristic diffusion length scales derived from Pb diffusivities (Cherniak, 2000; Smye et al., 2018) for 600 Myr of isothermal residence are ~4 µm at 500°C, ~20 µm at 550°C, and 80–86 µm at 600°C, consistent with the preservation of Mesoproterozoic dates observed in the analyzed rutile grains (Fig. 9A). Thus we suggest that for most of its history, the lower crust remained at 500–600°C—at temperatures hot enough for partial Pb loss, but cool enough to avoid complete rutile resetting.

In addition to EAO-related metamorphism, there is evidence for rift-related overprinting of the deep crust from apatite in two-pyroxene granulites (Fig. 5). CL-dark patches occur close to grain rims and along cracks and resemble fluid infiltration textures (e.g., Harlov et al., 2005). Depth profiles show that these are young domains with elevated Sr and LREE signatures that overprint homogeneous, older cores—2.3–1.8 Ga in sample LB04-36 and ca. 400 Ma in sample LB04-86 (Fig. 5D, E). These older core dates likely correspond to original cooling. Notably, U-Pb dates, Sr, and LREE contents vary over similar length scales (~2–3 µm), indicating they do not solely reflect element mobility by thermally-mediated volume diffusion (Fig. 9B).

Rift-related overprinting in Labait granulite xenoliths was suggested by Mansur et al. (2014) based on pyroxene rims that recorded elevated temperatures (~780°C). Additionally, grain-boundary alteration around plagioclase in an anorthosite xenolith has Pb isotopic ratios

that lie along a present-day geochron (Bellucci et al., 2011). The young ages of Labait apatite rims further implicates a rift-related process. This overprinting, which is associated with elevated LREE contents, may be due to carbonatite melt interactions. Similar LREE enrichments have been observed along grain-boundaries in other Tanzanian xenoliths, including Lashaine garnet granulites (Mansur et al., 2014; this study) and peridotites (Ridley and Dawson, 1975), and in clinopyroxene dunite xenoliths from Olmani (Rudnick et al., 1993), where carbonatitic melts have extensively altered portions of the mantle lithosphere. We speculate that these low-viscosity, low-degree partial melts intruded along grain boundaries in response to rifting and generated the metasomatized domains observed in the apatite.

Although heating and fluid infiltration associated with rifting has affected the deep crust of the craton—as evidenced by textures and dates of apatites and pyroxene rims in some two-pyroxene granulites—it has not yet erased earlier metamorphic/thermal histories. The preservation of older Archean–Proterozoic dates in rutile and apatite in granulite xenoliths imposes key constraints in the duration of rift-related heating. As discussed previously, rift-related heating must have been short in duration (<4 Myr) in order for rutile to retain Proterozoic and older dates. Assuming isothermal residence at ~780°C (pyroxene rims temperatures described above), ~100 kyr would result in diffusion length scales of >500 μm in apatite and ~100 μm in rutile, ~1 kyr would yield diffusive length scales of ~100 μm in apatite and ~10 μm in rutile, and <0.1 kyr corresponds to diffusion length scales of ~10 μm in apatite and <1 μm in rutile (Fig. 9D). The latter matches the data discussed above. The short duration of rift-related heating of the lower crust is consistent with low surface heat

flow on the craton (e.g., Nyblade, 1997; Weeraratne et al., 2003), as well as the relatively recent initiation of rift volcanism in this region (Dawson, 1992).

Finally, the post-Archean thermal history inferred from the rutile and apatite analyses of granulite xenoliths appears, at first glance, to conflict with previously reported feldspar Pb isotopic data, which suggested that the lower crust of the craton remained quiescent since the Archean (Bellucci et al., 2011). The discrepancies between the inferred thermal histories can be reconciled if feldspar did not undergo isotopic exchange with high U/Pb phases—like apatite—during post-Archean thermal events. Given that temperatures were high enough to enable Pb exchange between feldspar and other phases, the fact that feldspar only exhibits Archean Pb isotopic signatures may reflect the short duration nature of later heating, or alternatively, that post-Archean isotopic signatures were not captured by previous in situ methods, which focused on the grain interiors away from rims where overprinting would be first recorded (Bellucci et al., 2011).

1.6.3 Thermal evolution of the East African Orogen

1.6.3.1 Neoproterozoic metamorphism and post-orogenic cooling of the Eastern and Western Granulites

Granulites exist at the surface of the Mozambique Belt and as xenoliths from the underlying lower plate (Fig. 1). Petrochronological analyses of the Eastern Granulite cover and the Western Granulites enable distinction from granulite xenoliths. Additionally, when combined with previously published dates (Möller et al., 2000), the data offer insight into the tectonic and thermal history of the orogen.

Samples from the Eastern Granulite cover record protracted zircon growth from 915–630 Ma and lack any Archean inheritance (Fig. 5A; Möller et al., 1998; Sommer et al., 2005;

Hauzenberger et al., 2007; Tenczer et al., 2006; 2013). The range of zircon dates in these rocks overlap with arc rocks elsewhere in the orogen (Fritz et al., 2013) and support previous suggestions that the Eastern Granulites cover and basement are derived from an outboard arc terrane that was accreted onto Africa during the EAO (e.g., Appel et al., 1998; Möller et al. 2000). TiZ temperatures in garnet granulites record crystallization from 800°C at 780–700 Ma to ~700°C at 640 Ma (Fig. 6D) along a retrograde cooling path (e.g., Kelsey and Powell, 2011; Kohn, 2017). Initial garnet growth, as recorded by elevated Gd/Yb_N ratios in zircon at 780–760 Ma (Fig. 6B), occurred shortly before the onset of cooling. Growth of clinopyroxene over garnet, like those observed in our samples, was interpreted as evidence of isobaric cooling of the Eastern Granulites (e.g., Appel et al., 1998), and the zircon temperature trends may record part of this cooling period.

The Western and Eastern Granulites underwent metamorphism during Gondwana consolidation (i.e., the Malagasy orogen; Stern, 1994; Meert, 2003; Fritz et al., 2009). The youngest zircon and monazite U-Pb dates from the Eastern Granulites are 645–630 Ma (Möller et al., 2000; Tenczer et al., 2013; this study) and have been interpreted to date metamorphism during the EAO (Appel et al., 1998; Möller et al., 2000). Neoproterozoic zircon rims from the Western Granulites (630–615 Ma; Sommer et al., 2003; Cutten et al., 2006; this study) are younger than those from the Eastern Granulite cover, but older than the onset of continental collision (560–550 Ma; Fritz et al., 2013). Similarly, metamorphic titanite dates in the Eastern Granulites (620–610 Ma; Möller et al., 2000; this study) are coincident with the Western Granulite zircon dates, indicating that metamorphism occurred in both terranes prior to 560–550 Ma collision. Meert (2003) proposed at least two collisional events during the assembly of Gondwana: one ca. 630–610 Ma, representing the

timing of accretion of outboard arc terranes and continental blocks onto West Gondwana/East Africa (i.e., the East African Orogeny), and another 570–530 Ma marking collision between the newly amalgamated West Gondwana terranes with East Gondwana (Kuungan/Malagasy Orogeny). Consequently, 630–610 Ma metamorphic zircon and titanite dates record metamorphism during emplacement of the Eastern Granulite basement/cover onto the East African margin.

Rutile and apatite in the Western and Eastern Granulites record cooling following the collisional events discussed above. Cooling rates are calculated using the U-Pb dates of two or more phases in a sample and their respective Pb closure temperatures. In the Western Granulites, 545 Ma titanite dates (this study) and 560–540 Ma metamorphic zircon and monazite dates (Le Goff et al., 2010; Tenczer et al., 2013) document metamorphism during continental collision. This was followed by cooling through rutile Pb closure at ~515 Ma and apatite Pb closure at ~510 Ma and ~460 Ma (Table 2), yielding time-averaged cooling rates of 4–30°C/Myr from 540–510 Ma (assuming cooling from at ~775°C; Table S4). The Loibor Serrit Eastern Granulite cover samples record cooling after accretion at 620–610 Ma (titanite data; Möller et al., 1998; this study); these rocks cooled through rutile closure ca. 560 Ma and apatite closure from 520–460 Ma, or at a rate of 1–6°C/Myr from 620–460 Ma. Similar cooling rates were determined using integrated U-Pb TIMS dating of zircon, monazite, titanite, and rutile and K-Ar and Ar-Ar dating of hornblende, biotite, muscovite, and K-feldspar of gneisses from the Eastern Granulite basement along strike in eastern Tanzania (Maboko et al., 1989; Möller et al., 2000).

1.6.3.2 Post-collisional cooling history of the mid–lower crust

Mid-crustal xenoliths record cooling rates similar to those of outcrops. Some mid-crustal xenoliths have 640–545 Ma monazite and zircon dates that suggest metamorphism during the EAO (Fig. 7; Table 2). Titanites in Natron and Arusha orthogneiss and amphibolite xenoliths are ca. 530 Ma and 540–480 Ma, respectively (Table 2). These dates are generally younger than those in either the Western and Eastern Granulites (Table 2; Möller et al., 2000) and do not appear to correspond to any discrete tectonic event in the area. The titanite dates could reflect growth after peak metamorphism or resetting by some later processes (e.g., fluid interactions; Spencer et al., 2013), but are probably not cooling dates as they crystallized below the nominal >800°C titanite Pb closure temperature (Table 2). Rutile and apatite dates (Fig. 7) are 520–470 Ma for the Natron xenoliths and 500–440 Ma for the Arusha xenoliths, and are interpreted to constrain cooling from 550–400°C (e.g., Smye et al., 2018). Cooling rates of mid-crustal xenoliths are 2–7°C/Myr for the Natron and 1–3°C/Myr for the Arusha xenoliths from ~550–440 Ma. Both rates are similar to one another and are within the range of cooling rates calculated for the upper crust in this study.

Accessory phases from Natron and Arusha lower crustal garnet granulite xenoliths have U-Pb dates distinct from those from the upper and in middle crustal xenoliths (Fig. 7). Zircon is exclusively Archean, but rutile, apatite, and titanite in these lower crustal xenoliths are significantly younger than those at higher crustal levels. These data provide insight into the post-collisional cooling history of the lower crust of the EAO.

Peak metamorphic pressures for lower crustal xenoliths from the Natron and Arusha areas are up to 2.0 GPa during the EAO (Mansur et al., 2014; this study). Because the crust is ~40 km thick today (Julià et al., 2005), the crust as a whole has undergone significant

thinning or exhumation since orogeny. Near-zero age rutile and apatite from the granulite xenoliths (Fig. 7) preclude determining a specific exhumation/cooling history for the lower crust: these dates could reflect protracted residence above closure temperatures (600–700°C) or recent heating by rift magmas (>800°C) (see previous discussion).

In contrast to rutile and apatite, titanites in Lashaine and Kisite garnet granulite xenoliths capture the post-collisional thermal history of the lower crust, with titanite overgrowths on rutile (Fig. 10) tracking the retrograde path (e.g., Manning and Bohlen, 1991; Ernst and Liu, 1998; Kohn, 2017). Pseudosection modeling of garnet granulite xenoliths derived from the lowermost crust (samples 89-729 and 89-731)—with sample 89-729 shown for reference in Figure 10—places the rutile-titanite transition between 1.0–1.6 GPa at 550–850°C. The high-pressure stability of titanite over rutile tracks near isobaric cooling at the outset of collision. The occurrence of fine-grained kyanite in samples 89-729 and 89-731 (e.g., Fig. 3 in Mansur et al., 2014) is consistent with high P-T experiments of Manning and Bohlen (1991) that documented the reaction titanite + kyanite = rutile + anorthite, with titanite + kyanite being the higher pressure assemblage. Manning and Bohlen (1991) noted that the presence of hydrous phases, like zoisite, can influence the position and slope of the titanite-rutile reaction line—the addition of even modest amounts of H_2O can stabilize rutile to pressures greater than titanite. These xenoliths are, however, dry, refractory, and lack any hydrous phases (Mansur et al., 2014), supporting the stability field of titanite shown in Figure 10.

ZiT thermometry constrains the retrograde P-T path into the titanite stability field, and the magnitude of cooling depends on the $aSiO_2$ and $aZrSiO_4$ used to calculate apparent titanite temperatures. Granulites 89-729 and 89-731 lack quartz, so $aSiO_2$ is certainly less

than 1. Using $aSiO_2 = 0.5$ as a minimum bound—based on the presence of feldspars instead of feldspathoids (Ferry and Watson, 2007)—a possible cooling path from 840°C (peak temperatures from Mansur et al., 2014) to ≤750°C is inferred (intersection of ZiT apparent temperatures at the titanite-rutile phase boundary; solid black arrow in Fig. 10). Further cooling and decompression towards 1.2 GPa (i.e., the present-day Moho) is inferred for the lower crust (dashed black arrow in Fig. 10).

Titanite U-Pb dates provide constraints on the timing and rate of lower crust cooling. Spot analyses and depth profiles of lower crustal titanites yield dates as old as 560 Ma in all the samples (taken as growth following peak metamorphism in the EAO), and extend to Paleozoic and younger dates—<100 Ma in depth profiles through titanites in granulites 89-729 and 89-731 (Fig. 8A–D), to as young as 440 Ma in granulite KS04-10 (Fig. 8E, F). The spread to younger dates likely relate to the cooling history, and may reflect: 1) Pb diffusion from the grain during residence at elevated temperatures; 2) protracted titanite growth during cooling; 3) partial resetting by fluids, melts, etc. during exhumation; or 4) mechanical mixing with a thin, young rim during laser ablation. Each of these possibilities is considered in turn.

Diffusional Pb loss can be eliminated based on depth profiles through the titanites. Titanites in Arusha samples 89-729 and 89-731 reveal monotonically decreasing dates toward the grain rims that co-vary with multiple trace elements. Although the U-Pb profiles appear to follow a topology resembling diffusive Pb loss (Fig. 8B, D), elements with different diffusivities—like Sr, Nd, and Zr (Cherniak, 1995; Kohn, 2017; Holder et al., 2019)—vary in concentrations over similar distances, contrary to the pattern predicted by thermally-mediated volume diffusion (Fig. 9C; see also discussion in Stearns et al., 2016).

For example, length scales of diffusion for Zr for ~100 Myr residence at ~700°C are expected to be an order of magnitude greater than for Pb, Sr, and Nd (Fig. 9C). Additionally, maximum ZiT temperatures (assuming that aSiO2 = 1) are 780–810°C at ~1.6 GPa (Fig. 10), which lie at the lower end of the proposed range of titanite Pb closure temperatures (>800°C; using titanite Pb diffusivities reported in Kohn, 2017). Thus, the titanites did not lose Pb diffusively during slow cooling following the EAO, and the younger Paleozoic titanite dates are interpreted to reflect process 2, 3 or 4 listed above.

Protracted titanite growth during cooling is also unlikely. Were this the case, titanite dates would be expected to correlate with ZiT temperatures, but they do not (Fig. 8). Isothermal titanite growth for >300 Myr in the lower crust is also improbable because the upper and middle crust had undergone significant cooling and exhumation from 560–460 Ma (Table 2). The variable titanites dates thus correspond to resetting by non-diffusional processes and/or mixed sampling of discrete age domains.

Several studies have suggested that titanite can be reset via fluid infiltration during retrogression (Frost et al., 2001; Bonamici et al., 2015; Garber et al., 2017; Marsh and Smye, 2017; Walters and Kohn, 2017; Holder and Hacker, 2019). The outermost 5 μm of titanites from the Lashaine mafic garnet granulites have trace-element patterns that are consistent with growth from a near-homogeneous medium along grain boundaries (fluid or melt). Alteration along grain boundaries alteration in Lashaine garnet granulites is LREE-enriched and Pb isotopes suggest this alteration occurred very recently (Mansur et al., 2014), implicating the influence of rift-related metasomatism. High-resolution X-ray mapping using wave-length dispersive spectroscopy (WDS) documents the presence of variable thickness (3–30 μm) titanite rims enriched in Nd and Ce relative to the grain interior (Fig.

S20). We conclude that the 550–250 Ma spot analyses (Fig. 8)—like the <10 Ma and LREE-enriched rims of Labait apatite—are the result of mixing between an older Proterozoic core with a rim that formed during the Cenozoic, likely during rift-related metasomatism (i.e., processes 3 and 4 listed above). Titanite in garnet granulite xenolith KS04-10 from the Natron region has U-Pb dates that range from 550–440 Ma (Fig. 8C, F), but does not exhibit near-rim variations like those observed in the Lashaine granulites; this sample therefore eluded rift-related metasomatism and preserves the original data range associated with cooling and exhumation of the lower crust.

In sum, titanite petrochronology suggests that the lower crust cooled from >840°C to temperatures as low as 750°C shortly after the EAO (as early as 560 Ma), followed by prolonged cooling (~0.2°C/Myr) and decompression to the present-day Moho. Because diffusional Pb loss is not observed in the titanites, we infer that the lower crust has remained well below the Pb closure temperature of titanite since the Proterozoic. The absence of radiogenic Pb in rutile and apatite in lower crustal xenoliths implies residence above the Pb closure temperatures of these phases. These data point to present-day lower crustal temperatures of >650°C (total radiogenic Pb loss in rutile; Kooijman et al., 2010) and <750°C (ZiT temperatures; Fig. 11).

1.6.3.3 Modern thermal structure of the lithosphere

The data discussed above provide constraints on the present-day thermal structure of the lithosphere. Surface heat flow in the EAO is higher than on the craton (average 47 ± 8 mW/m^2 for the EAO versus 38 ± 8 mW/m^2 [all ± 1SD] at the craton margin; Nyblade, 1997), reflecting greater crustal heat production and/or mantle heat flow beneath the orogen. Crustal heat production is probably not much greater in the EAO given the scarcity of heat-

producing element enriched plutons (e.g., Appel et al., 1998; Fritz et al., 2005) and the presence of refractory, Archean-aged crust beneath the orogen (Mansur et al., 2014). Hotter Moho temperatures—derived from residence temperatures of garnet granulite xenoliths—for the EAO compared to the Tanzanian Craton (650–750°C vs. 500–600°C, respectively) also suggest greater heat input from the underlying mantle, and may be a consequence of the greater intensity of rift-related heating below the orogen.

To gain first-order insight into the potential causes of variable mantle heat flow across NE Tanzania, we calculate 1-D steady state geotherms assuming conductive heat flow through the lithosphere and an exponential decrease in heat production with depth (Fig. 12; see Appendix A for details of calculations and model parameters). We do not incorporate the effects of depth-dependent thinning of the lithosphere. Inferred Moho temperatures for the craton margin at Labait are 500–600°C and fall between 40–50 mW/m^2 geotherms (Fig. 12), typical of cratons elsewhere (e.g., Rudnick et al., 1998; Hasterok and Chapman, 2011). Higher temperatures of 650–750°C inferred for the lower crust of the EAO correspond to higher geotherms of 40–50 mW/m2 geotherms (Fig. 12), similar to other Proterozoic orogens (e.g., Jaupart and Mareschal, 2014). Importantly, the geotherms that encompass the range of orogenic Moho temperatures intersect the mantle adiabat at shallower depths, indicating a thinner mantle lithosphere below the orogen (<120 km lithospheric thickness, but it could be thinner if crustal heat production is lower than what we have modeled). This is an inference also supported by Rayleigh wave tomography (~100 km lithosphere thickness; Weeraratne et al., 2003) and the general scarcity of garnet-bearing mantle lithologies throughout the EAO (Cohen et al., 1984; Dawson and Smith, 1988; Rudnick et al., 1994; Lee and Rudnick, 1999; Aulbach et al., 2011).

A thinner mantle lithosphere below the EAO is the likely cause of increased mantle heat flow beneath the orogen compared to the craton margin. However, whether greater mantle heat flow reflects an intrinsically thinner mantle lithosphere or a lithosphere thinned by rifting is unclear. Most mantle xenoliths from the orogen are refractory and ancient (Rudnick et al., 1994; Burton et al., 2000)—though many have also undergone metasomatism during orogeny and rifting—suggesting the mantle keel is still relatively intact (e.g., Rudnick et al., 1994; Aulbach et al., 2011). Additionally, although some crustal xenoliths from the EAO record recent reheating (Jones et al., 1983; Mansur et al., 2014), the petrochronological data presented here do not require additional advective heat sources to explain lower-crustal temperatures of 650–750°C for the orogen. Thus, if thinning by recent rifting has occurred, it has been relatively minor and has not resulted in catastrophic removal of the mantle lithosphere below the EAO.

1.7 CONCLUSIONS

New multi-phase U-Pb and trace element data from cross sections through the crust provided by outcrops and deep crustal xenoliths elucidate the thermal histories of the Archean Tanzanian Craton and adjacent EAO. The data suggest the following:

1) The upper–middle crust of the Tanzanian Craton margin (Labait) has eluded major thermal perturbations during the East African Orogeny and Cenozoic rifting. In contrast, the lower crust of the craton margin experienced Neoarchean UHT metamorphism/melting, EAO-related heating, post-orogenic slow cooling and rift-related fluid/melt interactions. The retention of older age domains in rutile, apatite and feldspars in lower crustal granulite xenoliths (Bellucci et al., 2011; this study)

suggest minimal reheating by rifting (at most 0.1 kyr of heating assuming ~780°C) and residence at 500–600°C prior to eruption

2) Metamorphism of the Eastern and Western Granulites occurred ca. 630–610 Ma (zircon and titanite dates) during accretion of the Eastern Granulites onto the East African margin (Meert, 2003) (Fig. 11). At the time of collision ca. 560–550 Ma, the Eastern Granulite basement and cover had cooled below rutile closure (Möller et al., 2000; this study), but the Western Granulites did not cool below rutile closure until ca. 515 Ma. By ca. 450 Ma, both the Eastern and Western Granulites had cooled below apatite closure (Fig. 11), consistent with the thermal histories constrained by K-Ar and Ar-Ar hornblende, biotite, muscovite, and K-feldspar dates (e.g., Maboko et al., 1989; Möller et al., 2000). Rutile and apatite dates from mid-crustal xenoliths erupted through the orogen overlaps those from outcrops, indicating similar cooling histories.
3) Lower crustal xenoliths from below the orogen at the Natron and Arusha sites record post-collisional thermal histories. Titanite U-Pb dates document cooling from over 800°C to ~750°C by 550 Ma, followed by slower exhumation to present-day crustal thickness of ~40 km (Fig. 10). Near-zero age rutile and apatite suggest that the lower crust resided above the Pb closure temperatures of rutile and apatite during post-collisional cooling, or that these minerals were reset by recent rift-related heating. The absence of thermally-mediated volume diffusion in titanite suggests minimal perturbation by heating and further suggest pre-eruptive residence temperatures below 750°C. Near-zero age rutile and apatite suggests residence above 650°C and need not reflect recent reheating.

4) Lower-crustal temperatures for the EAO are higher than inferred for the Tanzanian Craton (650–750°C vs. 500–600°C, respectively), consistent with the surface heat flow observed for the orogen (Nyblade et al., 1990; Nyblade, 1997). Data from the orogen suggest a hotter geotherm compared to the craton, and are compatible with increased mantle heat flow below the orogen as a result from a thinner mantle lithosphere there than beneath the craton (e.g., Rudnick et al., 1994; Lee and Rudnick, 1999; Weeraratne et al., 2003; Aulbach et al., 2011). Conductive heat transfer through a thinner mantle lithosphere can explain the without additional advective heat sources, suggesting that rifting has only a limited impact on the thermal structure of the crust and did not result in significant removal of the mantle keel.

Table 1. Sample descriptions

Sample locations and names	Rock type	Major phases	Accessory phases	Present-day crustal level
		Tanzanian Craton		
Labait (4°34'02"S, 35°25'53"E)				
LB04-86	granite	Pl + Qtz + Kfs + Ms + Chl	**Zrn** + **Ap**	upper crust
LB04-05	schist	Pl + Qtz + Kfs + Bt + Ms	**Zrn** + **Ap**	middle crust
LB04-89	amphibolite	Pl + Qtz + Hbl + Ep + Bt	**Zrn** + **Rtl** + **Ap**	middle crust
LB04-92	amphibolite	Pl + Qtz + Hbl + Bt	**Zrn** + **Ap**	middle crust
LB04-36	two-pyroxene granulite	Pl + Qtz + Cpx + Opx	**Zrn** + **Ap** + Ilm	lower crust
LB04-19	two-pyroxene granulite	Pl + Kfs + Cpx + Opx	**Zrn** + **Ap** + Ilm	lower crust
LB04-82	two-pyroxene granulite	Pl + Qtz + Kfs + Cpx + Opx + Bt	**Zrn** + **Ap** + Ilm	lower crust
LB04-91	garnet orthopyroxene granulite	Grt + Pl + Qtz + Kfs + Opx	**Zrn** + **Rtl** + Ap	lower crust
LB04-39	garnet orthopyroxene granulite	Grt + Pl + Qtz + Opx	**Zrn** + **Rtl** + Ap	lower crust
LB04-74	garnet orthopyroxene granulite	Grt + Pl + Qtz + Kfs + Opx	**Zrn** + **Rtl**	lower crust
		Natron area		
Naibor Soito (2°46'53"S, 36°00'50"E)				
NS04-96	two-pyroxene granulite	Pl + Qtz + Cpx + Opx	**Zrn** + **Ap** + Ilm	lower crust
NS04-150	two-pyroxene granulite	Pl + Cpx + Opx + Hbl + Bt	**Zrn** + **Ap** + Ilm	lower crust
NS04-60	garnet two-pyroxene granulite	Grt + Pl + Cpx + Opx + Hbl + Bt	**Zrn** + **Rtl** + **Ap** + Ilm	lower crust
NS04-01	garnet two-pyroxene granulite	Grt + Pl + Qtz + Kfs + Cpx + Opx	**Zrn** + **Rtl** + **Ap** + Ilm	lower crust
W3S-1	garnet two-pyroxene granulite	Grt + Pl + Qtz + Cpx + Opx	**Zrn** + **Rtl** + **Ap**	lower crust
Kisite (2°50'25"S, 36°00'56"E)				
KS04-01	orthogneiss	Pl + Qtz + Kfs + Opx + Bt + Grt + Cc	**Zrn** + Rtl + Ilm	middle crust
KS04-10	garnet two-pyroxene granulite	Pl + Qtz + Opx + Cpx + Grt	**Ttn** + **Rtl**	lower crust
Pello Hill (2°45'54"S, 36°01'05"E)				
PH04-02	amphibolite	Pl + Qtz + Hbl + Bt	**Zrn** + **Ttn** + **Ap**	middle crust
PH04-05	garnet two-pyroxene granulite	Pl + Grt + Cpx + Opx + Qtz	**Zrn** + **Rtl**	lower crust
Eledoi (2°45'25"S, 36°01'40"E)				
EL04-01	orthogneiss	Pl + Qtz + Kfs + Bt	**Zrn** + **Mnz** + **Ap**	middle crust
		Arusha area		
Lashaine (3°22'10"S, 36°25'30"E)				
89-733	garnet biotite two-pyroxene granulite	Grt + Pl + Cpx + Opx + Hbl + Bt	**Zrn** + Ap	middle crust
89-745	garnet biotite two-pyroxene granulite	Grt + Pl + Cpx + Opx + Hbl + Bt	**Zrn** + **Ap**	middle crust
89-729	garnet clinopyroxene granulite	Grt + Pl + Cpx	**Ttn** + **Rtl** + **Ap** + Ky	lower crust
89-731	garnet clinopyroxene granulite	Grt + Pl + Cpx	**Ttn** + **Rtl** + **Ap** + Ky	lower crust
LS04-09	garnet clinopyroxene granulite	Grt + Pl + Cpx	**Rtl**	lower crust
Lemugur (3°26'30"S, 36°32'30"E)				
LG04-09	schist	Grt + Pl + Qtz + Kfs + Bt + Ms	**Zrn** + **Mnz** + **Rtl** + **Ap**	middle crust
LG04-37	amphibolite	Pl + Qtz + Kfs + Hbl + Bt	**Zrn** + **Ttn** + Ap	middle crust
LG04-35	garnet clinopyroxene granulite	Grt + Pl + Cpx	**Rtl**	lower crust
LG04-38	garnet two-pyroxene granulite	Grt + Pl + Cpx + Opx	**Rtl**	lower crust
Loljoro (3°27'09"S, 36°36'23"E)				
LJ04-08	quartzite	Pl + Qtz + Kfs + Bt + Ms	**Zrn** + **Mnz** + **Rtl** + **Ap**	middle crust
LJ04-26	orthogneiss	Pl + Qtz + Kfs + Bt	**Zrn** + **Ttn** + **Ap**	middle crust
Olmani (3°23'50"S, 36°45'20"E)				
OM04-13	orthogneiss	Pl + Qtz + Cpx + Grt + Bt	**Zrn** + **Ttn** + **Ap**	middle crust

		Mozambique Belt: Eastern Granulite cover		
Loibor Serrit (4°10'59"S, 36°24'45"E)				
LR04-05	two-pyroxene granulite	Pl + Qtz + Kfs + Cpx + Opx + Hbl + Bt	**Zrn** + **Ap**	upper crust
LS06-01	orthogneiss	Pl + Qtz + Kfs + Cpx + Hbl + Bt	**Zrn** + **Ap**	upper crust
LS06-02	orthogneiss	Pl + Qtz + Kfs + Cpx + Hbl + Bt	**Zrn** + **Ap**	upper crust
LR04-01	garnet two-pyroxene granulite	Grt + Pl + Qtz + Kfs + Cpx + Opx	**Zrn** + **Ap**	upper crust
LS06-12	garnet clinopyroxene granulite	Grt + Pl + Cpx	**Zrn** + **Ttn** + **Rtl** + **Ap**	upper crust
		Mozambique Belt: Western Granulites		
Longido (2°46'28"S, 36°30'13"E)				
LK06-02	orthogneiss	Grt + Pl + Qtz + Opx + Hbl + Bt	**Zrn** + **Ttn** + **Ap**	upper crust
Magugu (3°49'31"S, 35°50'5"E)				
MG04-01	orthogneiss	Grt + Pl + Qtz + Opx + Hbl + Bt	**Zrn** + **Rtl** + **Ap**	upper crust

Italicized samples are ones described in Mansur et al. (2014).

Petrochronological data is presented for phases in bold lettering.

Mineral abbreviations: Ap, apatite; Bt, biotite; Cc, calcium carbonate; Chl, chlorite; Cpx, clinopyroxene; Ep, Epidoite; Grt, garnet; Hbl, hornblende; Ilm, ilmenite; Kfs, K-feldspar; Ky, kyanite; Mnz, monazite; Ms, muscovite; Opx, orthopyroxene; Pl, plagioclase; Qtz, quartz; Rtl, rutile; Ttn, titanite; Zrn, zircon

Crustal levels for xenoliths are inferred using major-element thermobarometry and/or pseudosection models

Table 2. Summary of petrochronologic data

Sample	Rock type	Phase	Best dates (Ma)[1]	± 2σ (n)[2]	T estimates[3] (°C)	± 2σ (n)[4]	Notes
			Tanzanian Craton				
Labait							
LB04-86	granite	Zrn	discordant	-	-		metamict
		Ap	2525	31 (21)			
LB04-05	schist	Zrn	discordant	-	-		metamict
		Ap	2496	30 (25)			
LB04-89	amphibolite	Zrn	2678	17 (1)	680	40 (1)	single concordant point
		Rtl	2621	31 (22)	520–730	- (24)	
		Ap	2533	40 (21)			
LB04-92	amphibolite	Zrn	2649	4 (22)	680	10 (25)	
		Ap	2560	47 (18)			
LB04-36	two-pyroxene granulite	Zrn	2840–2587		770	10 (39)	
		Ap	2600–0	- (29)			LREE enriched rims
LB04-19	two-pyroxene granulite	Zrn	2725–2598	- (27)	940	10 (29)	low U
		Ap	-	-			U b.d.l.
LB04-82	two-pyroxene granulite	Zrn	2728–2612	- (24)	810	20 (24)	
		Ap	1200–340	- (23)			LREE enriched rims
LB04-91	garnet orthopyroxene granulite	Zrn	2761–2595	- (44)	920	10 (45)	
		Rtl	discordant	- (30)	-		
LB04-39	garnet orthopyroxene granulite	Zrn	3027–2537	- (28)	950	10 (33)	
		Rtl	discordant	- (24)	-		
LB04-74	garnet orthopyroxene granulite	Zrn	2619–2572	- (8)	780–915	- (8)	
		Rtl	discordant	- (24)	-		
			Natron area				
Naibor Soito							
NS04-96	two-pyroxene granulite	Zrn	2703–2520	- (8)	820	10 (36)	
		Ap	11	17 (19)			
NS04-150	two-pyroxene granulite	Zrn	2717–2484	- (20)	780	10 (44)	
		Ap	2.4	10 (20)			
NS04-60	garnet two-pyroxene granulite	Zrn	2696–2567	- (6)	760	10 (21)	discordant cores
		Rtl	0.1	0.1 (15)	N/A		
		Ap	1.5	2.1 (15)			
NS04-01	garnet two-pyroxene granulite	Zrn	2880–2599	- (21)	780	10 (40)	
		Rtl	0.1	0.1 (18)	770	10 (18)	
		Ap	0.0	1.4 (22)			
W3S-1	garnet two-pyroxene granulite	Zrn	2690–2528	- (6)	820	10 (37)	
		Rtl	0.1	0.1 (18)	690	10 (18)	
		Ap	0.8	2.5 (25)			
Kisite							
KS04-01	orthogneiss	Zrn	2862–2585	- (5)	760	10 (25)	
KS04-10	garnet two-pyroxene granulite	Ttn	540–440	- (38)	770	10 (38)	
		Rtl	0.4	0.3 (27)	N/A		no zrn in sample
Pello Hill							
PH04-02	amphibolite	Zrn	588	9 (3)	670	30 (3)	
		Ttn	533	7 (33)	760	10 (34)	
		Ap	524	30 (16)			low U
PH04-05	garnet two-pyroxene granulite	Zrn	2591–2461	- (28)	N/A		no Qtz in sample
		Rtl	2.6	0.9 (20)	N/A		no Qtz in sample

Eledoi							
EL04-01	orthogneiss	Zrn	2737–2666	- (15)	740	10 (15)	younger, discordant rims
		Mnz	2633	5 (20)			
			546	12 (1)			Single concordant depth profile
		Ap	467	10 (23)			
			Arusha area				
Lashaine							
89-733	garnet biotite two-pyroxene granulite	Zrn	2560	18 (1)	770	50 (1)	single concordant core date
			607	9 (3)	710	40 (3)	
89-745	garnet biotite two-pyroxene granulite	Zrn	581	8 (3)	690	30 (3)	
		Ap	487	14 (23)			
89-729	garnet clinopyroxene granulite	Ttn	560–330	- (29)	740	10 (29)	T is maximum (assuming *a* SiO2 = 1, but no Qtz in rock)
		Rtl	0.7	0.6 (23)	N/A		no Zrn or Qtz in sample
		Ap	-	-			U b.d.l.
89-731	garnet clinopyroxene granulite	Ttn	550–260	- (33)	730	10 (33)	T is maximum (assuming *a* SiO2 = 1, but Qtz in rock)
		Rtl	1.8	0.6 (20)	N/A		no Zrn or Qtz in sample
Lemugur		Ap	-	-			U b.d.l.
LS04-09	garnet clinopyroxene granulite	Rtl	0.5	0.1 (49)	N/A		no Zrn or Qtz in sample
LG04-09	schist	Zrn	discordant	-	-		metamict
		Mnz	605–567	- (56)			high Y rims compared to cores
		Rtl	500	4 (27)	710	10 (27)	
		Ap	444	24 (16)			
LG04-37	amphibolite	Zrn	2530	10 (10)	740	20 (10)	younger, discordant rims
		Ttn	540–480	- (35)	770	10 (35)	
LG04-35	garnet clinopyroxene granulite	Rtl	1.0	0.6 (26)	N/A		no Zrn or Qtz in sample
LG04-38	garnet clinopyroxene granulite	Rtl	-	-	N/A		U b.d.l.; no Zrn or Qtz in sample
Loljoro							
LJ04-08	quartzite	Zrn	3479–2661	- (13)	700	10 (13)	younger, discordant rims
		Mnz	588	2 (28)			
		Rtl	498	3 (58)	700	10 (58)	
		Ap	473	13 (28)			
LJ04-26	orthogneiss	Zrn	2519	10 (3)	690	30 (3)	
			643	13 (1)	-		Single concordant depth profile
		Ttn	528	9 (56)	750	10 (56)	
		Ap	499	15 (20)			
Olmani							
OM04-13	orthogneiss	Zrn	2706	9 (5)	700	20 (5)	
			607	6 (6)	700	20 (6)	
		Ttn	514	10 (38)	770	10 (38)	
		Ap	480	19 (23)			
			Mozambique Belt: Eastern Granulite cover				
Loibor							
LR04-05	two-pyroxene granulite	Zrn	917–732	- (18)	720	10 (18)	
		Ap	507	6 (23)			
LS06-01	orthogneiss	Zrn	728–645	- (20)	730	10 (20)	
		Ap	498	4 (24)			
LS06-02	orthogneiss	Zrn	905–722	- (23)	710	10 (23)	
		Ap	521	6 (25)			
LR04-01	garnet two-pyroxene granulite	Zrn	773–642	- (10)	720	10 (10)	
		Ap	513	8 (27)			

LS06-12	garnet two-pyroxene granulite	Zrn	890–632	- (30)	640–830	- (30)	
		Ttn	614	3 (23)	860–900	- (23)	cross calibrated ZiR and ZiT
		Rtl	568	18 (6)	860–900	- (6)	cross calibrated ZiR and ZiT
		Ap	458	7 (26)			
			Mozambique Belt: Western Granulites				
Longido							
LK06-02	orthogneiss	Zrn	2516	6 (10)	750	30 (10)	
			613	4 (15)	620	20 (15)	
		Ttn	543	13 (38)	750	10 (38)	
		Ap	457	25 (19)			low U
Magugu							
MG04-01	orthogneiss	Zrn	2944, 2422	20, 17 (2)	760	30 (2)	
			630	16 (1)	530	90 (1)	single concordant date; large T
		Rtl	515	8 (6)	680	20 (6)	
		Ap	510	9 (26)			

Mineral abbreviations same as in Table 1

[1]Best dates for zircon and monazite are dates within 5% concordance (between $^{238}U/^{206}Pb$ and $^{207}Pb/^{206}Pb$ dates), and ^{207}Pb-corrected U-Pb dates for titanite, rutile, and apatite (applying common Pb compositions reported in Table S3).

[2]Uncertainities are internal only. Dates reported outside this study should adopt uncertainities associated with long-term reproducibilty of analyzed homogeneous lab standards (1–3%; see Supplements for details). Dash denotes data that does not conform to a single population; n is the number of data used to calculate mean and 2σ uncertainty, or number of data in specified range.

[3]Calculated using 4+ cation thermometers of Ferry and Watson (2007) for zircon, Tomkins et al. (2007) for rutile, and Hayden et al. (2008) for titanite. Temperatures are averages, unless where shown as ranges, and rounded up.

[4]Uncertainties for temperatures account for analytical uncertainities and uncertainties in Si and Ti activities (± 0.1) , but not thermometer calibrations. Pressures of 1 GPa for granulites and 0.6 GPa for amphibolites and orthogneisses are used for temperature calculations (assuming ± 0.1 GPa uncertainty) (see Supplements for details). Dash denotes data that does not conform to a single population; n is the number of data used to calculate mean and 2σ uncertainty, or number of data in

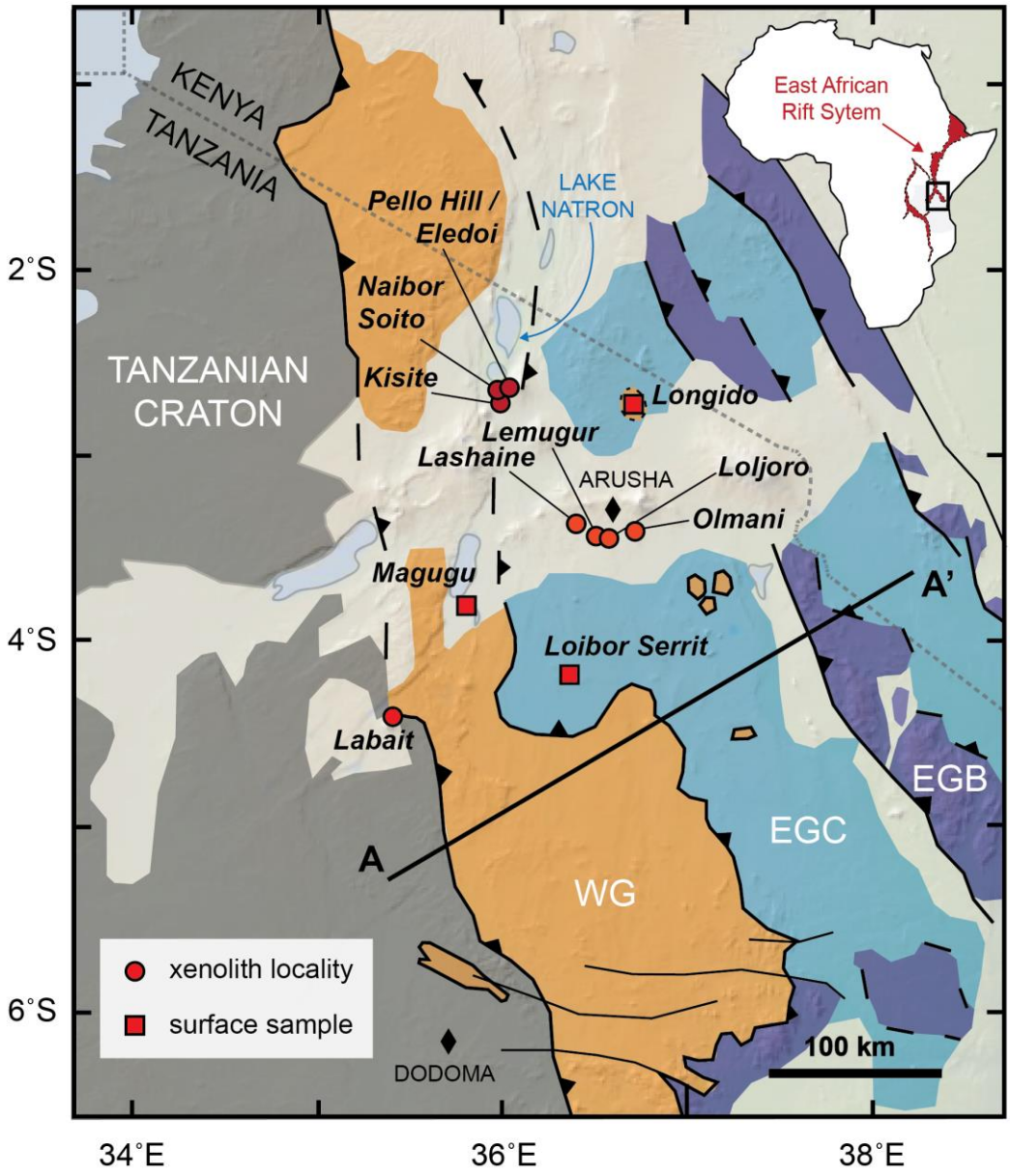

Figure 1. Simplified geologic map of northern Tanzania with sample locations. Areas in light grey are Quaternary–Tertiary volcanic and sedimentary cover. Red areas in inset represent the East African Rift system. Modified from Fritz et al. (2009). Background topography is from GeoMapApp. Abbreviations: WG, Western Granulites; EGC, Eastern Granulite cover; EGB, Eastern Granulite basement.

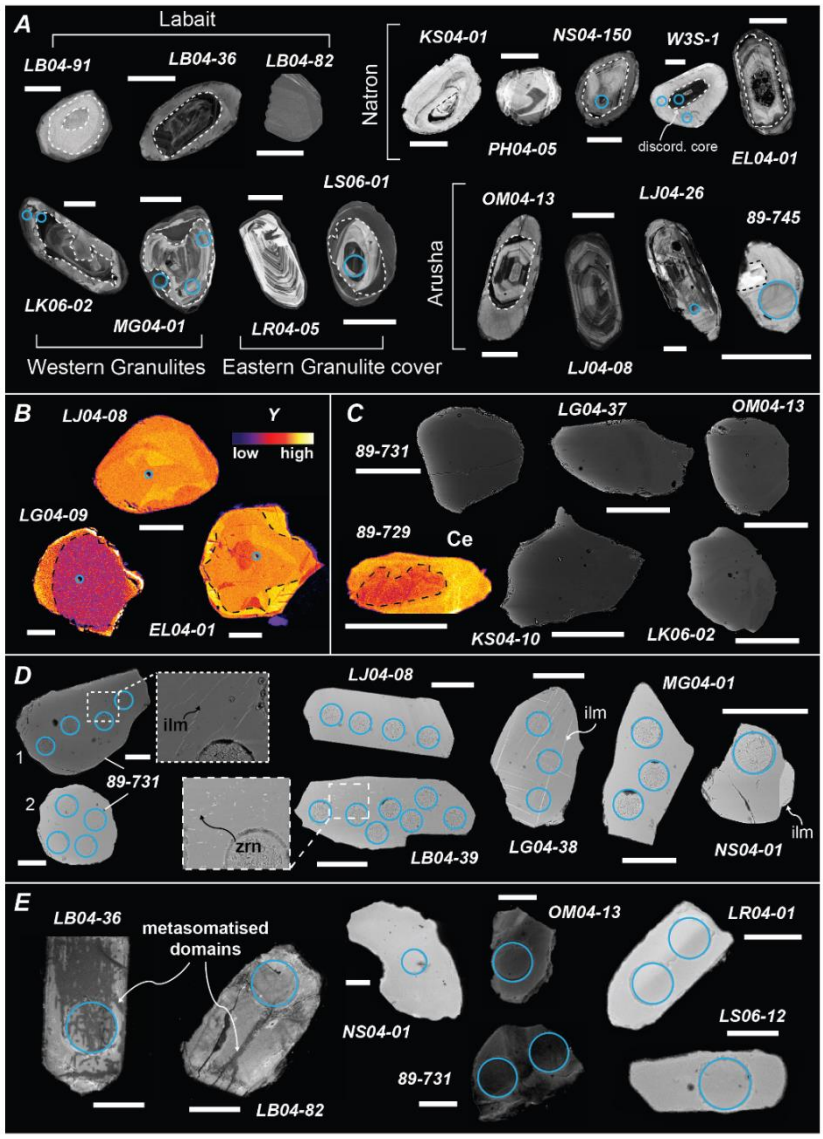
A
Labait
LB04-91
LB04-36
LB04-82
Natron
KS04-01
NS04-150
W3S-1
PH04-05
discord. core
EL04-01
LS06-01
LK06-02
MG04-01
LR04-05
Western Granulites
Eastern Granulite cover
Arusha
OM04-13
LJ04-26
89-745
LJ04-08
B
LJ04-08
Y
low high
LG04-09
EL04-01
C
89-731
LG04-37
OM04-13
89-729
Ce
KS04-10
LK06-02
D
ilm
1
89-731
2
zrn
LJ04-08
LB04-39
ilm
LG04-38
MG04-01
NS04-01
ilm
E
LB04-36
metasomatised domains
LB04-82
NS04-01
OM04-13
LR04-01
LS06-12
89-731

Figure 2. Images of representative grains analyzed. White bars are 50 μm wide. Blue circles represent laser spots. A) Representative zircon grains (CL). Rims are denoted in dashed lines. See text for discussion of different rim/core dates. B) Qualitative Y intensity maps of representative monazite grains. Despite the faint variations in Y concentrations within monazite from samples LJ04-08 and LG04-09, all dates are consistently Neoproterozoic. Monazite from sample EL04-01 yielded Neoarchean and Neoproterozoic dates; the former is associated with brighter patches around the rim. C) Representative titanite grains (X-ray and BSE). Qualitative Ce intensity maps of a titanite grain from sample 89-729 clearly shows a core and mantle. Titanite grains in other granulite xenolith show faint internal structures in BSE, suggesting they too contain complexities. Titanite grains in mid-crustal xenoliths and surface outcrops appear to lack any apparent zonations in BSE, consistent with U-Pb and trace-element data. D) Representative rutile grains (BSE). Rutile from off-craton garnet granulite xenoliths (89-731 grain 1, LG04-38, and NS04-01) contain fine ilmenite exsolution lamellae or ilmenite overgrowths (although not all grains do; e.g., 89-731 grain 2). Rutile from on-craton garnet granulites often contain zircon exsolutions like those shown in LB04-39. Rutile grains from mid-crustal xenoliths (LJ04-08) and surface outcrops (MG04-01) are devoid of any exsolutions. E) Representative apatite grains. Note the complex structure in grains from Labait granulite xenoliths, consistent with the variable U-Pb dates observed. Darker patches in the apatites are interpreted to have formed via melt interactions during or slightly before eruption. Apatite from other garnet granulite xenoliths (NS04-01), mid-crustal xenoliths (mid-crustal; OM04-13), and surface outcrops (LR04-01 and LS06-12) lack any apparent internal structure.

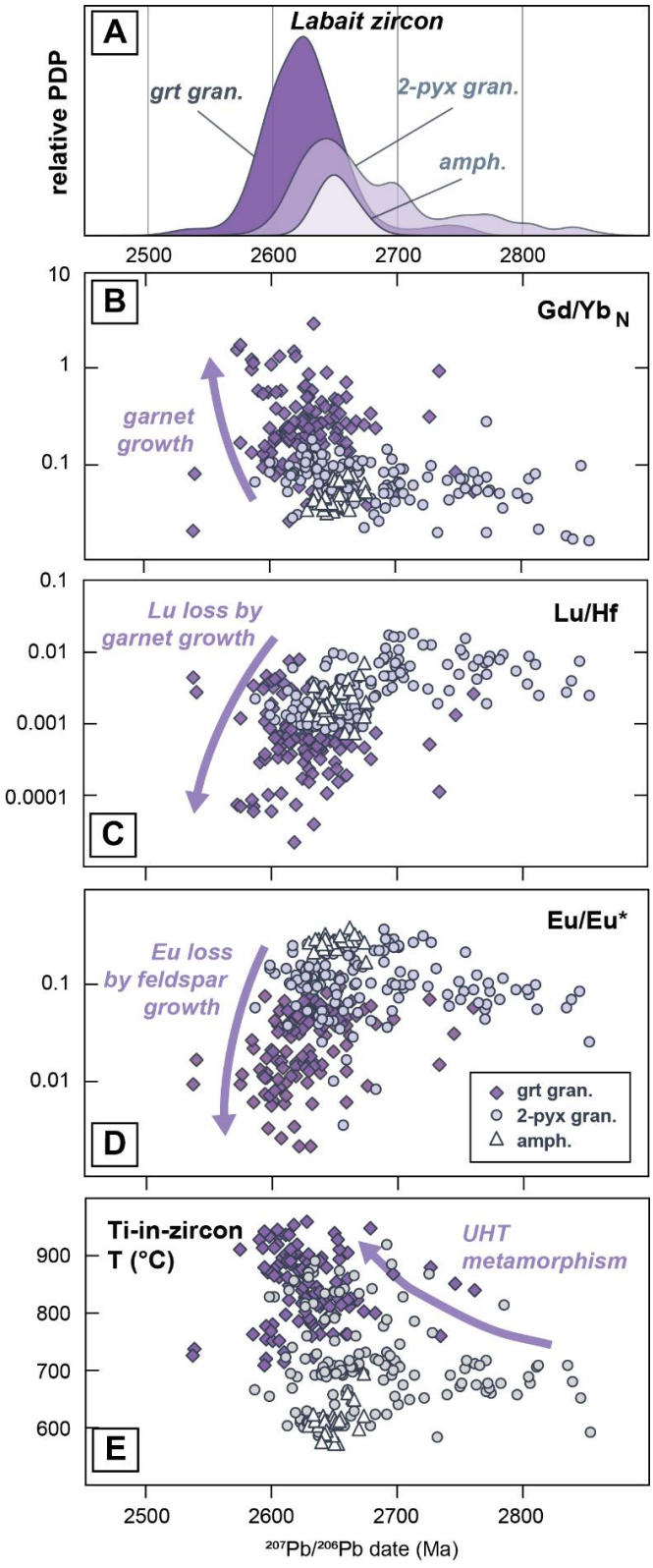

Figure 3. Labait zircon data. Only dates within 5% concordance are plotted. A) Probability distribution plot (PDP) of zircon U-Pb dates from the different xenolith types. B–E) Trace-element variations with zircon dates. Differences in trace-element patterns among the different samples occur at ca. 2.64 Ga and include increases in the chondrite-normalized (using values of McDonough and Sun, 1995) Gd/Yb ratios and TiZ temperatures, as well as decreases in zircon Eu anomaly and Lu/Hf, which are attributed to growth of garnet and elemental fractionation by protracted zircon growth from a melt (see text for details).

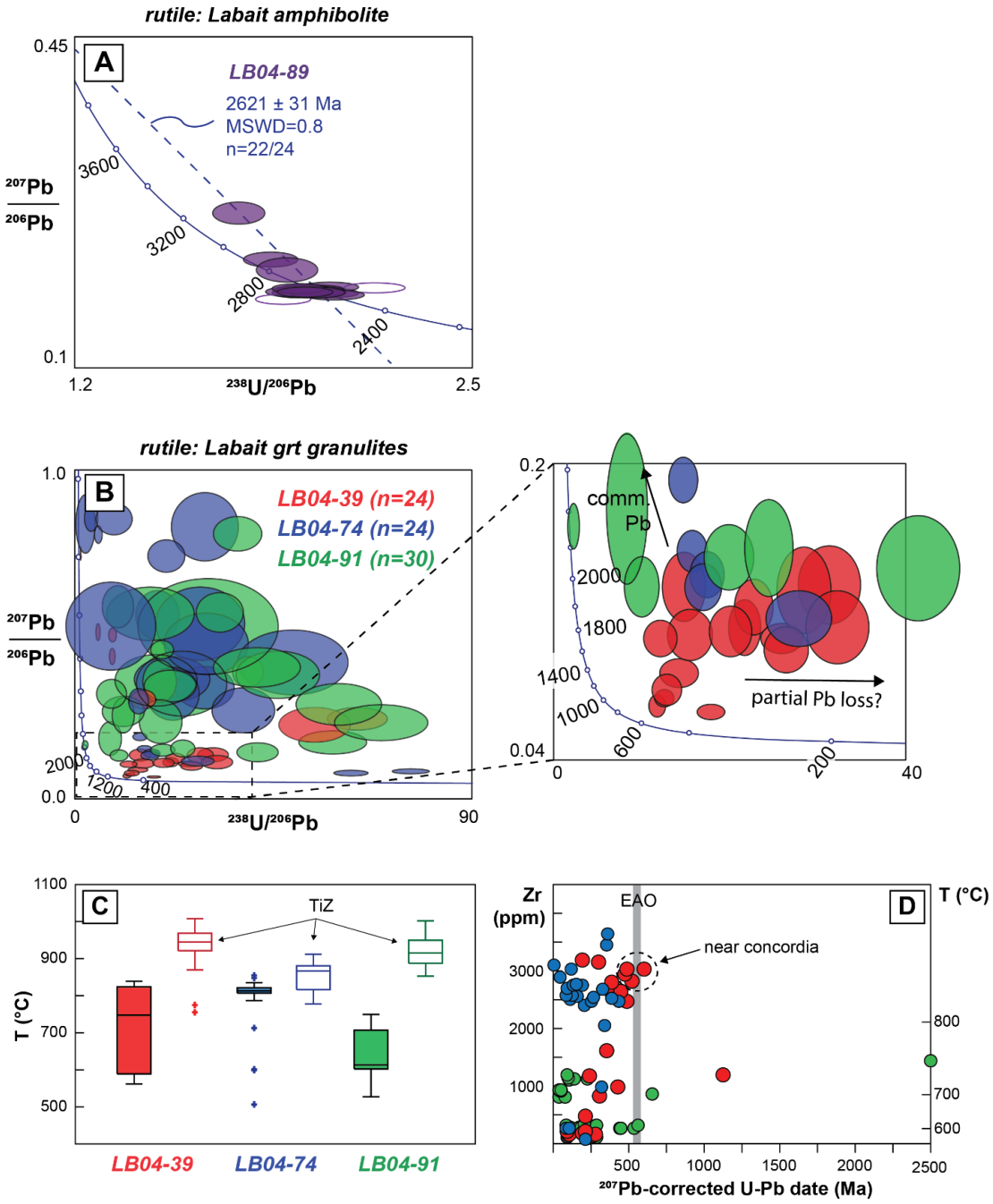

Figure 4. Labait rutile data. A) Tera-Wasserberg concordia plot of rutile spot analyses from amphibolite xenolith LB04-89. B) Tera-Wasserberg concordia plot of all rutile spot analyses from garnet granulite xenoliths (colored by sample). The inset shows a subset of analyses that lie near concordia at 600–500. C) Box-and-whisker plot comparing ZiR (filled) and TiZ (unfilled) temperatures in the different garnet granulite xenoliths. Note how ZiR temperatures are lower. D) Common-Pb corrected U-Pb date vs. Zr contents. No discernable correlation exists in any of the samples. Same color scheme as in panels B/C.

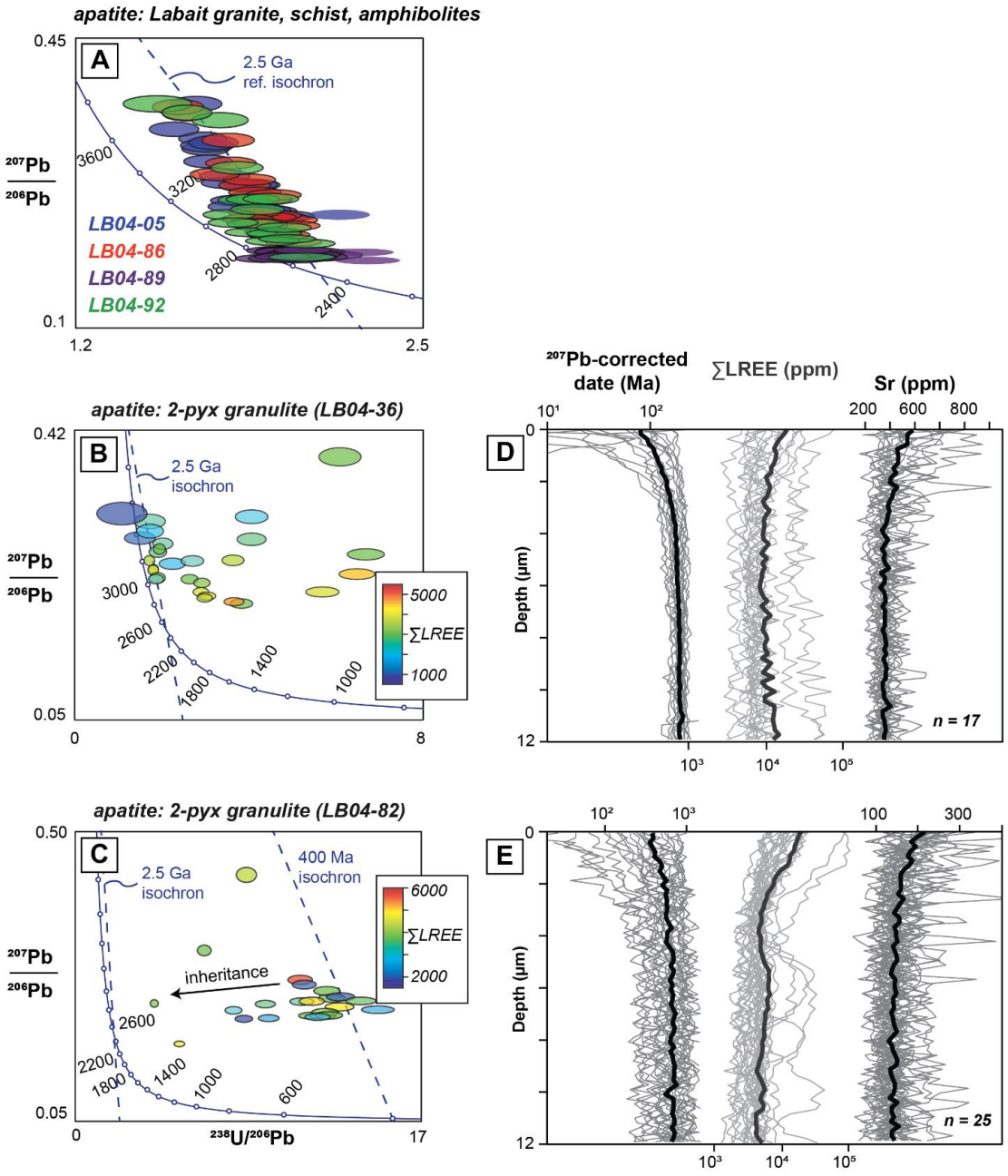

Figure 5. Labait apatite data. A) Tera-Wasserberg concordia plot of apatite spot analyses from granite, schist, and amphibolite xenoliths. Most of the data fall along a 2.5 Ga reference isochron (see Table 2 for individual dates). B–C) Tera-Wasserberg plots of apatite spot analyses from two-pyroxene granulites. Both samples yield a spread of dates from 2.5 Ga to <1 Ga with younger spots exhibiting higher LREE contents. D–E) Apatite depth profiles showing common-Pb corrected U-Pb date, LREE, and Sr core-rim variations. Rims are distinctly enriched in LREE and Sr contents, likely from melt interactions (see text for discussion). Lighter, thinner lines are individual profiles, and darker, bolder lines are averages of all profiles.

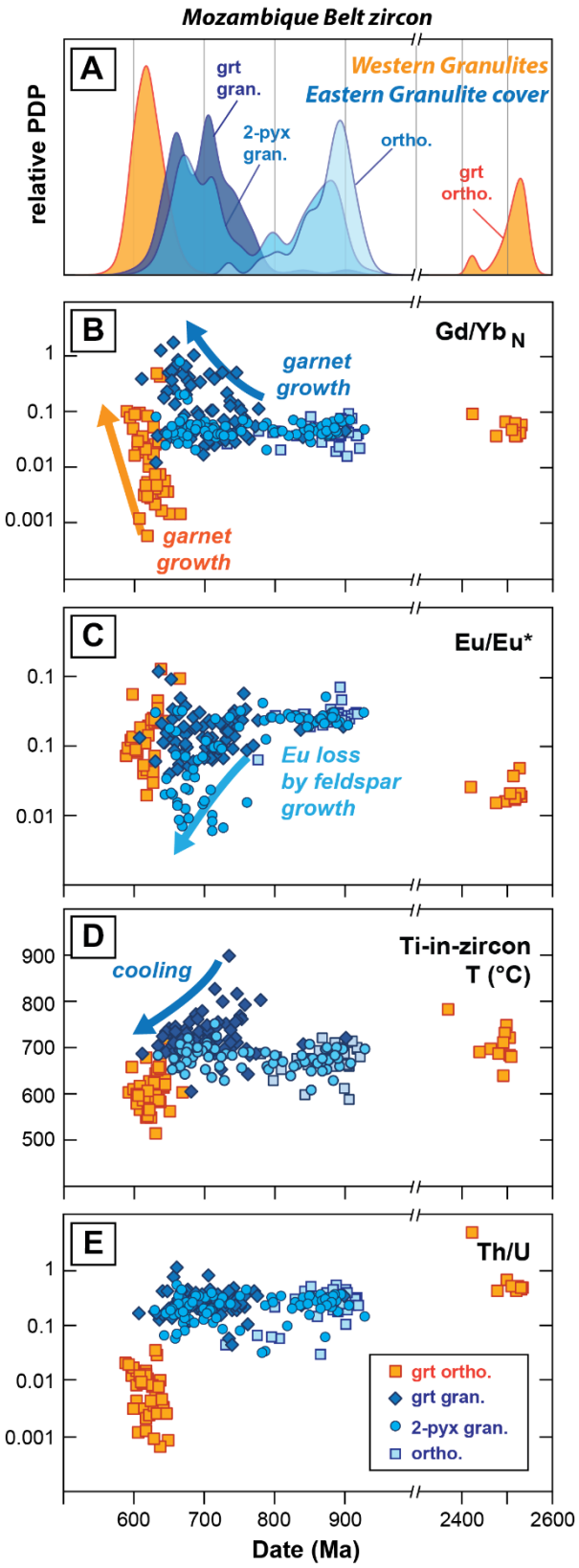

Figure 6. Zircon from the Western Granulites and Eastern Granulite cover, Mozambique Belt. A) PDPs of U-Pb dates. Zircon from the Western Granulites (orange) display a distinct bimodal distribution, with one Archean peak (2.6–2.4 Ga) and another Proterozoic peak (ca. 610 Ma). Zircon from the Eastern Granulites display a range of Proterozoic dates that differ among different sample types. Garnet-absent samples vary between 950 and 660 Ma, with prominent peaks at ca. 900 and 700 Ma, whereas garnet-bearing samples are largely centered between 800–660 Ma. B–E) Trace-element and age variations. Note the distinct shifts in Gd/Yb, Eu/Eu*, and TiZ temperatures at ~770 Ma in garnet granulites from the Eastern Granulite cover. U-Pb date is the $^{238}U/^{206}Pb$ date <1400 Ma and the $^{207}Pb/^{206}Pb$ date for >1400 Ma.

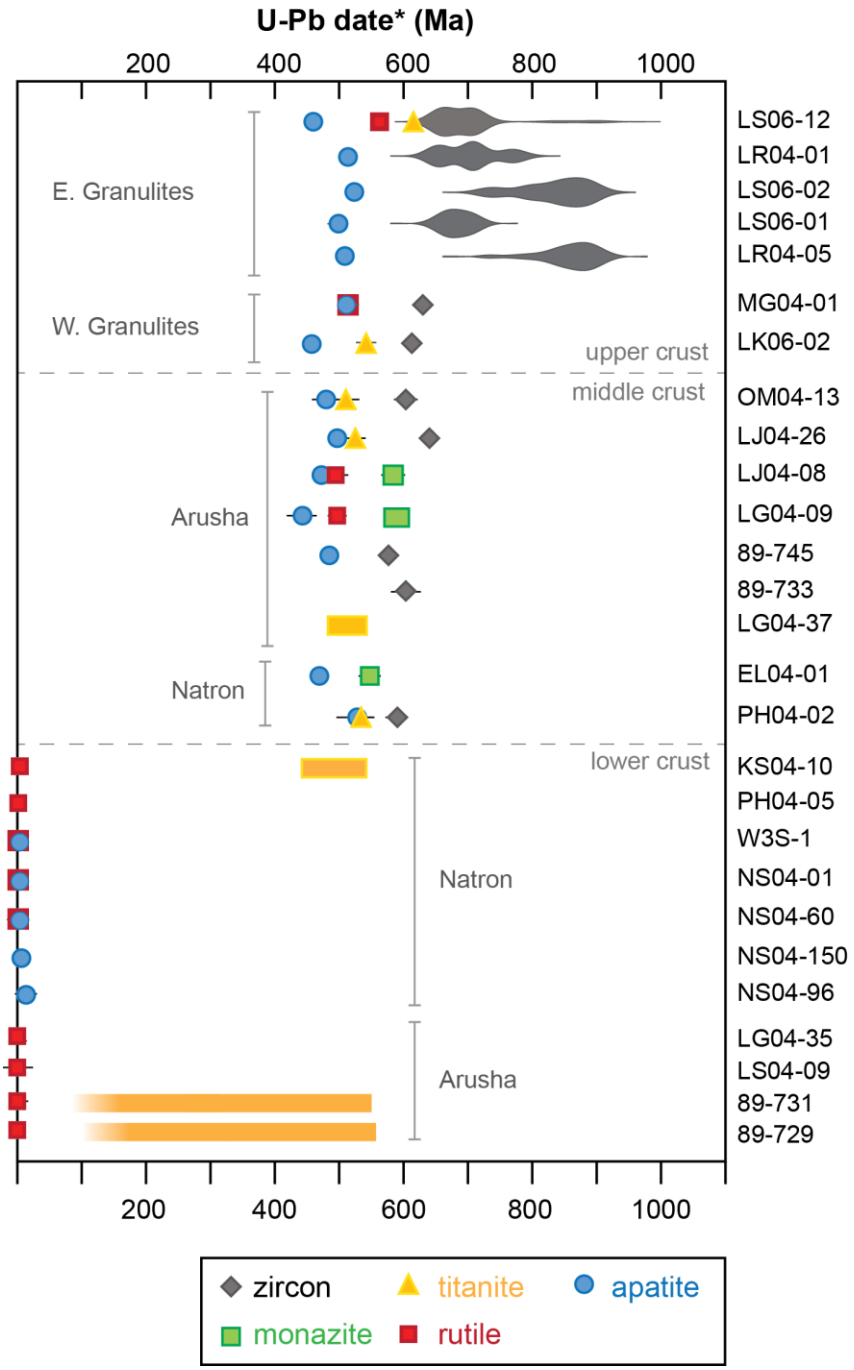

Figure 7. Comparison of accessory phase U-Pb dates from xenoliths and surface outcrops from the Mozambique Belt. For zircon and monazite, only grains within 5% concordance are shown. All titanite, rutile, and apatite dates are common-Pb corrected. Bars represent ranges of dates. Grey blobs in Eastern Granulite cover zircon are PDPs.

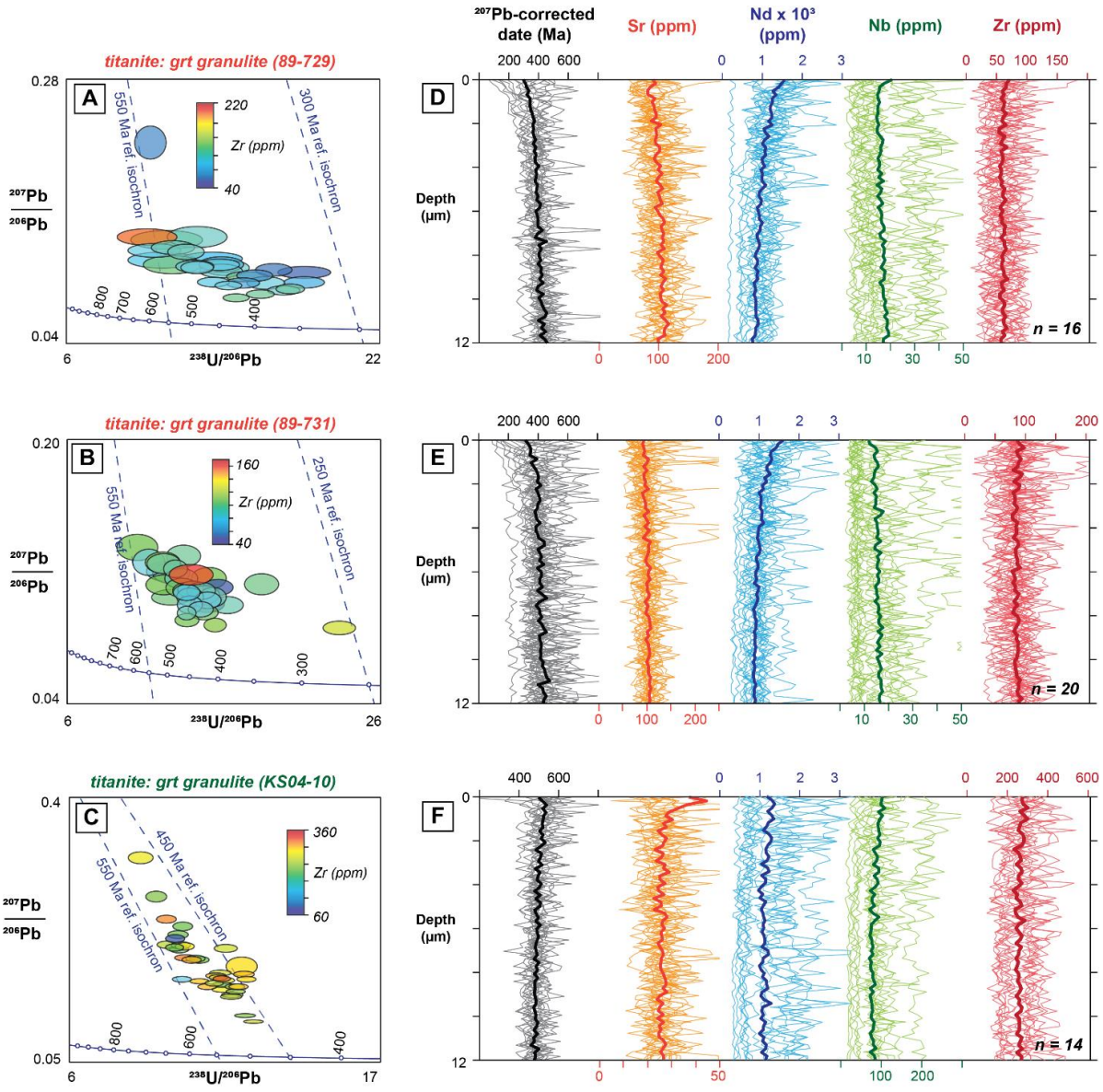

Figure 8. Titanite data from lower-crustal xenoliths. A–C) Spot analyses across titanite grains range from 550–250 Ma for the Lashaine granulites and 550–450 Ma for the Kisite granulite. See Table 2 for calculated ZiT temperatures. D–E) Depth profiling of Lashaine whole titanite grains confirms the presence of young rims mantling cores. The selected trace-elements are ordered from faster to slower diffusing from left to right (after Cherniak, 1995; Kohn, 2017; Holder et al., 2019). The topologies of the different elements vary over similar length scales, contrary to variable topologies that would be produced by thermally-mediated volume diffusion. Instead, age and elemental variations could reflect mixing of a thin young rim with an older core, similar to what was observed in the metasomatised Labait apatite. F) Depth profiles of Kisite titanites. Note how unlike the Lashaine titanites, these titanites have generally uniform compositions with depth.

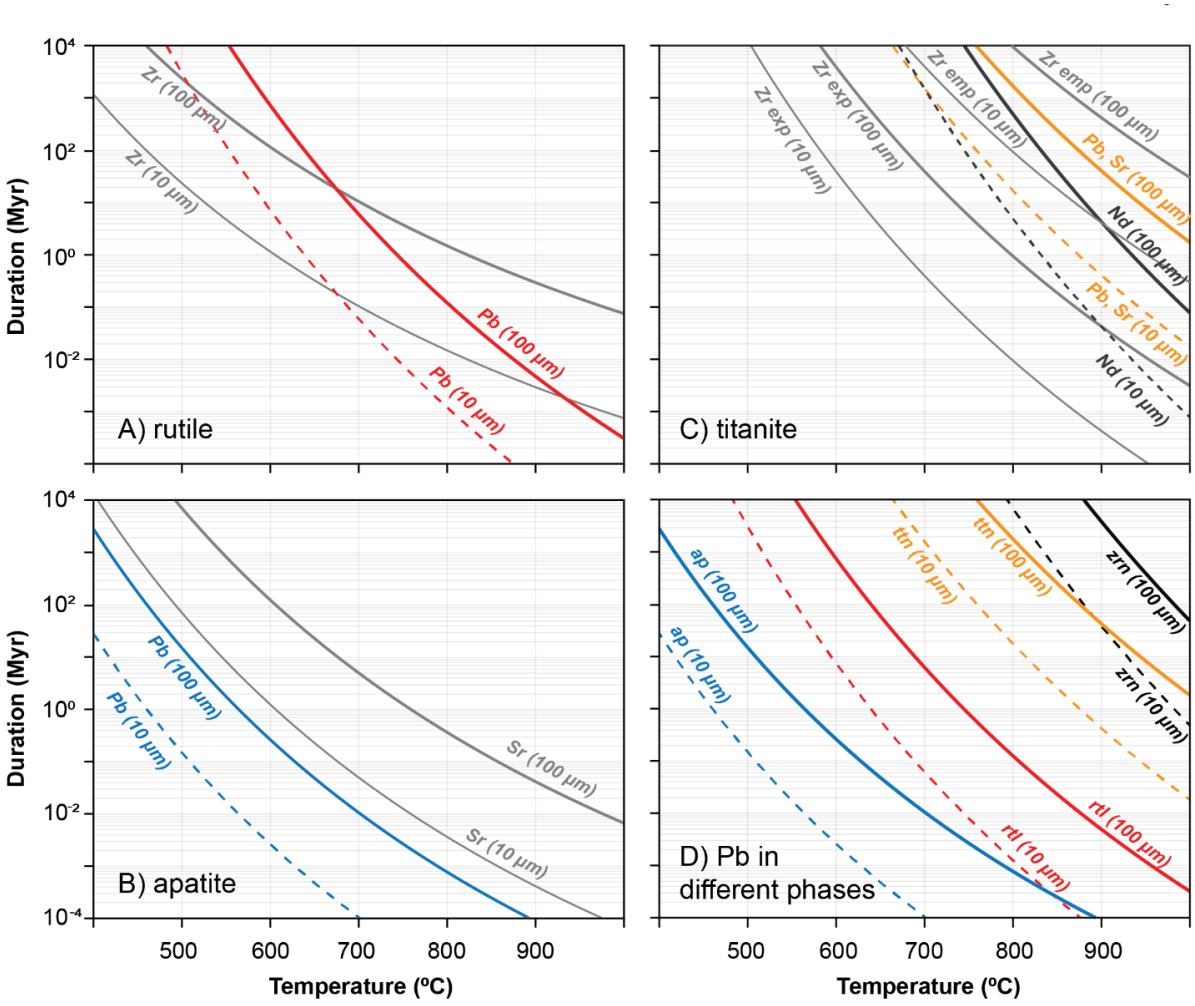

Figure 9. Characteristic length-scales of diffusion for different elements in different phases across relevant temperatures and durations. Length-scales of key elements would be expected to vary by orders magnitude were thermally-mediated volume diffusion at play. A) Comparing Zr and Pb length-scales for rutile. Diffusivity data for Zr from Cherniak (2006) and Pb from Cherniak (1993). B) Comparing Sr and Pb length-scales for apatite. Diffusivity data for Sr and Pb from Cherniak et al. (1991). C) Comparing Zr, Nd, Sr, and Pb length-scales for titanite. Diffusivity data Nd from Cherniak (1995) and Sr and Pb from Kohn (2017) and Holder et al. (2019). Experimental Zr diffusivity data from Cherniak (2006) (Zr exp) and empirical Zr diffusivity data from Holder et al. (2019) (Zr emp). D) Comparing characteristic length-scales of diffusion for Pb in different phases. Diffusivity data for rutile, apatite, and titanite same as other panels. Zircon Pb diffusivity data from Cherniak (2010).

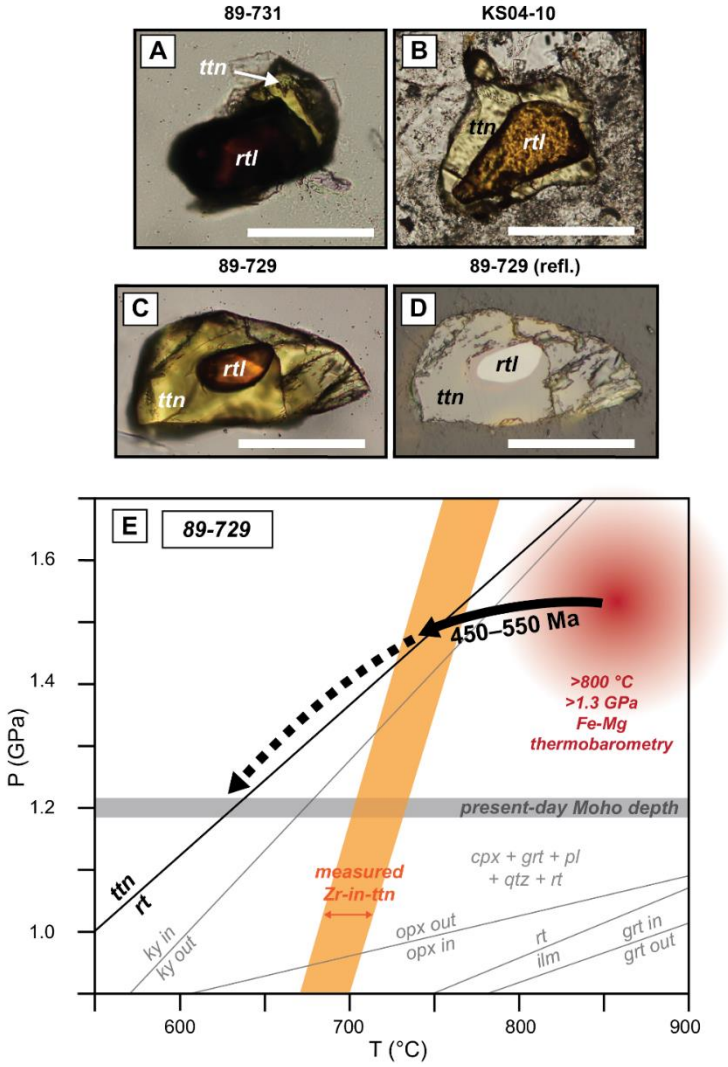

Figure 10. P-T path for the lower crust from titanite-rutile pairs. A–D) Rutile core in titanites from the Lashaine and Kisite granulite xenoliths indicate titanite growth during cooling and decompression after peak metamorphism. White bars are ~100 µm wide. E) Phase diagram for Lashaine granulite 89-729 (taken to be representative for all the granulites). The titanite-rutile phase boundary is from pseudosection modelling conducted in this study (see Appendix A). Orange bars represent constraints from ZiT thermometry for 89-729 titanite (similar to titanite from the other samples) using aSiO2 = 0.5 as a minimum bound, (Ferry and Watson, 2007). Zr contents in titanite suggest formation during cooling after peak metamorphism (red circle; P-T constraints from Mansur et al., 2014). Dashed arrow represents a possible P-T path from peak conditions, through the titanite-rutile boundary, and to pressures corresponding to the present-day Moho (horizontal grey bar).

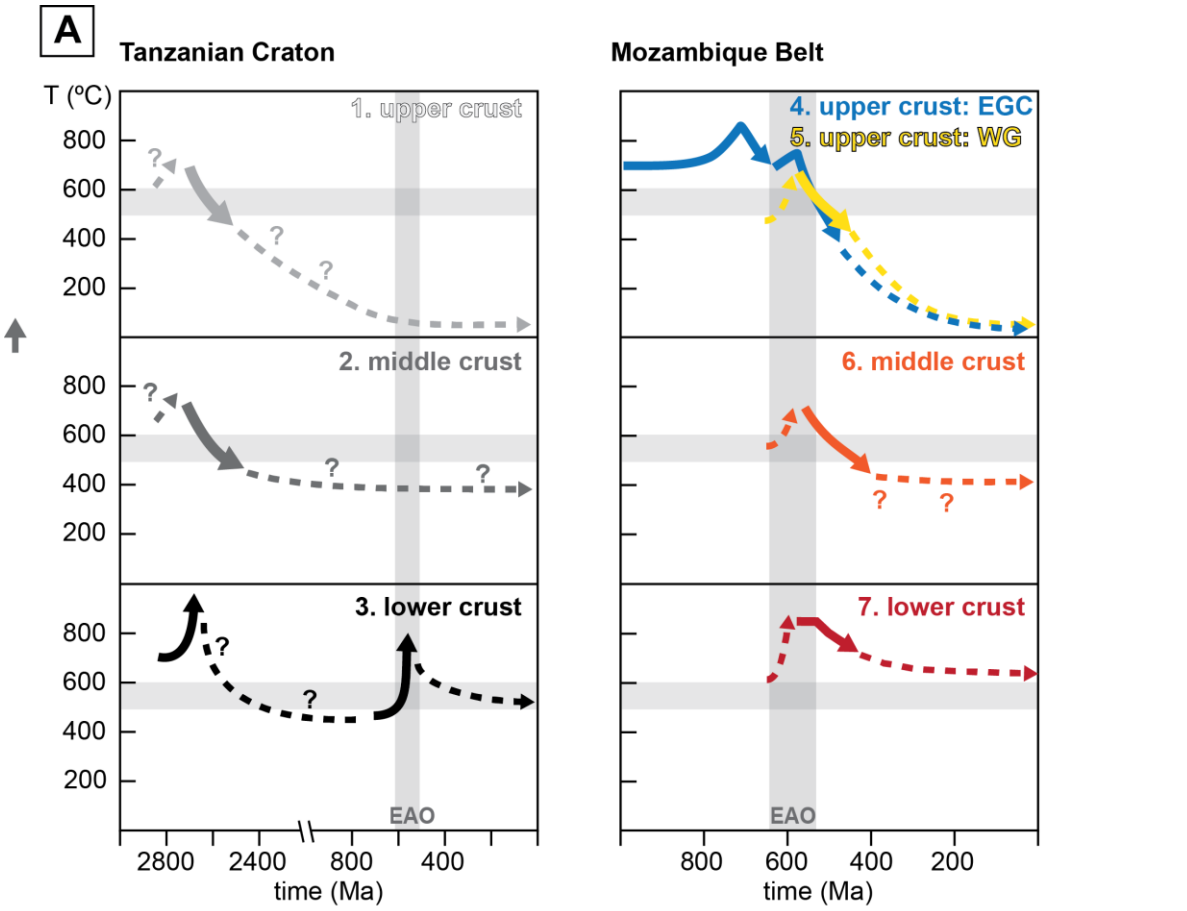
A
Tanzanian Craton
Mozambique Belt
T (ºC)
1. upper crust
2. middle crust
3. lower crust
4. upper crust: EGC
5. upper crust: WG
6. middle crust
7. lower crust
EAO
2800
2400
800
400
time (Ma)
800
600
400
200

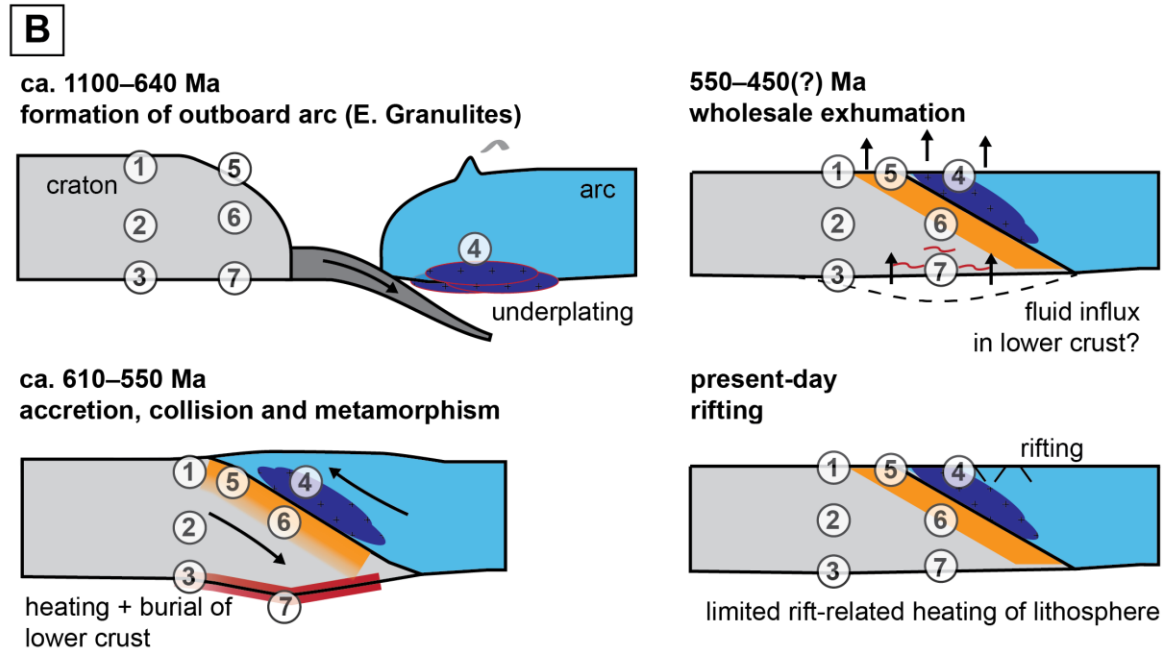
B
ca. 1100–640 Ma
formation of outboard arc (E. Granulites)
craton
arc
underplating
550–450(?) Ma
wholesale exhumation
fluid influx
in lower crust?
ca. 610–550 Ma
accretion, collision and metamorphism
heating + burial of
lower crust
present-day
rifting
rifting
limited rift-related heating of lithosphere

Figure 11. A) Schematic diagram illustrating cooling rates of the different crustal levels of the Tanzanian Craton and Mozambique Belt. Solid lines represent cooling paths constrained by petrochronology, whereas dashed lines represent inferred cooling paths (with question marks indicating highly uncertain paths). From the craton, Labait granite xenoliths are taken as representative of the upper crust, schist and amphibolite xenoliths as sampling the middle crust, and granulite xenoliths from the lower crust. From the Mozambique Belt, outcrops are taken as upper crustal samples, amphibolite and orthogneiss xenoliths from the middle crust, and granulite xenoliths from lower crust. The upper crust of the craton appears to record Archean cooling, whereas the lower crust underwent heating during the EAO and recently during rifting (not shown). In contrast to the craton, the entire crust of the Mozambique Belt underwent relatively rapid cooling following the EAO, with differences in the post-collisional thermal histories relating to later melt/fluid metasomatism during later slow cooling (also not shown). The horizontal grey bar represents the nominal range of Pb closure temperatures for rutile and apatite; above this bar, both phases are open to total Pb loss, and below it, both phases retain radiogenic Pb. B) Cartoon showing tectonic interpretations. Numbered circles correspond to numbers in panel A.

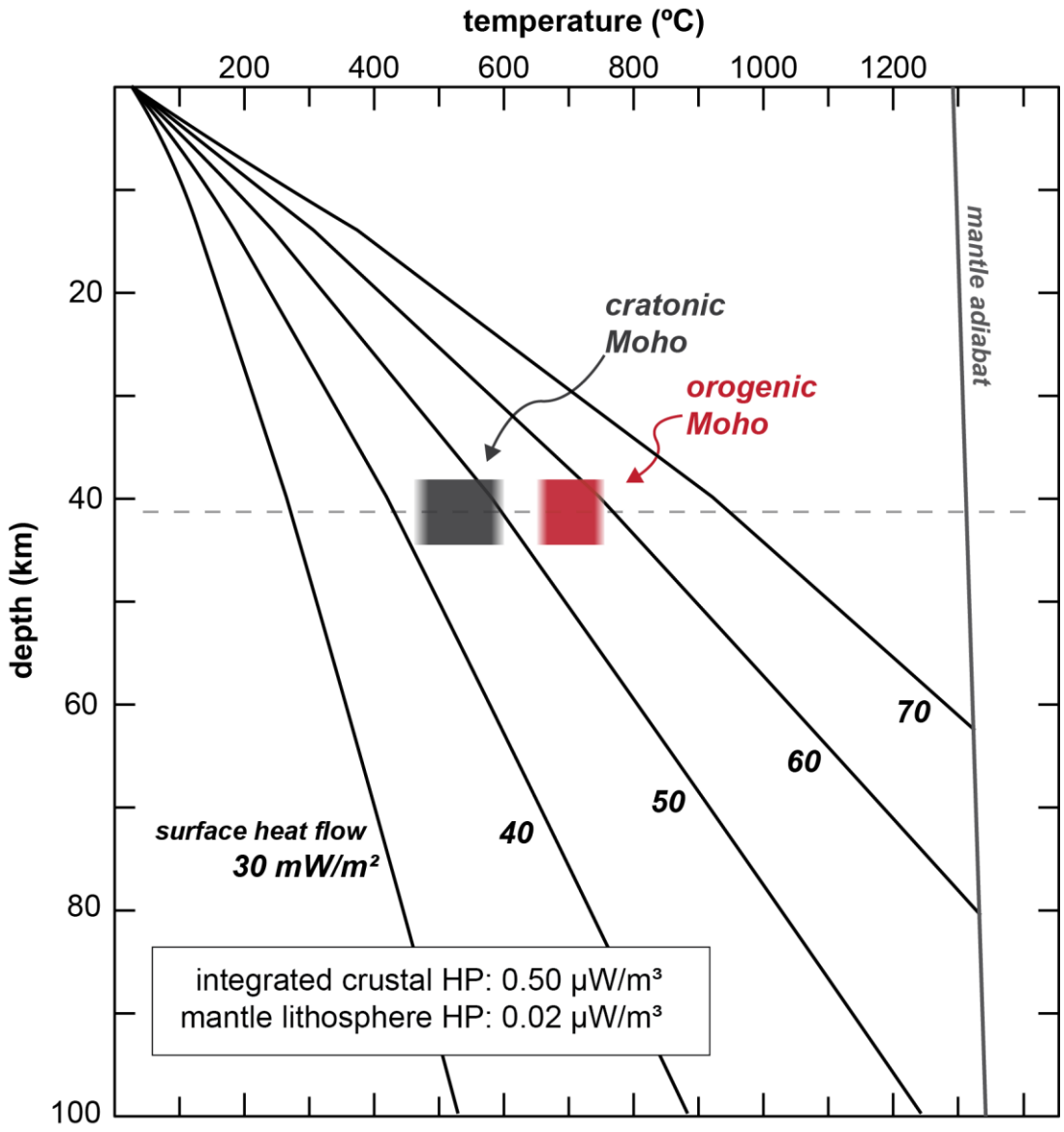

Figure 12. Comparison of inferred Moho temperatures for the craton margin (Labait; grey) and the EAO (Lashaine; red) with modeled geotherms. Bar widths represent the inferred range of Moho temperatures based on titanite-rutile petrochronology. All the geotherms are modeled by assuming purely conductive heat flow through the lithosphere and the same lithospheric heat production (HP) profile (Furlong and Chapman, 2013); only mantle heat flow is varied.

Chapter II. Heat transfer and production in cratonic continental crust: Constraints from U-Pb thermochronology of xenoliths from the Siberian craton

Submitted to Geochemistry, Geophysics, Geosystems in 2022

With co-authors Roberta L. Rudnick[1], Dmitri Ionov[2], John M. Cottle[1], Jean-François Moyen[3], Alexander Golovin[4,5], and Andrey Koraskov[4]

[1]Department of Earth Science, University of California, Santa Barbara, CA 93106, USA

[2]Géosciences Montpellier, Université de Montpellier, Montpellier, France

[3]Université Jean-Monnet, Laboratoire Magmas et Volcans, UCA-CNRS-IRD, Aubière

[4]Sobolev Institute of Geology and Mineralogy, Siberian Branch, Russian Academy of Sciences, Novosibirsk, Russian Federation

[5]Institute of the Earth's Crust, Siberian Branch, Russian Academy of Sciences, Russian Federation

ABSTRACT

Coupled U-Pb and trace-element analyses of accessory phases in crustal xenoliths from the Late Devonian Udachnaya kimberlite (Siberian craton, Russia) constrain Moho temperature and crustal heat production. Rutile and apatite in lower-crustal garnet granulite xenoliths record U-Pb dates that extend from 1.8 Ga to 360 Ma (timing of kimberlite eruption). This contrasts with upper-crustal tonalite and amphibolite xenoliths that contain solely Paleoproterozoic apatite. Depth profiling of rutile from the lower-crustal xenoliths show that U-Pb dates increase gradually from rim to core over μm-scale distances, with Al, Zr, and Fe increasing in concentration across similar length-scales. The U-Pb and trace element gradients in rutile are incompatible with partial Pb loss during slow cooling in the lower crust and instead require depth-dependent heating of the crust for <1 Myr prior to eruption. The preservation of Paleoproterozoic rutile and apatite dates require that long-term ambient lower-crustal temperatures before this thermal perturbation were cooler than their respective Pb closure temperatures (<400 °C). The lower-crustal temperature bounds from these data are consistent with pressure-temperature arrays of Udachnaya peridotite xenoliths that suggest relatively cool geothermal gradients, signifying that the mantle xenoliths accurately capture the thermal state of the lithosphere prior to eruption. Combined, the xenolith data imply low crustal heat production for the Siberian craton (~0.3 $\mu W/m^3$). Nevertheless, such values produce surface heat flow values of 20–40 mW/m^2, higher than measured around Udachnaya (average 19 mW/m^2), suggesting that the surface heat flow measurements are inaccurate. Such low heat production, in turn, suggest a mafic bulk composition for the central Siberian craton.

2.1 INTRODUCTION

Temperatures of the lower crust and Moho are key boundary conditions for models of heat transfer and production in the lithosphere, information that also impacts models of the bulk composition of the continental crust (e.g., Rudnick et al., 1998; Sandiford and McLaren, 2002; Jaupart and Mareschal, 2014; Hacker et al., 2015). Surface heat flow measurements reveal the total amount of heat exiting the lithosphere (a combination of mantle heat flow entering the base of the crust and heat production within the crust), yet temperatures across the Moho are poorly constrained, making it difficult to unravel the respective contributions of the mantle and crust to the total heat budget of the lithosphere. Seismic wavespeeds and other geophysical observations can provide snapshots of the thermal profile of the crust (e.g., Goes et al., 2020), but only xenoliths—fragments derived from *in situ* lower crust transported rapidly to the surface by volcanism—yield direct insights into long-term thermal histories (e.g., Rudnick et al., 1998; Hasterok and Chapman, 2011).

Thermobarometry of xenoliths can, in principle, be used to establish temperatures at the depth at which they equilibrated. However, a long recognized issue with this approach—especially for stable cratonic regions—is that different lithologies record disparate geothermal gradients through the lithosphere (e.g., Semprich and Simon, 2014). Pressure-temperature (P-T) arrays for cratonic mantle xenoliths define relatively cool geothermal gradients through the lithosphere (30–45 mW/m^2 geotherms) and projections of these gradients to the Moho suggests temperatures of 400–600°C (Hasterok and Chapman, 2011; Garber et al., 2018). Mantle xenoliths, however, only provide indirect constraints on Moho temperatures because robust thermobarometric calibrations are restricted to lithologies that

equilibrated within the high-pressure garnet stability field (e.g., Brey and Köhler, 1990). Granulite xenolith derived from the deep crust could provide direct constraints on the thermal state of the deep crust, yet thermobarometry of granulite xenoliths suggests geothermal gradients higher than peridotite xenoliths from the same pipes (e.g., >60 mW/m2; Jones et al., 1983; Semprich and Simon, 2014). This likely reflects the failure of these anhydrous granulites to react and equilibrate beyond peak metamorphic conditions (e.g., Frost and Chacko, 1989; Pattison and Begin, 1990).

The U-Pb isotope system holds much promise for extracting long-term thermal histories of the deep crust from xenoliths (Davis, 1997; Davis et al. 2003; Schmitz and Bowring, 2003; Blackburn et al., 2011; 2012; Edwards and Blackburn, 2018; Apen et al., 2020; O'Sullivan et al., 2021). U-Pb thermochronology exploits both the radioactive decay of U to Pb and the temperature-dependent retention (closure) of Pb in different accessory minerals. At temperatures above Pb closure, Pb will diffuse out of a crystal and at temperatures below Pb closure, Pb will be retained (Dodson, 1973). For zircon, Pb closure temperatures are >1000 °C, for rutile ~500–600 °C, and apatite ~350–450 °C (all assuming a 50–500-µm-radius sphere and 0.01–0.1 °C/Myr cooling rates; Cherniak, 2010; Smye et al., 2018). These phases are expected to experience different degrees of Pb diffusion due to residence near or above their respective Pb closure temperatures in the lower crust (Schmitz and Bowring, 2003; Blackburn et al., 2011). For example, at 500 °C Pb diffusion in zircon and rutile is sluggish and the U-Pb system should exhibit closed-system behavior such that dates older than magmatic entrainment can be retained in these phases. At the same temperature, Pb diffusion in apatite would be significant (open-system behavior), resulting in U-Pb dates that overlap the timing of eruption, reflecting rapid cooling upon eruption.

A central tenet in developing thermal models for the lower crust based on U-Pb thermochronology is the notion that Pb undergoes thermally-mediated volume diffusion at ambient lower-crustal temperatures. Indeed, xenolith transport in kimberlites and alkali basalts is too rapid (on the order of hours to days; Spera, 1984) to significantly disturb the U-Pb system in most accessory phases (Schmitz and Bowring, 2003). Xenoliths, however, may be heated during episodes of advective magmatic heating or fluid flow before their entrainment and such heating could induce partial Pb loss in thermochronometers (e.g., Hacker et al., 2000; Smit et al., 2016; Jollands et al., 2018). Any inferences on lithospheric thermal structure based on xenoliths and their mineral constituents must therefore delineate primary signatures of crustal relaxation (on the order of 100–1,000 Myrs) from shorter-term heating by magmatic intrusion or metasomatism (<1 Myr). Spatially-resolved analysis of multiple trace elements with different diffusivities can discriminate signatures of long-term cooling from shorter-term heating events in the lower crust: diffusive length scales should vary according to diffusivities, with faster diffusing elements showing more pronounced length-scales of diffusion than slower diffusing ones (Stearns et al., 2016; Holder et al., 2018; Garber et al., 2020; Apen et al., 2020).

To test the fidelity of U-Pb thermochronology as a tool for constraining the long-term thermal history of the deep crust, we have undertaken laser ablation split stream U-Pb and trace-element analyses of accessory phases in crustal xenoliths from the Udachnaya kimberlite located within the Siberian craton (Fig. 1). The xenolith suite covers a broad range of lithologies, including granitoids, amphibolites, and garnet-bearing granulites. This lithological diversity is interpreted as sampling different levels of the crustal column at Udachnaya. The new laser ablation data, combined with new thermobarometry and

pseudosection modeling, are used to infer the thermal state of the crust prior to eruption and develop models of heat transfer and production within the Siberian craton.

2.2 GEOLOGIC BACKGROUND AND PREVIOUS XENOLITH WORK

Most of the Siberian craton is buried under thick Phanerozoic sedimentary and volcanic cover, but information about crust formation and structure is gleaned from limited basement outcrops and kimberlite-hosted xenoliths (Fig. 1). Based on geophysical data and outcrops in the Anabar shield, the craton is divided into five major terranes: Tungus, Magan, Daldyn-Markha, Olenek, and Aldan (see summaries in Rosen, 2002). Basement gneisses and granulites exposed in the Anabar shield reveal that the craton is composed of Archean crust (ca. 3.6–2.7 Ga) reworked throughout the Archean and Proterozoic as well as juvenile Proterozoic crust (2.1–1.8 Ga) (Fig. 1; Rosen, 1989; Smelov et al., 2012; Paquette et al., 2017; Moyen et al., 2017). Collision of the Tungus, Magan, Daldyn-Markha, and Olenek terranes to form the Siberian craton occurred 2.1–1.8 Ga based on the geochronology and geochemistry of Paleoproterozoic granitoids and metamorphic rocks of the Anabar shield (Rosen, 2002; Rosen et al., 2006).

Kimberlites abound throughout the northern part of the craton (Fig. 1). Most kimberlites were emplaced in the Paleozoic (450–340 Ma) and Mesozoic (250–130 Ma) (Kinny et al., 1999; Sun et al., 2014) and are rich sources of xenoliths/xenocrysts that provide information on the age and structure of the craton where it is otherwise concealed (e.g., Griffin et al., 1999; Rosen, 2002; Kostrovitsky et al., 2016). The diamondiferous Udachnaya kimberlite pipe erupted through the Daldyn-Markha terrane ca. 360 Ma (U-Pb perovskite; Kinny et al., 1999; Sun et al., 2014) and hosts an extensive suite of mantle and crustal xenoliths.

Thermobarometry of Udachnaya garnet peridotite xenoliths suggest that the lithosphere is thick (> 200 km) and cold (Fig. 2; Boyd, 1984; Agashev et al., 2013; Goncharov et al., 2013; Doucet et al., 2013; Ionov et al., 2010; 2015; 2020; Liu et al., 2022). Radiogenic isotopes in garnet peridotites (Re-Os, Lu-Hf, Sm-Nd) suggest a dominantly Proterozoic age for lithosphere formation (2.2–0.9 Ga; Doucet et al., 2015; Ionov et al., 2015; 2020), but spinel peridotites, eclogites, and olivine megacrysts indicate Archean ages (Re-Os and Sm-Nd model ages up to 3.2 Ga; Pearson et al., 1995; Ionov et al., 2020). Re-Os model ages as young as 360 Ma are also present and have been interpreted to reflect Re addition during kimberlite emplacement (Ionov et al., 2015; 2020).

Crustal xenoliths from Udachnaya include granitoids, amphibolites, mafic garnet granulites, and felsic garnet granulites, some of which are probably sedimentary in origin (e.g., Koreshkova et al., 2009; 2011; Moyen et al., 2017; Shatsky et al., 2014; 2019; Jin et al., 2021). Zircon U-Pb dates from lower-crustal granulite xenoliths are dominantly Paleoproterozoic—ranging between 1.9 and 1.8 Ga—though some granulite xenoliths contain zircon with Archean inheritance (2.8–2.7 Ga) (Rosen, 2002; Rosen et al., 2006; Koreshkova et al., 2009; Shatsky et al., 2016; 2019; Moyen et al., 2017). This contrasts with shallower granitoid and amphibolite xenoliths that contain Archean zircon with no concordant Paleoproterozoic dates (e.g., Moyen et al., 2017). Net-transfer reaction and cation exchange thermobarometry of garnet granulite xenoliths indicate equilibration at 0.6–1.2 GPa and 800–900 °C (Koreshkova et al., 2011; Jin et al., 2021). Significant 100–200 °C cooling is also recorded by Fe-Mg temperatures from garnet and pyroxene rims and by the presence of retrograde amphibole in some granulite xenoliths (Koreshkova et al., 2011; Jin et al., 2021).

The crust in the vicinity of Udachnaya is 44–46 km thick (Mackey et al., 1998; Cherepanova et al., 2013). Surface heat flow data across the Siberian craton are sparse, but the six measurements within ~100 km of Udachnaya yield an average value of 19 ± 3 mW/m2 (1SD) (Fuchs and Norden, 2021, and references therein). As it stands, these data are among the lowest surface heat flow values observed for any craton (cf., Jaupart et al., 2016). If accurate, they require either exceedingly low heat production in the crust, a low mantle heat flux, or both (Rudnick et al., 1998; Jaupart et al., 2016). Alternatively, the surface heat flow measurements may be inaccurate, possibly compromised by the thick sedimentary/volcanic cover overlying the crystalline basement around Udachnaya (Cherepanova et al., 2013), regional brine aquifers (Kitayama et al., 2017, and references therein), and/or recent glaciation (Birch, 1948; Jaupart and Marescahl, 2007).

2.3 SAMPLES

The sample suite consists of 18 xenoliths analyzed and discussed by Moyen et al. (2017), as well as five new xenoliths. Petrographic descriptions with photomicrographs for the new samples are provided in Appendix B. Rather than detailing the work done on all 23 samples (mostly U-Pb), we selected a subset of seven representative samples for in-depth investigation that are inferred to sample different levels of the crustal column at Udachnaya: two tonalites (samples 01-104 and 02-154), one amphibolite (sample 02-114), and four garnet granulites (samples 01-34, 79-14, 01-95, and 36-14) (Fig. 3). Three of the granulites (01-34, 79-14, and 01-95) are mafic garnet granulites composed of garnet + clinopyroxene + plagioclase ± orthopyroxene, and one (36-14) is a felsic garnet granulite composed of garnet + orthopyroxene + plagioclase + quartz + graphite. All of the granulites exhibit granoblastic

textures, and their mineral assemblages are well-preserved, showing minor degrees of alteration (Fig. 3).

We present results from thermobarometry and coupled U-Pb and trace-element analyses of accessory phases for the seven xenoliths. Zircon and apatite were analyzed for the tonalites and amphibolite (these rocks contained no other phases datable by U-Pb). Apatite and rutile were analyzed in all four of the granulites, whereas zircon was only found in two of the granulites (01-95 and 36-14).

2.4 METHODS

2.4.1 Electron microprobe analyses and thermobarometry

Quantitative elemental analyses of major mineral phases were done using a Cameca SX-100 electron probe micro analyzer (EPMA) housed at the University of California, Santa Barbara (UCSB), using an accelerating voltage of 20 kV, a beam current of 200 nA and a defocused beam of 2–5 μm diameter.

Pressures and temperatures for the xenoliths were estimated using end-member equilibria among key minerals (mode 2 in THERMOCALC; Powell et al., 1998). Equilibration pressures and temperatures for the mafic garnet granulites were determined using garnet-clinopyroxene Fe-Mg exchange, garnet-clinopyroxene-plagioclase-quartz (GADS) equilibria, and albite-jadeite-quartz equilibria (AJQ) (Holland, 1980; Brey and Köhler, 1990; Newton and Perkins, 1982; O'Brien and Rötzler, 2003); because no free quartz is present in the three mafic garnet granulites, the calculated GADS and AJQ pressures represent maxima. Further, because we assumed no Fe^{3+} in the minerals, Fe-Mg

exchange temperatures should also be considered maxima (Nimis et al., 2015). For felsic granulite 36-14, garnet-orthopyroxene Fe-Mg exchange thermometry and garnet-orthopyroxene-plagioclase-quartz (GAHS) constrain equilibration P-T (Newton and Perkins, 1982). These data were supplemented with single-mineral cation thermobarometry, including: Ca- and Al-in-orthopyroxene and Zr-in-rutile, (Brey and Kohler, 1990; Tomkins et al., 2007). For the tonalite and amphibolite, we utilized the edenite-richterite thermometer of Holland and Blundy (1994) in tandem with the amphibole-plagioclase barometer of Molina et al. (2016).

We compared results from net-transfer and exchange reactions to pseudosection models developed using Perple_X (Connolly, 2009; Connolly and Kerrick, 1987). Models used the internally-consistent thermodynamic dataset of Holland and Powell (2011) and the metabasite set of solution models recommended by Green et al. (2016) and Palin et al. (2016). Whole-rock data used for pseudosection modeling are from Moyen et al. (2017); the whole-rock compositions of the newly analyzed xenoliths were determined using X-ray florescence at the Geoanalytical Lab at Washington State University. Details are reported in Appendix B.

2.4.2 Laser ablation split-stream analyses

Coupled U-Pb and trace-element analyses of zircon, rutile, and apatite were carried out using laser ablation split stream inductively coupled plasma mass spectrometry (LASS) at UC Santa Barbara using a Cetac Teledyne 193 nm excimer Analyte laser with a HelEx ablation cell coupled to a Nu Instruments Plasma high-resolution multi-collector inductively couple plasma mass spectrometer (MC-ICPMS) for U-Pb isotopes and Agilent 7700S

quadrupole ICPMS for trace-element abundances. For spot analyses on polished grain interiors, laser spot sizes and fluences varied depending on the analyzed phases: 25 μm, 4 Hz, 100% of 2 mJ for zircon; 35–40 μm, 4 Hz, 100% of 4 mJ for rutile; and 50 μm, 4 Hz, 100% of 2 mJ for apatite. The data were collected using standard-sample bracketing techniques and were calibrated against matrix-matched reference materials (RMs) for U-Pb analyses and glass standards for trace-element analyses, following the methods of Kylander-Clark et al. (2013) with modifications outlined in McKinney et al. (2015). Raw U-Pb ratios were baseline subtracted and corrected for laser- and plasma-induced element fractionation, and instrument drift using the Iolite software package (v. 2.5; Paton et al., 2011) in the Igor Pro interactive software environment.

The quoted uncertainties for all laser ablation data are 2σ and incorporate analytical uncertainty as well as additional uncertainties associated with reproducibility of secondary RMs (Horstwood et al., 2012). Zircon U-Pb analyses employed zircon 91500 (1065 Ma, ID-TIMS; Wiedenbeck et al., 1995) as the primary bracketing standard with zircons GJ1 (602 Ma, ID-TIMS; Jackson et al., 2004) and Plesovice (337 Ma, ID-TIMS; Sláma et al., 2008) analyzed as secondary standards. Rutile analyses employed rutile Kragero (1091 Ma, TIMS; Luvizotto et al., 2009) as the primary bracketing standard; rutiles Wodgina (2845 Ma, SIMS; Ewing et al., 2015), 9826J (382 Ma, TIMS; Kylander-Clark et al., 2008) and LJ04-08 (501 Ma, LASS-MC-ICP-MS; Apen et al., 2020) were analyzed as secondary standards. For apatite U-Pb analyses, apatite MAD-UCSB (467 Ma, ID-TIMS; Apen et al., 2021) as the primary bracketing standard with apatite RMs McClure (524 Ma, ID-TIMS; Schoene and Bowring, 2006) and OD306 (1597 Ma, ID-ICPMS age; 1545 Ma, LA-ICPMS age; Thompson et al., 2016) used as secondary standards. Trace-element concentrations were

also calculated in Iolite using an internal element standard (Liu et al., 2008). Reported uncertainties for trace-element data are 2σ and only include analytical uncertainties. Repeat analyses of secondary RMs over the course of this study indicate that each $^{238}U/^{206}Pb$ and $^{207}Pb/^{206}Pb$ measurements require an additional 1.9 % and 0.9 % for zircon analyses, 3.1 % and 1.8 % for rutile analyses, and 2.8 % and 1.6 % for apatite analyses (all 2σ), to account for the long-term variability in laser ablation analyses; these values were added in quadrature to the internal error of each U-Pb datum and considered when calculating intercept ages (Horstwood et al., 2016). Final U-Pb ratios and associated uncertainties were plotted using IsoplotR (Vermeesch, 2018). The quoted U-Pb dates for apatite and rutile are common-Pb corrected assuming a Stacey and Kramers (1975) initial $^{207}Pb/^{206}Pb$ composition.

Rutile depth profiling analyses were preformed using the same instruments described above. Analyses used a 50-µm-diameter spot size, operating at a frequency of 2 Hz and 50 % of 5 mJ laser power. Each ablation sequence consisted of two cleaning shots, followed by 25 s of monitored washout, and 75 s of continuous ablation, equating to final pit depths of ~13 µm (pit depths measured by SEM). Rutile depth profiles were also processed in Iolite. The depth profile data were averaged at 1 s intervals rather than output at their natural 0.5 s interval in order to reduce instrumental noise throughout each analysis while still maintaining a high-resolution sampling interval.

Whole profiles are exported from Iolite without formal uncertainties, so we approximated the uncertainty of each data point within a given profile based on the reproducibility of secondary reference rutiles (9826J and LJ04-08). A normal distribution was fitted to the U-Pb data from each reference rutile and the mean (µ) and standard

deviation (σ) of the $^{238}U/^{206}Pb$ and $^{207}Pb/^{206}Pb$ distributions were examined. The 2σ associated with LJ04-08 was 6.7% ($^{238}U/^{206}Pb$) and 4.3% ($^{207}Pb/^{206}Pb$); the 2σ associated with 9826J was 3.5 % ($^{238}U/^{206}Pb$) and 2.6% ($^{207}Pb/^{206}Pb$). We adopted the more conservative 2σ associated with LJ04-08 as the 2σ for the unknowns.

In addition to U-Pb ratios, we also report Pb concentration profiles, which we divided into radiogenic Pb (Pb*) and non-radiogenic (common) Pb (Pbc) (see also Holder et al., 2019; Garber et al., 2020). The total concentrations of $^{207,206}Pb$ at each depth interval were calculated using the measured $^{238}U/^{206}Pb$ ratio, $^{207}Pb/^{206}Pb$ ratio, and U concentration and assuming an invariant $^{238}U/^{235}U$ ratio of 137.818 (Heiss et al., 2012). Concentrations of $^{207,206}Pb^*$ were determined using common-Pb corrected dates and measured U concentrations. From this, we calculated the proportion of Pb_c by subtracting $^{207,206}Pb^*$ from the total $^{207,206}Pb$ concentrations. The final $^{207,206}Pb^*$ profiles were further corrected for radiogenic Pb ingrowth following kimberlite eruption at 360 Ma.

2.4.3. Diffusion modeling

In order to quantify temperatures and timescales of diffusion using U, Pb, and other elements, we consider the inverse error functions (erf^{-1}) of element gradients (Crank, 1975), expressed as:

$$erf^{-1}\left(\frac{C_x - C_r}{C_c - C_r}\right) = \left(\frac{1}{\sqrt{4 \times D(T) \times t}}\right)x$$

where C_x is the concentration at a given position within the grain, C_r is the concentration at the rim, C_c is the concentration at the core, D(T) is temperature-dependent diffusivity, and t is the time that the mineral spent at temperature T. The length-scales of diffusion for

elements in rutile are constrained by experiments. Diffusivities of Pb, Al, Si, Cr, Fe, Zr, Nb, Hf, and Ta in rutile vary by orders of magnitude, with relative diffusivities in the following order: $D_{Al} > D_{Si} > D_{Hf} \approx D_{Zr} > D_{Pb} > D_{Ta} \approx D_{Nb} > D_{Cr} > D_{Fe}$ (Sasaki et al., 1985; Cherniak, 2000; Cherniak et al., 2007; Marschall et al., 2013; Cherniak and Watson, 2019).

In addition to diffusion modeling, comparing U-Pb dates of different accessory phases aids in reconstructing thermal histories. Experimentally- and empirically-derived Pb diffusion coefficients in rutile and apatite suggest that rutile has a higher Pb closure temperature than apatite (e.g., Smye et al., 2018). For simple linear cooling and similar grain sizes, one would then predict U-Pb dates from rutile to be exclusively older than apatite (Dodson, 1973). We discuss the thermal history of the Siberian craton lower crust within this framework.

2.5 RESULTS

2.5.1 P-T estimates and pseudosection modeling

The stability fields of the observed mineral assemblages provide first-order P-T estimates for the xenoliths. The garnet-clinopyroxene-plagioclase-rutile stability field for the mafic garnet granulites encompasses a large P-T range (1.0–1.6 GPa and 600–900 °C). These estimates are consistent with the intersections of GADS, AJQ, and Fe-Mg garnet-pyroxene reactions determined using THERMOCALC (0.9–1.5 GPa and 750–900 °C), despite the absence of quartz in the xenolith's main mineral assemblage. The presence of relict orthopyroxene in mafic garnet granulite 01-95 documents crystallization at slightly lower pressures; assuming relict orthopyroxene was in equilibrium with garnet, Ca-in-orthopyroxene thermometry suggests earlier metamorphism at 1.0 GPa and 825 °C.

Temperatures based on the composition of garnet and pyroxene rims indicate cooler temperatures of 630–710 °C. Intersections of garnet isopleths in Perple_X did not produce results compatible with the P-T data from endmember equilibria (see Appendix B for further details); this could reflect contamination of the xenolith's whole rock compositions by the kimberlite and associated fluids (e.g., Koreshkova et al., 2011), or limitations in the application of activity models (e.g., pyroxene; Forshaw et al., 2019). No whole-rock data exists for felsic granulite 36-14 so we rely on the positions and intersections of net-transfer and exchange reactions determined from THERMOCALC. The average P-T is 1.3 ± 0.4 GPa and 950 ± 120 °C; Fe-Mg temperatures from garnet and orthopyroxene rims are 700–750 °C. Amphibole-plagioclase thermobarometry for both tonalites and amphibolites yield 0.4–0.5 GPa pressures and 700–750 °C temperatures.

2.5.2 U-Pb and trace element data

Zircon in tonalite xenoliths 01-104 and 02-154 and amphibolite xenolith 02-114 show variable amounts of Pb loss (Fig. 4). Concordant zircon populations are Neoarchean (ca. 2.7 Ga), consistent with findings of Moyen et al. (2017). Two spot analyses in sample 02-154 yield younger ca. 2.5 Ga and 1.9 Ga dates. Concordant Neoarchean zircon spot analyses have positively sloped heavy rare earth element (HREE) patterns (solid lines in Fig. 4) and Ti concentrations of 2–25 ppm, corresponding to 610–830 °C temperatures using the Ti-in-zircon thermometer calibration of Ferry and Watson (2007). Apatite in the same xenoliths yields Paleoproterozoic U-Pb isochrons (1.86–1.76 Ga; Fig. 5) and is characterized by HREE-depleted REE patterns and negative Eu anomalies.

Zircon in garnet granulite xenoliths 01-95 and 36-14 yields a range of Paleoproterozoic U-Pb dates (2.1–1.8 Ga) with the youngest population in both samples overlapping in age (ca. 1.83 Ga) (Fig. 4). Zircon in felsic granulite 36-14 has negative Eu anomalies, flat HREE patterns, and Ti concentrations of 16–53 ppm, or temperatures of 840–930 °C. Zircon in mafic granulite 01-95 has mostly positively-sloped HREEs (but see Fig. 4) and negative Eu anomalies with Ti concentrations of 19–28 ppm or Ti-in-zircon temperatures in the range of 810–850 °C.

Apatite in granulites 36-14, 01-95, and 79-14 has sufficient U concentrations (>0.5 ppm) to obtain geologically useful U-Pb dates. Apatite in felsic garnet granulite 36-14 yields U-Pb ratios that scatter between 1.6 Ga and 600 Ma (assuming a Stacey and Kramers common-Pb composition; Fig. 5). Apatite in mafic garnet granulite 01-95 is relatively low in U (<4 ppm); using all but three spots yields a 399 ± 12 Ma isochron (MSWD=3.5; Fig. 5). Mafic garnet granulite 79-14 has apatite with common-Pb corrected U-Pb dates that range from 2.0 Ga and 400 Ma (Fig. 5). Many apatite grains from xenoliths 01-95 and 79-14 contain monazite exsolution lamellae (confirmed by EDS and BSE images; Fig. 6), and mixing between apatite and monazite is apparent in trace element vs. U-Pb date patterns. Spot analyses older than 1.1 Ga define a linear array, with the 2.0 Ga endmember of this array characterized by greater LREE concentrations and higher Th/U ratios (Fig. 6).

U-Pb data from rutile in the garnet granulites also shows significant variability. In felsic granulite 36-14, rutile U-Pb analyses fall along a linear array with an upper age intercept of 1381 ± 17 Ma and a lower intercept of 532 ± 27 Ma (MSWD=2.6; Fig. 7). Zr-in-rutile temperatures are internally coherent, but vary among different grains (740–810 °C, assuming a pressure of 1.3 GPa). Mafic granulites 01-95 and 79-14 both have common-Pb

corrected U-Pb dates that range from ca. 1.1 Ga to 360 Ma. Like the felsic garnet granulite, Zr-in-rutile temperatures in both samples are internally consistent but differ among grains (790–940 °C at 1.2 GPa for sample 01-95 and 820–840 °C at 0.8 GPa for sample 79-14). Rutile in mafic garnet granulite 01-34 has low U (<0.5 ppm) and clusters near concordia at ~1.6–1.4 Ga; some amount of discordance is observed, but uncertainties are too large to define meaningful age intercepts (Fig. 7). Zr-in-rutile temperatures for this sample are uniform, 875–890 °C (assuming a pressure of 1.5 GPa).

Of the analyzed samples, granulites 36-14 and 01-95 contain rutile with enough U to produce robust U-Pb age depth profiles (>1 ppm U). Common-Pb corrected U-Pb dates in rutile depth profiles for felsic garnet granulite 36-14 show a gradual increase from the rim towards the grain interior (Fig. 7); dates at the outermost rim approach the 360 Ma eruption age (Fig. 8). Profiles for 36-14 also show increases in Al concentrations towards the grain interior, whereas Si and Fe are higher in the rims and lower towards the core; most other trace-elements are largely invariant with depth (Fig. 8). In mafic garnet granulite 01-95, U-Pb date profiles increase linearly from 360 Ma at the rim to 1.2 Ga–600 Ma dates at the bottom of the pit (though two profiles are wholly 360 Ma throughout the profile; Fig. 8). The outermost 1–2 μm of some rutile grains show greater concentrations of U, Pbc, Zr, and Hf than in the interiors. Beyond the discrete rims, U, Al, Zr, and Fe gradually increase towards the grains' interior whereas all other elements show no significant variations with depth (Fig. 8).

2.6 DISCUSSION

2.6.1. Xenolith petrochronology

In order to link the thermal histories of the xenoliths to heat fluxes in the lithosphere, it is imperative to evaluate what portions of the xenoliths' P-T history correspond to thermal conditions prior to eruption vs. older metamorphism. The tonalite and amphibolites are Archean rocks that were heated above apatite Pb closure temperatures during ca. 1.8 Ga amalgamation of the Siberian craton (Rosen et al., 2006; Moyen et al., 2017; Paquette et al., 2017). The presence of 1.8–1.7 Ga apatite in these rocks implies rapid cooling from 700–750 °C (amphibole-plagioclase thermometry) to below 400–450 °C (nominal Pb closure temperature assuming 50–200 μm diameter grains and relevant cooling rates of 1–10 °C/Myr) at 0.4–0.5 GPa, or 15–20 km depth (i.e., the upper crust). These rock remained below such temperatures and were not significantly re-heated since 1.8–1.7 Ga (Fig. 5).

Establishing P-T paths for dry mafic granulites like those investigated in this study is difficult given the propensity of cation-exchange thermometers to equilibrate during retrogression more readily than net-transfer reactions (e.g., Frost and Chacko, 1989; Pattison and Begin, 1994). The 0.8–1.5 GPa equilibration pressures (or 40–60 km depth) determined from pseudosection modeling and GADS/GAHS thermobarometry likely reflect (near) peak metamorphic conditions at 1.9–1.8 Ga—as evidenced by HREE depletions in zircon that indicate garnet crystallization at this time (Fig. 4; see also Koreshkova et al., 2011)—and need not correspond to their position in the deep crust at 360 Ma. By contrast, the presence of relict orthopyroxene in mafic garnet granulite 01-95 implies a P-T path from 1.0 GPa to peak pressures at 1.2 GPa. The cooler 700–750 °C temperatures recorded by Fe-Mg

exchange thermometry in garnet and pyroxene rims indicate cooling that probably track some amount of decompression/exhumation. The cooler rim temperatures, however, are also unlikely to represent ambient temperatures at 360 Ma, but instead reflect diffusional closure of Fe-Mg exchange between garnet and pyroxene (Harley, 1989). In this regard, the U-Pb in rutile and apatite, which undergo diffusional closure at significantly cooler temperature (Smye et al., 2017), provide further insights into the temperature-time evolution of the Udachnaya lower crust.

In garnet granulite xenoliths, rutile and apatite record dates that are significantly younger than the well-documented 2.0–1.8 Ga period of craton amalgamation. In particular, the upper age intercept in rutile from three of the analyzed garnet granulites is 1.4–1.1 Ga (Fig. 7). These dates could be interpreted as the time when the rocks cooled below rutile Pb closure following slow cooling from 1.8 Ga or a discrete re-heating event at 1.4–1.1 Ga. If the rocks underwent monotonic cooling since 1.8 Ga, one would predict that apatite dates would be as young or younger than rutile dates (calculated Pb closure temperatures for rutile are 500–600 °C and for apatite are 350–450 °C using relevant 50–500-μm-radius grains and cooling rates of 0.01–0.1 °C/Myr). In mafic garnet granulite 01-95, apatite U-Pb dates are consistently younger than the rutile dates, and in felsic garnet granulite 36-14, all but two apatite U-Pb dates are younger than the 1.4 Ga rutile (Fig. 4). The exception in the Udachnaya xenolith suite is mafic garnet granulite 79-14, where about half of the apatite dates are significantly older than rutile (up as 2.0 Ga; Fig. 4). The presence of monazite exsolution lamellae in apatite from this sample complicates comparisons between apatite and rutile U-Pb dates. Assuming the monazite exsolved following Paleoproterozoic metamorphism, the large range of apatite U-Pb dates must partly reflect mixing of both

phases during laser ablation. In light of this, we conclude that apatite spot dates >1.1 Ga, which reflect mixed monazite/apatite analyses formed during Paleoproterozoic metamorphism (Fig. 4) and are therefore not geologically meaningful.

Based on apatite and rutile U-Pb dates, we suggest that the ca. 1.4–1.1 Ga upper age intercepts represent re-heating of the lower crust in the Mesoproterozoic by a discrete thermal event, rather than by monotonic cooling since 1.8 Ga. This interpretation is supported by the similar upper age intercepts in apatite and rutile that indicate rapid cooling through their nominal Pb closure temperature. No 1.4–1.1 Ga crystallization dates have been documented previously in outcrops or in xenoliths from the Siberian craton (Koreshkova et al., 2009; Priyatkina et al., 2016; Paquette et al., 2017), with the exception of rift-related dike swarms in the Anabar shield and Olenek uplift that record similar U-Pb dates (see Gladkochub et al., 2010, and references therein). We speculate that a similar dike emplacement event occurred around Udachnaya at 1.4–1.1 Ga, creating a thermal pulse that re-heated the lower crust above the Pb closure temperatures of rutile and apatite (akin to resetting of rutile in Slave craton xenoliths by dike swarm intrusion; Davis, 1997). The spread of rutile U-Pb dates down to 360 Ma provides further insight into the evolving thermal state of the deep crust prior to eruption.

2.6.2 Timescales of lower-crustal re-heating from depth profiles

The objective of multi-element depth profiling is to ascertain whether age and geochemical gradients within minerals are a result of thermally-mediated volume diffusion or re-/neo-crystallization. If Pb was diffusing out of rutile during slow cooling in the lower crust on the billion-year-timescale, this would imply residence at temperatures near the Pb

closure temperature (e.g., Schmitz and Bowring, 2003; Blackburn et al., 2011; O'Sullivan et al., 2020). On the other hand, if Pb loss was induced by a thermal event associated with kimberlite eruption, ambient lower crustal temperatures could have been cooler than the nominal Pb closure temperature of rutile.

In each of the rutile profiles, we compared the slope (m) of normalized gradients for different elements (Fig. 9), expecting that the slopes of elements should scale by $1/\sqrt{(4\times D(T))}$ in the case of slow cooling over the Pb closure temperatures of rutile from 1.1 Ga until kimberlite eruption at 360 Ma. In rutile from felsic garnet granulite 36-14, Pb* gradients occur in the outermost 2–5 μm (Fig. 8). The normalized slopes of Pb* and Al are not significantly different (Fig. 9) despite having diffusivities that differ by orders of magnitude (Cherniak and Watson, 2019). In mafic garnet granulite 01-95, the Pb* slope values are lower than slower-diffusing Al and Zr (Fig. 9), which would appear consistent with volume diffusion of Pb. These observations are, however, difficult to explain by thermally-mediated volume diffusion during protracted residence in the lower crust (at least with the available experimentally-determined diffusivities). For example, Al profiles have a topology that resembles outward diffusion across the outermost 2–8 μm portion of the profiles (Fig. 8). Aluminum diffusion over these length-scales would require isothermal residence at 800–850 °C for 1 Gyr (and hotter temperatures still for shorter timescales; Cherniak and Watson, 2019). At the same conditions, our calculations indicate complete open-system behavior of Pb* and Zr until eruption, contrary to the observed μm-scale concentration gradients and the preservation of rutile U-Pb dates as old as 1.1 Ga (Fig. 7). If the gradients captured in rutile are related to diffusion, they cannot be explained by slow

cooling in the lower crust. Rather, the rutile depth profiles represent (re)crystallization and/or shorter-term heating prior to eruption 360 Ma.

The similar zonation of trace elements with drastically different diffusivities in rutile suggest that (re)crystallization was the dominant process controlling U-Pb and elemental gradients. Thin rims (1–2 μm) on rutile in mafic garnet granulite 01-95 are characterized by spikes in U, Pbc, Hf, and notably, Zr. We interpret these features as reflecting neo- or re-crystallization of rutile associated with regional kimberlitic magmatism. This process is distinct from the eruption process itself because: i) timescales of transport to the surface are too short to cause significant Pb diffusion (Spera, 1984; Schmitz and Bowring, 2003; Doucet et al., 2014); and ii) shallower tonalite and amphibolite xneoliths from the same kimberlite pipe have apatite with undisturbed Paleoproterozoic U-Pb isochrons (Fig. 4). These observations indicate that neo- or re-crystallization of rutile corresponds to a heating event that occurred shortly before eruption, was depth-dependent, and focused in the lower crust.

The outermost rims of rutile in mafic garnet granulite 01-95 have Zr concentrations that indicate heating to high temperatures prior to eruption (e.g., 9000 ppm Zr in profile 13 equate to >1000 °C, and higher still in other profiles; Fig. 8). It is probable that such extreme temperatures prior to eruption induced Pb loss. Assuming that a portion of the rutile Pb profiles does reflect thermally-mediated volume diffusion (Fig. 9), bounds can be placed on the duration of heating. The observed Pb* gradients in mafic garnet granulite 01-95 are consistent with average heating time-scales of <18 Myr, <3 Myr, and <0.6 Myr at 900 °C, 1000 °C, and 1100 °C, respectively; time-scales of heating based on Pb* profiles in rutile from felsic garnet granulite 36-14 are <4 Myr, <0.6 Myr, and <0.1 Myr at 900 °C, 1000 °C, and 1100 °C, respectively. Because slower-diffusing Al shows similar gradients to Pb* in

the rutile profiles, the time-scales of heating calculated from Pb gradients are maxima. Nonetheless, the transient nature of this event is consistent with timescales of advective heating prior to eruption proposed for other xenolith suites, such as those from the North Atlantic craton (Smit et al., 2016), Kaapvaal craton (Jollands et al., 2021) and Tibetan Plateau (Hacker et al., 2000).

Partial U-Pb resetting of rutile from the Udachnaya lower crustal xenolith suite due to heat advection from melts or fluids prior to eruption is supported by the presence of pockets of fine-grained material and secondary biotite in the xenoliths, which may be remnants of a melt/fluid (Fig. 3). There is ample evidence for metasomatism in Udachnaya peridotite xenoliths (Boyd et al., 1997; Ionov et al., 2010; Shatsky et al., 2008; Koreshkova et al., 2011; Agashev et al., 2013; Golovin et al., 2018). Agashev et al. (2013) identified at least three types of metasomatism in the peridotite xenoliths: carbonatite metasomatism ca. 2 Ga (addition of Ca, Al, and LREE); silicate melt metasomatism (enrichment of REE, Y, and Zr resulting in formation of garnet and clinopyroxene in otherwise highly depleted peridotites; see also Boyd et al., 1997); and enriched-basaltic melt metasomatism (local enrichment of Fe and Ti). The timing of the latter two events is unknown, but Agashev et al. (2013) proposed that basaltic melt metasomatism occurred not long before kimberlite eruption given that Fe-Ti enrichments are more localized among the xenolith suite. In addition, Golovin et al. (2018) described Na-K-Ca-rich melt inclusions in olivine from sheared peridotite xenoliths that resulted from interactions with primitive kimberlite magmas in the mantle prior to eruption. In Udachnaya granulite xenoliths, Koreshkova et al. (2011) noted that kimberlite melt interactions are required to account for bulk enrichments of LREE, Th, and U (with contributions from kimberlite-related fluids; Kamenetsky et al., 2007). Melt

metasomatism could account for the near-eruption age rutile rims that are enriched U, Pbc, Hf, and Zr relative to the rutile interiors (Fig. 8) as well as heating that may have resulted in diffusional exchange with adjacent phases (garnet, plagioclase, pyroxene).

Finally, while lower crustal xenoliths were re-heated, there is no correlation between the extent of rutile U-Pb resetting and peak pressure (Table 1). If heating was depth-dependent, this then suggests that the samples with greater U-Pb resetting resided at greater depths relative to those with minimal overprinting (Fig. 7). Alternatively, advective heating was heterogeneous in the deep crust, an inference supported by data on mantle xenoliths (e.g., Liu et al., 2022; see also Fig. 1). Regardless, the preservation of Proterozoic rutile and apatite dates indicate that, up until a few Myrs prior to kimberlite eruption, the deep crust of the Siberian craton resided at temperatures cool enough that Pb was not actively diffusing out of the rutile and apatite crystal lattice (i.e., at temperatures below 400 °C for up to 1 Gyr; using Pb diffusivities reported in Cherniak et al., 1991, and Cherniak, 2000).

2.6.4 Crustal heat production models for the Siberian craton

The data discussed above provide a new avenue for constraining crustal heat production. Previous approaches to determining crustal heat production include using measured abundances of U, Th, and K in rare crustal cross sections exposed at the surface, or reconstructed from xenoliths (e.g., Nicolaysen et al., 1981; Sandiford et al., 2003; Gruber et al., 2021). The latter method has unquantifiable uncertainties because it is unknown how representative a xenolith suite is of a crustal column in general (i.e., whether the whole column was sampled and if it was sampled in direct proportion that it exists within the crust). Another approach entails using xenolith P-T data to constrain heat fluxes throughout

the lithosphere (including heat production; e.g., Rudnick et al., 1998). Here we model geothermal gradients using different crustal heat production scenarios and compare results to peridotite xenolith P-T data and the temperature bounds imparted by xenolith petrochronology (i.e., temperatures for the lower crust and Moho should be consistent with closed-system behavior of Pb in rutile and apatite).

We assess different heat production models for the lithospheric column at Udachnaya using steady-state one-dimensional conductive geotherms (following Hasterok and Chapman, 2011; Furlong and Chapman, 2013). Our goal is not to determine the exact crustal heat production value for Udachnaya, but rather to evaluate general trends in geotherms that match the available xenolith data. We evaluate three different distributions of heat production within the crust: a) uniform crustal heat production; b) stepwise decrease in crustal heat production with depth; and c) exponential decrease in heat production with depth (Fig. 10). In model A, we chose an average Archean crustal heat production of 0.65 $\mu W/m^3$ (after Jaupart and Mareschal, 2014). In model B, we modeled a stepwise change in heat production assuming two layers: an upper crust (0–15 km) and lower crust (15–45 km). A few more simplifying assumptions in model B were made: heat production values are based on whole-rock measurements of U, Th, and K (Moyen et al., 2017), which are likely biased towards greater values given the likelihood of contamination of kimberlite magma or related fluids (Kamanetsky et al., 2007; Golovin et al., 2018; 2020; Koreshkova et al., 2009); and we assumed the upper crust consists of tonalites only and the lower crust solely of mafic garnet granulite (even though felsic garnet granulites are present in the lower crust). The average upper crustal tonalite heat-production is 0.36 $\mu W/m^3$, whereas the lower crustal average heat production of mafic granulites is 0.26 $\mu W/m^3$ for a total crustal heat production

of 0.29 μW/m^3. Model C assumes an exponential decrease in heat production, starting with an average tonalite heat-production at the surface and grading to an average mafic granulite value at 45 km depth for an integrated crustal heat production of 0.30 μW/m^3. All of the models utilize a mantle lithosphere heat production value of 0.006 μm/m^3 (after McIntyre et al., 2021), a Moho depth of ~45 km (Cherepanova et al., 2013), and surface heat flow values between 20–50 mW/m^2 (encompassing the range observed in cratons globally; Jaupart and Mareschal, 2014).

There are some interesting observations that can be made based on the modeled geotherms. First, the geotherms encapsulating the peridotite P-T data suggest Moho temperatures that are cooler than the nominal Pb closure in rutile (490–600 °C for relevant 50–500-μm-radius grains and cooling rates of 0.01–0.1 °C/Myr) and cooler than or within the calculated Pb closure temperatures of apatite (330–430 °C for the same grain sizes and cooling rates). Second, in all sets of models the Udachnaya peridotite P-T data are inconsistent with the measured surface heat flow value of 19 ± 3 mW/m^2 (represented approximately by the 20 mW/m^2 geotherms in Fig. 10). The xenolith data are, however, consistent with the global average range of 30–40 mW/m^2 surface heat flow for cratons (Jaupart et al., 2016). The spread in peridotite P-T data partly reflects lithospheric heating prior to eruption (see Liu et al., 2022), such that the ambient geotherm at 360 Ma was closer to the cooler geotherms (and hence cooler Moho temperatures; Fig. 10). Even so, reconciling the peridotite P-T data with the observed low surface heat flow around Udachnaya would require substantial cooling of the lower crust since kimberlite emplacement 360 Ma; the secular decay of radioactive elements alone could not account for this (e.g., Jaupart et al., 2016). More likely, surface heat flow measurements made in the

central Siberian craton are inaccurate, having been potentially compromised by the thick and permeable sedimentary and volcanic cover (Cherepanova et al., 2013), largely infiltrated by brines (Alexeev et al., 2005; 2022; Kitayama et al., 2021), or the chilling effect of Pleistocene glaciations (Birch, 1948).

The xenolith data overall support low crustal heat production in the Siberian craton. This could reflect a bulk mafic crust composition (e.g., Rudnick and Gao, 2014) or extensive depletion of heat-producing elements during high-temperature cratonization (e.g., Carlson et al., 2005). The presence of lower-crustal felsic granulites at Udachnaya and nearby sites require some amount of silicic material at depth (e.g., Koreshkova et al., 2011; Moyen et al., 2017; Shatsky et al., 2019). Previous studies have shown that accessory phases in high-grade felsic rocks retain Th even after undergoing extensive melt depletion (e.g., Rudnick and Fountain, 1995; Bea, 1996; Alessio et al., 2018). High heat-producing felsic lithologies therefore may be subordinate to mafic lithologies in the deep crust of the Siberian craton.

2.7 CONCLUSIONS

New laser ablation split-stream U-Pb and trace-element data from accessory phases in xenoliths from the ca. 360 Ma Udachnaya kimberlite, Siberian craton, show that the U-Pb system is sensitive to transient heating of the lower crust and not just slow cooling. Length-scales of U-Pb and trace element gradients revealed by depth profiling of rutile suggest that depth-dependent heating of the deep crust occurred for <1 Myr before eruption. If disturbances to the U-Pb system occurred just prior to eruption and Pb was not actively diffusing out of the rutile crystal lattice during residence in the lower crust, this implies that long-term lower-crustal temperatures were cooler than the nominal closure temperatures of

rutile (<500 °C) and probably apatite (<400 °C). The lower-crustal temperature bounds imparted by these data are consistent with pressure-temperature arrays of Udachnaya peridotite xenoliths that suggest relatively cool geothermal gradients, signifying that the mantle xenoliths accurately capture the thermal state of the lithosphere prior to eruption. Combined, the xenolith data imply low crustal heat production for the Siberian craton (~0.3 $\mu W/m^3$). Such values still produce surface heat flow values higher than measured around Udachnaya (average 19 mW/m^2), suggesting that the surface heat flow measurements are too low (possible compromised by thick sedimentary cover and deep regional aquifers). Collectively, the xenolith data support low crustal heat production in the Siberian craton and a relatively mafic bulk crust composition.

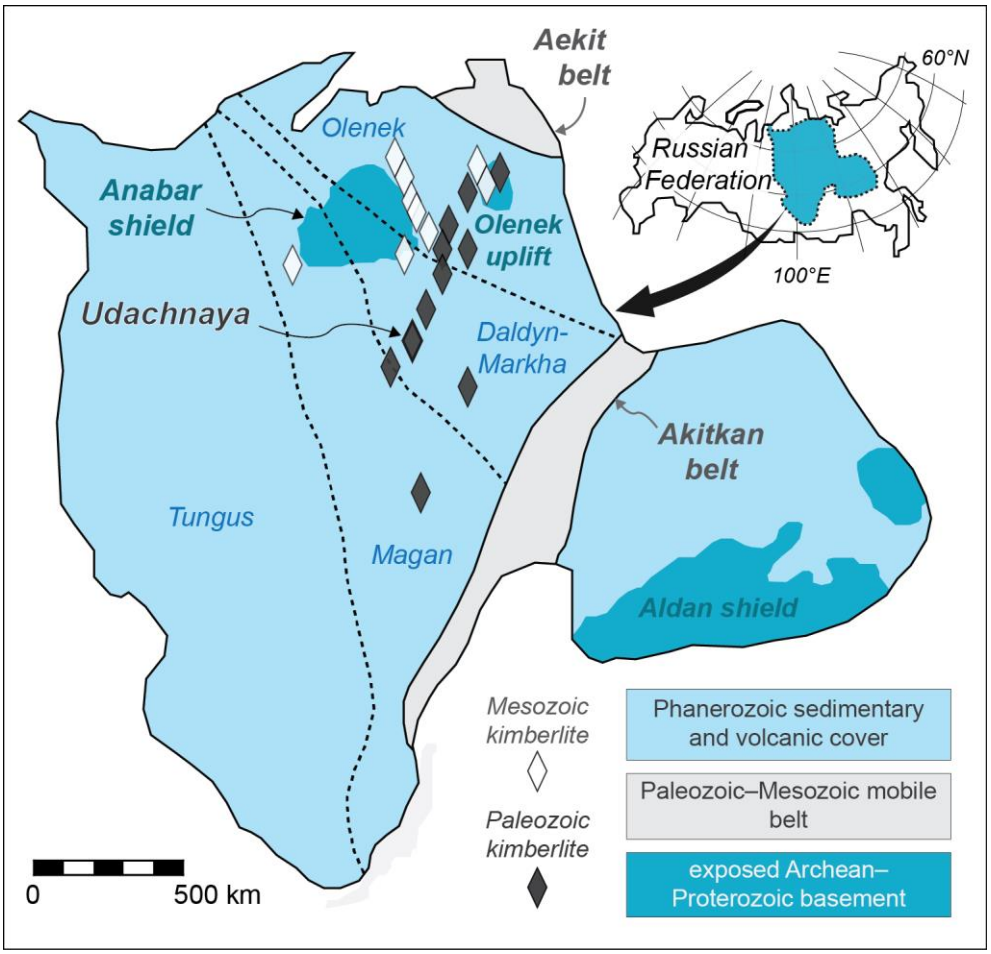

Figure 1. Simplified geologic map of the Siberian craton (after Moyen et al., 2017). Dashed lines delineate the boundaries of different blocks that make up the craton. Diamonds denote the location of kimberlites, with white diamonds corresponding to Mesozoic kimberlites and grey diamonds showing Paleozoic kimberlites.

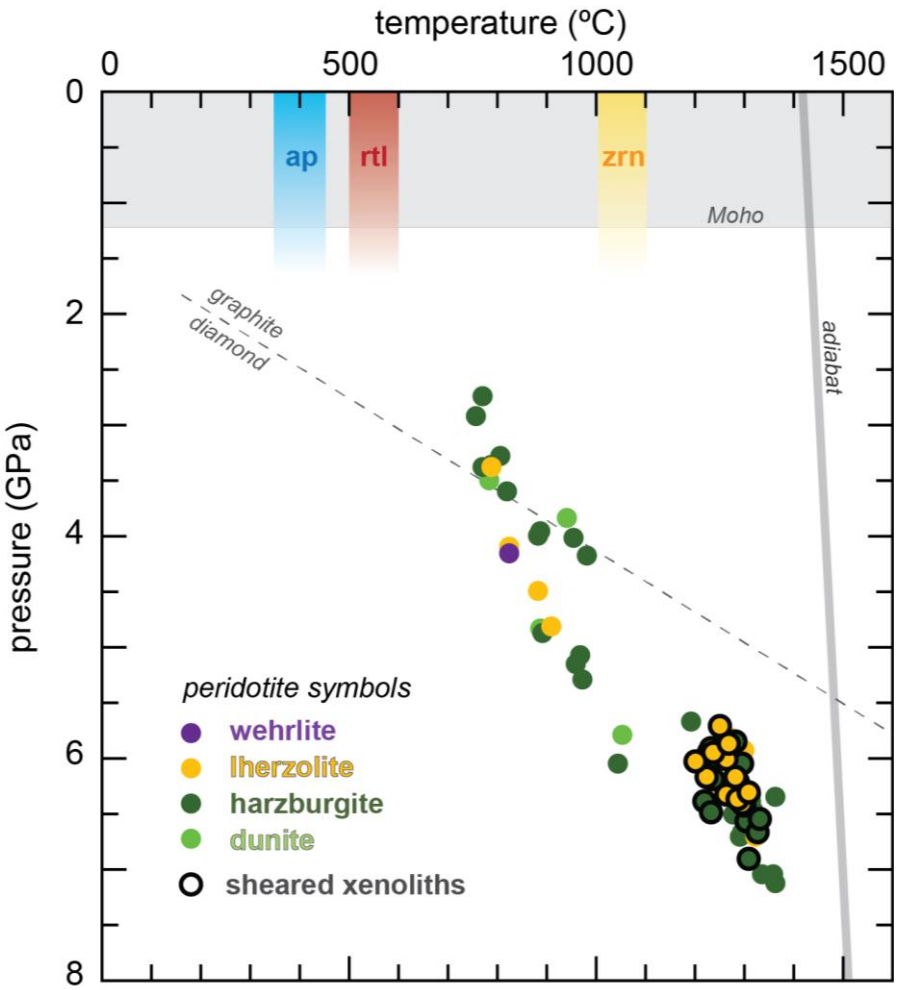

Figure 2. Udachnaya peridotite PT array. The graphite–diamond transition is after Day (2015). Pb closure temperatures for rutile and apatite are calculated using a 50–500-µm-radius sphere and 0.01–0.1 °C/Myr cooling rates (Cherniak, 2010; Smye et al., 2018). Peridotite xenolith data are from compilation reported in Liu et al. (2022).

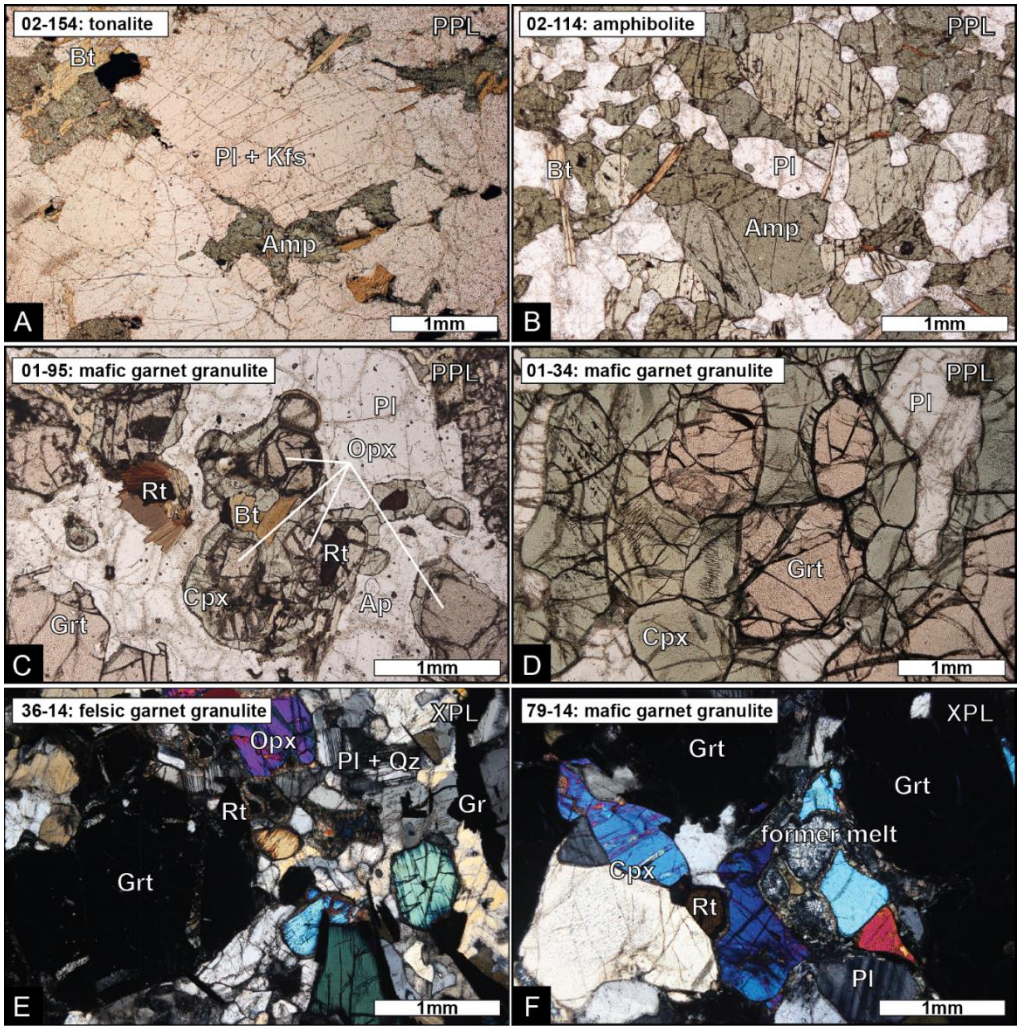

Figure 3. Representative photomicrographs of Udachnaya crustal xenoliths. Mineral abbreviations after Whitney and Evans (2002). PPL, plane polarized light; XPL, crossed polarized light.

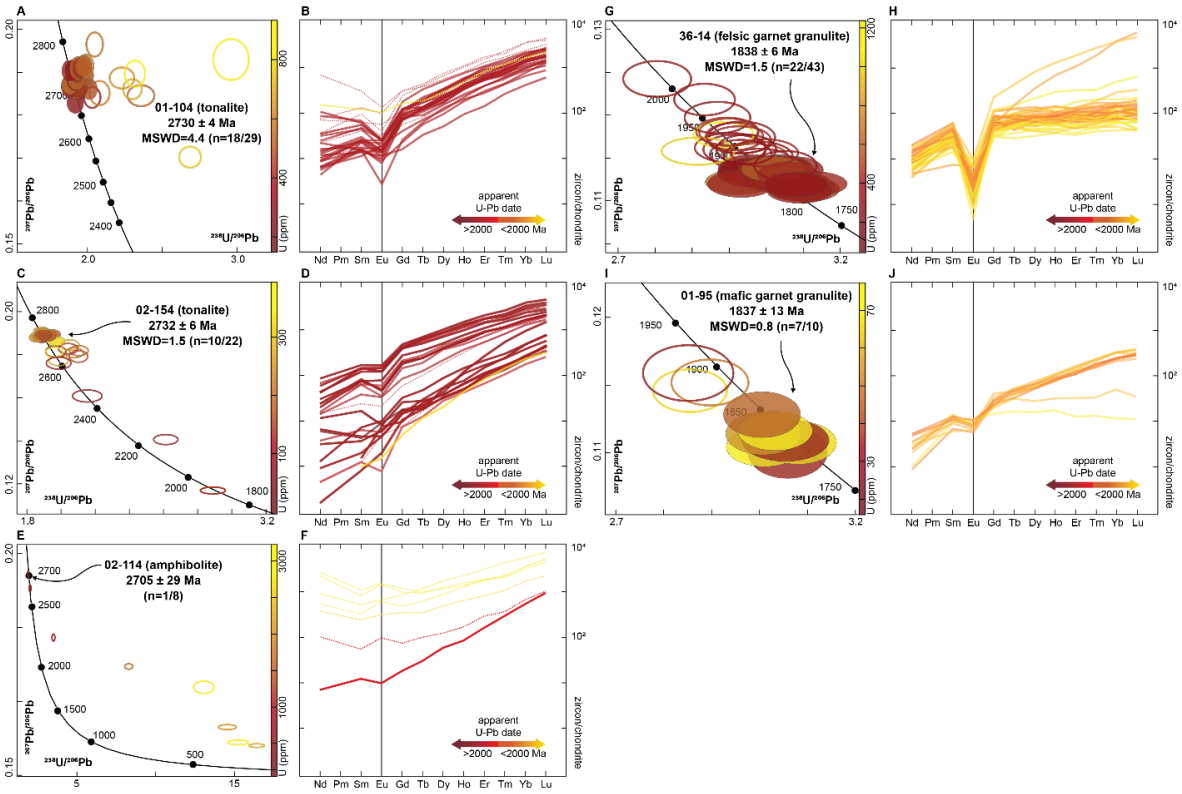

Figure 4. Zircon LASS data. Ellipses shown in the concordia diagrams are 2σ and are colored by U concentration. Chondrite-normalized REE patterns are colored by apparent U-Pb date. Solid lines are concordant U-Pb date (<5% discordance) and dashed as discordant U-Pb data (>5% discordance).

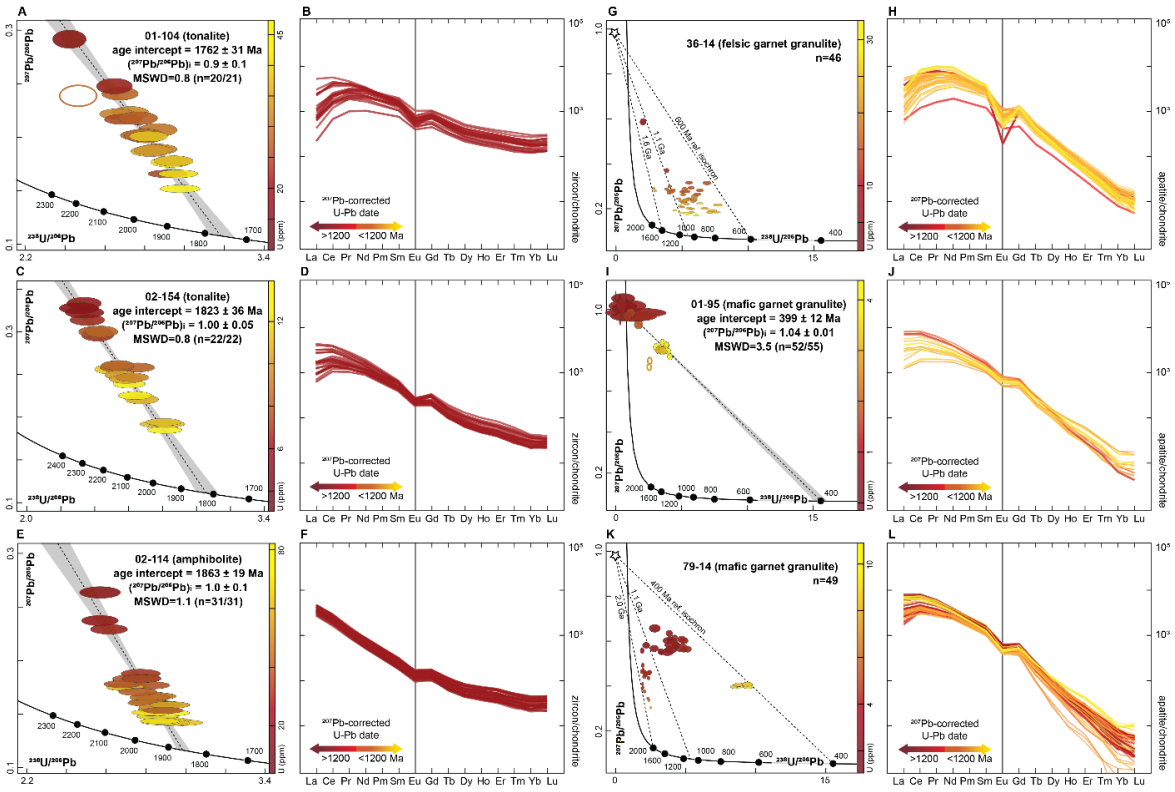

Figure 5. Apatite LASS data. Ellipses shown in the concordia diagrams are 2σ and are colored by U concentration. Isochrons for tonalities and amphibolites are from York-regressions through the data (A, C, E), whereas reference isochrons for granulites (G, I, K) are anchored from a Stacey and Kramers (1975) model common-Pb composition. Chondrite-normalized REE patterns are colored by apparent U-Pb date.

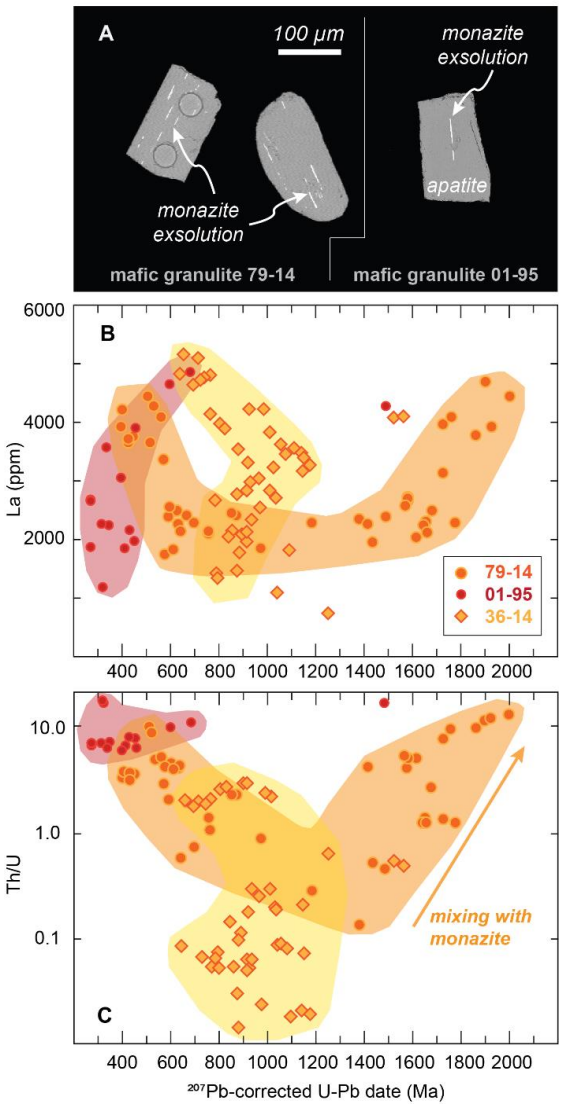

Figure 6. Monazite exsolutions in apatite from garnet granulite xenoliths. A) BSE images of apatite showing scale of monazite exsolutions. B) Common-Pb corrected U-Pb date vs. La concentrations in apatite spot analyses. C) Common-Pb corrected U-Pb date vs. Th/U ratios in apatite spot analyses. Note that spots older than 1.1–1.4 Ga form positive correlations, consistent with mixing between apatite and monazite during laser ablation analyses.

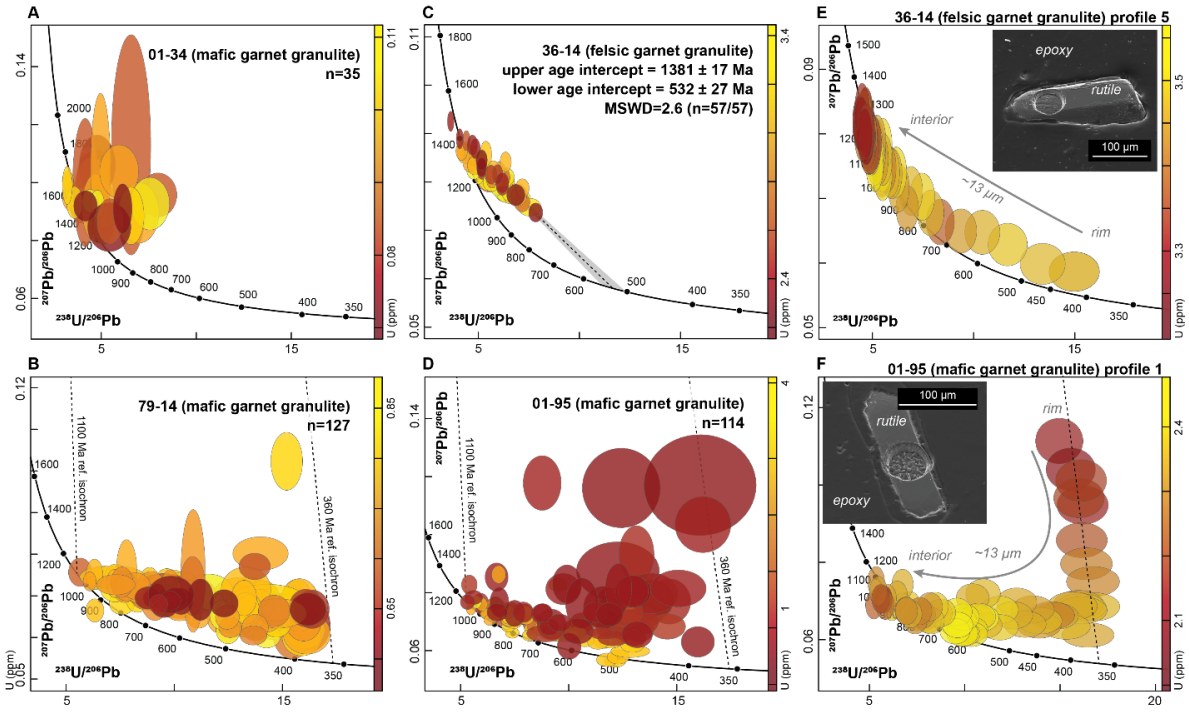

Figure 7. Rutile U-Pb data. Ellipses shown in the concordia diagrams are 2σ and are colored by U concentration. Panels A–D are data from analyses on polished grain interiors. Panels E and F are example depth profiles. Insets are BSE images of depth profiled grains).

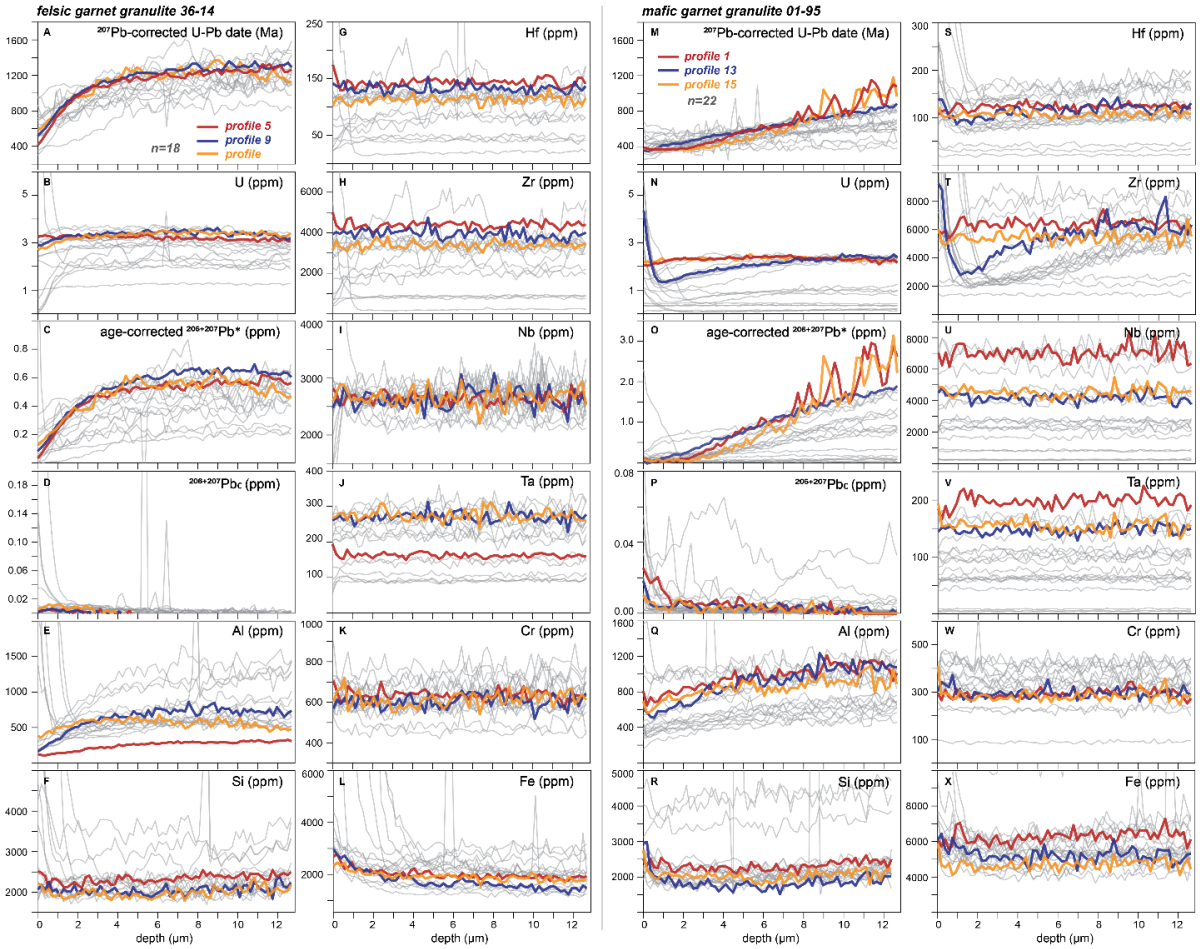

Figure 8. Example of rutile depth profiles with domains (shaded in grey) designated as possible diffusion profiles; the slopes of these gradients are used for diffusion modeling. The area in yellow demarcates a neo-/re-crystallized rim (not used for modeling).

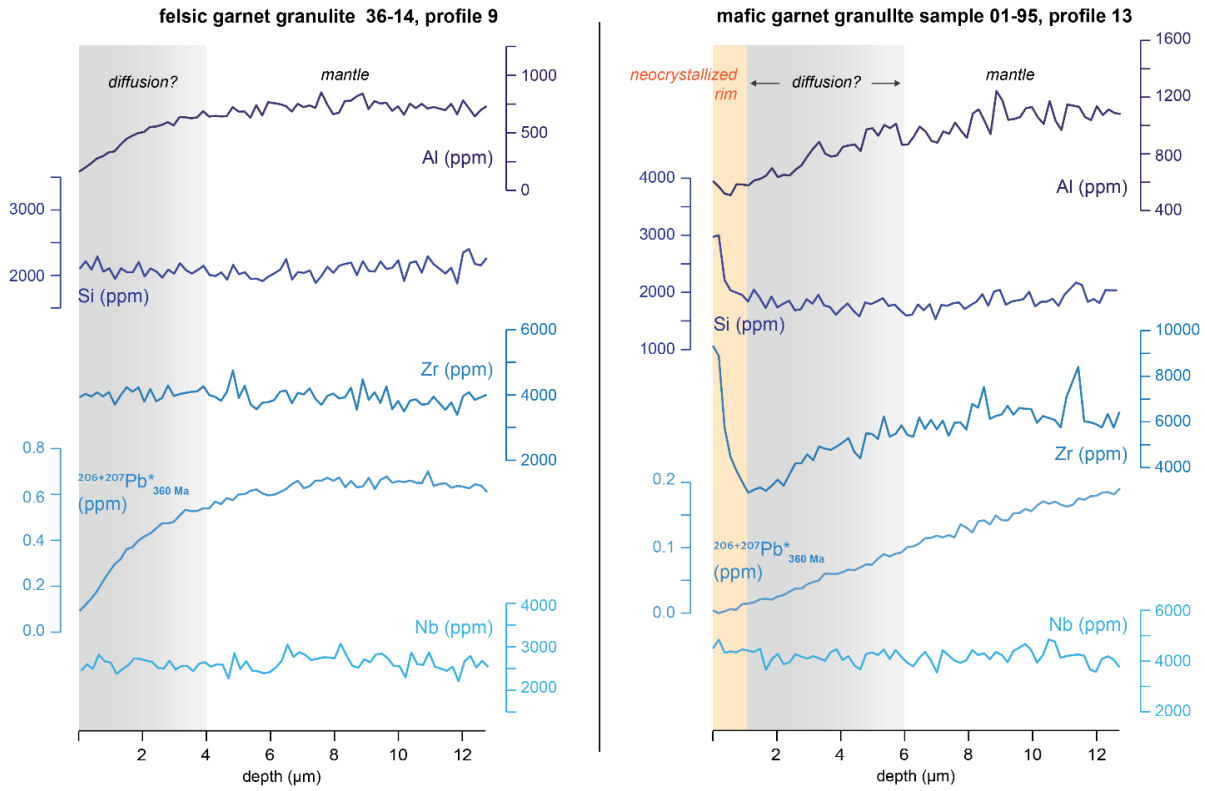

Figure 9. Rutile LASS depth profiles. For each sample, three representative profiles are colored to highlight variations in profile topology. The other profiles are shown in grey. A distinctive feature of LASS profiles in sample 01-95 is the increase in U, Si, and Zr at the grain edge.

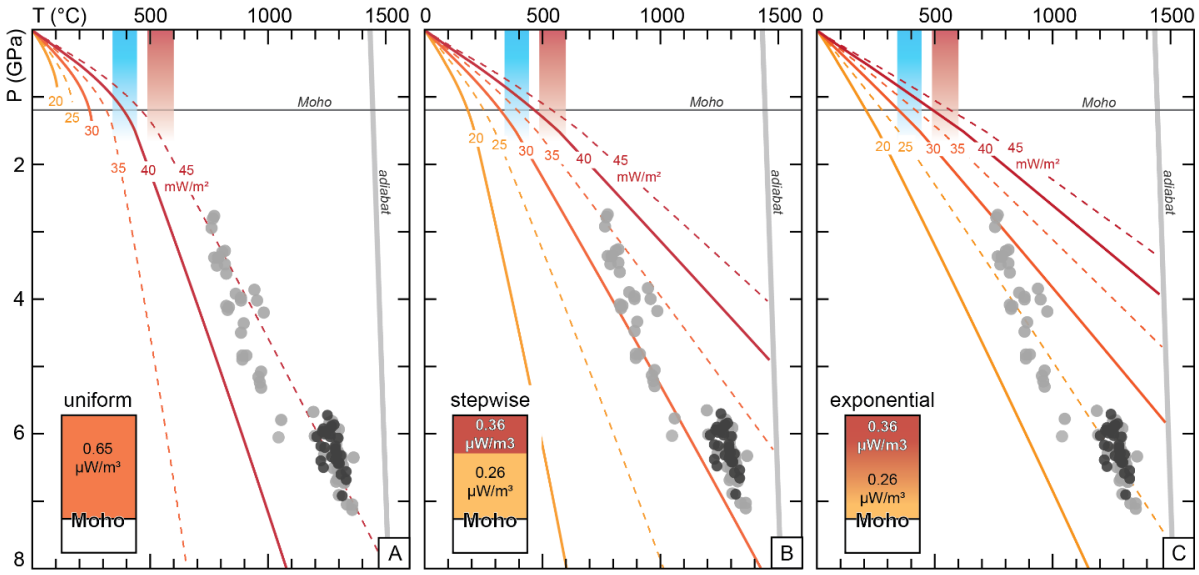

Figure 10. Conductive geotherm models. Model A assumes uniform crustal heat production (average heat production value of Jaupart et al., 2016). Model B assumes a stepwise change in heat production at 15 km. Model C assumes an exponential decrease in crustal heat production. All models employ heat production value of 0.006 µW/m3 for the mantle lithosphere (after McIntrye et al., 2021). Moho is at 45 km (after Cherepanova et al., 2013). Garnet peridotite P-T data are shown in grey, with darker grey spots representing sheared peridotites (see also Fig. 2). In all cases, the measured surface heat flow value (~20 mW/m2) is consistent with residence below the Pb closure temperature of rutile and apatite (blue and red bars, respectively), but is incompatible with the peridotite P-T data (>20 mW/m2).

Chapter III. Apatites for destruction: Reference apatites from Morocco and Brazil for U-Pb petrochronology and Nd and Sr isotope geochemistry

As published in Chemical Geology in 2022

With co-authors John M. Cottle[1], Corey J. Wall[2], Mark D. Schmitz[2], Andrew R. C. Kylander-Clark[1], and Gareth G.E. Seward[1]

[1]Department of Earth Science, University of California, Santa Barbara, CA 93106, USA

[2]Department of Geoscience, Boise State University, Boise, ID 83706, USA

ABSTRACT

In situ apatite U-Pb petrochronology and Sr-Nd isotope geochemistry require well-characterized and matrix-matched references materials (RMs), yet only a few suitable apatite RMs are currently available. To ameliorate this issue, we determined the U-Pb, Sm-Nd, and Sr isotopic and elemental compositions of a suite of prospective apatite RMs using isotope dilution (ID) TIMS and laser ablation (LA) ICP-MS. The two RMs, from Morocco (MRC-1) and Brazil (BRZ-1), are cm-sized and available in significant quantities. The U-Pb ID-TIMS data yield an isochron age of 153.3 ± 0.2 Ma for MRC-1. This age is consistent with laser ablation split stream ICP-MS (LASS) analyses that produce a 152.7 ± 0.6 Ma isochron. The weighted mean of ID-TIMS analyses for $^{143}Nd/^{144}Nd$ analyses is 0.512677 ± 3, for $^{147}Sm/^{144}Nd$ is 0.10923 ± 9, and for $^{87}Sr/^{86}Sr$ is 0.707691 ± 2. The range and mean of TIMS Sm-Nd isotopic data are reproducible by LA-ICP-MS, but laser ablation Sr data are consistently offset towards more radiogenic values. For BRZ-1 apatite, ID-TIMS U-Pb analyses are dispersed, but a subset of the data yields a coherent age intercept of 2078 ± 13 Ma. The vast majority of LASS spot transects across the apatite produce an isochron that define a younger age of 2038 ± 14 Ma. We interpret this as incorporation of cryptic, younger altered domains within BRZ-1. Discordant U-Pb spot analyses are associated with chemically distinct cracks, likely a result of fluid infiltration. The weighted means of ID-TIMS analyses of BRZ-1 yield $^{143}Nd/^{144}Nd=0.510989 \pm 5$, $^{147}Sm/^{144}Nd=0.10152 \pm 8$, and $^{87}Sr/^{86}Sr=0.709188 \pm 3$. The distribution of Nd isotopic compositions of this RM measured by LA-MC-ICP-MS analyses are comparable to TIMS analyses. By contrast, $^{87}Sr/^{86}Sr$ measurements by LA-ICP-MS are inaccurate and exhibit large uncertainties, but this RM can be useful for empirically correcting *in situ* $^{87}Sr/^{86}Sr$ measurements.

3.1 INTRODUCTION

Apatite is common accessory mineral in a variety of rock types—both terrestrial and extra-terrestrial (Piccoli and Candela, 2002; Spear and Pyle, 2002; McCubbin and Jones, 2015)—and can host substantial amounts of U, Th, Sr, Nd, and other incompatible elements, making it a useful geochronometer and isotope tracer of petrogenetic processes (Spear and Pyle, 2002; Prowatke and Klemme, 2006; McFarlane and McCulloch, 2007; Horstwood et al., 2008; Chew et al., 2011; Henrichs et al., 2018). Accordingly, apatite studies have diverse applications including, but not limited to: resolving thermal histories in the 400–600 °C temperature range with the U-Pb system (e.g., Krogstad and Walker, 1994; Chamberlain and Bowring, 2000; Schoene and Bowring, 2006; 2007; Chew et al., 2011; Cochrane et al., 2014; Seymour et al., 2016; Ibanez-Mejia et al., 2018; Kirkland et al., 2018; Paul et al., 2019; Apen et al., 2020), tracking sediment provenance (e.g., Morton and Yaxley, 2007; Carrapa et al., 2009; Henderson et al., 2010; Chew et al., 2011; Thomson et al., 2012; Braund et al., 2017; O'Sullivan et al., 2018; 2020; O'Sullivan and Chew, 2020), use as a pathfinder for mineral deposits (e.g., Belousova et al., 2002; Mao et al., 2016; Glorie et al., 2019), and fingerprinting the petrogenesis of metamorphic and igneous rocks with Sr or Nd isotopes, providing insights into the growth and modification of Earth's oldest continental fragments (e.g., Emo et al., 2018; Hammerli et al., 2019; Antoine et al., 2020; Braund et al., 2020; Fisher et al., 2020a, b; Ravindran et al, 2020; Gillespie et al., 2021b). Coupled with the relatively rapid acquisition and high-spatial resolution capabilities of in situ microbeam methods—laser ablation inductively coupled plasma mass spectrometry (LA-ICP-MS) and secondary-ion mass spectrometry (SIMS) (e.g., Sano et al., 1999; Chew et al., 2011; 2017; Kylander-Clark, 2017; Gillespie et al., 2021a)—geochronological and geochemical analyses

of apatite are increasingly commonplace. Despite the rising use of apatite petrochronology and geochemistry, suitable apatite reference materials (RMs) available for inter-laboratory comparisons (homogeneous, well-characterized, and accessible) are scarce.

A critical component of in situ isotopic and elemental analyses by LA-ICP-MS is monitoring and correcting for plasma- and laser-induced element fractionation (Horn et al., 2000; Sylvester et al., 2008; Paton et al., 2011; Fisher et al., 2020b). As the degree of fractionation is related to the physical structure and chemical composition of the ablated material, robust corrections necessitate matrix-matched and isotopically-homogeneous RMs (e.g., Chew et al., 2014a). Among the most widely employed U-Pb primary RMs (Tables 1–3) are the McClure, Otter Lake, and Madagascar apatites, but they have limitations. The age of McClure apatite is well-established by multiple TIMS studies (Table 1), but its small grain size (<200-µm-width), low U concentrations (<30ppm U), and variable amounts of common Pb render it as a sub-optimal primary RM (Krestianinov et al., 2021). Heterogeneous U-Pb ratios in the Otter Lake RM has been shown to result in 1–3 % offsets between LA-ICP-MS and isotope dilution (ID) dates for secondary apatite RMs (Thompson et al., 2016). Madagascar apatite megacrysts have internally homogeneous U-Pb isotopic compositions, but can vary significantly between different grains (Table 1; Thomson et al., 2012; Fisher et al., 2020b). Likewise, apatite RMs for Sr and Nd isotopic analyses are limited. In a reconnaissance isotope dilution and laser ablation multi-collector ICP-MS study of Sr and Nd isotopes in 11 different apatite RMs, Yang et al. (2014) concluded that six are homogeneous enough for use as in situ RMs; these are Madagascar, Otter Lake, NW-1, SDG, AP1, and AP2. Since then, Thompson et al. (2016) introduced apatites 401 and OD306 as effective U-Pb RMs (Table 1), but these have yet to be characterized for their Sm-

Nd and Sr isotopes. Fisher et al. (2020b) presented Tory Hill apatite from Ontario, Canada, as a viable RM for in situ U-Pb and Nd isotopic analyses (Table 1). More recently, new U-Pb TIMS data for a suite of potential reference apatites from the Adirondack Mountains (Krestianinov et al., 2021) and Wilberforce, Canada (Paul et al., 2021) have been reported (Table 1), but no information on their Sm-Nd or Sr isotopic characteristics is available.

A vital step towards advancing the utility of apatite petrochronology and isotope geochemistry is to expand the suite of available reference materials. In this study, we have characterized the U-Pb, Sr, and Nd isotopic and elemental compositions of two natural apatites from Morocco and Brazil using isotope dilution thermal ionization mass spectrometry (ID-TIMS) and LA-ICP-MS—laser ablation split stream ICP-MS (LASS) for U-Pb and trace-element analyses and more conventional LA-ICP-MS for Sr and Nd isotopes. The prospects and pitfalls of these potential RMs are discussed below.

3.2 METHODS

3.2.1 Specimen preparation

Multiple untreated, gem-quality apatite crystals from Morocco (MRC) and Brazil (BRZ) were procured online. The former are pale green-yellow crystals from Imilchil, situated within the Triassic–Late Cretaceous Central High Atlas province of Morocco, and the latter are blue crystals derived from Minas Gerais, in the southeastern sector of the Mesoarchean–Paleoproterozoic Brazilian Shield.

A single MRC and BRZ crystal was selected for detailed study (henceforth MRC-1 and BRZ-1). Each crystal had its terminations cut off with a diamond saw and the remaining portions were sliced into mm-thick sections parallel to the c-axis (following protocols of

Chew et al., 2016) and cast in epoxy (Fig. 1). One mount was analyzed with cathodoluminescence (CL), electron microprobe, ID-TIMS, and LASS/LA-ICP-MS (Fig. 2A, C). Another mount containing additional c-axis parallel sections and a separate c-axis perpendicular piece of the crystal termination (Fig. 2B, D) was analyzed exclusively by LASS to further interrogate intra-crystal U-Pb and elemental heterogeneity.

3.2.2 Electron microprobe analysis (EPMA)

Cathodoluminescence images of MRC-1 and BRZ-1 crystal sections (Fig. 3) were generated using a FEI Quanta 400f field-emission scanning electron microscope (SEM) equipped with a KE Developments Centaurus CL detector, housed at the University of California, Santa Barbara (UCSB). Quantitative elemental analyses and X-ray maps were collected using a Cameca SX-100 electron probe micro analyzer (EPMA), running Probe for EPMA and Probe Image (Probe Software Inc.), also located at UCSB.

X-ray maps were produced using a 20 kV accelerating voltage, 200 nA beam current, and 2-µm-diameter beam (Fig. 3). Wavelength-dispersive spectrometers measured Sr and S using LPET crystals, Ce and Nd using LLIF crystals, and Th using a PET crystal. Maps of MRC-1 and BRZ-1 were developed using a 5 µm by 5 µm pixel spacing and 3 µm by 3 µm pixel spacing, respectively, all using a dwell time of 500 ms per pixel.

Quantitative EPMA ‘spots analyses’ were acquired with an accelerating voltage of 20 kV, a beam current of 200 nA and a 5-µm-diameter defocused beam. The location of the spot transects are shown in Figure 2. X-ray intensity measurements were made for La, Ce, Nd, Pr, Si, Na, Th, Gd, Sm, Sr, Y, and S using wavelength-dispersive spectrometers. A series of natural and synthetic standards were analyzed, including: ThO_2 for Th mα, strontium titanate (SrTiO3) for Sr lα, Cazadero albite for Si kα, Na kα, anhydrite (CaSO4)

UC # 5555 for S kα, Edinburgh REE Glass for Y lα, La lα, Ce lα, Pr lβ, Nd lα, Sm lβ, and Gd lα. Representative averages are reported in Table 4.

3.2.3 U-Pb ID-TIMS

Seven ~0.1 mg fractions were taken from the MRC-1 apatite, and eight ~0.3 mg fractions from the BRZ-1 crystal were separated at Boise State University using a diamond saw. Approximate locations shown as yellow circles in Figure 2. In the case of the MRC-1 crystal, different growth zones were targeted to assess potential intra-crystal heterogeneity. For the BRZ-1 apatite, seven fragments were separated from the interior of the crystal, away from CL-bright cracks, and one fragment was separated from near the rim for comparison.

All apatite crystal fragments were cleaned in an ultrasonic ethanol bath. The fragments were then spiked with an enriched ^{205}Pb-^{233}U-^{235}U tracer (BSU-1B calibrated against EARTHTIME gravimetric standards), and dissolved in concentrated HF at 220 °C for 48 hours in PFA fluoropolymer capsules nested within PTFE fluoropolymer-lined high-pressure steel dissolution vessels. After dissolution, drying to salts, and re-equilibration in 6M HCl at 180 °C for 12 hours, Pb and U were separated from the solutions using dilute HBr- and HCl-based anion exchange chromatography (Krogh, 1973).

The U-Pb aliquots were loaded in a silica gel emitter (Gerstenberger and Haase, 1997) to outgassed, zone-refined Re filaments. Isotopic determinations were performed using an IsotopX PhoeniX-62 TIMS. A correction for mass-dependent Pb fractionation was applied based on repeated measurements of NBS 982 (Catanzaro et al., 1968) Pb on both the Daly ion counter [0.16 (± 0.03 %) amu–1; 1s] and the Faraday cups [0.10 × (1 ± 0.02 %) amu–1; 1s]. Uranium was run as an oxide (UO_2) and measured in static mode on Faraday detectors

equipped with 1012 Ω resistors. The U mass fractionation for the same analyses was calculated using the $^{233}U/^{235}U$ ratio of the double spike solution (0.99506 % ± 0.01 %, 1s).

The U-Pb dates and uncertainties for each analysis were calculated using the algorithms of Schmitz and Schoene (2007), the U decay constants of Jaffey et al. (1971), and a value of $^{238}U/^{235}U$=137.818. Uranium oxide measurements were corrected for isobaric interferences using an $^{18}O/^{16}O$ value of 0.00206. Uncertainties are based upon random analytical errors, including counting statistics, instrumental fractionation, tracer subtraction, and blank subtraction. Non-radiogenic Pb was attributed to laboratory blank (~0.5 pg, determined by total procedural blanks measurements) and intrinsic common Pb in the apatite (compositions estimated from LA data or assuming a model Pb composition from Stacey and Kramers (1975), discussed below). These error estimates should be considered when comparing our $^{206}Pb/^{238}U$ dates with those from other laboratories that used tracer solutions calibrated against the EARTHTIME gravimetric standards. When comparing our dates with those derived from other decay schemes (e.g., $^{40}Ar/^{39}Ar$, ^{187}Re-^{187}Os), the uncertainties in tracer calibration (0.03 %; Condon et al., 2015; McLean et al., 2015) and U decay constants (0.108 %; Jaffey et al., 1971) should be added to the internal error in quadrature. Quoted errors for calculated weighted means are in the form ± X (Y) [Z], where X is solely analytical uncertainty, Y is the combined analytical and tracer uncertainty, and Z is the combined analytical, tracer, and ^{238}U decay constant uncertainty.

3.2.4 Sm-Nd and Sr ID-TIMS

Six TIMS aliquots from each apatite were further processed for Sm-Nd and Sr isotopic measurements. Washes from apatite crystal fragments dissolved and separated for U-Pb were spiked with mixed ^{149}Sm-^{150}Nd and ^{87}Rb-^{84}Sr tracers, dried, and re-dissolved in 5 mL

1M HCl + 0.1M HF at 120 °C overnight. Sr and bulk rare earth elements were separated by standard dilute HCl- and HNO3-based cation exchange chemistry on 6 mm inner diameter (i.d.) x 20 cm long columns of AG-50W-X8 resin (H+ form, 200–400 mesh). Sr was further purified by loading on 0.05 ml c.v. of Sr-spec crown ether resin and elution of matrix elements with 1.3 mL 3.5M HNO_3, followed by elution of Sr in ultrapure water. Sm and Nd were separated by reverse phase HDEHP chromatography on 4 mm i.d. x 10 cm long columns of Eichrom Ln-spec resin, 50-100 mesh. All separated fractions were dissolved and re-dried with 30 mL16M HNO_3, 30 mL 30 % H_2O_2, and 5 mL 0.1N H_3PO_4.

The Nd fraction was loaded in 2 mL of 1M HNO_3 on the side filament of a triple Re filament assembly, whereas the Sm fraction was loaded on a single Re filament in 2 mL 1M HNO_3 along with 3 mL of tantalum oxide emitter solution. Sm and Nd isotopes were measured on an IsotopX Phoenix X62 multi-collector thermal ionization mass spectrometer in static and dynamic Faraday modes, respectively. Instrumental mass fractionation of Sm and Nd isotopes was corrected with an exponential law relative to $^{146}Nd/^{144}Nd=0.7219$ and $^{152}Sm/^{147}Sm=1.7831$. The quoted uncertainty for each analysis is the internal standard error; the external reproducibility (standard deviation) of the JNdi-1 standard over the course of the study was 0.512105 ± 4 (2σ) for runs at ~3V ^{144}Nd (n=8) and 0.512105 ± 8 (2σ) for runs at ~0.3V ^{144}Nd (n=9). Uncertainty in [Sm], [Nd], and $^{147}Sm/^{144}Nd$ are estimated at ≤0.022 % (2σ), including systematic tracer calibration errors.

The Sr fraction was loaded in 2 mL 1M HNO3 along with 3 mL of tantalum oxide emitter solution on single degassed Re filaments, and its isotope ratios measured on the IsotopX Phoenix X62 multi-collector TIMS in the Boise State University Isotope Geology Laboratory. Sr isotope ratios were analyzed in dynamic mode, fractionation-corrected with

an exponential law relative to $^{86}Sr/^{88}Sr=0.1194$. The quoted uncertainty for each analysis is the internal standard error; the external reproducibility of the NBS-987 standard over the course of the study was 0.710244 ± 6 (2σ) for runs at 4V ^{88}Sr (n=7).

3.2.5 U-Pb and trace element LASS

Combined U-Pb and trace-element data were collected using the LASS system at UCSB during different sessions over a two-year period. The system consists of a Photon Machines 193 nm excimer Analyte laser with a HelEx-2 ablation cell coupled to two mass spectrometers: a MC-ICP-MS for U-Pb isotopes and a quadrupole (Q)-ICP-MS for simultaneous trace element determinations (see also Kylander-Clark et al., 2013). A Nu Instruments Plasma 3D MC-ICP-MS was used for the first phase of the study, and a Nu Instruments Plasma HR-ES MC-ICP-MS for the second phase. An Agilent 7700S Q-ICP-MS was utilized for all trace-element analyses. Instrument parameters are summarized in Table 5. On the Plasma 3D MC-ICP-MS, ^{202}Hg, $^{204}(Pb+Hg)$, ^{206}Pb, ^{207}Pb, ^{208}Pb were measured on Daly detectors and ^{238}U and ^{232}Th were measured on Faraday collectors. Similarly, on the Plasma HR $^{204}(Pb+Hg)$, ^{206}Pb, ^{207}Pb, ^{208}Pb were measured on Secondary Electron Multipliers and ^{238}U and ^{232}Th were measured on Faraday collectors. On the Q-ICP-MS, the following masses were measured: ^{28}Si, ^{44}Ca, ^{88}Sr, ^{89}Y, ^{90}Zr, ^{139}La, ^{140}Ce, ^{141}Pr, ^{146}Nd, ^{147}Sm, ^{153}Eu, ^{157}Gd, ^{159}Tb, ^{163}Dy, ^{165}Ho, ^{166}Er, ^{169}Tm, ^{172}Yb, ^{175}Lu ± ^{49}Ti ± ^{55}Mn ± ^{56}Fe ± ^{137}Ba.

Apatite was ablated using a 40-µm-diameter laser spot operating at a 4 Hz repetition rate, 50 % of 5 mJ laser power, and a laser fluence of ~1 J/cm^2. Each ablation sequence consisted of two cleaning shots, followed by 20 s of monitored washout and 15 s of ablation, equating to final pit depths of ~7 µm. Raw U-Pb ratios were baseline subtracted and

corrected for laser- and plasma-induced element fractionation, and instrument drift using the Iolite software package (v. 2.5; Paton et al., 2011) in the Igor Pro interactive software environment (or Iolite as a shorthand).

Apatite RM MAD—denoted here as MAD-UCSB, an apatite crystal from Madagascar provided by Stuart Thompson and subsequently analyzed via ID-TIMS at the Boise State Isotope Geology Lab for this study—served as the primary bracketing reference apatite for LASS analyses. All of the analyzed fractions of MAD-UCSB have homogeneous U-Pb ratios (Fig. 4), and we adopted the weighted mean and associated 2σ error of the data as the canonical U-Pb isotopic compositions for LASS standardization. Details of this RM are reported in section 3.3.2.

All of the secondary apatite RMs contain variable amounts of common-Pb, so the U-Pb age quoted herein is the concordia intercept age determined from a York regression through the data. Repeat analyses of secondary RMs over the course of this study indicate that each $^{238}U/^{206}Pb$ and $^{207}Pb/^{206}Pb$ measurements require an additional 2.4 % and 1.8 % (2σ), respectively, to account for the long-term variability in laser ablation analyses; these values were added in quadrature to the internal error of each U-Pb datum and considered when calculating intercept ages (Horstwood et al., 2016). Final U-Pb ratios and associated uncertainties were plotted using IsoplotR (Vermeesch, 2018). The concordia intercept ages of the secondary RMs overlap their established ages with these designated uncertainties (Table 6).

Trace-element abundances in apatite were calculated in Iolite using ^{44}Ca as the internal standard element and assuming stoichiometric abundances of Ca in fluoroapatite (39.74 %).

The NIST 612 silicate glass (Pearce et al., 1997) was used for calibration (preferred values of Jochum et al., 2011). The uncertainty of each element reflects only the internal error.

3.2.6 Sm-Nd LA-MC-ICP-MS

Isotopes of Sm-Nd were measured using a Photon Machines 193 nm excimer Analyte laser with a HelEx-2 ablation cell coupled to a Nu Instruments Plasma 3D MC-ICP-MS. Masses 140–158 were measured on 16 Faradays collectors at 1-amu spacing (Table 5). Apatite was ablated for 300 laser pulses using a 15 Hz repetition rate at 100 % of 5 mJ laser power during two consecutive sessions: one utilizing a 50 µm diameter spot and the other an 85 µm diameter spot. Each ablation sequence consisted of two cleaning shots, followed by 50 s of monitored washout, 20 s of ablation—amounting to final pit depths of 20–22 µm—and 3 s of wash out prior to the next sequence.

Mass bias, isobaric interferences, and laser-induced (downhole) fractionation can be significant sources of uncertainty and must be corrected for in order to obtain accurate $^{143}Nd/^{144}Nd$ and $^{147}Sm/^{144}Nd$ measurements by LA-MC-ICP-MS (e.g., Vance and Thirlwall, 2002; Fisher et al., 2011; 2020b). Our approach to these corrections follows that of Fisher et al. (2011) and Poletti et al. (2016) and is summarized below. Mass-bias correction for Sm was based on internal standardization using the natural ratio of $^{147}Sm/^{149}Sm$ (0.22332; Isnard et al., 2005). The isobaric interference of ^{144}Sm on ^{144}Nd was calculated using the calculated mass bias and assuming a natural ratio of $^{144}Sm/^{149}Sm=1.08680$ (Dubois et al., 1992). For Nd isotopes, mass-bias correction was based on the natural ratio of $^{146}Nd/^{144}Nd=0.7219$. All of these corrections—as well as baseline subtractions and corrections for instrumental drift—were done in Iolite (v. 3.5) using the Sm-Nd data reduction scheme developed by Fisher et al. (2020b). Downhole corrections to the mass-bias- and interference-corrected

$^{147}Sm/^{144}Nd$ and $^{143}Nd/^{144}Nd$ ratios were made using an exponential fit and using MAD-UCSB as the primary RM (using $^{147}Sm/^{144}Nd$ and $^{143}Nd/^{144}Nd$ compositions determined by TIMS as part of this study; Table 7). Secondary reference apatites analyzed during each run include McClure, Durango, OD306, and 401 (Table 3). Reported uncertainties are 2σ and only include in-run errors; for both the 50 and 85 μm diameter spot analyses, repeated analyses of secondary RMs yielded weighted means with MSWDs that are consistent with a uniform population (Wendt and Carl, 1991), the exceptions being Durango and OD306. These latter two RMs are known to exhibit Nd isotopic heterogeneity (Fisher et al., 2011; Yang et al., 2014) or have not yet been characterized for their Sm-Nd systematics by TIMS analyses.

3.2.7 Sr LA-MC-ICP-MS

Multiple isobaric interferences can impair Sr isotopic measurements by LA-MC-ICP-MS, including Kr in the carrier He gas and plasma Ar gas, doubly-charged REEs—e.g., Er^{2+} and Yb^{2+}—and Ca-dimers from the apatite matrix (e.g., Ramos et al., 2004; Horstwood et al, 2008). Sr isotopes were measured at UCSB using the same set up described above for Sm-Nd analyses. The detector array covered masses 81.5–89.5 with a 0.5-amu spacing; all measurements were made on Faraday collectors. These laser ablation analyses were completed in two consecutive sessions, the first using an 85 μm diameter spot and the second a 50 μm diameter spot (Table 5). Laser settings and ablation sequences used for Sr analyses are the same as described for our Sm-Nd isotopic analyses except that a 50 s baseline was collected following the main ablation pass (i.e., a single sequence consisted of two cleaning shots, 50 s baseline, 20 s ablation pass, and 50 s baseline).

Accurate Sr isotopic determinations are dependent not only on corrections for isobaric interferences, but also the order in which corrections are applied (e.g., Horstwood et al, 2008; Yang et al., 2014). First, given the relatively long baseline before and after each ablation pass (50 s each), $^{86,84,82}Kr^{+}$ interferences were subtracted using a step-forward baseline subtraction (Bizzarro et al, 2003). Following this, interferences from various doubly-charged REEs on Sr and Rb isotopes and Ca-dimers were calculated—$^{176}Yb^{2+}$ and $^{176}Lu^{2+}$ on ^{88}Sr, $^{174}Yb^{2+}$ on ^{87}Sr, $^{172}Yb^{2+}$ on ^{86}Sr, $^{170}Yb^{2+}$ and $^{170}Er^{2+}$ on ^{85}Rb (used for ^{87}Rb corrections on ^{87}Sr), $^{168}Yb^{2+}$ and $^{168}Er^{2+}$ on ^{84}Sr, and $^{164}Er^{2+}$ and $^{164}Dy^{2+}$ on mass-82. Each REE interference intensity was calculated using the mass bias derived from the measured $^{87}Sr/^{86}Sr$ (low REE concentrations across the apatite RMs prevented determinations of mass bias factors for individual REEs). Interferences from Er isotopes were computed using the ^{167}Er signal at the 83.5 half-mass and the natural ratios of Er isotopes: $^{170}Er/^{167}Er=0.65111$, $^{168}Er/^{167}Er=1.16790$, and $^{164}Er/^{167}Er=0.04779$. Similarly, Yb interferences were calculated with the ^{173}Yb half mass and the natural ratios of Yb isotopes: $^{176}Yb/^{173}Yb=0.79107$, $^{174}Yb/^{173}Yb=1.97702$, $^{172}Yb/^{173}Yb=1.35338$, $^{170}Yb/^{173}Yb=0.18847$, and $^{168}Yb/^{173}Yb=0.00806$. For the $^{176}Lu^{2+}$ interference, we employed the measured ^{175}Lu half mass and the natural ratio of $^{176}Lu/^{175}Lu=0.02659$. The ^{164}Dy interference was calculated using ^{163}Dy (at the 81.5 half mass) using a natural ratio of $^{164}Dy/^{163}Dy=1.13173$. Rare-earth-element corrections were first applied to mass-82, and the residual signal was assumed to correspond entirely to $^{40}(Ca,Ar)^{42}Ca$ (see also Horstwood et al., 2008); this value was used to estimate Ca-dimer interferences on masses 84–88 by applying natural Ca abundances. Given the similar relative isotopic abundances of ^{40}Ca and ^{40}Ar, we assumed that interferences from Ca-argides were also accounted for in correcting for the Ca-dimers (Horstwood et al., 2008).

Interferences from REEs and Ca-dimers were stripped to ascertain $^{84,86,87,88}Sr$ and ^{85}Rb, the latter of which was used to compute and subtract the final interference of ^{87}Rb on ^{87}Sr based on an $^{87}Rb/^{85}Rb$ ratio=0.38561.

Baseline subtractions and drift-corrections, as well corrections for the isobaric interferences listed above, were carried out in Iolite. Apatite RMs MAD-UCSB, McClure, Durango, OD306, and 401, United States Geological Survey (USGS) silicate glass BHVO-2G and USGS carbonate MACS-3 were analyzed during the run to monitor the accuracy and precision of the final Sr isotopic analyses (Table 3). Additional uncertainties derived from repeat analyses of each RM were propagated to the REE-, Ca-dimer, and Rb-corrected $^{87}Sr/^{86}Sr$ internal error (~0.02 %; 2σ). Final $^{87}Sr/^{86}Sr$ values were not standardized.

3.3 RESULTS

3.3.1 CL and EPMA

Quantitative X-ray maps and CL imaging reveal internal structures and provide a basis for interpreting potentially complex dates and elemental patterns. In the case of MRC-1, imaging shows intra-crystal zonation (Figs. 2 and 3), most apparent in the S map (though Sr, Nd, Th, and Ce maps also show variability to lesser extent; Fig. 3A). Apatite BRZ-1 does not display any apparent growth zones based on X-ray maps and CL images. Instead, imaging reveals chemical heterogeneity associated with wispy networks of micron-scale cracks that branch out over 5–20 μm into the main matrix (Figs. 2 and 3). The X-ray maps indicate these cracks have similar Sr and Th contents compared to the unaltered matrix, but have lower S concentrations and higher Ce and Nd abundances (Fig. 3B).

To ensure comparability, electron microprobe analyses La, Ce, Nd, Pr, Si, Na, Th, Gd, Sm, Sr, Y, and S (Table 4) were measured along transects within the same areas used to develop X-ray maps. EPMA confirm a general decrease in measured trace element abundances from the interior to the exterior of the mapped MRC-1 grain. Aside from outliers associated with cracks or altered zones, BRZ-1 displays uniform elemental abundances across the grain (Fig. 3).

3.3.2 TIMS U-Pb, Sm-Nd, Sr isotopes

The primary MAD-UCSB apatite contains U-Pb compositions that are distinct from other previously reported Madagascar apatite ID-TIMS data (Thomson et al., 2012; Fisher et al., 2020b), differing in their degree of discordance (Fig. 4). MAD-UCSB apatite has an average U=22 ppm and average Th=545 ppm (Table 6). The concordia age of MAD-UCSB as determined by the total Pb-U isochron method, which incorporates the measured $^{204}Pb/^{206}Pb$ ratios (Schoene and Bowring, 2006; Ludwig, 2012), is 467.4 ± 8.4 (9.8) Ma and yields a $(^{207}Pb/^{206}Pb)_i$ intercept of 0.71 ± 0.10 (0.12) (n=6; MSWD=0.2) (Fig. 4), similar to results from an unanchored York regression in a Tera-Wasserburg concordia diagram (isochron age of 467 ± 9 Ma and a $(^{207}Pb/^{206}Pb)_i$ intercept of 0.71 ± 0.1; MSWD=0.003; all 2σ analytical uncertainty).

MRC-1 apatite has average concentrations of U=31 ppm and Th=285 ppm, equivalent to a Th/U≈9 (Table 6). All seven TIMS fractions define a single isochron (Fig. 5). The total Pb-U isochron method applied to these data yields an intercept age of 153.37 ± 0.40 (0.42) Ma and a $(^{207}Pb/^{206}Pb)_i$ intercept of 0.85 ± 0.04 (0.04) (MSWD=1.9). The average U and Th concentrations of eight BRZ-1 ID-TIMS fractions are 65 ppm U and 892 ppm Th, or Th/U≈14. The U-Pb data are highly dispersed (Fig. 5), but three fractions conform to a

single population within an acceptable MSWD (Wendt and Carl, 1991). The total Pb-U isochron method for the these three fractions yields an intercept age of 2078 ± 9 (12) Ma and a ($^{207}Pb/^{206}Pb)_i$ intercept of 1.14 ± 0.07 (0.09) (MSWD=0.2).

MAD-UCSB has $^{143}Nd/^{144}Nd$ ratios that range between 0.511305 ± 13 to 0.511342 ± 10 (all present-day values), with an average $^{143}Nd/^{144}Nd$=0.511312 ± 3 (n=6; MSWD=8.2) or ε_{Nd}=-25.7 ± 0.11 (values normalized to $(^{143}Nd/^{144}Nd)_{CHUR}$=0.512630; Bouvier et al., 2008). Corresponding $^{147}Sm/^{144}Nd$ ratios span 0.07732 ± 15 to 0.07787 ± 16 and produce an average $^{147}Sm/^{144}Nd$ =0.07763 ± 4 (Table 6). For MRC-1, $^{143}Nd/^{144}Nd$ values cover a range from 0.512668 ± 10 to 0.512686 ± 5 (Fig. 6); the mean of the six measurements is 0.512677 ± 3 (n=6; MSWD=6.3), or ε_{Nd}=0.9 ± 0.1. The $^{147}Sm/^{144}Nd$ ratios for MRC-1 are between 0.10588 ± 21 and 0.11755 ± 24, with a mean $^{147}Sm/^{144}Nd$ of 0.10923 ± 9. For BRZ-1, TIMS $^{143}Nd/^{144}Nd$ ratios are between 0.510961 ± 15 and 0.511025 ± 13 with a weighted mean of 0.510989 ± 5, or ε_{Nd}=-32.0 ± 0.1 (n=6; MSWD=10) (Fig. 6). The $^{147}Sm/^{144}Nd$ values vary from 0.10076 ± 20 to 0.10247 ± 20, with mean $^{147}Sm/^{144}Nd$ =0.10152 ± 8 (Table 7).

The TIMS $^{87}Sr/^{86}Sr$ ratios of MAD-UCSB are between 0.711700 ± 9 and 0.711798 ± 8 and produce a weighted mean $^{87}Sr/^{86}Sr$ =0.711773 ± 2 (Table 8). The $^{87}Sr/^{86}Sr$ ratios of MRC-1 range from 0.707688 ± 6 to 0.707695 ± 5 and yield a mean $^{87}Sr/^{86}Sr$ =0.707691 ± 2 (MSWD=0.7) (Fig. 7). The BRZ-1 $^{87}Sr/^{86}Sr$ TIMS values range from 0.709136 ± 11 to 0.709231 ± 8 and result in a mean $^{87}Sr/^{86}Sr$ ratio of 0.709188 ± 3 (MSWD=134) (Fig. 7). Although the weighted mean $^{87}Sr/^{86}Sr$ value for BRZ-1 does not represent statistically single population, we note that variability at this scale cannot be readily distinguished by LA-ICP-MS (see section 3.4.).

3.3.3 LASS U-Pb and trace elements

A total of 93 LASS spots collected across MRC-1—including a c-axis perpendicular section—comport to an isochron and overlap the seven ID-TIMS fractions (Fig. 5). Laser ablation spot analyses corroborate elemental variability within MRC-1 (Fig. 8), however, all spots show similar REE patterns: they are LREE-enriched (La/YbN≈20–30) and display a negative Eu anomaly (Eu/Eu*≈0.4, where $Eu/Eu^* = Eu_N/\sqrt{(Sm_N \times Gd_N)}$) (Fig. 5).

Most LASS spots collected from the BRZ-1 apatite (n=188/196) fall along a well-defined isochron, including those measured perpendicular to the c-axis (Fig. 5). Some data fall off this isochron and project to dates as young as ca. 865 Ma. Notably, LASS spots document that HREEs and U are enriched in younger domains associated with these cracks (Figs. 8 and 9). Portions of BRZ-1 away from cracks are LREE-enriched (La/YbN≈20–28) and have a negative Eu anomaly (Eu/Eu*≈0.6–0.8) (Fig. 5).

3.3.4 LA-ICP-MS Sm-Nd and Sr isotopes

Thirty-three 50-µm-diameter spots across MRC-1 overlap the ID-TIMS values and yield a weighted mean $^{143}Nd/^{144}Nd$ of 0.512710 ± 18 (ε_{Nd}=1.4 ± 0.4; MSWD=1.3), which are slightly higher than the TIMS mean (Table 7; Fig. 6). The corresponding $^{147}Sm/^{144}Nd$ values vary from 0.1078 ± 1 to 0.1247 ± 2, which partially overlap the TIMS $^{147}Sm/^{144}Nd$ range but are typically higher (Fig. 6). Twenty 85-µm-diameter spots yield $^{143}Nd/^{144}Nd$ values produce a weighted mean of 0.512689 ± 13 (ε_{Nd}=1.0 ± 0.3; MSWD=2.4); this value is indistinguishable within 2σ uncertainty from the mean of the 50-µm-diameter spots and TIMS data. The $^{147}Sm/^{144}Nd$ values determined using an 85-µm-diameter spot vary from 0.1171 ± 3 to 0.1237 ± 3, which like the 50-µm spots, tend to be on the higher end of TIMS $^{147}Sm/^{144}Nd$ range (Fig. 6). Laser ablation data for BRZ-1 with a 50-µm-diameter spot

produce $^{143}Nd/^{144}Nd$ values that overlap the TIMS range and yield a weighted mean $^{143}Nd/^{144}Nd$ =0.510994 ± 70 (ƐNd=-32.1 ± 1.4; MSWD=0.9, n=35); $^{147}Sm/^{144}Nd$ values vary from 0.0949 ± 2 to 0.1017 ± 4, which generally fall within the TIMS $^{147}Sm/^{144}Nd$ range (Table 7; Fig. 6). Analyses utilizing an 85-µm-diameter spot result in a mean $^{143}Nd/^{144}Nd$=0.510887 ± 46 (ƐNd=-34.2 ± 0.9; MSWD=1.1, n=20) (Fig. 6). While the mean of the 85 µm spots are offset from the TIMS mean, the ranges of the LA data are wholly consistent with the TIMS data (Fig. 6). The $^{147}Sm/^{144}Nd$ values have a range between 0.0973 ± 2 and 0.1018 ± 2, which largely overlap the TIMS $^{147}Sm/^{144}Nd$ values but do not extend to as high values (Fig. 6).

Despite corrections for Kr, REEs, Ca-dimer, and Rb interferences, $^{87}Sr/^{86}Sr$ measurements collected by LA-ICP-MS were persistently offset from TIMS reference values (Fig. 7). For MRC-1, the average corrected $^{87}Sr/^{86}Sr$ value of the 50 µm spot analyses is 0.70809 ± 18 (MSWD=1.3, n=10), which is ~0.05 % higher than its TIMS average (Table 8; Fig. 7). The average $^{87}Sr/^{86}Sr$ value collected using an 85-µm-diameter spot is ~0.08 % higher than the TIMS average ($^{87}Sr/^{86}Sr$ =0.708325 ± 80, MSWD=2.3, n=15). Offsets between LA and TIMS averages of BRZ-1 are more dramatic. The $^{87}Sr/^{86}Sr$ average determined using a 50-µm-diameter spot are $^{87}Sr/^{86}Sr$ =0.71055 ± 56 (~0.19 % higher than TIMS); using an 85-µm-diameter spot produces an average $^{87}Sr/^{86}Sr$ =0.710768 ± 178 (~0.22 % higher than TIMS; Fig. 7). The other analyzed RMs are also offset from the TIMS reference value, and are anti-correlated with the inverse of the measured ^{88}Sr signal (Fig. 10). Normalization to a primary RM (e.g., MAD-UCSB) does not remove this trend, but only shifts the averages toward more radiogenic values. Though $^{87}Rb/^{86}Sr$ ratios were not

analyzed by TIMS, in situ $^{87}Rb/^{86}Sr$ ratios are low (<0.0002), indicating negligible ingrowth of radiogenic ^{87}Sr.

3.4 DISCUSSION

3.4.1 Common-Pb corrections and U-Pb ages

Apatite incorporates significant amounts of non-radiogenic (common) Pb as it crystallizes, necessitating corrections to obtain geologically meaningful U-Pb dates. Common-Pb corrections can be done using different methods: from unanchored linear regression through multiple data points that form isochrons, using the total Pb-U isochron method that incorporates 204Pb measurements (see section 2.5.), by implementing the Pb growth model of Stacey and Kramers (1975), or by analyzing Pb isotopes in co-genetic, low U/Pb phases (e.g., feldspar; Chamberlain and Bowring, 2000; Schoene and Bowring, 2006; Chew et al., 2014a). The latter is not applicable here because the analyzed apatites were obtained as individual crystals. In addition, because ^{204}Pb cannot always be accurately measured by LA-ICP-MS given isobaric interferences with ^{204}Hg present in the He carrier gas and Ar plasma gas, the total Pb-U approach cannot be readily applied to our laser ablation data.

Applying different common-Pb correction schemes has no significant effect on the calculated intercept ages of the RMs (Table 6). In the case of MRC-1, the concordia age derived from the total Pb-U method applied to the TIMS data is 153.4 ± 0.4 Ma, which is indistinguishable from an unanchored York regression in Tera-Wasserburg concordia space (153.5 ± 0.4 Ma) and an anchored regression to a Stacey and Kramers (1975) model ($^{207}Pb/^{206}Pb)_i$ (153.4 ± 0.4 Ma; Table 6). The LASS data yield comparable concordia ages of

152.7 ± 0.6 Ma for data anchored to the $(^{207}Pb/^{206}Pb)_i$ value derived from the total Pb-U method of the TIMS data and 152.8 ± 0.9 Ma using the Stacey and Kramers (1975) model; unanchored regressions through the LASS data are not possible. For the three data that conform to a single population in BRZ-1 TIMS data set, the total Pb-U method yields a concordia age of 2078 ± 12 Ma, which overlaps within uncertainty age intercepts derived from unanchored regressions (2077 ± 14 Ma) and a Stacey and Kramers (1975) common-Pb model (2069 ± 11 Ma). The LASS data for BRZ-1 produce consistent U-Pb ages. Applying the $(^{207}Pb/^{206}Pb)_i$ value derived from the total Pb-U method of the TIMS data yields 2038 ± 14 Ma; this age overlaps the unanchored isochron age of 2042 ± 12 Ma and Stacey and Kramers (1975) anchored age of 2038 ± 11 Ma (Table 6). Regardless of the chosen $(^{207}Pb/^{206}Pb)_i$ the LASS and TIMS BRZ-1 ages are offset beyond their respective internal 2σ uncertainties (Fig. 6). This deviation is likely to reflect minor incorporation of younger, reset age domains during LASS spot analyses, as discussed below.

3.4.2 Fluid-assisted U-Pb resetting in BRZ-1 apatite

Although the choice of common-Pb composition does not significantly affect the age intercepts of the individual BRZ-1 ID-TIMS and LASS data sets, there is a persistent ~1.6 % difference in the mean ages (Fig. 5). This difference is unlikely to reflect matrix effects (e.g., Gehrels et al., 2008; Sylvester et al., 2008; Thompson et al., 2014) because there are no significant correlations among age offset vs. elemental compositions of the RMs (Appendix C). The age differences for BRZ-1 also cannot simply be a result of U-Pb heterogeneity in the primary MAD-UCSB reference apatite because all other secondary RMs (including MRC-1) are within uncertainty of their established ages, and shifting the U-Pb composition

of MAD-UCSB to bring the BRZ-1 TIMS and LASS dates to parity would cause offsets in these other RMs.

Overprinting or partial Pb loss is the likely root cause of the age shifts BRZ-1 data sets. It is clear from CL imaging and elemental X-ray maps that compositional heterogeneity is closely associated with cracks (Fig. 3B). Generally, LASS spots overlapping/near these cracks deviate the most from the ca. 2.07 Ga isochron, but it is also apparent that relatively young dates occur in the absence of any obvious cracks in a few cases (Fig. 8). In these cases, we suspect that some portion of the LASS spot analyses intersected cracks at depth, skewing the isochron toward a younger intercept age (Fig. 9). Minor amounts of the altered domains are likely incorporated into most of the LASS analyses given that heterogeneity occurs at a scale that is beyond the typical precision of LASS. The TIMS analyses highlight the fine-scale at which heterogeneity occurs. Three TIMS fractions from BRZ-1 form a coherent population, two other points lie slightly off the 2.07 Ga isochron, and three are clearly situated away with the isochron (Fig. 5); the uncertainty of individual LASS analyses is unable to resolve minor amounts of mixing with the younger domains (i.e., the two slightly discordant TIMS fractions) and helps explain why the LASS analyses yield an apparently younger intercept age.

Evidence for fluid-mediated isotopic resetting in BRZ-1 apatite is observed as μm-scale fractures with distinct elemental compositions (Fig. 2C). Both EPMA and LASS spot analyses reveal that altered domains are characterized by elevated REE and Th concentrations relative to the unaltered matrix. The exact nature of the fluid is uncertain but reactions with aqueous fluids would be expected to deplete REEs in apatite (e.g., Harlov et al., 2005), which is contrary to the observed increase in REE concentrations associated with

cracks (Fig. 9). Experiments exploring REE partitioning between apatite and silicate melt indicate that REEs are compatible in apatite over melts (Prowatke and Klemme, 2006), but it is unclear how such viscous fluids would infiltrate through the fine-grained cracks. Rigorous testing of fluid compositions would require further petrological context, but regardless of the exact nature of the metasomatic agent, it is clear that monitoring and screening of BRZ-1 analyses are required if it is to be employed as an effective RM.

Coupled U-Pb and trace-element data can be useful in screening altered domains in BRZ-1. Figure 9 shows that highly discordant spot analyses correlated with higher concentrations of some trace elements, including U and MREEs and HREEs, in agreement with findings from EPMA (Fig. 3). Unfortunately, these trends are apparent for spot analyses showing extreme discordance; trace elements are unable to discriminate minor degrees of mixing with younger age domains in BRZ-1 (Fig. 5). Another way to optimize this apatite for petrochronology would be to preferentially break the apatite along altered cracks and remove the exterior of different crystal fragments either by hand-polishing or air abrasion, ensuring only pristine areas are targeted.

3.4.3. Limitations of in situ Sr isotopes and ways forward

In situ Sr isotope analyses of the apatite RMs can differ from TIMS reference values by up to 0.02 % (Fig. 10). While there are multiple unresolved interferences in our study that could account for these offsets—like Hf, MnP, and Fe-oxides, which both occur as trace elements within apatite (Ramos et al., 2004; Gillespie et al., 2021b)—a critical interference is likely to be $^{40}Ca^{31}P^{16}O^{+}$ (CaPO), a molecule formed of major elements within apatite. Indeed, Horstwood et al. (2008) observed a similar deviation trend, wherein apatite with lower Sr concentrations are more offset towards radiogenic values than those with higher Sr

contents. Horstwood et al. suggested that CaPO can contribute significantly to the ^{87}Sr signal (up to 1 %) and that $^{87}Sr/^{86}Sr$ compositions by LA-ICP-MS are likely only accurate to 0.03–0.4 % without correcting for this interference. Hence, apatite with lower Sr concentrations is expected to yield greater differences given the relatively greater contribution of CaPO on ^{87}Sr. Unfortunately, monitoring the contributions of CaPO on the ^{87}Sr signal requires measurement of mass-71 (corresponding to $^{40}Ca^{31}P$) and precise knowledge of oxide production during an analytical session, information we are unable to obtain with the MC-ICP-MS set-up used in this study. There is also the likelihood that LREE-oxides create some interferences on middle REEs used to correct isobaric interferences with Sr (e.g., Kent and Ungerer, 2005). Despite these complexities, we suggest that calibrations against multiple apatite RMs provide an alternative way to obtain accurate $^{87}Sr/^{86}Sr$ measurements by LA-ICP-MS.

Analyses of apatite whose TIMS Sr isotopic compositions have been determined for the purpose of this study (MAD-UCSB, BRZ-1, and MRC-1) define a strong anti-correlation between $^{87}Sr/^{86}Sr$ offset—defined here as $100 \times [1 - (^{87}Sr/^{86}Sr)_{LA} / (^{87}Sr/^{86}Sr)_{TIMS}]$—and 1/corrected-$^{88}Sr$ signal intensity (R^2=0.99 for analyses using 50- and 85-µm-diameter laser spot sizes; Fig. 10). The empirical trend could be used to correct in situ Sr isotopic measurements. We find that McClure apatite is also situated along this empirical trend, but our Sr analyses of Durango are not (Fig. 10). This could signify that the effects of CaPO and other interferences are non-linear or that different Durango crystals have distinct intracrystal $^{87}Sr/^{86}Sr$ compositions. Multiple ID-TIMS analyses of different Durango crystals are consistent with one another (McFarlane and McCulloch, 2008; Horstwood et al., 2008; Hou

et al., 2013; Yang et al., 2014; Table 3), suggesting yet another unresolved interference hampers in situ $^{87}Sr/^{86}Sr$ measurements.

Although the Sr isotopic compositions of 401 and OD306 apatites (Thompson et al., 2016) have not been previously analyzed, we can estimate their $^{87}Sr/^{86}Sr$ compositions based on our observed empirical trend and average measured ^{88}Sr intensities. For 401 apatite, corrected $^{87}Sr/^{86}Sr$ values are 0.706406 ± 489 (50 µm spot) and 0.706180 ± 150 (85 µm spot). For OD306, corrected $^{87}Sr/^{86}Sr$ values are 0.708741 ± 1694 (50 µm spot) and 0.708015 ± 448 (85 µm spot) (note that these the corrected $^{87}Sr/^{86}Sr$ values do not include errors of the fits). Large uncertainties notwithstanding, the corrected Sr value for OD306 should be accurate giving that Cl concentrations are relatively low (~0.1 wt.% Cl; Thompson et al., 2016), whereas 401 could be considerably more inaccurate (~0.7 wt.% Cl; Thompson et al., 2016).

Finally, the Sr isotopic compositions of silicate glass BHVO-2G and carbonate MACS-3 determined by LA-ICP-MS in this study are consistently more accurate than our apatite analyses at similar Sr concentrations (typically within 2σ uncertainty of their preferred GeoReM TIMS $^{87}Sr/^{86}Sr$ compositions; Table 3; Fig. 10). Both BHVO-2G and MACS-3 are characterized by significantly lower Ca, P, and REEs contents for similar Sr concentrations compared the apatite RMs (Table 3). These observations support the interpretation that CaPO interferences, among other interferences, may be significant hindrances in obtaining accurate in situ $^{87}Sr/^{86}Sr$ in apatite. In total, our study strongly suggests that analyzing a suite of matrix-matched RMs with well-characterized $^{87}Sr/^{86}Sr$ isotopic values and different Sr concentrations are critical for corrections and obtaining robust measurements by LA-ICP-MS.

3.5 CONCLUSIONS

Two prospective reference apatites from Morocco (MRC-1) and Brazil (BRZ-1) provide new tools for in situ apatite analyses. The MRC-1 apatite, despite being compositionally zoned, yields consistent U-Pb concordia dates (Fig. 5). The U-Pb compositions of MRC-1 vary along a well-defined isochron and can be employed as a primary standard using, for example, the VizualAge UcomPbine data reduction scheme for Iolite (Chew et al., 2014a), which can correct for variable amounts of common-Pb in different RMs. The Nd isotopic compositions determined by LA-ICP-MS for MRC-1 are consistent and comparable to those obtained by ID-TIMS, making it most useful as a $^{143}Nd/^{144}Nd$ isotopic RM. The ID-TIMS $^{87}Sr/^{86}Sr$ compositions for MRC-1 are remarkably homogeneous (Fig. 7) and is a strong candidate for a Sr RM; we emphasize the need for such an RM given the challenges of obtaining precise and accurate Sr compositions by LA-ICP-MS and SIMS in the face of confounding isobaric interferences (Gillespie et al., 2021b).

The data discussed above indicate that the BRZ-1 apatite is best utilized as a secondary standard. Its U concentrations are conducive for relatively precise dating (Table 6), and the vast majority of the matrix yields U-Pb data that fall along a single ca. 2.07 Ga isochron (Fig. 5). Heterogeneity in these crystals occurs as micron-scale cracks associated with secondary-alteration, which is a disadvantage of this RM. Imaging (either by BSE or CL) would be useful in guiding spot placement to ensure only pristine portions of the grain are targeted. Combined trace element analyses are useful for identifying U-Pb data that have been partially reset and emphasize the advantage of LASS in interpreting complex age patterns in apatite. The LA-ICP-MS Nd isotopic measurements of BRZ-1 are homogeneous within typical 2σ uncertainties (Fig. 7), agree well with the mean Nd isotopic compositions

determined by TIMS, and appear largely unaffected by micron-scale heterogeneity within our reported LA-ICP-MS 2σ uncertainties. Concentrations of Sr are low in BRZ-1 (average ~200–300 ppm), requiring large spot sizes (>85μm diameter) to obtain precise Sr isotopic measurements by LA-ICP-MS. However, BRZ-1 provides a useful anchor for empirical calibrations of deviation trends in $^{87}Sr/^{86}Sr$ measurements by LA-ICP-MS and SIMS.

Table 1. U-Pb age summary of some apatite RMs

Apatite	Origin	Reported age (Ma)[1]	Method[2]	References
Durango	Durango, Mexico	31.4 ± 0.2	Ar-Ar (feldspar)	McDowell et al. (2005)
		32.7 ± 0.1	U-Pb ID-TIMS	Paul et al. (2021)
Emerald Lake	British Columbia, Canada	92.2 ± 0.9	U-Pb ID-TIMS (titanite)	Coulson et al. (2002)
		90.5 ± 3.1	U-Pb LA-SC-ICP-MS	Chew et al. (2011)
Kovdor	Kola Peninsula, Russia	380.6 ± 2.6	U-Pb ID-TIMS	Amelin and Zaitzev (2002)
MAD1	Madagascar, Africa	486.6 ± 0.9	U-Pb ID-TIMS	Thomson et al. (2012)
MAD2		474.3 ± 0.4	U-Pb ID-TIMS	Thomson et al. (2012)
MAD2-TCD		475.4 ± 1.8	U-Pb ID-TIMS	Fisher et al. (2020b)
McClure	Colorado, United States	523.5 ± 1.5	U-Pb ID-TIMS	Schoene and Bowring (2006)
		524.6 ± 2.7	U-Pb ID-TIMS	Krestianinov et al. (2021)
		523.5 ± 1.7	U-Pb ID-TIMS	Schoene and Bowring (2006) with Krestianinov et al. (2021)
401	Iran	530.3 ± 1.5	U-Pb ID-MC-ICP-MS	Thompson et al. (2016)
		506.2 ± 7.0	U-Pb LA-MC-ICP-MS	Thompson et al. (2016)
Cheever mine	New York, United States	907 ± 14	U-Pb ID-TIMS	Krestianinov et al. (2021)
Old Bed mine	New York, United States	924 ± 13	U-Pb ID-TIMS	Krestianinov et al. (2021)
Otter Lake	Quebec, Canada	913 ± 7	Pb-Pb ID-MC-ICP-MS	Barford et al. (2005)
Wilberforce	Ontario, Canada	923 ± 14	U-Pb ID-TIMS	Paul et al. (2021)
Tory Hill	Ontario, Canada	1021 ± 3	U-Pb ID-TIMS	Fisher et al. (2019)
OD306	Southern Australia	1597 ± 7	U-Pb ID-MC-ICP-MS	Thompson et al. (2016)
		1545 ± 20	U-Pb LA-MC-ICP-MS	Thompson et al. (2016)

[1]Reported 2σ uncertainty

[2]All apatite analyses unless where noted; MC, multi collector; SC, single collector

Table 2. Previously reported Sm-Nd concentrations and isotopic compositions of select apatite RMs

Apatite	Average Sm [ppm]	Average Nd [ppm]	$^{147}Sm/^{144}Nd$[1]	$^{143}Nd/^{144}Nd$[1]	Method	References
MAD	182	1322	0.0818 ± 5	0.511348 ± 16	ID-MC-ICP-MS	Yang et al. (2014)
	n/a	n/a	0.0811 ± 17	0.511322 ± 53	LA-MC-ICP-MS	Yang et al. (2014)
	213	1654	0.0779 ± 5	0.511304 ± 13	ID-TIMS	Fisher et al. (2020b)
Durango	n/a	n/a	0.0765 ± 5	0.512469 ± 16	LA-MC-ICPMS	McFarlane and McCulloch (2008)
	127	1040	0.0763 ± 14	0.512449 ± 10	LA-MC-ICPMS	McFarlane and McCulloch (2008)
	n/a	n/a	0.0751 ± 25	0.512489 ± 12	ID-MC-ICP-MS	Fisher et al. (2011)
	n/a	n/a	0.0785 ± 58	0.512463 ± 48	LA-MC-ICPMS	Fisher et al. (2011)
	224	1568	0.0865 ± 17	0.512487 ± 13	ID-TIMS	Hou et al. (2013)
	n/a	n/a	0.0852 ± 10	0.512498 ± 25	LA-MC-ICPMS	Hou et al. (2013)
	243	1667	0.0881 ± 11	0.512493 ± 21	ID-MC-ICP-MS	Yang et al. (2014)
	n/a	n/a	0.0885 ± 19	0.512490 ± 46	LA-MC-ICPMS	Yang et al. (2014)
McClure	99	836	0.0712 ± 8	0.512282 ± 11	ID-MC-ICP-MS	Yang et al. (2014)
	n/a	n/a	0.0696 ± 72	0.512246 ± 80	LA-MC-ICP-MS	Yang et al. (2014)

[1]Reported weighted mean and 2σ uncertainty

Table 3. Previously reported Sr concentrations and isotopic compositions of select apatite RMs

Apatite	Average Sr [ppm]	$^{87}Sr/^{86}Sr$[1]	Method	References
MAD	1650	0.71108 ± 3	ID-MC-ICP-MS	Yang et al. (2014)
	n/a	0.71108 ± 11	LA-MC-ICPMS	Yang et al. (2014)
Durango	n/a	0.70633 ± 1	ID-TIMS	Horstwood et al. (2008)
	475	0.70629 ± 2	ID-TIMS	McFarlane and McCulloch (2008)
	n/a	0.70638 ± 13	LA-MC-ICPMS	McFarlane and McCulloch (2008)
	483	0.70634 ± 13	ID-TIMS	Hou et al. (2013)
	n/a	0.70629 ± 9	LA-MC-ICPMS	Hou et al. (2013)
	n/a	0.70633 ± 2	ID-MC-ICP-MS	Yang et al. (2014)
	486	0.70634 ± 14	LA-MC-ICPMS	Yang et al. (2014)
McClure	n/a	0.70369 ± 2	ID-MC-ICP-MS	Yang et al. (2014)
	3422	0.70371 ± 7	LA-MC-ICPMS	Yang et al. (2014)
BHVO	397	0.703469 ± 7	ID-TIMS	Elburg et al. (2006)
MACS-3	6640	0.707553 ± 4	ID-TIMS	Jochum et al. (2011)

[1]Reported weighted mean and 2σ uncertainty

Table 4. Average trace element concentrations determined by EPMA (full data set in Supplementary Table S1).

EMPA transect		La [ppm]	Ce [ppm]	Nd [ppm]	Pr [ppm]	Si [ppm]	Na [ppm]	Th [ppm]	Gd [ppm]	Sm [ppm]	Sr [ppm]	Y [ppm]	S [ppm]
BRZ-1													
20 µm line scan (n=30)	Av.	368.0	623.5	336.1	b.d.l	4054.2	408.5	813.7	79.3	b.d.l	292.2	136.9	3224.3
	1SD	59.6	114.3	46.5	b.d.l	82.8	38.6	51.6	34.8	b.d.l	21.3	29.3	173.0
5 µm line scan 1 (n=63)	Av.	313.0	656.9	251.4	b.d.l	3729.1	446.7	809.5	71.9	b.d.l	311.8	143.9	3315.3
	1SD	95.8	160.9	70.9	b.d.l	289.8	79.5	108.1	36.6	b.d.l	43.2	34.6	394.5
5 µm line scan 2 (n=24)	Av.	287.2	604.6	260.3	b.d.l	3809.8	430.0	770.3	66.3	b.d.l	298.5	134.7	3168.5
	1SD	79.4	78.1	78.3	b.d.l	226.9	77.9	73.2	33.5	b.d.l	32.9	28.7	259.8
5 µm line scan 3 (n=113)	Av.	321.3	690.0	264.0	b.d.l	3823.9	488.0	723.3	82.5	b.d.l	294.7	144.2	3160.5
	1SD	85.2	120.8	70.7	b.d.l	324.1	100.7	111.7	38.1	b.d.l	31.1	30.1	278.0
all scans (n=230)	Av.	321.5	663.4	269.6	b.d.l	3829.0	459.9	762.3	77.6	b.d.l	299.3	142.1	3209.2
	1SD	86.9	131.7	73.4	b.d.l	299.7	91.1	109.1	37.0	b.d.l	34.5	31.1	304.7
MRC-1													
20 µm line scan (n=147)	Av.	2456.9	3708.4	1487.4	302.6	3206.7	470.2	364.0	587.6	b.d.l	823.1	1454.5	1276.3
	1SD	179.7	267.4	100.1	75.9	389.1	73.7	68.9	62.1	b.d.l	41.9	89.2	274.2

*Averages discarded outliers beyond 2SD

b.d.l., below detection limit

Table 5. ICP instrument parameters for U-Pb/TE, Sm-Nd, and Sr isotopic analyses

Instruments			
Instrument model	Nu Instruments Plasma 3D MC-ICP-MS	Nu Instruments Plasma HR-ES MC-ICP-MS	Agilent 7700S quadrapole
RF power	1300 W	1300 W	
Make-up gas flow	0.7–0.8 L/min (U-Pb TE LASS) 1.07 L/min (Sm-Nd, Sr)	0.7–0.8 L/min (U-Pb TE LASS)	1.4 L/min (U-Pb TE LASS)
Masses measured	U-Pb+TE LASS: ^{204}Hg+Pb, ^{206,207,208}Pb on SEMs; ^{232}Th, ^{238}U on Faraday cups Sm-Nd: ^{142}Nd, ^{143}Nd, ^{144}Nd+Sm, ^{145}Nd, ^{146}Nd, ^{147}Sm, ^{148}Nd, ^{149}Sm, ^{150}Nd on Faraday cups Sr: $^{82}Kr^{+}+(^{164}Er^{++})+(^{40}Ca^{42}Ca)$, $^{167}Er^{++}$, $^{84}Sr^{+}+Kr^{+}+(^{168}Yb^{++}+Er^{++})$, $^{85}Rb^{+}+(^{170}Yb^{++}+Er^{++})$, $^{86}Sr^{+}+Kr^{+}+(^{172}Yb^{++})$, $^{173}Yb^{++}$, $^{87}Sr^{+}+Rb^{+}+(^{174}Yb^{++})$, $^{175}Lu^{++}$, $^{88}Sr^{+}+(^{176}Lu^{++}+Yb^{++})+(^{40}Ca^{48}Ca)$ on Faraday cups	U-Pb+TE LASS: ^{202}Hg, ^{204}Hg+Pb, ^{206,207,208}Pb on SEMs; ^{232}Th, ^{238}U on Faraday cups	U-Pb+TE LASS: ^{44}Ca, ^{88}Sr, ^{89}Y, ^{90}Zr, ^{139}La, ^{140}Ce, ^{141}Pr, ^{146}Nd, ^{147}Sm, ^{153}Eu, ^{157}Gd, ^{159}Tb, ^{163}Dy, ^{165}Ho, ^{166}Er, ^{169}Tm, ^{172}Yb, ^{175}Lu ± ^{49}Ti ± ^{55}Mn ± ^{56}Fe ± ^{137}Ba
Integration time per peak/dwell times; quadrupole sweep time	100 ms	500 ms	~200 ms
Total integration (sweep) time per output data point	0.5 s	0.5 s	0.5 s
Laser ablation system			
Make, Model and type	Cetac Teledyne 193 nm excimer Analyte laser		
Ablation cell and volume	HelEx-2 ablation cell (Eggins et al., 1998; Eggins et al., 2005)		
Laser wavelength	193 nm		
Pulse width	4 ns		
Fluence; pit depth/pulse	~1 J/cm^2; ~0.08–0.1 μm/pulse		
Repetition rate	4 Hz (U-Pb+TE LASS), 15 Hz (Sm-Nd, Sr);		
Ablation duration	15 s (U-Pb+TE LASS), 20 s (Sm-Nd, Sr)		
Spot diameter	40 μm (U-Pb + TE LASS), 50 μm + 85 μm (Sm-Nd, Sr)		
Sampling mode / pattern	Static spot ablation		
Carrier gas	100% He in the cell, Ar make-up gas combined in a glass mixing bulb		
Cell carrier gas flow	0.15 L/min total (0.12 L/min for cup, 0.03 L/min for cell)		
Data Processing			
Reference Materials	see Tables 1–3		
Data processing package	Iolite v. 2.5 (Paton et al., 2011); LIEF correction assumes reference material and samples behave identically.		
Common-Pb correction, composition and uncertainty	No common-Pb correction applied to the data; 2σ uncertainty of $(^{207}Pb/^{206}Pb)_i$ determined by linear regression through U-Pb data or assumed to be 0.5 for Stacey-Kramers model common-Pb		
Uncertainty level and propagation	Ages are quoted at 2*s* absolute, propagation is by quadratic addition. Reproducibility and age uncertainty of reference material and common-Pb composition uncertainty are propagated where appropriate.		

Table 6. Summary of U-Pb age results from this study

apatite	method	average U [ppm]	average Th [ppm]	intercept age (Ma)[1]	$(^{207}Pb/^{206}Pb)_i$	common-Pb correction
MAD-UCSB	ID-TIMS	22	545	467.4 ± 8.4	0.71 ± 0.10	Total Pb-U
MRC-1	ID-TIMS	31	285	153.4 ± 0.4	0.85 ± 0.04	Total Pb-U
				153.5 ± 0.4	0.86 ± 0.08	unanchored York regression
				153.4 ± 0.4	0.85 ± 0.05	Stacey-Kramers (153 Ma)
	LASS	34	330	152.7 ± 0.6	0.85 ± 0.04	Total Pb-U $(^{207}Pb/^{206}Pb)_i$
				152.8 ± 0.9	0.85 ± 0.05	Stacey-Kramers (153 Ma)
BRZ-1	ID-TIMS[2]	65	892	2078 ± 12	1.14 ± 0.09	Total Pb-U
				2077 ± 14	1.13 ± 0.08	unanchored York regression
				2069 ± 11	1.01 ± 0.05	Stacey-Kramers (153 Ma)
	LASS	76	879	2038 ± 14	1.14 ± 0.09	Total Pb-U $(^{207}Pb/^{206}Pb)_i$
				2042 ± 12	1.06 ± 0.06	unanchored York regression
				2038 ± 11	1.01 ± 0.05	Stacey-Kramers (153 Ma)
Durango	LASS	15	339	29.4 ± 1.2	0.84 ± 0.05	Stacey-Kramers (31 Ma)
McClure	LASS	17	43	517.0 ± 8.0	0.87 ± 0.04	unarchored York regression
401	LASS	17	125	508.4 ± 5.7	0.66 ± 0.30	unarchored York regression
OD306	LASS	23	64	1570 ± 15	1.5 ± 1.1	unarchored York regression

[1] 2σ, in-run errors with propogated long-term uncertainties (LASS) and tracer uncertainties (ID-TIMS).

[2] Includes only 3/8 cogenetic points

Table 7. Summary of Sm-Nd results from this study

Apatite	Method	Average Sm [ppm]	Average Nd [ppm]	Average $^{147}Sm/^{144}Nd$[1]	Average $^{143}Nd/^{144}Nd$[1]
MAD-UCSB	ID-TIMS	165	1283	0.07763 ± 4	0.511312 ± 3
	LA-ICP-MS (50 µm)	185	1514	0.07799 ± 4	0.511310 ± 32
	LA-ICP-MS (85 µm)	285	1513	0.07800 ± 9	0.511309 ± 26
MRC-1	ID-TIMS	206	1136	0.10923 ± 9	0.512677 ± 3
	LA-ICP-MS (50 µm)	284	1541	0.11717 ± 3	0.512710 ± 18
	LA-ICP-MS (85 µm)	285	1550	0.11674 ± 5	0.512689 ± 13
BRZ-1	ID-TIMS	24	143	0.10152 ± 8	0.510989 ± 5
	LA-ICP-MS (50 µm)	42	267	0.09854 ± 5	0.510994 ± 70
	LA-ICP-MS (85 µm)	42	266	0.09981 ± 6	0.510887 ± 46
Durango	LA-ICP-MS (50 µm)	189	1381	0.08760 ± 20	0.512485 ± 34
	LA-ICP-MS (85 µm)	192	1397	0.08720 ± 10	0.512470 ± 24
McClure	LA-ICP-MS (50 µm)	114	963	0.07420 ± 48	0.512351 ± 46
	LA-ICP-MS (85 µm)	120	1027	0.07180 ± 47	0.512266 ± 32
401	LA-ICP-MS (50 µm)	421	3007	0.08920 ± 1	0.512282 ± 22
	LA-ICP-MS (85 µm)	434	3070	0.09050 ± 4	0.512282 ± 16
OD306	LA-ICP-MS (50 µm)	346	2734	0.08060 ± 5	0.511238 ± 22
	LA-ICP-MS (85 µm)	331	2650	0.07870 ± 42	0.511212 ± 16

[1]Weighted mean and associated 2σ uncertainty; age uncorrected

Table 8. Summary of Sr results from this study

Apatite	Method	Average Sr [ppm]	$^{87}Sr/^{86}Sr$[1]	Offset[2]
MAD-UCSB	ID-TIMS	1847	0.711773 ± 2	-
	LA-ICP-MS (50 µm)	1577	0.711850 ± 120	-0.02
	LA-ICP-MS (85 µm)	1567	0.712028 ± 86	-0.04
MRC-1	ID-TIMS	779	0.707691 ± 2	-
	LA-ICP-MS (50 µm)	700	0.708092 ± 180	-0.06
	LA-ICP-MS (85 µm)	695	0.708325 ± 80	-0.09
BRZ-1	ID-TIMS	233	0.709188 ± 3	-
	LA-ICP-MS (50 µm)	243	0.710550 ± 560	-0.19
	LA-ICP-MS (85 µm)	246	0.710768 ± 178	-0.22
Durango	LA-ICP-MS (50 µm)	335	0.708380 ± 510	*-0.30*
	LA-ICP-MS (85 µm)	335	0.709030 ± 190	*-0.39*
McClure	LA-ICP-MS (50 µm)	3155	0.703655 ± 74	0.00
	LA-ICP-MS (85 µm)	2882	0.703778 ± 28	-0.01
401	LA-ICP-MS (50 µm)	383	0.707220 ± 490	-
	LA-ICP-MS (85 µm)	392	0.707180 ± 150	-
OD306	LA-ICP-MS (50 µm)	142	0.711200 ± 1700	-
	LA-ICP-MS (85 µm)	137	0.710890 ± 450	-
BHVO	LA-ICP-MS (50 µm)	184	0.703090 ± 940	0.05
	LA-ICP-MS (85 µm)	198	0.703440 ± 330	0.00
MACS-3	LA-ICP-MS (25 µm)	-	0.707390 ± 140	0.02

[1]Weighted mean and associated 2σ uncertainty; unnormalized

[2]Defined as $100 \times [1 - (^{87}Sr/^{86}Sr)_{LA} / (^{87}Sr/^{86}Sr)_{TIMS}]$

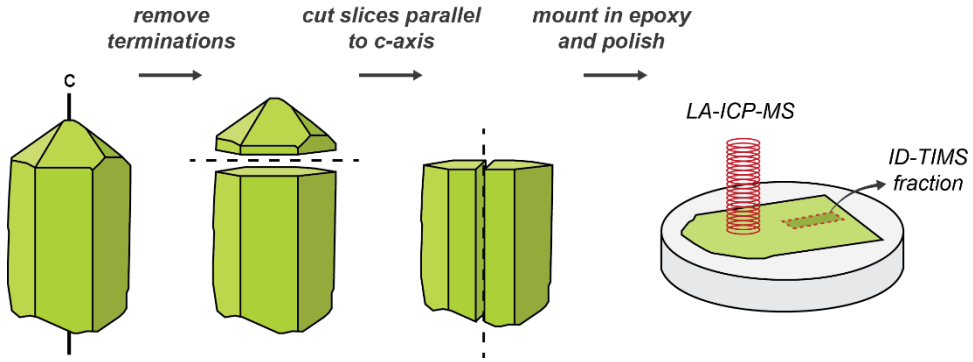

Figure 1. Cartoon of specimen preparations (following recommendations of Chew et al., 2016). Crystal terminations are sawn off, and the remaining prism is cut along its c-axis into mm-thick slices. In this study, a crystal section was analyzed using CL, EPMA, LASS/LA-ICP-MS, and ID-TIMS. An additional crystal section was analyzed by LASS to assess chemical heterogeneity (Fig. 2B and D).

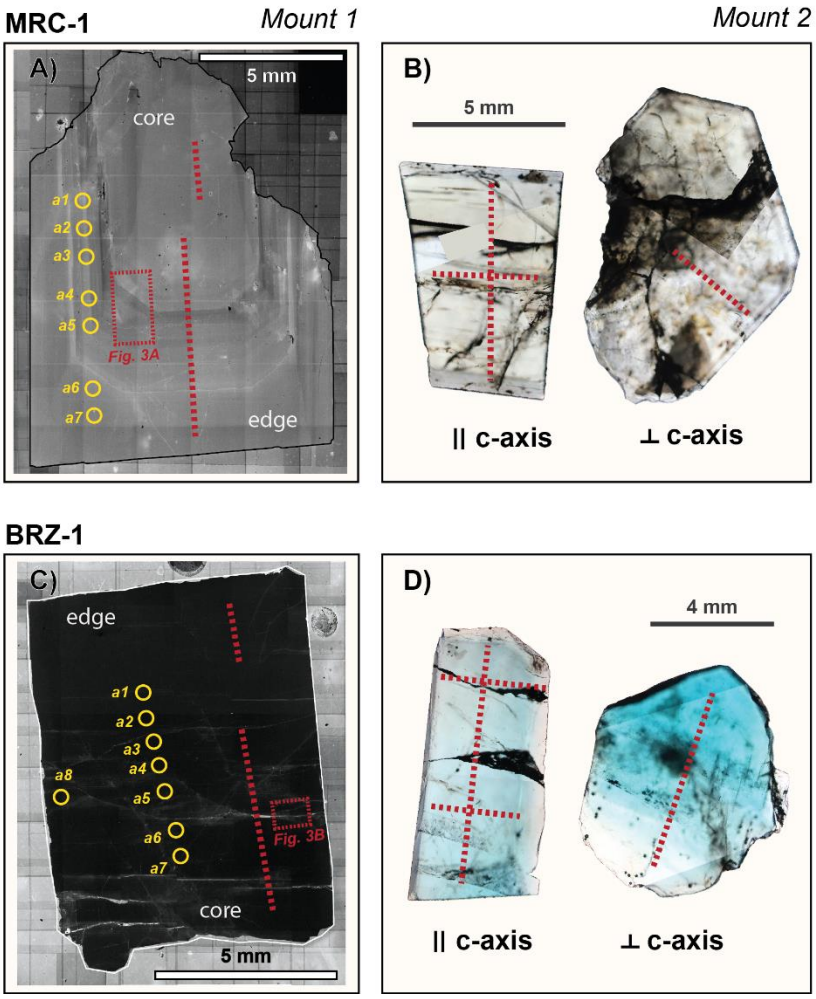

Figure 2. Left) CL maps of MRC-1 showing zonation and of BRZ-1 showing conspicuous cracks (white/grey wisps). Yellow circles indicate location of extracted TIMS fractions. Red dashed lines are approximate trajectories of LASS transects. Red dashed rectangles represent location of EPMA maps shown in Figure 3. Right) photomicrographs of additional c-axis parallel and perpendicular sections analyzed by LASS. Red dashed lines are approximate LASS paths.

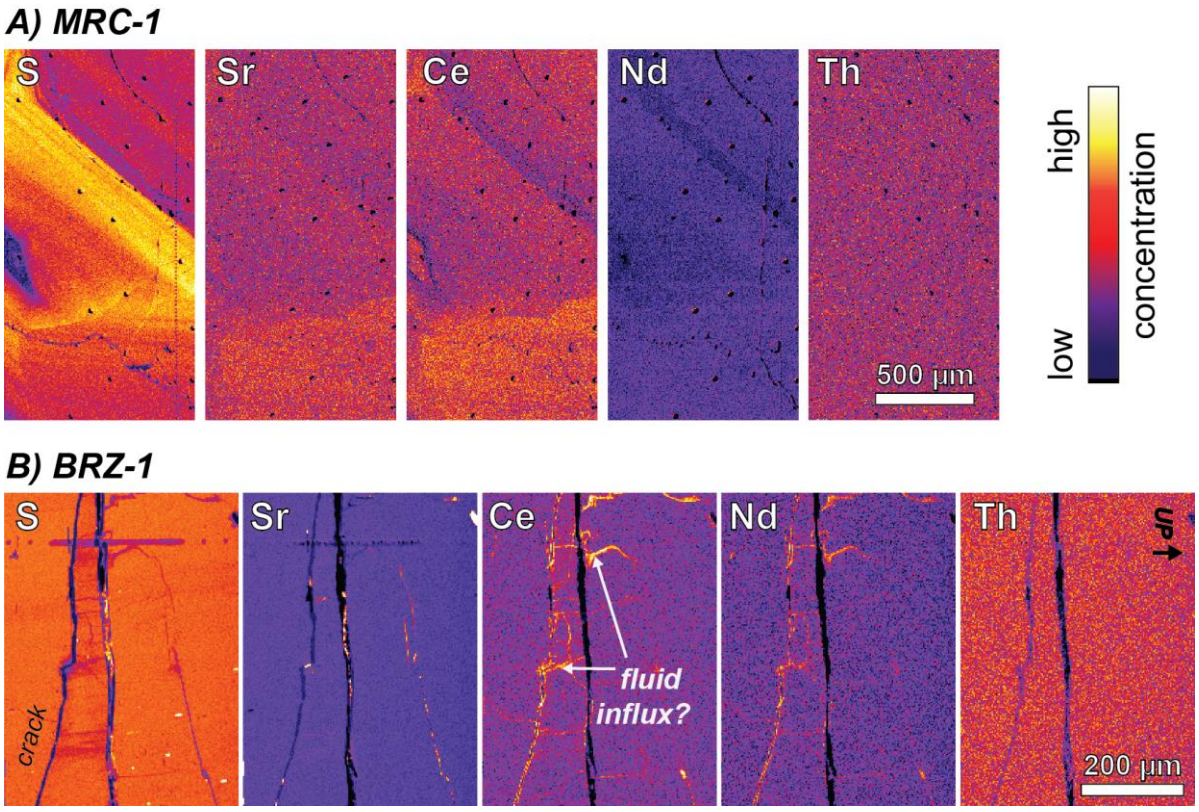

Figure 3. Qualitative X-ray maps of apatites. A) Zoning in MRC-1 is marked by differences in S, Sr, Ce, and Nd (no significant Th variation is captured by EPMA). B) Areas near cracks in BRZ-1 are compositionally distinct from the matrix (enriched in Ce and Nd relative to the matrix). Color scale on each map is qualitative and the colors were edited to emphasize contrast; warmer colors indicate higher concentrations relative to cooler colors.

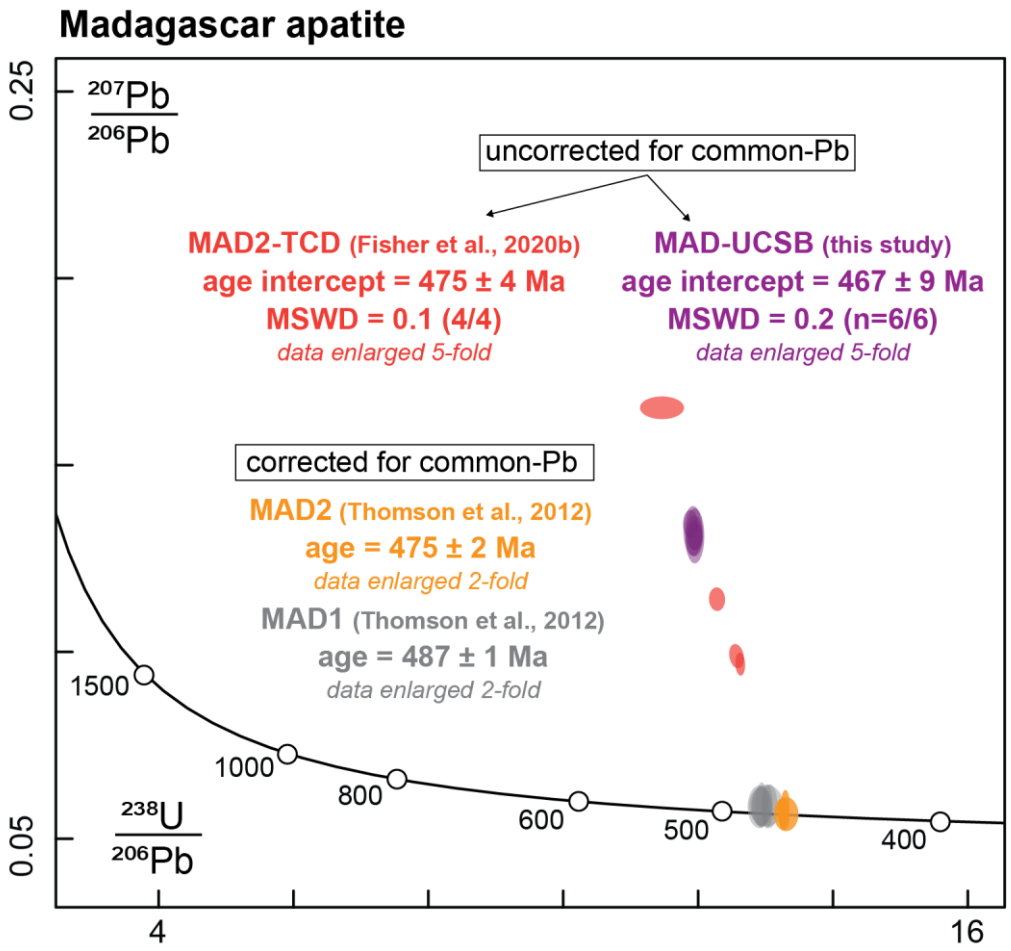

Figure 4. Tera-Wasserburg concordia diagram of Madagascar apatite data (Thomson et al., 2012; Fisher et al., 2020b; this study). MAD-UCSB and MAD2-TCD data are common-Pb uncorrected (MAD2-TCD data from C. Fisher, personal communication) whereas MAD1 and MAD2 are common-Pb corrected. Different MAD crystals have distinct U-Pb ratios, highlighting inter-crystal heterogeneity for this RM. Note that the data are enlarged for visualization.

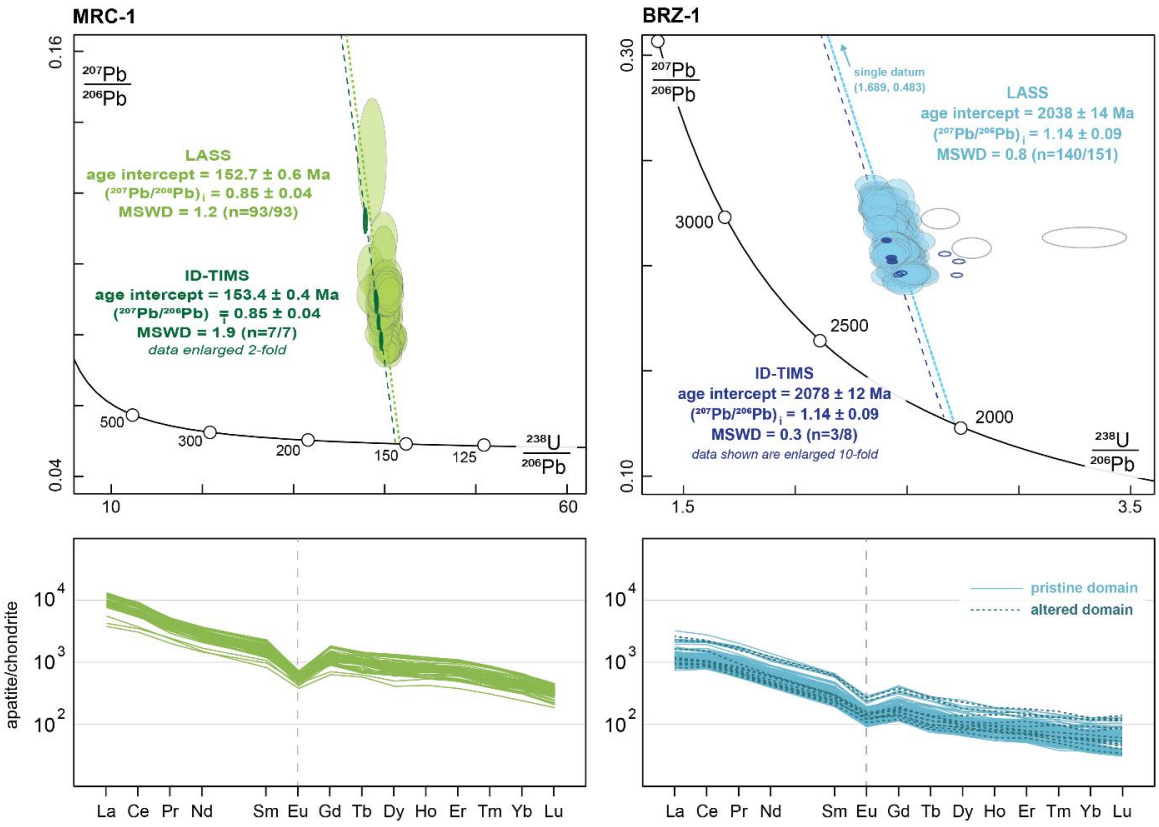

Figure 5. Top: Tera-Wasserburg concordia diagrams of MRC-1 (right) and BRZ-1 (left) LASS data. The ages of the TIMS data were derived using the total Pb-U method, and the resulting $(^{207}Pb/^{206}Pb)_i$ intercepts were used to correct the LASS data. Unfilled ellipses are data excluded from age regression. Note that TIMS data are enlarged to facilitate visual comparison to the LASS data. TIMS and LASS analyses of MRC-1 produce overlapping isochrons, but produce offset isochrons for BRC-1. Bottom: Chondrite-normalized REE plots showing consistent REE patterns in these RMs (reference chondrite values from McDonough and Sun, 1995).

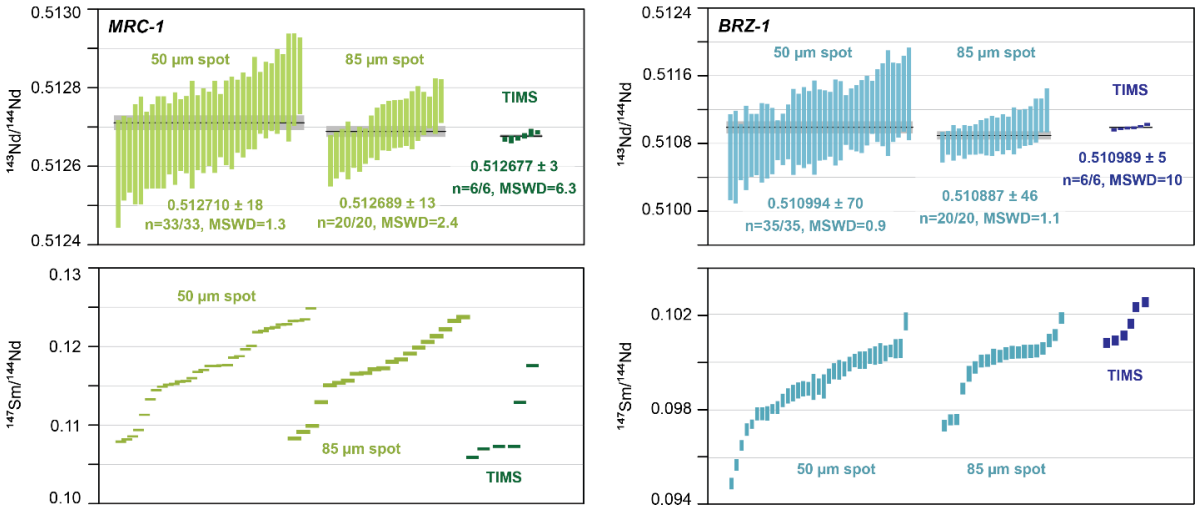

Figure 6. Comparing $^{143}Nd/^{144}Nd$ and $^{147}Sm/^{144}Nd$ ratios obtained by LA-ICP-MS and ID-TIMS (same color scheme as Fig. 5). The height of each data point is the 2σ uncertainty.

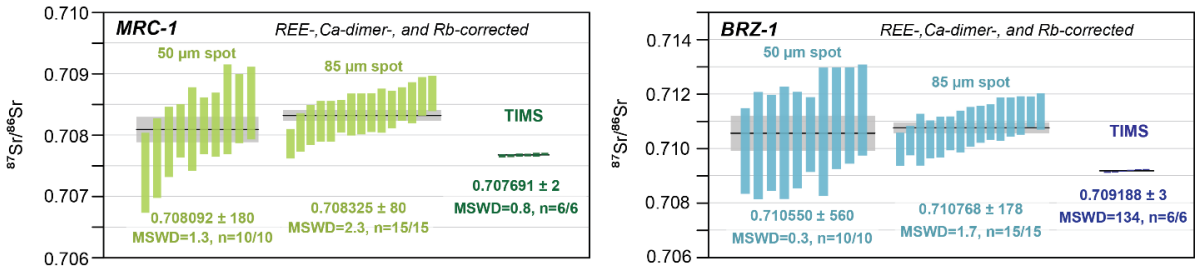

Figure 7. Comparing $^{87}Sr/^{86}Sr$ values obtained by LA-ICP-MS and ID-TIMS (same color scheme as Fig. 5). Laser ablation data are REE-, Ca-dimer, and Rb-corrected, and not normalized to a primary RM. Note that while laser ablation Sr values determined using 50 and 85 µm overlap on another, they are persistently offset from TIMS values. The height of each data point is the 2σ uncertainty.

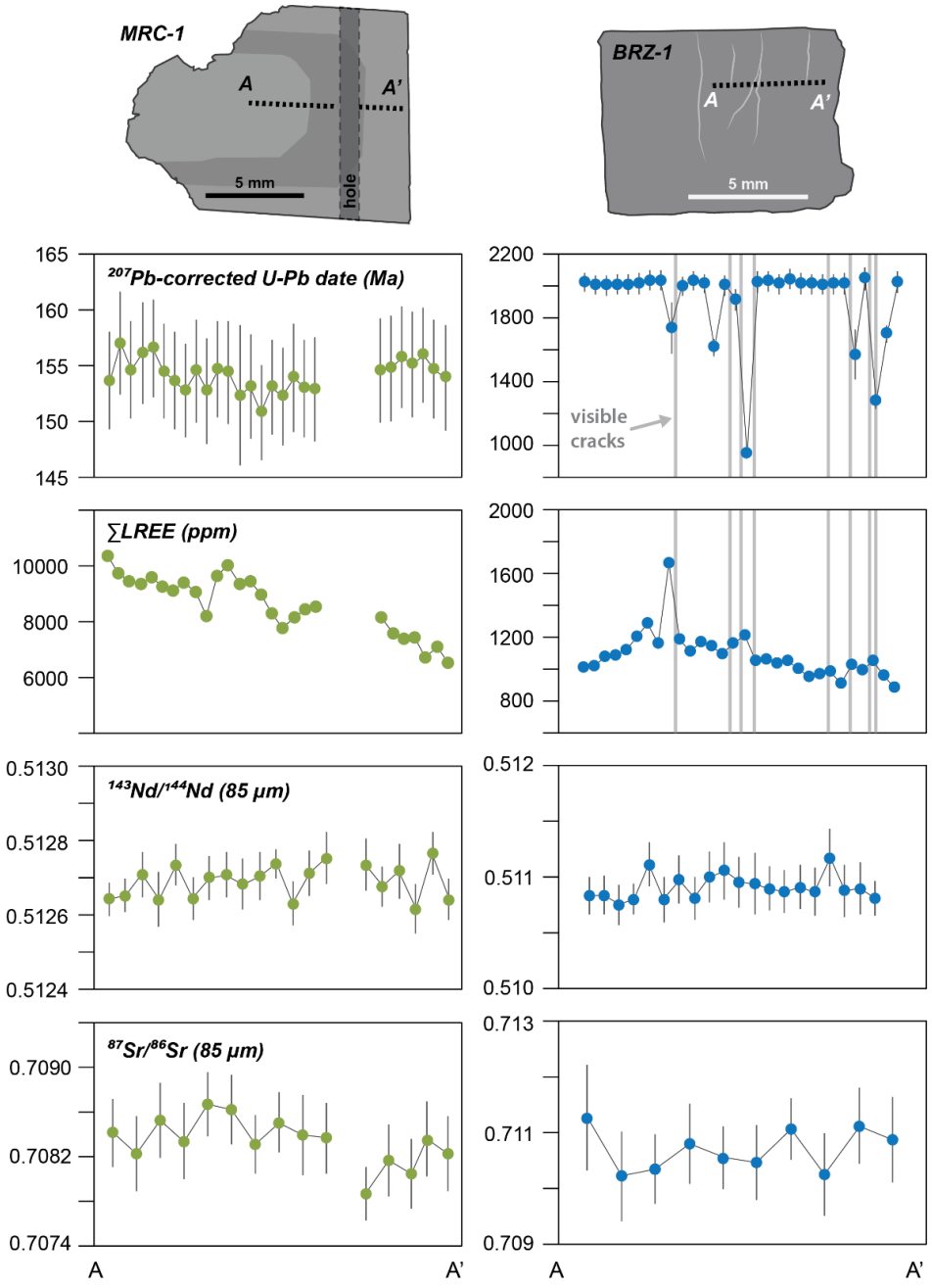

Figure 8. Comparing $^{87}Sr/^{86}Sr$ values obtained by LA-ICP-MS and ID-TIMS (same color scheme as Fig. 5). Laser ablation data are REE-, Ca-dimer, and Rb-corrected, and not normalized to a primary RM. Note that while laser ablation Sr values determined using 50 and 85 µm overlap on another, they are persistently offset from TIMS values. The height of each data point is the 2σ uncertainty.

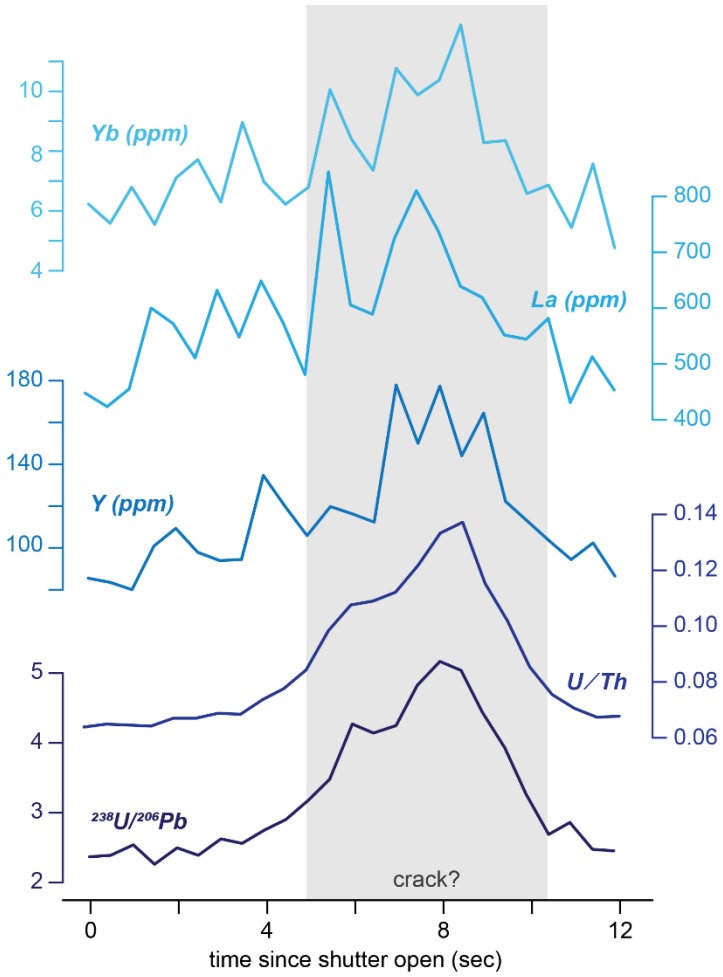

Figure 9. Time-resolved laser ablation split stream profile for a BRZ-1 spot analysis. U-Pb ratios spike at depth, coincident with increases in U/Th, Y, La, and Yb. These spikes indicate the presence of a chemically-distinct domain within the apatite (probably a crack; see Fig. 3). Spot analyses like this deviate from the 2.0 Ga isochron shown in Figure 5.

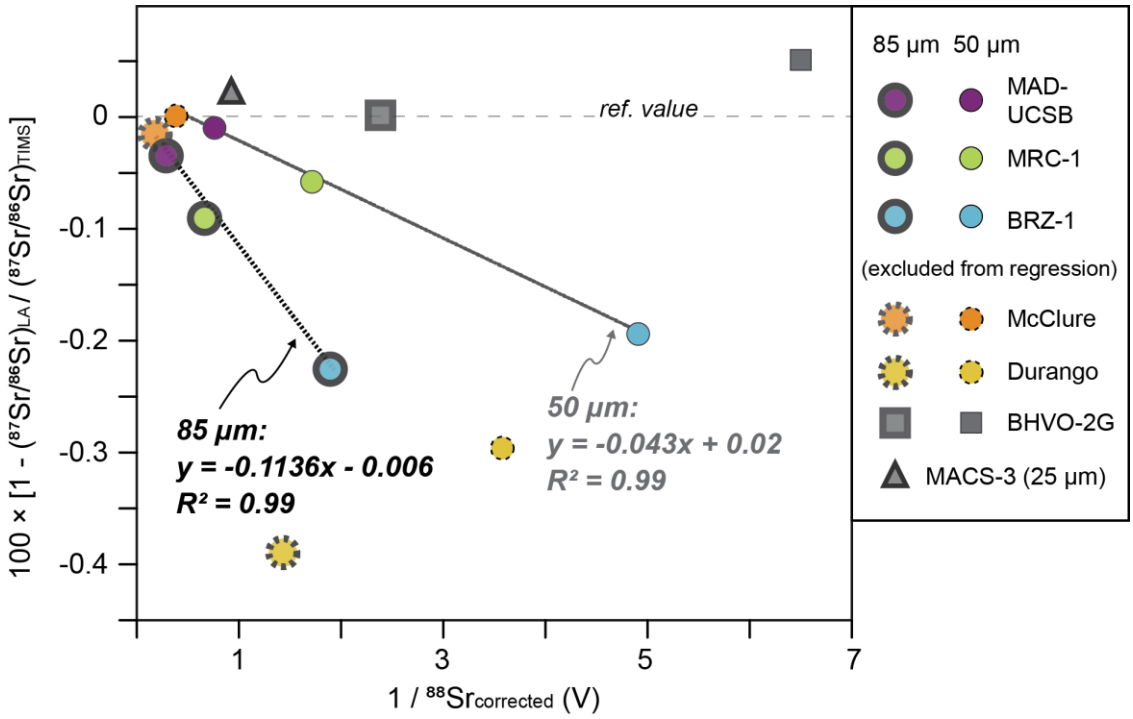

Figure 10. Offset between average $^{87}Sr/^{86}Sr$ ratios determined by LA-ICP-MS and ID-TIMS vs. inverse of interference-corrected ^{88}Sr signal intensity. Data for RMs from this study define a linear anti-correlation trend that could be used to empirically correct $^{87}Sr/^{86}Sr$. Typical 2σ uncertainties are smaller than the size of each symbol. Linear fits do not consider the uncertainty of individual datum.

SUMMARY AND OUTLOOK

The overarching goal of this dissertation was to use U-Pb thermochronology in xenoliths to constrain heat fluxes through the lithosphere and estimate crustal heat production. Chapter I demonstrated that rutile and apatite U-Pb thermochronology of lower-crustal xenoliths tracks variations in the thermal structure of the crust in northern Tanzania. Rutile in lower-crustal granulite xenoliths from the Tanzanian craton retain U-Pb dates as old as 600 Ma; this contrasts with garnet granulite xenoliths from the lower crust of the Mozambique Belt that exclusively yield near-zero age U-Pb isochrons for rutile and apatite. The implied differences in lower-crustal temperature must reflect regional variations in mantle heat flow, which ultimately manifests as higher surface heat flow in the Mozambique Belt relative to the Tanzanian craton. Higher mantle heat flow below the Mozambique Belt could be due to more intense advective heat flow by rifting there. Alternatively, geotherm modeling suggests that conductive heat flow through variable-thickness mantle lithosphere could also explain these results. More germane to the discussion of crustal heat production is the retention of relatively old rutile dates in the xenolith suite erupted on the Tanzanian craton at Labait. The retention of rutile U-Pb dates older than eruption in lower-crustal xenoliths is a feature observed in other cratonic xenolith suites, including the Kaapvaal (Schmitz et al., 2003b); Slave (Davis et al., 2003; Forster et al., 2017), Wyoming (Blackburn et al., 2012), and Superior cratons (Edwards and Blackburn, 2017). This observation is remarkable because it suggests that cratons worldwide—each one with its own unique tectonic history—have generally similar thermal structures. Each suite is characterized by rutile U-Pb dates that range over 100s of millions of years and typically project to the timing of xenolith eruption. These U-Pb age patterns can be interpreted as reflecting slow cooling of the lower crust

through the partial retention zone of Pb in rutile up until eruption or transient re-heating of the lower crust during/prior to eruption. Their distinctions are subtle, but these two endmember scenarios have important ramifications for modeling the thermal structure of the lithosphere. If partial Pb loss in rutile is due to slow cooling, as suggested by Blackburn et al. (2011), this restricts lower-crustal temperatures to a narrow interval of 450–600 °C (depending on grain sizes and cooling rates). If partial Pb loss is instead related to transient heating, the Pb closure temperature of accessory phases provide only a maximum bound on Moho temperature (i.e., they must be cooler than the Pb closure temperature of rutile). In the Labait garnet granulite xenoliths, the lack of any correlation between U-Pb date and trace element concentrations in rutile is consistent with diffusive decoupling of elements with different diffusivities during slow cooling since 600 Ma.

Seeking to interrogate the significance of U-Pb age variability in xenolithic rutile in more detail, Chapter II focused on rutile and apatite from lower-crustal xenoliths from the central Siberian craton. High-spatial resolution laser ablation depth profiling was used to distinguish slow cooling from rapid re-heating: if U-Pb age gradients were related to slow cooling, one would expect gradients of different elements to differ systematically according to their experimentally-determined diffusivities (e.g., Al, Si, Zr, Hf, Nb, Ta, etc.). Rutile depth profiling revealed U-Pb age gradients in the outermost 2–8 μm of individual rutile grains, however, trace-element data collected in tandem with U-Pb data also graded over similar length-scales. These data cannot be reconciled with slow cooling through the partial retention zone over billions of years. Rather, the U-Pb gradients could be explained if the lower crust was heated at 900–1000 °C for <10 Myr during a period of advective heating prior to eruption. Taking this a step further, I conclude that, up until a few Myrs prior to

kimberlite eruption, the deep crust of the Siberian craton resided at temperatures cool enough that Pb was not actively diffusing out of the rutile crystal lattice (i.e., at temperatures below 500 °C since the last thermal perturbation ca. 1.4 Ga; using Pb diffusivities reported in Cherniak et al., 1991, and Cherniak, 2000). Apatite dates as old as 1.4 Ga are also present in the same garnet granulite xenoliths, suggesting cooler temperatures still (i.e., <400 °C). Transient re-heating of the lower crust is a phenomenon well-documented in other xenolith suites (e.g., Smit et al., 2014; Hacker et al., 2000; 2005; Liu et al., 2022) and, as such, the broad range of rutile U-Pb dates observed in other cratonic xenolith suites (including in the Labait xenoliths) could correspond to a brief period of heating prior to eruption. I would argue that this interpretation—that most xenoliths experience a period of transient heating prior to eruption—is more parsimonious than a scenario wherein all cratonic lower crust exhumed slowly through the partial retention zone of Pb at the same rate.

"Seeing through" the effects of pre-eruptive heating reveals that cratonic lower continental crust—even in areas with disparate tectonic histories—is cooler than the Pb closure temperature of rutile, perhaps reflecting the presence of a thick, insulating lithospheric keel beneath most cratons (Carlson, 2005). Ultimately, rutile U-Pb thermochronology provides an upper bound on Moho temperatures beneath cratons, but this is a useful limit. Assuming an average surface heat flow for cratons (~40 mW/m^2), a 40-km-thick crust, and purely conductive heat flow, the 500–600 °C Pb closure temperature for rutile suggests at most 0.85 $\mu W/m^3$ crustal heat production (i.e., consonant with a relatively mafic lower crust or highly HPE-depleted felsic crust; Rudnick and Gao, 2014).

It is also remarkable that the upper bounds imposed by rutile U-Pb thermochronology conform to the cool geothermal gradients suggested by garnet peridotite xenoliths in the

same volcanic hosts (35–50 mW/m^2; Hasterok and Chapman, 2013). Multiple studies have focused on quantifying heat fluxes through the lithosphere using garnet peridotite P-T arrays (i.e., matching geotherms to P-T data assuming various models of mantle flow, surface heat flow and average crustal heat production; Rudnick et al., 2000; Mather et al., 2011; Hasterok and Chapman, 2013), yet such studies tend to neglect the effects of uneven HPE distribution in the crust (often times assuming uniform crustal heat production). The modeling results presented in Chapter II show that varying HPE distribution in the crust alone has a significant effect on the topology of geotherms. Bearing this in mind, a fruitful avenue to explore crustal heat production would be to account for the interplay of other model parameters—surface heat flow, lithosphere thickness, HPE distribution profiles within the crust and mantle lithosphere, and thermobarometer calibrations—in tandem with xenolith P-T-t data (e.g., Mather et al., 2011; Roy and Mareschal, 2011).

Chapter III presented U-Pb, Sm-Nd, and Sr isotopic data for a suite of new reference apatites. The U-Pb measurements made *in situ* on apatite mentioned in the aforementioned studies were only possible with the development of well-characterized reference materials. In particular, homogeneous reference materials are needed to correct robustly for laser-induced (downhole) fractionations during depth profiling (Cottle et al., 2011). This is especially relevant when analyzing apatite, rutile, and titanite, which are phases that can contain variable amounts of common Pb. Thus, the development of high-quality and matrix-matched reference materials lies at the heart of the aforementioned thesis chapters.

REFERENCES

Agashev, A. M., Ionov, D. A., Pokhilenko, N. P., Golovin, A. V., Cherepanova, Y., & Sharygin, I. S. (2013). Metasomatism in lithospheric mantle roots: Constraints from whole-rock and mineral chemical composition of deformed peridotite xenoliths from kimberlite pipe Udachnaya. *Lithos*, *160–161*(1), 201–215. https://doi.org/10.1016/j.lithos.2012.11.014

Ague, J. J., & Baxter, E. F. (2007). Brief thermal pulses during mountain building recorded by Sr diffusion in apatite and multicomponent diffusion in garnet. *Earth and Planetary Science Letters*, *261*(3–4), 500–516. https://doi.org/10.1016/j.epsl.2007.07.017

Alessio, K. L., Hand, M., Kelsey, D. E., Williams, M. A., Morrissey, L. J., & Barovich, K. (2018). Conservation of deep crustal heat production. *Geology*, *46*(4), 335–338. https://doi.org/10.1130/G39970.1

Alexeev, S. V., Alexeeva, L. P., Borisov, V. N., Shouakar-Stash, O., Frape, S. K., Chabaux, F., & Kononov, A. M. (2007). Isotopic composition (H, O, Cl, Sr) of ground brines of the Siberian Platform. *Russian Geology and Geophysics*, *48*(3), 225–236. https://doi.org/10.1016/j.rgg.2007.02.007

Alexeev, S. V., Alexeeva, L. P., & Trifonov, N. S. (2022). Equilibrium-non-equilibrium of the brine-kimberlite system in the Udachnaya pipe, Russia, based on physicochemical modeling. *Applied Geochemistry*, *138*(January), 105219. https://doi.org/10.1016/j.apgeochem.2022.105219

Amelin, Y., & Zaitsev, A. N. (2002). Precise geochronology of phoscorites and carbonatites: The critical role of U-series disequilibrium in age interpretations. *Geochimica et Cosmochimica Acta*, *66*(13), 2399–2419. https://doi.org/10.1016/S0016-7037(02)00831-1

Anderson, J. L., & Smith, D. R. (1995). The effects of temperature and f O2 on the Al-in-hornblende barometer. *American Mineralogist*, *80*(5–6), 549–559. https://doi.org/10.2138/am-1995-5-614

Antoine, C., Bruand, E., Guitreau, M., & Devidal, J. -L. (2020). Understanding Preservation of Primary Signatures in Apatite by Comparing Matrix and Zircon-Hosted Crystals From the Eoarchean Acasta Gneiss Complex (Canada). *Geochemistry, Geophysics, Geosystems*, *21*(7). https://doi.org/10.1029/2020GC008923

Apen, F. E., Rudnick, R. L., Cottle, J. M., Kylander-Clark, A. R. C., Blondes, M. S., Piccoli, P. M., & Seward, G. (2020). Four-dimensional thermal evolution of the East African Orogen: accessory phase petrochronology of crustal profiles through the Tanzanian Craton and Mozambique Belt, northeastern Tanzania. *Contributions to Mineralogy and Petrology*, *175*(11), 97. https://doi.org/10.1007/s00410-020-01737-6

Apen, F. E., Wall, C. J., Cottle, J. M., Schmitz, M. D., Kylander-Clark, A. R. C., & Seward, G. G. E. (2022). Apatites for destruction: Reference apatites from Morocco and Brazil for U-Pb petrochronology and Nd and Sr isotope geochemistry. *Chemical Geology*, *590*(December 2021), 120689. https://doi.org/10.1016/j.chemgeo.2021.120689

Appel, P., Möller*, A., & Schenk, V. (1998). High-pressure granulite facies metamorphism in the Pan-African belt of eastern Tanzania: P–T–t evidence against granulite formation by continent collision. *Journal of Metamorphic Geology*, *16*(4), 491–509. https://doi.org/10.1111/j.1525-1314.1998.00150.x

Aulbach, S., Rudnick, R. L., & McDonough, W. F. (2008). Li-Sr-Nd isotope signatures of the plume and cratonic lithospheric mantle beneath the margin of the rifted Tanzanian craton (Labait). *Contributions to Mineralogy and Petrology*, *155*(1), 79–92. https://doi.org/10.1007/s00410-007-0226-4

Aulbach, S., Rudnick, R. L., & McDonough, W. F. (2011). Evolution of the lithospheric mantle beneath the East African Rift in Tanzania and its potential signatures in rift magmas. *Special Paper of the Geological Society of America*, *478*(June), 105–125. https://doi.org/10.1130/2011.2478(06)

Barfod, G. H., Krogstad, E. J., Frei, R., & Albarède, F. (2005). Lu-Hf and PbSL geochronology of apatites from Proterozoic terranes: A first look at Lu-Hf isotopic closure in metamorphic apatite. *Geochimica et Cosmochimica Acta*, *69*(7), 1847–1859. https://doi.org/10.1016/j.gca.2004.09.014

Bea, F. (1996). Residence of REE, Y, Th and U in Granites and Crustal Protoliths; Implications for the Chemistry of Crustal Melts. *Journal of Petrology*, *37*(3), 521–552. https://doi.org/10.1093/petrology/37.3.521

Bellucci, J. J., McDonough, W. F., & Rudnick, R. L. (2011). Thermal history and origin of the Tanzanian Craton from Pb isotope thermochronology of feldspars from lower crustal xenoliths. *Earth and Planetary Science Letters*, *301*(3–4), 493–501. https://doi.org/10.1016/j.epsl.2010.11.031

Belousova, E. A., Griffin, W. L., O'Reilly, S. Y., & Fisher, N. I. (2002). Apatite as an indicator mineral for mineral exploration: trace-element compositions and their relationship to host rock type. *Journal of Geochemical Exploration*, *76*(1), 45–69. https://doi.org/10.1016/S0375-6742(02)00204-2

Bingen, B., Demaiffe, D., & Hertogen, J. (1996). Redistribution of rare earth elements, thorium, and uranium over accessory minerals in the course of amphibolite to granulite facies metamorphism: The role of apatite and monazite in orthogneisses from southwestern Norway. *Geochimica et Cosmochimica Acta*, *60*(8), 1341–1354. https://doi.org/10.1016/0016-7037(96)00006-3

Birch, A. F. (1948). The effects of Pleistocene climatic variations upon geothermal gradients. *American Journal of Science*, *246*(12), 729–760. https://doi.org/10.2475/ajs.246.12.729

Bizzarro, M., Simonetti, A., Stevenson, R. K., & Kurszlaukis, S. (2003). In situ 87Sr/86Sr investigation of igneous apatites and carbonates using laser-ablation MC-ICP-MS. *Geochimica et Cosmochimica Acta*, *67*(2), 289–302. https://doi.org/10.1016/S0016-7037(02)01048-7

Blackburn, T., Bowring, S. A., Schoene, B., Mahan, K., & Dudas, F. (2011). U-Pb thermochronology: creating a temporal record of lithosphere thermal evolution.

Contributions to Mineralogy and Petrology, *162*(3), 479–500. https://doi.org/10.1007/s00410-011-0607-6

Blackburn, T. J., Bowring, S. A., Perron, J. T., Mahan, K. H., Dudas, F. O., & Barnhart, K. R. (2012). An Exhumation History of Continents over Billion-Year Time Scales. *Science*, *335*(6064), 73–76. https://doi.org/10.1126/science.1213496

Bohlen, S. R., & Mezger, K. (1989). Origin of granulite terranes and the formation of the lowermost continental crust. *Science*, *244*(4902), 326–329. https://doi.org/10.1126/science.244.4902.326

Bonamici, C. E., Fanning, C. M., Kozdon, R., Fournelle, J. H., & Valley, J. W. (2015). Combined oxygen-isotope and U-Pb zoning studies of titanite: New criteria for age preservation. *Chemical Geology*, *398*, 70–84. https://doi.org/10.1016/j.chemgeo.2015.02.002

Bouvier, A., Vervoort, J. D., & Patchett, P. J. (2008). The Lu-Hf and Sm-Nd isotopic composition of CHUR: Constraints from unequilibrated chondrites and implications for the bulk composition of terrestrial planets. *Earth and Planetary Science Letters*, *273*(1–2), 48–57. https://doi.org/10.1016/j.epsl.2008.06.010

Boyd, F. R., Pokhilenko, N. P., Pearson, D. G., Mertzman, S. A., Sobolev, N. V., & Finger, L. W. (1997). Composition of the Siberian cratonic mantle: evidence from Udachnaya peridotite xenoliths. *Contributions to Mineralogy and Petrology*, *128*(2–3), 228–246. https://doi.org/10.1007/s004100050305

Brey, G. P., & K Hler, T. (1990). Geothermobarometry in Four-phase Lherzolites II. New Thermobarometers, and Practical Assessment of Existing Thermobarometers. *Journal of Petrology*, *31*(6), 1353–1378. https://doi.org/10.1093/petrology/31.6.1353

Bruand, E., Fowler, M., Storey, C., Laurent, O., Antoine, C., Guitreau, M., et al. (2020). Accessory mineral constraints on crustal evolution: elemental fingerprints for magma discrimination. *Geochemical Perspectives Letters*, *13*, 7–12. https://doi.org/10.7185/geochemlet.2006

Bruand, Emilie, Fowler, M., Storey, C., & Darling, J. (2017). Apatite trace element and isotope applications to petrogenesis and provenance. *American Mineralogist*, *102*(1), 75–84. https://doi.org/10.2138/am-2017-5744

Burton, K. W., Schiano, P., Birck, J.-L., Allègre, C. J., Rehkämper, M., Halliday, A. N., & Dawson, J. B. (2000). The distribution and behaviour of rhenium and osmium amongst mantle minerals and the age of the lithospheric mantle beneath Tanzania. *Earth and Planetary Science Letters*, *183*(1–2), 93–106. https://doi.org/10.1016/S0012-821X(00)00259-4

Canil, D., O'Neill, H. S. C., Pearson, D. G., Rudnick, R. L., McDonough, W. F., & Carswell, D. A. (1994). Ferric iron in peridotites and mantle oxidation states. *Earth and Planetary Science Letters*, *123*(1–3), 205–220. https://doi.org/10.1016/0012-821X(94)90268-2

Carlson, R. W., Pearson, D. G., & James, D. E. (2005). Physical, chemical, and

chronological characteristics of continental mantle. *Reviews of Geophysics*, *43*(1), 1–24. https://doi.org/10.1029/2004RG000156

Carrapa, B., DeCelles, P. G., Reiners, P. W., Gehrels, G. E., & Sudo, M. (2009). Apatite triple dating and white mica 40Ar/39Ar thermochronology of syntectonic detritus in the Central Andes: A multiphase tectonothermal history. *Geology*, *37*(5), 407–410. https://doi.org/10.1130/G25698A.1

Catanzaro, E. J., Murphy, T. J., Shields, W. R., & Garner, E. L. (1968). Absolute isotopic abundance ratios of common, equal-atom, and radiogenic lead isotopic standards. *Journal of Research of the National Bureau of Standards Section A: Physics and Chemistry*, *72A*(3), 261. https://doi.org/10.6028/jres.072A.025

Chamberlain, K. R., & Bowring, S. A. (2001). Apatite–feldspar U–Pb thermochronometer: a reliable, mid-range (~450°C), diffusion-controlled system. *Chemical Geology*, *172*(1–2), 173–200. https://doi.org/10.1016/S0009-2541(00)00242-4

Chambers, J. A., & Kohn, M. J. (2012). Titanium in muscovite, biotite, and hornblende: Modeling, thermometry, and rutile activities of metapelites and amphibolites. *American Mineralogist*, *97*(4), 543–555. https://doi.org/10.2138/am.2012.3890

Cherepanova, Y., Artemieva, I. M., Thybo, H., & Chemia, Z. (2013). Crustal structure of the Siberian craton and the West Siberian basin: An appraisal of existing seismic data. *Tectonophysics*, *609*, 154–183. https://doi.org/10.1016/j.tecto.2013.05.004

Cherniak, D. J. (2000). Pb diffusion in rutile. *Contributions to Mineralogy and Petrology*, *139*(2), 198–207. https://doi.org/10.1007/PL00007671

Cherniak, D. J. (2006). Zr diffusion in titanite. *Contributions to Mineralogy and Petrology*, *152*(5), 639–647. https://doi.org/10.1007/s00410-006-0133-0

Cherniak, D. J. (2010). Diffusion in Accessory Minerals: Zircon, Titanite, Apatite, Monazite and Xenotime. *Reviews in Mineralogy and Geochemistry*, *72*(1), 827–869. https://doi.org/10.2138/rmg.2010.72.18

Cherniak, D. J., Lanford, W. A., & Ryerson, F. J. (1991). Lead diffusion in apatite and zircon using ion implantation and Rutherford Backscattering techniques. *Geochimica et Cosmochimica Acta*, *55*(6), 1663–1673. https://doi.org/10.1016/0016-7037(91)90137-T

Cherniak, D.J. (1993). Lead diffusion in titanite and preliminary results on the effects of radiation damage on Pb transport. *Chemical Geology*, *110*(1–3), 177–194. https://doi.org/10.1016/0009-2541(93)90253-F

Cherniak, D.J. (1995). Sr and Nd diffusion in titanite. *Chemical Geology*, *125*(3–4), 219–232. https://doi.org/10.1016/0009-2541(95)00074-V

Cherniak, D.J., Manchester, J., & Watson, E. B. (2007). Zr and Hf diffusion in rutile. *Earth and Planetary Science Letters*, *261*(1–2), 267–279. https://doi.org/10.1016/j.epsl.2007.06.027

Cherniak, Daniele J., & Watson, E. B. (2019). Al and Si diffusion in rutile. *American Mineralogist*, *104*(11), 1638–1649. https://doi.org/10.2138/am-2019-7030

Chesley, J. T., Rudnick, R. L., & Lee, C.-T. (1999). Re-Os systematics of mantle xenoliths from the East African Rift: age, structure, and history of the Tanzanian craton. *Geochimica et Cosmochimica Acta*, *63*(7–8), 1203–1217. https://doi.org/10.1016/S0016-7037(99)00004-6

Chew, D.M., Petrus, J. A., & Kamber, B. S. (2014). U–Pb LA–ICPMS dating using accessory mineral standards with variable common Pb. *Chemical Geology*, *363*, 185–199. https://doi.org/10.1016/j.chemgeo.2013.11.006

Chew, David M., Sylvester, P. J., & Tubrett, M. N. (2011). U–Pb and Th–Pb dating of apatite by LA-ICPMS. *Chemical Geology*, *280*(1–2), 200–216. https://doi.org/10.1016/j.chemgeo.2010.11.010

Chew, David M., Donelick, R. A., Donelick, M. B., Kamber, B. S., & Stock, M. J. (2014). Apatite Chlorine Concentration Measurements by LA-ICP-MS. *Geostandards and Geoanalytical Research*, *38*(1), 23–35. https://doi.org/10.1111/j.1751-908X.2013.00246.x

Chew, David M., Babechuk, M. G., Cogné, N., Mark, C., O'Sullivan, G. J., Henrichs, I. A., et al. (2016). (LA,Q)-ICPMS trace-element analyses of Durango and McClure Mountain apatite and implications for making natural LA-ICPMS mineral standards. *Chemical Geology*, *435*, 35–48. https://doi.org/10.1016/j.chemgeo.2016.03.028

Chew, David M., Petrus, J. A., Kenny, G. G., & McEvoy, N. (2017). Rapid high-resolution U–Pb LA-Q-ICPMS age mapping of zircon. *Journal of Analytical Atomic Spectrometry*, *32*(2), 262–276. https://doi.org/10.1039/C6JA00404K

Chin, E. J. (2018). Deep crustal cumulates reflect patterns of continental rift volcanism beneath Tanzania. *Contributions to Mineralogy and Petrology*, *173*(10), 85. https://doi.org/10.1007/s00410-018-1512-z

Christensen, N. I., & Mooney, W. D. (1995). Seismic velocity structure and composition of the continental crust: a global view. *Journal of Geophysical Research*, *100*(B6), 9761–9788. https://doi.org/10.1029/95JB00259

Clark, C., Taylor, R. J. M., Johnson, T. E., Harley, S. L., Fitzsimons, I. C. W., & Oliver, L. (2019). Testing the fidelity of thermometers at ultrahigh temperatures. *Journal of Metamorphic Geology*, *37*(7), 917–934. https://doi.org/10.1111/jmg.12486

Cochrane, R., Spikings, R. A., Chew, D., Wotzlaw, J.-F., Chiaradia, M., Tyrrell, S., et al. (2014). High temperature (>350°C) thermochronology and mechanisms of Pb loss in apatite. *Geochimica et Cosmochimica Acta*, *127*, 39–56. https://doi.org/10.1016/j.gca.2013.11.028

Cohen, R. S., O'Nions, R. K., & Dawson, J. B. (1984). Isotope geochemistry of xenoliths from East Africa: Implications for development of mantle reservoirs and their interaction. *Earth and Planetary Science Letters*, *68*(2), 209–220. https://doi.org/10.1016/0012-821X(84)90153-5

Condie, K. C., & Selverstone, J. (1999). The crust of the Colorado Plateau: New views of an old arc. *Journal of Geology*, *107*(4), 387–397. https://doi.org/10.1086/314363

Condon, D. J., Schoene, B., McLean, N. M., Bowring, S. A., & Parrish, R. R. (2015). Metrology and traceability of U–Pb isotope dilution geochronology (EARTHTIME Tracer Calibration Part I). *Geochimica et Cosmochimica Acta*, *164*, 464–480. https://doi.org/10.1016/j.gca.2015.05.026

Coolen, J. J. M. M. ., Priem, H. N. ., Verdurmen, E. A. T., & Verschure, R. . (1982). Possible zircon U-Pb evidence for Pan-African granulite-facies metamorphism in the Mozambique belt of southern Tanzania. *Precambrian Research*, *17*(1), 31–40. https://doi.org/10.1016/0301-9268(82)90152-8

Corfu, F., Hanchar, J. M., Hoskin, P. W. O., & Kinny, P. D. (2003). Atlas of Zircon Textures. *Reviews in Mineralogy and Geochemistry*, *53*(1), 469–500. https://doi.org/10.2113/0530469

Cottle, J. M., Horstwood, M. S. A., & Parrish, R. R. (2009). A new approach to single shot laser ablation analysis and its application to in situ Pb/U geochronology. *Journal of Analytical Atomic Spectrometry*, *24*(10), 1355. https://doi.org/10.1039/b821899d

Cottle, John M., Jessup, M. J., Newell, D. L., Horstwood, M. S. A., Noble, S. R., Parrish, R. R., et al. (2009). Geochronology of granulitized eclogite from the Ama Drime Massif: Implications for the tectonic evolution of the South Tibetan Himalaya. *Tectonics*, *28*(1), n/a-n/a. https://doi.org/10.1029/2008TC002256

Coulson, I. M., Villeneuve, M. E., Dipple, G. M., Duncan, R. A., Russell, J. K., & Mortensen, J. K. (2002). Time-scales of assembly and thermal history of a composite felsic pluton: Constraints from the Emerald Lake area, northern Canadian Cordillera, Yukon. *Journal of Volcanology and Geothermal Research*, *114*(3–4), 331–356. https://doi.org/10.1016/S0377-0273(01)00294-3

Cutten, H., Johnson, S. P., & Waele, B. De. (2006). Protolith Ages and Timing of Metasomatism Related to the Formation of Whiteschists at Mautia Hill, Tanzania: Implications for the Assembly of Gondwana. *The Journal of Geology*, *114*(6), 683–698. https://doi.org/10.1086/507614

Davis, W. J. (1997). U-Pb zircon and rutile ages from granulite xenoliths in the Slave province: Evidence for mafic magmatism in the lower crust coincident with Proterozoic dike swarms. *Geology*, *25*(4), 343. https://doi.org/10.1130/0091-7613(1997)025<0343:UPZARA>2.3.CO;2

Davis, W. J., Canil, D., MacKenzie, J. M., & Carbno, G. B. (2003). Petrology and U–Pb geochronology of lower crustal xenoliths and the development of a craton, Slave Province, Canada. *Lithos*, *71*(2–4), 541–573. https://doi.org/10.1016/S0024-4937(03)00130-0

Dawson, J. B. (1992). Neogene tectonics and volcanicity in the North Tanzania sector of the Gregory Rift Valley: contrasts with the Kenya sector. *Tectonophysics*, *204*(1–2). https://doi.org/10.1016/0040-1951(92)90271-7

Dawson, J. B. (2002). Metasomatism and Partial Melting in Upper-Mantle Peridotite Xenoliths from the Lashaine Volcano, Northern Tanzania. *Journal of Petrology*, *43*(9), 1749–1777. https://doi.org/10.1093/petrology/43.9.1749

Dawson, J. B., & Smith, J. V. (1988). Metasomatised and veined upper-mantle xenoliths from Pello Hill, Tanzania: evidence for anomalously-light mantle beneath the Tanzanian sector of the East African Rift Valley. *Contributions to Mineralogy and Petrology*, *100*(4), 510–527. https://doi.org/10.1007/BF00371380

Dawson, J. B., & Smith, J. V. (1992). Olivine-mica pyroxenite xenoliths from northern Tanzania: metasomatic products of upper-mantle peridotite. *Journal of Volcanology and Geothermal Research*, *50*(1–2), 131–142. https://doi.org/10.1016/0377-0273(92)90041-B

Dawson, J. B., Powell, D. G., & Reid, A. M. (1970). Ultrabasic xenoliths and lava from the lashaine Volcano, Northern Tanzania. *Journal of Petrology*, *11*(3), 519–548. https://doi.org/10.1093/petrology/11.3.519

Day, H. W. (2012). A revised diamond-graphite transition curve. *American Mineralogist*, *97*(1), 52–62. https://doi.org/10.2138/am.2011.3763

Dodson, M. H. (1973). Closure temperature in cooling geochronological and petrological systems. *Contributions to Mineralogy and Petrology*, *40*, 259–274.

Donskaya, T. V. (2020). Assembly of the Siberian Craton: Constraints from Paleoproterozoic granitoids. *Precambrian Research*, *348*(July), 105869. https://doi.org/10.1016/j.precamres.2020.105869

Doucet, L.S., Ionov, D. A., Golovin, A. V., & Pokhilenko, N. P. (2012). Depth, degrees and tectonic settings of mantle melting during craton formation: inferences from major and trace element compositions of spinel harzburgite xenoliths from the Udachnaya kimberlite, central Siberia. *Earth and Planetary Science Letters*, *359–360*, 206–218. https://doi.org/10.1016/j.epsl.2012.10.001

Doucet, Luc S., Peslier, A. H., Ionov, D. A., Brandon, A. D., Golovin, A. V., Goncharov, A. G., & Ashchepkov, I. V. (2014). High water contents in the Siberian cratonic mantle linked to metasomatism: An FTIR study of Udachnaya peridotite xenoliths. *Geochimica et Cosmochimica Acta*, *137*, 159–187. https://doi.org/10.1016/j.gca.2014.04.011

Dubois, J. C., Retali, G., & Cesario, J. (1992). Isotopic analysis of rare earth elements by total vaporization of samples in thermal ionization mass spectrometry. *International Journal of Mass Spectrometry and Ion Processes*, *120*(3), 163–177. https://doi.org/10.1016/0168-1176(92)85046-3

Ebinger, C. J. (1989). Tectonic development of the western branch of the East African rift system. *Geological Society of America Bulletin*, *101*(7), 885–903. https://doi.org/10.1130/0016-7606(1989)101<0885:TDOTWB>2.3.CO;2

Edwards, G. H., & Blackburn, T. (2018). Detecting the extent of ca. 1.1 Ga Midcontinent Rift plume heating using U-Pb thermochronology of the lower crust. *Geology*, *46*(10), 911–914. https://doi.org/10.1130/G45150.1

Elburg, M., Vroon, P., van der Wagt, B., & Tchalikian, A. (2005). Sr and Pb isotopic composition of five USGS glasses (BHVO-2G, BIR-1G, BCR-2G, TB-1G, NKT-1G).

Chemical Geology, *223*(4), 196–207. https://doi.org/10.1016/j.chemgeo.2005.07.001

Emo, R. B., Smit, M. A., Schmitt, M., Kooijman, E., Scherer, E. E., Sprung, P., et al. (2018). Evidence for evolved Hadean crust from Sr isotopes in apatite within Eoarchean zircon from the Acasta Gneiss Complex. *Geochimica et Cosmochimica Acta*, *235*(2018), 450–462. https://doi.org/10.1016/j.gca.2018.05.028

Ernst, W. G., & Liu, J. (1998). Experimental phase-equilibrium study of Al- and Ti-contents of calcic amphibole in MORB; a semiquantitative thermobarometer. *American Mineralogist*, *83*(9–10), 952–969. https://doi.org/10.2138/am-1998-9-1004

Ewing, T. A., Hermann, J., & Rubatto, D. (2013). The robustness of the Zr-in-rutile and Ti-in-zircon thermometers during high-temperature metamorphism (Ivrea-Verbano Zone, northern Italy). *Contributions to Mineralogy and Petrology*, *165*(4), 757–779. https://doi.org/10.1007/s00410-012-0834-5

Ewing, T. A., Rubatto, D., Beltrando, M., & Hermann, J. (2015). Constraints on the thermal evolution of the Adriatic margin during Jurassic continental break-up: U–Pb dating of rutile from the Ivrea–Verbano Zone, Italy. *Contributions to Mineralogy and Petrology*, *169*(4). https://doi.org/10.1007/s00410-015-1135-6

Ferry, J. M., & Watson, E. B. (2007). New thermodynamic models and revised calibrations for the Ti-in-zircon and Zr-in-rutile thermometers. *Contributions to Mineralogy and Petrology*, *154*(4), 429–437. https://doi.org/10.1007/s00410-007-0201-0

Fisher, C. M., McFarlane, C. R. M., Hanchar, J. M., Schmitz, M. D., Sylvester, P. J., Lam, R., & Longerich, H. P. (2011). Sm–Nd isotope systematics by laser ablation-multicollector-inductively coupled plasma mass spectrometry: Methods and potential natural and synthetic reference materials. *Chemical Geology*, *284*(1–2), 1–20. https://doi.org/10.1016/j.chemgeo.2011.01.012

Fisher, C. M., Bauer, A. M., & Vervoort, J. D. (2020). Disturbances in the Sm–Nd isotope system of the Acasta Gneiss Complex—Implications for the Nd isotope record of the early Earth. *Earth and Planetary Science Letters*, *530*, 115900. https://doi.org/10.1016/j.epsl.2019.115900

Fisher, C. M., Bauer, A. M., Luo, Y., Sarkar, C., Hanchar, J. M., Vervoort, J. D., et al. (2020). Laser ablation split-stream analysis of the Sm-Nd and U-Pb isotope compositions of monazite, titanite, and apatite – Improvements, potential reference materials, and application to the Archean Saglek Block gneisses. *Chemical Geology*, *539*(February), 119493. https://doi.org/10.1016/j.chemgeo.2020.119493

Forshaw, J. B., Waters, D. J., Pattison, D. R. M., Palin, R. M., & Gopon, P. (2019). A comparison of observed and thermodynamically predicted phase equilibria and mineral compositions in mafic granulites. *Journal of Metamorphic Geology*, *37*(2), 153–179. https://doi.org/10.1111/jmg.12454

Foster, A., Ebinger, C., Mbede, E., & Rex, D. (1997). Tectonic development of the northern Tanzanian sector of the East African Rift System. *Journal of the Geological Society*, *154*(4), 689–700. https://doi.org/10.1144/gsjgs.154.4.0689

Fritz, H., Abdelsalam, M., Ali, K. A., Bingen, B., Collins, A. S., Fowler, A. R., et al. (2013). Orogen styles in the East African Orogen: A review of the Neoproterozoic to Cambrian tectonic evolution. *Journal of African Earth Sciences*, *86*, 65–106. https://doi.org/10.1016/j.jafrearsci.2013.06.004

Fritz, Harald, Tenczer, V., Hauzenberger, C. A., Wallbrecher, E., Hoinkes, G., Muhongo, S., & Mogessie, A. (2005). Central Tanzanian tectonic map: A step forward to decipher proterozoic structural events in the East African Orogen. *Tectonics*, *24*(6). https://doi.org/10.1029/2005TC001796

Fritz, Harald, Tenczer, V., Hauzenberger, C., Wallbrecher, E., & Muhongo, S. (2009). Hot granulite nappes - Tectonic styles and thermal evolution of the Proterozoic granulite belts in East Africa. *Tectonophysics*, *477*(3–4), 160–173. https://doi.org/10.1016/j.tecto.2009.01.021

Frost, B. R., Chamberlain, K. R., & Schumacher, J. C. (2001). Sphene (titanite): phase relations and role as a geochronometer. *Chemical Geology*, *172*(1–2), 131–148. https://doi.org/10.1016/S0009-2541(00)00240-0

Fuchs, S., Norden, B., & Commission, I. H. F. (2021). The Global Heat Flow Database: Release 2021. https://doi.org/https://doi.org/10.5880/fidgeo.2021.014

Fuhrman, M. L., & Lindsley, D. H. (1988). Ternary-feldspar modeling and thermometry. *American Mineralogist*, *73*, 201–215.

Furlong, K. P., & Chapman, D. S. (2013). Heat Flow, Heat Generation, and the Thermal State of the Lithosphere. *Annual Review of Earth and Planetary Sciences*, *41*(1), 385–410. https://doi.org/10.1146/annurev.earth.031208.100051

Le Gall, B., Nonnotte, P., Rolet, J., Benoit, M., Guillou, H., Mousseau-Nonnotte, M., et al. (2008). Rift propagation at craton margin. Distribution of faulting and volcanism in the North Tanzanian Divergence (East Africa) during Neogene times. *Tectonophysics*, *448*(1–4), 1–19. https://doi.org/10.1016/j.tecto.2007.11.005

Le Gall, Bernard, Gernigon, L., Rolet, J., Ebinger, C., Gloaguen, R., Nilsen, O., et al. (2004). Neogene-Holocene rift propagation in central Tanzania: Morphostructural and aeromagnetic evidence from the Kilombero area. *Bulletin of the Geological Society of America*, *116*(3–4), 490–510. https://doi.org/10.1130/B25202.1

Gao, S., Luo, T. C., Zhang, B. R., Zhang, H. F., Han, Y. W., Zhao, Z. D., & Hu, Y. K. (1998). Chemical composition of the continental crust as revealed by studies in east China. *Geochimica et Cosmochimica Acta*, *62*(11), 1959–1975. https://doi.org/10.1016/S0016-7037(98)00121-5

Garber, J. M., Hacker, B. R., Kylander-Clark, A. R. C., Stearns, M., & Seward, G. (2017). Controls on Trace Element Uptake in Metamorphic Titanite: Implications for Petrochronology. *Journal of Petrology*, *58*(6), 1031–1057. https://doi.org/10.1093/petrology/egx046

Garber, Joshua M., Maurya, S., Hernandez, J., Duncan, M. S., Zeng, L., Zhang, H. L., et al. (2018). Multidisciplinary Constraints on the Abundance of Diamond and Eclogite in

the Cratonic Lithosphere. *Geochemistry, Geophysics, Geosystems*, *19*(7), 2062–2086. https://doi.org/10.1029/2018GC007534

Garber, Joshua M., Smye, A. J., Feineman, M. D., Kylander-Clark, A. R. C., & Matthews, S. (2020). Decoupling of zircon U–Pb and trace-element systematics driven by U diffusion in eclogite-facies zircon (Monviso meta-ophiolite, W. Alps). *Contributions to Mineralogy and Petrology*, *175*(6), 1–25. https://doi.org/10.1007/s00410-020-01692-2

Gehrels, G. E., Valencia, V. A., & Ruiz, J. (2008). Enhanced precision, accuracy, efficiency, and spatial resolution of U-Pb ages by laser ablation-multicollector-inductively coupled plasma-mass spectrometry. *Geochemistry, Geophysics, Geosystems*, *9*(3), n/a-n/a. https://doi.org/10.1029/2007GC001805

Gerstenberger, H., & Haase, G. (1997). A highly effective emitter substance for mass spectrometric Pb isotope ratio determinations. *Chemical Geology*, *136*(3–4), 309–312. https://doi.org/10.1016/S0009-2541(96)00033-2

Gillespie, J., Kinny, P. D., Kirkland, C. L., Martin, L., Nemchin, A. A., Cavosie, A. J., & Hasterok, D. (2021). Isotopic modelling of Archean crustal evolution from comagmatic zircon–apatite pairs. *Earth and Planetary Science Letters*, *575*, 117194. https://doi.org/10.1016/j.epsl.2021.117194

Gillespie, J., Nemchin, A. A., Kinny, P. D., Martin, L., Aleshin, M., Roberts, M. P., et al. (2021). Strontium isotope analysis of apatite via SIMS. *Chemical Geology*, *559*(August 2020), 119979. https://doi.org/10.1016/j.chemgeo.2020.119979

Gladkochub, D. P., Donskaya, T. V., Ernst, R., Mazukabzov, A. M., Sklyarov, E. V., Pisarevsky, S. A., et al. (2012). Proterozoic basic magmatism of the Siberian Craton: Main stages and their geodynamic interpretation. *Geotectonics*, *46*(4), 273–284. https://doi.org/10.1134/S0016852112040024

Glorie, S., Jepson, G., Konopelko, D., Mirkamalov, R., Meeuws, F., Gilbert, S., et al. (2019). Thermochronological and geochemical footprints of post-orogenic fluid alteration recorded in apatite: Implications for mineralisation in the Uzbek Tian Shan. *Gondwana Research*, *71*, 1–15. https://doi.org/10.1016/j.gr.2019.01.011

Goes, S., Hasterok, D., Schutt, D. L., & Klöcking, M. (2020). Continental lithospheric temperatures: A review. *Physics of the Earth and Planetary Interiors*, *306*(May), 106509. https://doi.org/10.1016/j.pepi.2020.106509

Le Goff, E., Deschamps, Y., & Guerrot, C. (2010). Tectonic implications of new single zircon Pb-Pb evaporation data in the Lossogonoi and Longido ruby-districts, Mozambican metamorphic Belt of north-eastern Tanzania. *Comptes Rendus - Geoscience*, *342*(1), 36–45. https://doi.org/10.1016/j.crte.2009.10.003

Golovin, A. V., Sharygin, I. S., Kamenetsky, V. S., Korsakov, A. V., & Yaxley, G. M. (2018). Alkali-carbonate melts from the base of cratonic lithospheric mantle: Links to kimberlites. *Chemical Geology*, *483*(February), 261–274. https://doi.org/10.1016/j.chemgeo.2018.02.016

Golovin, A. V., Sharygin, I. S., Korsakov, A. V., Kamenetsky, V. S., & Abersteiner, A.

(2020). Can primitive kimberlite melts be alkali-carbonate liquids: Composition of the melt snapshots preserved in deepest mantle xenoliths. *Journal of Raman Spectroscopy*, *51*(9), 1849–1867. https://doi.org/10.1002/jrs.5701

Goncharov, A. G., Ionov, D. A., Doucet, L. S., & Pokhilenko, L. N. (2012). Thermal state, oxygen fugacity and C□O□H fluid speciation in cratonic lithospheric mantle: New data on peridotite xenoliths from the Udachnaya kimberlite, Siberia. *Earth and Planetary Science Letters*, *357–358*, 99–110. https://doi.org/10.1016/j.epsl.2012.09.016

Green, E. C. R., White, R. W., Diener, J. F. A., Powell, R., Holland, T. J. B., & Palin, R. M. (2016). Activity-composition relations for the calculation of partial melting equilibria in metabasic rocks. *Journal of Metamorphic Geology*, *34*(9), 845–869. https://doi.org/10.1111/jmg.12211

Griffin, W. ., Ryan, C. ., Kaminsky, F. ., O'Reilly, S. Y., Natapov, L. ., Win, T. ., et al. (1999). The Siberian lithosphere traverse: mantle terranes and the assembly of the Siberian Craton. *Tectonophysics*, *310*(1–4), 1–35. https://doi.org/10.1016/S0040-1951(99)00156-0

Gruber, B., Chacko, T., Pearson, D. G., Currie, C., & Menzies, A. (2021). Heat production and moho temperatures in cratonic crust: evidence from lower crustal xenoliths from the slave craton. *Lithos*, *380–381*, 105889. https://doi.org/10.1016/j.lithos.2020.105889

Hacker, B., Luffi, P., Lutkov, V., Minaev, V., Ratschbacher, L., Plank, T., et al. (2005). Near-Ultrahigh Pressure Processing of Continental Crust: Miocene Crustal Xenoliths from the Pamir. *Journal of Petrology*, *46*(8), 1661–1687. https://doi.org/10.1093/petrology/egi030

Hacker, B. R., Gnos, E., Ratschbacher, L., Grove, M., McWilliams, M., Sobolev, S. V., et al. (2000). Hot and Dry Deep Crustal Xenoliths from Tibet. *Science*, *287*(5462), 2463–2466. https://doi.org/10.1126/science.287.5462.2463

Hacker, B. R., Kelemen, P. B., & Behn, M. D. (2015). Continental Lower Crust. *Annual Review of Earth and Planetary Sciences*, *43*(1), 167–205. https://doi.org/10.1146/annurev-earth-050212-124117

Hammerli, J., Kemp, A. I. S., & Whitehouse, M. J. (2019). In situ trace element and Sm-Nd isotope analysis of accessory minerals in an Eoarchean tonalitic gneiss from Greenland: Implications for Hf and Nd isotope decoupling in Earth's ancient rocks. *Chemical Geology*, *524*(March), 394–405. https://doi.org/10.1016/j.chemgeo.2019.06.025

Harley, S. L. (1989). The origins of granulites: a metamorphic perspective. *Geological Magazine*, *126*(3), 215–247. https://doi.org/10.1017/S0016756800022330

Harlov, D. E., Wirth, R., & Förster, H.-J. (2005). An experimental study of dissolution–reprecipitation in fluorapatite: fluid infiltration and the formation of monazite. *Contributions to Mineralogy and Petrology*, *150*(3), 268–286. https://doi.org/10.1007/s00410-005-0017-8

Hasterok, D., & Chapman, D. S. (2011). Heat production and geotherms for the continental lithosphere. *Earth and Planetary Science Letters*, *307*(1–2), 59–70.

https://doi.org/10.1016/j.epsl.2011.04.034

Hauzenberger, C. A., Sommer, H., Fritz, H., Bauernhofer, A., Kröner, A., Hoinkes, G., et al. (2007). SHRIMP U–Pb zircon and Sm–Nd garnet ages from the granulite-facies basement of SE Kenya: evidence for Neoproterozoic polycyclic assembly of the Mozambique Belt. *Journal of the Geological Society*, *164*(1), 189–201. https://doi.org/10.1144/0016-76492005-081

Hayden, L. A., Watson, E. B., & Wark, D. A. (2008). A thermobarometer for sphene (titanite). *Contributions to Mineralogy and Petrology*, *155*(4), 529–540. https://doi.org/10.1007/s00410-007-0256-y

Henderson, A. L., Foster, G. L., & Najman, Y. (2010). Testing the application of in situ Sm–Nd isotopic analysis on detrital apatites: A provenance tool for constraining the timing of India–Eurasia collision. *Earth and Planetary Science Letters*, *297*(1–2), 42–49. https://doi.org/10.1016/j.epsl.2010.06.001

Henrichs, I. A., O'Sullivan, G., Chew, D. M., Mark, C., Babechuk, M. G., McKenna, C., & Emo, R. (2018). The trace element and U-Pb systematics of metamorphic apatite. *Chemical Geology*, *483*(January), 218–238. https://doi.org/10.1016/j.chemgeo.2017.12.031

Holder, R. M., Hacker, B. R., Seward, G. G. E., & Kylander-Clark, A. R. C. (2019a). Interpreting titanite U–Pb dates and Zr thermobarometry in high-grade rocks: empirical constraints on elemental diffusivities of Pb, Al, Fe, Zr, Nb, and Ce. *Contributions to Mineralogy and Petrology*, *174*(5), 42. https://doi.org/10.1007/s00410-019-1578-2

Holder, R. M., Hacker, B. R., Seward, G. G. E., & Kylander-Clark, A. R. C. (2019b). Interpreting titanite U–Pb dates and Zr thermobarometry in high-grade rocks: empirical constraints on elemental diffusivities of Pb, Al, Fe, Zr, Nb, and Ce. *Contributions to Mineralogy and Petrology*, *174*(5). https://doi.org/10.1007/s00410-019-1578-2

Horn, I., Rudnick, R. L., & McDonough, W. F. (2000). Precise elemental and isotope ratio determination by simultaneous solution nebulization and laser ablation-ICP-MS: application to U–Pb geochronology. *Chemical Geology*, *164*(3–4), 281–301. https://doi.org/10.1016/S0009-2541(99)00168-0

Horstwood, M.S.A., Evans, J. A., & Montgomery, J. (2008). Determination of Sr isotopes in calcium phosphates using laser ablation inductively coupled plasma mass spectrometry and their application to archaeological tooth enamel. *Geochimica et Cosmochimica Acta*, *72*(23), 5659–5674. https://doi.org/10.1016/j.gca.2008.08.016

Horstwood, Matthew S. A., Košler, J., Gehrels, G., Jackson, S. E., McLean, N. M., Paton, C., et al. (2016). Community-Derived Standards for LA-ICP-MS U-(Th-)Pb Geochronology – Uncertainty Propagation, Age Interpretation and Data Reporting. *Geostandards and Geoanalytical Research*, *40*(3), 311–332. https://doi.org/10.1111/j.1751-908X.2016.00379.x

Huang, Y., Chubakov, V., Mantovani, F., Rudnick, R. L., & McDonough, W. F. (2013). A reference Earth model for the heat-producing elements and associated geoneutrino flux. *Geochemistry, Geophysics, Geosystems*, *14*(6), 2003–2029.

https://doi.org/10.1002/ggge.20129

Ibanez-Mejia, M., Bloch, E. M., & Vervoort, J. D. (2018). Timescales of collisional metamorphism from Sm-Nd, Lu-Hf and U-Pb thermochronology: A case from the Proterozoic Putumayo Orogen of Amazonia. *Geochimica et Cosmochimica Acta*, *235*, 103–126. https://doi.org/10.1016/j.gca.2018.05.017

Ionov, D. A., Doucet, L. S., & Ashchepkov, I. V. (2010). Composition of the lithospheric mantle in the siberian craton: New constraints from fresh peridotites in the Udachnaya-East Kimberlite. *Journal of Petrology*, *51*(11), 2177–2210. https://doi.org/10.1093/petrology/egq053

Ionov, D. A., Doucet, L. S., Carlson, R. W., Golovin, A. V., & Korsakov, A. V. (2015). Post-Archean formation of the lithospheric mantle in the central Siberian craton: Re–Os and PGE study of peridotite xenoliths from the Udachnaya kimberlite. *Geochimica et Cosmochimica Acta*, *165*, 466–483. https://doi.org/10.1016/j.gca.2015.06.035

Ionov, D. A., Liu, Z., Li, J., Golovin, A. V., Korsakov, A. V., & Xu, Y. (2020). The age and origin of cratonic lithospheric mantle: Archean dunites vs. Paleoproterozoic harzburgites from the Udachnaya kimberlite, Siberian craton. *Geochimica et Cosmochimica Acta*, *281*, 67–90. https://doi.org/10.1016/j.gca.2020.05.009

Isnard, H., Brennetot, R., Caussignac, C., Caussignac, N., & Chartier, F. (2005). Investigations for determination of Gd and Sm isotopic compositions in spent nuclear fuels samples by MC ICPMS. *International Journal of Mass Spectrometry*, *246*(1–3), 66–73. https://doi.org/10.1016/j.ijms.2005.08.008

Jaffey, A. H., Flynn, K. F., Glendenin, L. E., Bentley, W. C., & Essling, A. M. (1971). Precision Measurement of Half-Lives and Specific Activities of 235U and 238U. *Physical Review C*, *4*(5), 1889–1906. https://doi.org/10.1103/PhysRevC.4.1889

Jaupart, C., & Mareschal, J.-C. (2014). Constraints on Crustal Heat Production from Heat Flow Data. In *Treatise on Geochemistry* (2nd ed., Vol. 4, pp. 53–73). Elsevier. https://doi.org/10.1016/B978-0-08-095975-7.00302-8

Jaupart, C., & Mareschal, J. (2007). Heat Flow and Thermal Structure of the Lithosphere. In *Volume 6: Crust and Lithosphere Dynamics* (Vol. 6, pp. 217–251). Elsevier. https://doi.org/10.1016/B978-044452748-6/00104-8

Jaupart, Claude, Mareschal, J.-C., & Iarotsky, L. (2016). Radiogenic heat production in the continental crust. *Lithos*, *262*(August), 398–427. https://doi.org/10.1016/j.lithos.2016.07.017

Jin, T., Wang, Q., Shatsky, V., & Liao, Y. (2021). Water Content and Deformation of the Lower Crust beneath the Siberian Craton: Evidence from Granulite Xenoliths. *The Journal of Geology*, *129*(5), 475–498. https://doi.org/10.1086/716514

Jochum, K. P., Weis, U., Stoll, B., Kuzmin, D., Yang, Q., Raczek, I., et al. (2011). Determination of Reference Values for NIST SRM 610-617 Glasses Following ISO Guidelines. *Geostandards and Geoanalytical Research*, *35*(4), 397–429. https://doi.org/10.1111/j.1751-908X.2011.00120.x

Johnson, S. P., Cutten, H. N. C., Muhongo, S., & De Waele, B. (2003). Neoarchaean magmatism and metamorphism of the western granulites in the central domain of the Mozambique belt, Tanzania: U-Pb shrimp geochronology and PT estimates. *Tectonophysics*, *375*(1–4), 125–145. https://doi.org/10.1016/j.tecto.2003.06.003

Jollands, M. C., Hanger, B. J., Yaxley, G. M., Hermann, J., & Kilburn, M. R. (2018). Timescales between mantle metasomatism and kimberlite ascent indicated by diffusion profiles in garnet crystals from peridotite xenoliths. *Earth and Planetary Science Letters*, *481*, 143–153. https://doi.org/10.1016/j.epsl.2017.10.021

Jones, A. P., Smith, J. V., Dawson, J. B., & Hansen, E. C. (1983). Metamorphism, Partial Melting, and K-Metasomatism of Garnet-Scapolite-Kyanite Granulite Xenoliths from Lashaine, Tanzania. *The Journal of Geology*, *91*(2), 143–165. https://doi.org/10.1086/628753

Jöns, N., & Schenk, V. (2004). Petrology of Whiteschists and Associated Rocks at Mautia Hill (Tanzania): Fluid Infiltration during High-Grade Metamorphism? *Journal of Petrology*, *45*(10), 1959–1981. https://doi.org/10.1093/petrology/egh044

Julià, J., Ammon, C. J., & Nyblade, A. A. (2005). Evidence for mafic lower crust in Tanzania, East Africa, from joint inversion of receiver functions and Rayleigh wave dispersion velocities. *Geophysical Journal International*, *162*(2), 555–569. https://doi.org/10.1111/j.1365-246X.2005.02685.x

Kapp, P., Manning, C. E., & Tropper, P. (2009). Phase-equilibrium constraints on titanite and rutile activities in mafic epidote amphibolites and geobarometry using titanite-rutile equilibria. *Journal of Metamorphic Geology*, *27*(7), 509–521. https://doi.org/10.1111/j.1525-1314.2009.00836.x

Kelsey, D. E., & Powell, R. (2011). Progress in linking accessory mineral growth and breakdown to major mineral evolution in metamorphic rocks: A thermodynamic approach in the Na 2O-CaO-K 2O-FeO-MgO-Al 2O 3-SiO 2-H 2O-TiO 2-ZrO 2 system. *Journal of Metamorphic Geology*, *29*(1), 151–166. https://doi.org/10.1111/j.1525-1314.2010.00910.x

Kent, A. J. R., & Ungerer, C. A. "Andy." (2005). Production of barium and light rare earth element oxides during LA-ICP-MS microanalysis. *Journal of Analytical Atomic Spectrometry*, *20*(11), 1256. https://doi.org/10.1039/b505734e

Kinny, P. D., Griffin, B. J., & Brakhfogel, F. F. (1995). Shrimp U/Pb ages of perovskite and zircon from Yakutian kimberlites. In *International Kimberlite Conference Extended Abstracts 1995* (Vol. 8, p. 55). University of Alberta Library. https://doi.org/10.29173/ikc1860

Kirkland, C. L., Yakymchuk, C., Szilas, K., Evans, N., Hollis, J., McDonald, B., & Gardiner, N. J. (2018). Apatite: a U-Pb thermochronometer or geochronometer? *Lithos*, *318–319*, 143–157. https://doi.org/10.1016/j.lithos.2018.08.007

Kitayama, Y., Thomassot, E., Galy, A., Golovin, A., Korsakov, A., d'Eyrames, E., et al. (2017). Co-magmatic sulfides and sulfates in the Udachnaya-East pipe (Siberia): A record of the redox state and isotopic composition of sulfur in kimberlites and their

mantle sources. *Chemical Geology*, *455*, 315–330. https://doi.org/10.1016/j.chemgeo.2016.10.037

Kitayama, Y., Thomassot, E., Galy, A., Korsakov, A., Golovin, A., & D'Eyrames, E. (2021). Geochemical evidence for carbon and chlorine enrichments in the mantle source of kimberlites (Udachnaya pipe, Siberian craton). *Geochimica et Cosmochimica Acta*, *315*, 295–316. https://doi.org/10.1016/j.gca.2021.09.021

Kohn, M. J. (2017). Titanite Petrochronology. *Reviews in Mineralogy and Geochemistry*, *83*(1), 419–441. https://doi.org/10.2138/rmg.2017.83.13

Kohn, M. J., & Kelly, N. M. (2017). Petrology and Geochronology of Metamorphic Zircon. In *Microstructural Geochronology: Planetary Records Down to Atom Scale* (pp. 35–61). https://doi.org/10.1002/9781119227250.ch2

Kohn, M. J., Penniston-Dorland, S. C., & Ferreira, J. C. S. (2016). Implications of near-rim compositional zoning in rutile for geothermometry, geospeedometry, and trace element equilibration. *Contributions to Mineralogy and Petrology*, *171*(10), 78. https://doi.org/10.1007/s00410-016-1285-1

Kooijman, E., Mezger, K., & Berndt, J. (2010). Constraints on the U-Pb systematics of metamorphic rutile from in situ LA-ICP-MS analysis. *Earth and Planetary Science Letters*, *293*(3–4), 321–330. https://doi.org/10.1016/j.epsl.2010.02.047

Kooijman, E., Smit, M. A., Mezger, K., & Berndt, J. (2012). Trace element systematics in granulite facies rutile: implications for Zr geothermometry and provenance studies. *Journal of Metamorphic Geology*, *30*(4), 397–412. https://doi.org/10.1111/j.1525-1314.2012.00972.x

Korenaga, J. (2008). Urey ratio and the structure and evolution of Earth's mantle. *Reviews of Geophysics*, *46*(2), 1–32. https://doi.org/10.1029/2007RG000241

Koreshkova, M., Downes, H., Nikitina, L., Vladykin, N., Larionov, A., & Sergeev, S. (2009). Trace Element And Age Characteristics Of Zircons In Granulite xenoliths from the Udachnaya kimberlite pipe, Siberia. *Precambrian Research*, *168*(3–4), 197–212. https://doi.org/10.1016/j.precamres.2008.09.007

Koreshkova, M. Y., Downes, H., Levsky, L. K., & Vladykin, N. V. (2011). Petrology and Geochemistry of Granulite Xenoliths from Udachnaya and Komsomolskaya Kimberlite Pipes, Siberia. *Journal of Petrology*, *52*(10), 1857–1885. https://doi.org/10.1093/petrology/egr033

Kostrovitsky, S. I., Skuzovatov, S. Y., Yakovlev, D. A., Sun, J., Nasdala, L., & Wu, F.-Y. (2016). Age of the Siberian craton crust beneath the northern kimberlite fields: Insights to the craton evolution. *Gondwana Research*, *39*, 365–385. https://doi.org/10.1016/j.gr.2016.01.008

Krestianinov, E., Amelin, Y., Neymark, L. A., & Aleinikoff, J. N. (2021). U-Pb systematics of uranium-rich apatite from Adirondacks: Inferences about regional geological and geochemical evolution, and evaluation of apatite reference materials for in situ dating. *Chemical Geology*, *581*(November 2020), 120417.

https://doi.org/10.1016/j.chemgeo.2021.120417

Krogstad, E. J., & Walker, R. J. (1994). High closure temperatures of the U-Pb system in large apatites from the Tin Mountain pegmatite, Black Hills, South Dakota, USA. *Geochimica et Cosmochimica Acta*, *58*(18), 3845–3853. https://doi.org/10.1016/0016-7037(94)90367-0

Kylander-Clark, A.R.C., Hacker, B. R., & Mattinson, J. M. (2008). Slow exhumation of UHP terranes: Titanite and rutile ages of the Western Gneiss Region, Norway. *Earth and Planetary Science Letters*, *272*(3–4), 531–540. https://doi.org/10.1016/j.epsl.2008.05.019

Kylander-Clark, Andrew R. C. (2017). Petrochronology by Laser-Ablation Inductively Coupled Plasma Mass Spectrometry. *Reviews in Mineralogy and Geochemistry*, *83*(1), 183–198. https://doi.org/10.2138/rmg.2017.83.6

Kylander-Clark, Andrew R.C., Hacker, B. R., & Cottle, J. M. (2013). Laser-ablation split-stream ICP petrochronology. *Chemical Geology*, *345*, 99–112. https://doi.org/10.1016/j.chemgeo.2013.02.019

Lee, C. T. A., & Rudnick, R. L. (1999). Compositionally stratified cratonic lithosphere: petrology and geochemistry of peridotite xenoliths the Labait volcano, Tanzania. *Proc. 7th Internatl. Kimberlite Conf., Vol I: The Dawson Volume*, (January 1999), 503–521.

Liu, Y., Hu, Z., Gao, S., Günther, D., Xu, J., Gao, C., & Chen, H. (2008). In situ analysis of major and trace elements of anhydrous minerals by LA-ICP-MS without applying an internal standard. *Chemical Geology*, *257*(1–2), 34–43. https://doi.org/10.1016/j.chemgeo.2008.08.004

Maboko, M., Pedersen, R., Manya, S., Torssander, P., & Mwache, M. (2009). The origin of late archaean granitoids in the Sukumaland greenstone belt of Northern Tanzania: geochemical and isotopic constraints. *Tanzania Journal of Science*, *32*(1). https://doi.org/10.4314/tjs.v32i1.18431

Maboko, M. A. H. (1997). P-T conditions of metamorphism in the Wami River granulite complex, central coastal Tanzania: implications for Pan-African geotectonics in the Mozambique Belt of eastern Africa. *Journal of African Earth Sciences*, *24*(1–2), 51–64. https://doi.org/10.1016/S0899-5362(97)00026-2

Maboko, M. A. H. (2000). Nd and Sr isotopic investigation of the Archean-Proterozoic boundary in north eastern Tanzania: Constraints on the nature of Neoproterozoic tectonism in the Mozambique Belt. *Precambrian Research*, *102*(1–2), 87–98. https://doi.org/10.1016/S0301-9268(00)00060-7

Maboko, M. A. H. (2001). Dating Post-Metamorphic Cooling of the Eastern Granulites in the Mozambique Belt of Northern Tanzania Using the Garnet Sm-Nd Method. *Gondwana Research*, *4*(3), 329–336. https://doi.org/10.1016/S1342-937X(05)70333-6

Maboko, M. A. H., & Nakamura, E. (2002). Isotopic dating of Neoproterozoic crustal growth in the Usambara Mountains of northeastern Tanzania: Evidence for coeval crust formation in the Mozambique Belt and the Arabian-Nubian Shield. *Precambrian*

Research, *113*(3–4), 227–242. https://doi.org/10.1016/S0301-9268(01)00213-3

Maboko, M. A. H., McDougall, I., & Zeitler, P. K. (1989). Dating late Pan-African cooling in the Uluguru granulite complex of Eastern Tanzania using the 40Ar□39Ar technique. *Journal of African Earth Sciences (and the Middle East)*, *9*(1), 159–167. https://doi.org/10.1016/0899-5362(89)90017-1

Mackey, K. G., Fujita, K., & Ruff, L. J. (1998). Crustal thickness of northeast Russia. *Tectonophysics*, *284*(3–4), 283–297. https://doi.org/10.1016/S0040-1951(97)00180-7

Manning, C. F., & Bohlen, S. R. (1991). The Reaction Titanite+Kyanite=Anorthite+Rutile and Titanite-Rutile Barometry in Eclogites. *Contributions to Mineralogy and Petrology*, *109*(1), 1–9. https://doi.org/10.1007/BF00687196

Mansur, A. T., Manya, S., Timpa, S., & Rudnick, R. L. (2014). Granulite-Facies Xenoliths in Rift Basalts of Northern Tanzania: Age, Composition and Origin of Archean Lower Crust. *Journal of Petrology*, *55*(7), 1243–1286. https://doi.org/10.1093/petrology/egu024

Manya, S., & Maboko, M. A. H. (2003). Dating basaltic volcanism in the Neoarchaean Sukumaland Greenstone Belt of the Tanzania Craton using the Sm-Nd method: Implications for the geological evolution of the Tanzania Craton. *Precambrian Research*, *121*(1–2), 35–45. https://doi.org/10.1016/S0301-9268(02)00195-X

Manya, Shukrani, & Maboko, M. A. H. (2008a). Geochemistry and geochronology of Neoarchaean volcanic rocks of the Iramba–Sekenke greenstone belt, central Tanzania. *Precambrian Research*, *163*(3–4), 265–278. https://doi.org/10.1016/j.precamres.2008.01.001

Manya, Shukrani, & Maboko, M. A. H. (2008b). Geochemistry of the Neoarchaean mafic volcanic rocks of the Geita area, NW Tanzania: Implications for stratigraphical relationships in the Sukumaland greenstone belt. *Journal of African Earth Sciences*, *52*(4–5), 152–160. https://doi.org/10.1016/j.jafrearsci.2008.06.003

Manya, Shukrani, Kobayashi, K., Maboko, M. A. H., & Nakamura, E. (2006). Ion microprobe zircon U-Pb dating of the late Archaean metavolcanics and associated granites of the Musoma-Mara Greenstone Belt, Northeast Tanzania: Implications for the geological evolution of the Tanzania Craton. *Journal of African Earth Sciences*, *45*(3), 355–366. https://doi.org/10.1016/j.jafrearsci.2006.03.004

Manya, Shukrani, Maboko, M. A. H., & Nakamura, E. (2007). The geochemistry of high-Mg andesite and associated adakitic rocks in the Musoma-Mara Greenstone Belt, northern Tanzania: Possible evidence for Neoarchaean ridge subduction? *Precambrian Research*, *159*(3–4), 241–259. https://doi.org/10.1016/j.precamres.2007.07.002

Mao, M., Rukhlov, A. S., Rowins, S. M., Spence, J., & Coogan, L. A. (2016). Apatite trace element compositions: A robust new tool for mineral exploration. *Economic Geology*, *111*(5), 1187–1222. https://doi.org/10.2113/econgeo.111.5.1187

Marschall, H. R., Dohmen, R., & Ludwig, T. (2013). Diffusion-induced fractionation of niobium and tantalum during continental crust formation. *Earth and Planetary Science*

Letters, *375*, 361–371. https://doi.org/10.1016/j.epsl.2013.05.055

McCubbin, F. M., & Jones, R. H. (2015). Extraterrestrial Apatite: Planetary Geochemistry to Astrobiology. *Elements*, *11*(3), 183–188. https://doi.org/10.2113/gselements.11.3.183

McDonough, W. F., & Sun, S. -s. (1995). The composition of the Earth. *Chemical Geology*, *120*(3–4), 223–253. https://doi.org/10.1016/0009-2541(94)00140-4

McDowell, F. W., McIntosh, W. C., & Farley, K. A. (2005). A precise 40Ar–39Ar reference age for the Durango apatite (U–Th)/He and fission-track dating standard. *Chemical Geology*, *214*(3–4), 249–263. https://doi.org/10.1016/j.chemgeo.2004.10.002

McFarlane, C. R. M., & McCulloch, M. T. (2007). Coupling of in-situ Sm–Nd systematics and U–Pb dating of monazite and allanite with applications to crustal evolution studies. *Chemical Geology*, *245*(1–2), 45–60. https://doi.org/10.1016/j.chemgeo.2007.07.020

McIntyre, T., Kublik, K., Currie, C., & Pearson, D. G. (2021). Heat Generation in Cratonic Mantle Roots—New Trace Element Constraints From Mantle Xenoliths and Implications for Cratonic Geotherms. *Geochemistry, Geophysics, Geosystems*, *22*(9), 1–25. https://doi.org/10.1029/2021GC009691

McKinney, S. T., Cottle, J. M., & Lederer, G. W. (2015). Evaluating rare earth element (REE) mineralization mechanisms in Proterozoic gneiss, Music Valley, California. *Geological Society of America Bulletin*, *127*(7–8), B31165.1. https://doi.org/10.1130/B31165.1

McLean, N. M., Condon, D. J., Schoene, B., & Bowring, S. A. (2015). Evaluating uncertainties in the calibration of isotopic reference materials and multi-element isotopic tracers (EARTHTIME Tracer Calibration Part II). *Geochimica et Cosmochimica Acta*, *164*, 481–501. https://doi.org/10.1016/j.gca.2015.02.040

Meert, J. (1995). Paleomagnetic investigation of the Neoproterozoic Gagwe lavas and Mbozi complex, Tanzania and the assembly of Gondwana. *Precambrian Research*, *74*(4), 225–244. https://doi.org/10.1016/0301-9268(95)00012-T

Meert, J. G. (2003). A synopsis of events related to the assembly of eastern Gondwana. *Tectonophysics*, *362*(1–4), 1–40. https://doi.org/10.1016/S0040-1951(02)00629-7

Mole, D. R., Barnes, S. J., Taylor, R. J. M., Kinny, P. D., & Fritz, H. (2018). A relic of the Mozambique Ocean in south-east Tanzania. *Precambrian Research*, *305*(February 2017), 386–426. https://doi.org/10.1016/j.precamres.2017.10.009

Molina, J. F., Moreno, J. A., Castro, A., Rodríguez, C., & Fershtater, G. B. (2015). Calcic amphibole thermobarometry in metamorphic and igneous rocks: New calibrations based on plagioclase/amphibole Al-Si partitioning and amphibole/liquid Mg partitioning. *Lithos*, *232*, 286–305. https://doi.org/10.1016/j.lithos.2015.06.027

Moller, A., Appel, P., Mezger, K., & Schenk, V. (1995). Evidence for a 2 Ga subduction zone: eclogites in the Usagaran belt of Tanzania. *Geology*, *23*(12), 1067–1070. https://doi.org/10.1130/0091-7613(1995)023<1067:EFAGSZ>2.3.CO;2

Möller, A., Mezger, K., & Schenk, V. (1998). Crustal age domains and the evolution of the

continental crust in the Mozambique Belt of Tanzania: Combined Sm-Nd, Rb-Sr, and Pb-Pb isotopic evidence. *Journal of Petrology*, *39*(4), 749–783. https://doi.org/10.1093/petroj/39.4.749

Möller, A., Mezger, K., & Schenk, V. (2000). U-Pb dating of metamorphic minerals: Pan-African metamorphism and prolonged slow cooling of high pressure granulites in Tanzania, East Africa. *Precambrian Research*, *104*(3–4), 123–146. https://doi.org/10.1016/S0301-9268(00)00086-3

Morton, A., & Yaxley, G. (2007). Detrital apatite geochemistry and its application in provenance studies. In *Sedimentary Provenance and Petrogenesis: Perspectives from Petrography and Geochemistry* (Vol. 420, pp. 319–344). Geological Society of America. https://doi.org/10.1130/2006.2420(19)

Moyen, J.-F., Paquette, J.-L., Ionov, D. A., Gannoun, A., Korsakov, A. V., Golovin, A. V., & Moine, B. N. (2017). Paleoproterozoic rejuvenation and replacement of Archaean lithosphere: Evidence from zircon U–Pb dating and Hf isotopes in crustal xenoliths at Udachnaya, Siberian craton. *Earth and Planetary Science Letters*, *457*, 149–159. https://doi.org/10.1016/j.epsl.2016.09.046

Muhongo, S., & Lenoir, J. L. (1994). Pan-African granulite-facies metamorphism in the Mozambique Belt of Tanzania: U-Pb zircon geochronology. *Journal of the Geological Society*, *151*(2), 343–347. https://doi.org/10.1144/gsjgs.151.2.0343

Muhongo, S., & Tuisku, P. (1996). Pan-African high pressure isobaric cooling: Evidence from the mineralogy and thermobarometry of the granulite-facies rocks from the Uluguru Mountains, eastern Tanzania. *Journal of African Earth Sciences*, *23*(3), 443–463. https://doi.org/10.1016/S0899-5362(97)00012-2

Muhongo, S., Tuisku, P., & Mtoni, Y. (1999). Pan-African pressure-temperature evolution of the Merelani area in the Mozambique Belt in northeast Tanzania. *Journal of African Earth Sciences*, *29*(2), 353–365. https://doi.org/10.1016/S0899-5362(99)00102-5

Newton, R. C., & Perkins, D. (1982). Thermodynamic calibration of geobarometers based on the assemblages garnet - plagioclase - orthopyroxene (clinopyroxene) - quartz. *American Mineralogist*, *67*(3–4), 203–222.

Nicolaysen, L. O., Hart, R. J., & Gale, N. H. (1981). The Vredefort radioelement profile extended to supracrustal strata at Carletonville, with implications for continental heat flow. *Journal of Geophysical Research: Solid Earth*, *86*(B11), 10653–10661. https://doi.org/10.1029/JB086iB11p10653

Nimis, P., Goncharov, A., Ionov, D. A., & McCammon, C. (2015). Fe3+ partitioning systematics between orthopyroxene and garnet in mantle peridotite xenoliths and implications for thermobarometry of oxidized and reduced mantle rocks. *Contributions to Mineralogy and Petrology*, *169*(1). https://doi.org/10.1007/s00410-014-1101-8

Nyblade, A. A. (1997). Heat flow across the East African Plateau. *Geophysical Research Letters*, *24*(16), 2083–2086. https://doi.org/10.1029/97GL01952

Nyblade, A. A., & Brazier, R. A. (2002). Precambrian lithospheric controls on the

development of the East African rift system. *Geology*, *30*(8), 755–758. https://doi.org/10.1130/0091-7613(2002)030<0755:PLCOTD>2.0.CO;2

Nyblade, A. A., Pollack, H. N., Jones, D. L., Podmore, F., & Mushayandebvu, M. (1990). Terrestrial heat flow in east and southern Africa. *Journal of Geophysical Research*, *95*(B11), 17371. https://doi.org/10.1029/JB095iB11p17371

O'Brien, P. J., & Rotzler, J. (2003). High-pressure granulites: formation, recovery of peak conditions and implications for tectonics. *Journal of Metamorphic Geology*, *21*(1), 3–20. https://doi.org/10.1046/j.1525-1314.2003.00420.x

O'Sullivan, G., Chew, D., Kenny, G., Henrichs, I., & Mulligan, D. (2020). The trace element composition of apatite and its application to detrital provenance studies. *Earth-Science Reviews*, *201*(November 2019), 103044. https://doi.org/10.1016/j.earscirev.2019.103044

O'Sullivan, G. J., Chew, D. M., Morton, A. C., Mark, C., & Henrichs, I. A. (2018). An Integrated Apatite Geochronology and Geochemistry Tool for Sedimentary Provenance Analysis. *Geochemistry, Geophysics, Geosystems*, *19*(4), 1309–1326. https://doi.org/10.1002/2017GC007343

O'Sullivan, Gary J., & Chew, D. M. (2020). The clastic record of a Wilson Cycle: Evidence from detrital apatite petrochronology of the Grampian-Taconic fore-arc. *Earth and Planetary Science Letters*, *552*, 116588. https://doi.org/10.1016/j.epsl.2020.116588

O'Sullivan, Gary John, Thakurdin, Y., Bolhar, R., Horváth, P., Hoare, B. C., & Collerson, K. D. (2021). The Great Falls Tectonic Zone after the assembly of Laurentia: evidence for long-term tectonic stability from xenolith apatite. *Lithos*, *384–385*, 105977. https://doi.org/10.1016/j.lithos.2021.105977

Pape, J., Mezger, K., & Robyr, M. (2016). A systematic evaluation of the Zr-in-rutile thermometer in ultra-high temperature (UHT) rocks. *Contributions to Mineralogy and Petrology*, *171*(5), 1–20. https://doi.org/10.1007/s00410-016-1254-8

Paquette, J. L., Ionov, D. A., Agashev, A. M., Gannoun, A., & Nikolenko, E. I. (2017). Age, provenance and Precambrian evolution of the Anabar shield from U-Pb and Lu-Hf isotope data on detrital zircons, and the history of the northern and central Siberian craton. *Precambrian Research*, *301*(September), 134–144. https://doi.org/10.1016/j.precamres.2017.09.008

Paton, C., Hellstrom, J., Paul, B., Woodhead, J., & Hergt, J. (2011). Iolite: Freeware for the visualisation and processing of mass spectrometric data. *Journal of Analytical Atomic Spectrometry*, *26*(12), 2508. https://doi.org/10.1039/c1ja10172b

Paul, Andre N., Spikings, R. A., Chew, D., & Daly, J. S. (2019). The effect of intra-crystal uranium zonation on apatite U-Pb thermochronology: A combined ID-TIMS and LA-MC-ICP-MS study. *Geochimica et Cosmochimica Acta*, *251*, 15–35. https://doi.org/10.1016/j.gca.2019.02.013

Paul, André N., Spikings, R. A., & Gaynor, S. P. (2021). U-Pb ID-TIMS reference ages and initial Pb isotope compositions for Durango and Wilberforce apatites. *Chemical*

Geology, *586*(October), 120604. https://doi.org/10.1016/j.chemgeo.2021.120604

Pearce, N. J. G., Perkins, W. T., Westgate, J. A., Gorton, M. P., Jackson, S. E., Neal, C. R., & Chenery, S. P. (1997). A Compilation of New and Published Major and Trace Element Data for NIST SRM 610 and NIST SRM 612 Glass Reference Materials. *Geostandards and Geoanalytical Research*, *21*(1), 115–144. https://doi.org/10.1111/j.1751-908X.1997.tb00538.x

Perry, C., Rosieanu, C., Mareschal, J.-C., & Jaupart, C. (2010). Thermal regime of the lithosphere in the Canadian Shield. Canadian Journal of Earth Sciences, 47(4), 389–408. https://doi.org/10.1139/E09-059

Pearson, D. G., Shirey, S. B., Carlson, R. W., Boyd, F. R., Pokhilenko, N. P., & Shimizu, N. (1995). Re-Os, Sm-Nd, and Rb-Sr isotope evidence for thick Archaean lithospheric mantle beneath the Siberian craton modified by multistage metasomatism. *Geochimica et Cosmochimica Acta*, *59*(5), 959–977. https://doi.org/10.1016/0016-7037(95)00014-3

Petrus, J. A., & Kamber, B. S. (2012). VizualAge: A Novel Approach to Laser Ablation ICP-MS U-Pb Geochronology Data Reduction. *Geostandards and Geoanalytical Research*, *36*(3), 247–270. https://doi.org/10.1111/j.1751-908X.2012.00158.x

Piccoli, P. M., & Candela, P. A. (2002). Apatite in Igneous Systems. *Reviews in Mineralogy and Geochemistry*, *48*(1), 255–292. https://doi.org/10.2138/rmg.2002.48.6

Poletti, J. E., Cottle, J. M., Hagen-Peter, G. A., & Lackey, J. S. (2016). Petrochronological Constraints on the Origin of the Mountain Pass Ultrapotassic and Carbonatite Intrusive Suite, California. *Journal of Petrology*, *57*(8), egw050. https://doi.org/10.1093/petrology/egw050

Pollack, H. N., Hurter, S. J., & Johnson, J. R. (1993). Heat flow from the Earth's interior: Analysis of the global data set. *Reviews of Geophysics*, *31*(3), 267. https://doi.org/10.1029/93RG01249

Priyatkina, N., Khudoley, A. K., Collins, W. J., Kuznetsov, N. B., & Huang, H. Q. (2016). Detrital zircon record of Meso- and Neoproterozoic sedimentary basins in northern part of the Siberian Craton: Characterizing buried crust of the basement. *Precambrian Research*, *285*, 21–38. https://doi.org/10.1016/j.precamres.2016.09.003

Prowatke, S., & Klemme, S. (2006). Trace element partitioning between apatite and silicate melts. *Geochimica et Cosmochimica Acta*, *70*(17), 4513–4527. https://doi.org/10.1016/j.gca.2006.06.162

Ramos, F. C., Wolff, J. A., & Tollstrup, D. L. (2004). Measuring 87Sr/86Sr variations in minerals and groundmass from basalts using LA-MC-ICPMS. *Chemical Geology*, *211*(1–2), 135–158. https://doi.org/10.1016/j.chemgeo.2004.06.025

Ravindran, A., Mezger, K., Balakrishnan, S., Kooijman, E., Schmitt, M., & Berndt, J. (2020). Initial 87Sr/86Sr as a sensitive tracer of Archaean crust-mantle evolution: Constraints from igneous and sedimentary rocks in the western Dharwar Craton, India. *Precambrian Research*, *337*(June 2019), 105523. https://doi.org/10.1016/j.precamres.2019.105523

Ritsema, J., Nyblade, A. A., Owens, T. J., Langston, C. A., & VanDecar, J. C. (1998). Upper mantle seismic velocity structure beneath Tanzania, east Africa: Implications for the stability of cratonic lithosphere. *Journal of Geophysical Research: Solid Earth*, *103*(B9), 21201–21213. https://doi.org/10.1029/98jb01274

Rosen, O. M. (1989). Two geochemically different types of Precambrian crust in the Anabar Shield, North Siberia. *Precambrian Research*, *45*(1–3), 129–142. https://doi.org/10.1016/0301-9268(89)90035-1

Rosen, O. M. (2002). Siberian craton - a fragment of a Paleoproterozoic supercontinent. *Russian Journal of Earth Sciences*, *4*(2), 103–119. https://doi.org/10.2205/2002ES000090

Rosen, O. M., Condie, K. C., Natapov, L. M., & Nozhkin, A. D. (1994). Archean and Early Proterozoic Evolution of the Siberian Craton: A Preliminary Assessment. In K. C. Condie (Ed.), *Archean Crustal Evolution* (pp. 411–459). Amsterdam: Elsevier. https://doi.org/10.1016/S0166-2635(08)70228-7

Rosen, O. M., Levskii, L. K., Zhuravlev, D. Z., Rotman, A. Y., Spetsius, Z. V., Makeev, A. F., et al. (2006). Paleoproterozoic accretion in the Northeast Siberian craton: Isotopic dating of the Anabar collision system. *Stratigraphy and Geological Correlation*, *14*(6), 581–601. https://doi.org/10.1134/S0869593806060013

Roy, R. F., Blackwell, D. D., & Birch, F. (1968). Heat generation of plutonic rocks and continental heat flow provinces. *Earth and Planetary Science Letters*, *5*(C), 1–12. https://doi.org/10.1016/S0012-821X(68)80002-0

Roy, S., & Mareschal, J. C. (2011). Constraints on the deep thermal structure of the Dharwar craton, India, from heat flow, shear wave velocities, and mantle xenoliths. *Journal of Geophysical Research: Solid Earth*, *116*(2), 1–15. https://doi.org/10.1029/2010JB007796

Rubatto, D. (2002). Zircon trace element geochemistry: partitioning with garnet and the link between U–Pb ages and metamorphism. *Chemical Geology*, *184*(1–2), 123–138. https://doi.org/10.1016/S0009-2541(01)00355-2

Rudnick, R.L., & Gao, S. (2014). Composition of the Continental Crust. In *Treatise on Geochemistry* (2nd ed., Vol. 4, pp. 1–51). Elsevier. https://doi.org/10.1016/B978-0-08-095975-7.00301-6

Rudnick, R. L, McDonough, W. F., & Chappell, B. C. (1993). Carbonatite metasomatism in the northern Tanzanian mantle. *Earth Planet. Sci. Lett.*, *114*, 463–475.

Rudnick, R.L. (1994). Northern Tanzanian peridotite xenoliths: a comparison with Kaapvaal peridotites and inferences on metasomatic interactions. *International Kimberlite Conference*, (January), 336–353.

Rudnick, R. L., McDonough, W. F., & O'Connell, R. J. (1998). Thermal structure, thickness and composition of continental lithosphere. *Chemical Geology*, *145*(3–4), 395–411. https://doi.org/10.1016/S0009-2541(97)00151-4

Rudnick, R. L, & Fountain, D. M. (1995). Nature and composition of the continental crust: A lower crustal perspective. *Reviews of Geophysics*, *33*(3), 267. https://doi.org/10.1029/95RG01302

Sammon, L. G., & McDonough, W. F. (2021). A Geochemical Review of Amphibolite, Granulite, and Eclogite Facies Lithologies: Perspectives on the Deep Continental Crust. *Journal of Geophysical Research: Solid Earth*, *126*(12), 1–26. https://doi.org/10.1029/2021JB022791

Sanislav, I. V., Wormald, R. J., Dirks, P. H. G. M., Blenkinsop, T. G., Salamba, L., & Joseph, D. (2014). Zircon U-Pb ages and Lu-Hf isotope systematics from late-tectonic granites, Geita Greenstone Belt: Implications for crustal growth of the Tanzania Craton. *Precambrian Research*, *242*, 187–204. https://doi.org/10.1016/j.precamres.2013.12.026

Sanislav, I. V., Dirks, P. H. G. M., Blenkinsop, T., & Kolling, S. L. (2018). The tectonic history of a crustal-scale shear zone in the Tanzania Craton from the Geita Greenstone Belt, NW-Tanzania Craton. *Precambrian Research*, *310*(February), 1–16. https://doi.org/10.1016/j.precamres.2018.02.025

Sano, Y., Oyama, T., Terada, K., & Hidaka, H. (1999). Ion microprobe U–Pb dating of apatite. *Chemical Geology*, *153*(1–4), 249–258. https://doi.org/10.1016/S0009-2541(98)00163-6

Sasaki, J., Peterson, N. L., & Hoshino, K. (1985). Tracer impurity diffusion in single-crystal rutile (TiO2−x). *Journal of Physics and Chemistry of Solids*, *46*(11), 1267–1283. https://doi.org/10.1016/0022-3697(85)90129-5

Schmitz, M. D., & Bowring, S. A. (2003a). Constraints on the thermal evolution of continental lithosphere from U-Pb accessory mineral thermochronometry of lower crustal xenoliths, southern Africa. *Contributions to Mineralogy and Petrology*, *144*(5), 592–618. https://doi.org/10.1007/s00410-002-0419-9

Schmitz, M. D., & Bowring, S. A. (2003b). Ultrahigh-temperature metamorphism in the lower crust during Neoarchean Ventersdorp rifting and magmatism, Kaapvaal Craton, southern Africa. *Geological Society of America Bulletin*, *115*(5), 533–548. https://doi.org/10.1130/0016-7606(2003)115<0533:UMITLC>2.0.CO;2

Schmitz, M. D., & Schoene, B. (2007). Derivation of isotope ratios, errors, and error correlations for U-Pb geochronology using 205 Pb- 235 U-(233 U)-spiked isotope dilution thermal ionization mass spectrometric data. *Geochemistry, Geophysics, Geosystems*, *8*(8), n/a-n/a. https://doi.org/10.1029/2006GC001492

Schoene, B., & Bowring, S. A. (2006). U–Pb systematics of the McClure Mountain syenite: thermochronological constraints on the age of the 40Ar/39Ar standard MMhb. *Contributions to Mineralogy and Petrology*, *151*(5), 615–630. https://doi.org/10.1007/s00410-006-0077-4

Schoene, B., & Bowring, S. A. (2007). Determining accurate temperature–time paths from U–Pb thermochronology: An example from the Kaapvaal craton, southern Africa. *Geochimica et Cosmochimica Acta*, *71*(1), 165–185. https://doi.org/10.1016/j.gca.2006.08.029

Schutt, D. L., Lowry, A. R., & Buehler, J. S. (2018). Moho temperature and mobility of lower crust in the western United States. *Geology*, *46*(3), 219–222. https://doi.org/10.1130/G39507.1

Sclater, J. G., Jaupart, C., & Galson, D. (1980). The heat flow through oceanic and continental crust and the heat loss of the Earth. *Reviews of Geophysics*, *18*(1), 269. https://doi.org/10.1029/RG018i001p00269

Semprich, J., & Simon, N. S. C. (2014). Inhibited eclogitization and consequences for geophysical rock properties and delamination models: Constraints from cratonic lower crustal xenoliths. *Gondwana Research*, *25*(2), 668–684. https://doi.org/10.1016/j.gr.2012.08.018

Seymour, N. M., Stockli, D. F., Beltrando, M., & Smye, A. J. (2016). Tracing the thermal evolution of the Corsican lower crust during Tethyan rifting. *Tectonics*, *35*(10), 2439–2466. https://doi.org/10.1002/2016TC004178

Shatsky, V., Ragozin, A., Zedgenizov, D., & Mityukhin, S. (2008). Evidence for multistage evolution in a xenolith of diamond-bearing eclogite from the Udachnaya kimberlite pipe. *Lithos*, *105*(3–4), 289–300. https://doi.org/10.1016/j.lithos.2008.04.008

Shatsky, V. S., Malkovets, V. G., Belousova, E. A., Tretiakova, I. G., Griffin, W. L., Ragozin, A. L., et al. (2016). Tectonothermal evolution of the continental crust beneath the Yakutian diamondiferous province (Siberian craton): U–Pb and Hf isotopic evidence on zircons from crustal xenoliths of kimberlite pipes. *Precambrian Research*, *282*, 1–20. https://doi.org/10.1016/j.precamres.2016.06.022

Shatsky, V. S., Wang, Q., Skuzovatov, S. Y., & Ragozin, A. L. (2019). The crust-mantle evolution of the Anabar tectonic province in the Siberian Craton: Coupled or decoupled? *Precambrian Research*, *332*(July), 105388. https://doi.org/10.1016/j.precamres.2019.105388

Shaw, D. M., Cramer, J. J., Higgins, M. D., & Truscott, M. G. (1986). Composition of the Canadian Precambrian shield and the continental crust of the earth. *Geological Society, London, Special Publications*, *24*(1), 275–282. https://doi.org/10.1144/GSL.SP.1986.024.01.24

Smelov, A. P., Kotov, A. B., Sal'nikova, E. B., Kovach, V. P., Beryozkin, V. I., Kravchenko, A. A., et al. (2012). Age and duration of the formation of the Billyakh tectonic melange zone, Anabar shield. *Petrology*, *20*(3), 286–300. https://doi.org/10.1134/S0869591112030058

Smit, M. A., Waight, T. E., & Nielsen, T. F. D. (2016). Millennia of magmatism recorded in crustal xenoliths from alkaline provinces in Southwest Greenland. *Earth and Planetary Science Letters*, *451*(2016), 241–250. https://doi.org/10.1016/j.epsl.2016.06.047

Smye, A.J., Marsh, J. H., Vermeesch, P., Garber, J. M., & Stockli, D. F. (2018). Applications and limitations of U-Pb thermochronology to middle and lower crustal thermal histories. *Chemical Geology*, *494*(July), 1–18. https://doi.org/10.1016/j.chemgeo.2018.07.003

Smye, Andrew J., & Stockli, D. F. (2014). Rutile U–Pb age depth profiling: A continuous record of lithospheric thermal evolution. *Earth and Planetary Science Letters*, *408*, 171–182. https://doi.org/10.1016/j.epsl.2014.10.013

Sommer, H., Kröner, A., Hauzenberger, C., Muhongo, S., & Wingate, M. T. D. (2003). Metamorphic petrology and zircon geochronology of high-grade rocks from the central Mozambique Belt of Tanzania: Crustal recycling of Archean and Palaeoproterozoic material during the Pan-African orogeny. *Journal of Metamorphic Geology*, *21*(9), 915–934. https://doi.org/10.1111/j.1525-1314.2003.00491.x

Sommer, Holger, Kröner, A., Hauzenberger, C., & Muhongo, S. (2005). Reworking of archaean and Palaeoproterozoic crust in the Mozambique belt of central Tanzania as documented by SHRIMP zircon geochronology. *Journal of African Earth Sciences*, *43*(4), 447–463. https://doi.org/10.1016/j.jafrearsci.2005.09.005

Sommer, Holger, Hauzenberger, C., Kröner, A., & Muhongo, S. (2008). Isothermal decompression history in the "Western Granulite" terrain, central Tanzania: Evidence from reaction textures and trapped fluids in metapelites. *Journal of African Earth Sciences*, *51*(3), 123–144. https://doi.org/10.1016/j.jafrearsci.2008.01.003

Spear, F. S., & Pyle, J. M. (2002). Apatite, Monazite, and Xenotime in Metamorphic Rocks. *Reviews in Mineralogy and Geochemistry*, *48*(1), 293–335. https://doi.org/10.2138/rmg.2002.48.7

Spencer, K. J., Hacker, B. R., Kylander-Clark, A. R. C., Andersen, T. B., Cottle, J. M., Stearns, M. A., et al. (2013). Campaign-style titanite U-Pb dating by laser-ablation ICP: Implications for crustal flow, phase transformations and titanite closure. *Chemical Geology*, *341*(September), 84–101. https://doi.org/10.1016/j.chemgeo.2012.11.012

Spera, F. J. (1984). Carbon dioxide in petrogenesis III: role of volatiles in the ascent of alkaline magma with special reference to xenolith-bearing mafic lavas. *Contributions to Mineralogy and Petrology*, *88*(3), 217–232. https://doi.org/10.1007/BF00380167

Stacey, J. S., & Kramers, J. D. (1975). Approximation of terrestrial lead isotope evolution by a two-stage model. *Earth and Planetary Science Letters*, *26*(2), 207–221. https://doi.org/10.1016/0012-821X(75)90088-6

Stearns, M. A., Cottle, J. M., Hacker, B. R., & Kylander-Clark, A. R. C. (2016). Extracting thermal histories from the near-rim zoning in titanite using coupled U-Pb and trace-element depth profiles by single-shot laser-ablation split stream (SS-LASS) ICP-MS. *Chemical Geology*, *422*, 13–24. https://doi.org/10.1016/j.chemgeo.2015.12.011

Stern, R. J. (1994). Arc Assembly and Continental Collision in the Neoproterozoic East African Orogen: Implications for the Consolidation of Gondwanaland. *Annual Review of Earth and Planetary Sciences*, *22*(1), 319–351. https://doi.org/10.1146/annurev.ea.22.050194.001535

Sun, J., Liu, C.-Z., Tappe, S., Kostrovitsky, S. I., Wu, F.-Y., Yakovlev, D., et al. (2014). Repeated kimberlite magmatism beneath Yakutia and its relationship to Siberian flood volcanism: Insights from in situ U–Pb and Sr–Nd perovskite isotope analysis. *Earth and Planetary Science Letters*, *404*, 283–295.

https://doi.org/10.1016/j.epsl.2014.07.039

Sylvester, P. J. (2008). LA-(MC)-ICP-MS Trends in 2006 and 2007 with Particular Emphasis on Measurement Uncertainties. *Geostandards and Geoanalytical Research*, *32*(4), 469–488. https://doi.org/10.1111/j.1751-908X.2008.00924.x

Taylor-Jones, K., & Powell, R. (2015). Interpreting zirconium-in-rutile thermometric results. *Journal of Metamorphic Geology*, *33*(2), 115–122. https://doi.org/10.1111/jmg.12109

Taylor, R. J. M., Harley, S. L., Hinton, R. W., Elphick, S., Clark, C., & Kelly, N. M. (2015). Experimental determination of REE partition coefficients between zircon, garnet and melt: A key to understanding high-T crustal processes. *Journal of Metamorphic Geology*, *33*(3), 231–248. https://doi.org/10.1111/jmg.12118

Taylor, S. R., & Mclennan, S. M. (2009). Planetary crusts: their composition, origin and evolution. *Choice Reviews Online*, *46*(12), 46-6776-46–6776. https://doi.org/10.5860/CHOICE.46-6776

Taylor, S. R., & McLennan, S. M. (1995). The geochemical evolution of the continental crust. *Reviews of Geophysics*, *33*(2), 241. https://doi.org/10.1029/95RG00262

Tenczer, V., Hauzenberger, C. A., Fritz, H., Whitehouse, M. J., Mogessie, A., Wallbrecher, E., et al. (2006). Anorthosites in the Eastern Granulites of Tanzania-New SIMS zircon U-Pb age data, petrography and geochemistry. *Precambrian Research*, *148*(1–2), 85–114. https://doi.org/10.1016/j.precamres.2006.03.004

Tenczer, V., Hauzenberger, C., Fritz, H., Hoinkes, G., Muhongo, S., & Klötzli, U. (2013). Crustal age domains and metamorphic reworking of the deep crust in Northern-Central Tanzania: A U/Pb zircon and monazite age study. *Mineralogy and Petrology*, *107*(5), 679–707. https://doi.org/10.1007/s00710-012-0210-1

Thomas, R. J., Spencer, C., Bushi, A. M., Baglow, N., Boniface, N., de Kock, G., et al. (2016). Geochronology of the central Tanzania Craton and its southern and eastern orogenic margins. *Precambrian Research*, *277*, 47–67. https://doi.org/10.1016/j.precamres.2016.02.008

Thompson, J., Meffre, S., Maas, R., Kamenetsky, V., Kamenetsky, M., Goemann, K., et al. (2016). Matrix effects in Pb/U measurements during LA-ICP-MS analysis of the mineral apatite. *Journal of Analytical Atomic Spectrometry*, *31*(6), 1206–1215. https://doi.org/10.1039/C6JA00048G

Thomson, S. N., Gehrels, G. E., Ruiz, J., & Buchwaldt, R. (2012). Routine low-damage apatite U-Pb dating using laser ablation-multicollector-ICPMS. *Geochemistry, Geophysics, Geosystems*, *13*(2), n/a-n/a. https://doi.org/10.1029/2011GC003928

Tomkins, H. S., Powell, R., & Ellis, D. J. (2007). The pressure dependence of the zirconium-in-rutile thermometer. *Journal of Metamorphic Geology*, *25*(6), 703–713. https://doi.org/10.1111/j.1525-1314.2007.00724.x

Trail, D., Bruce Watson, E., & Tailby, N. D. (2012). Ce and Eu anomalies in zircon as proxies for the oxidation state of magmas. *Geochimica et Cosmochimica Acta*, *97*, 70–

87. https://doi.org/10.1016/j.gca.2012.08.032

Vance, D., & Thirlwall, M. (2002). An assessment of mass discrimination in MC-ICPMS using Nd isotopes. *Chemical Geology*, *185*(3–4), 227–240. https://doi.org/10.1016/S0009-2541(01)00402-8

Vauchez, A., Dineur, F., & Rudnick, R. (2005). Microstructure, texture and seismic anisotropy of the lithospheric mantle above a mantle plume: Insights from the Labait volcano xenoliths (Tanzania). *Earth and Planetary Science Letters*, *232*(3–4), 295–314. https://doi.org/10.1016/j.epsl.2005.01.024

Vermeesch, P. (2018). IsoplotR: A free and open toolbox for geochronology. *Geoscience Frontiers*, *9*(5), 1479–1493. https://doi.org/10.1016/j.gsf.2018.04.001

Walters, J. B., & Kohn, M. J. (2017). Protracted thrusting followed by late rapid cooling of the Greater Himalayan Sequence, Annapurna Himalaya, Central Nepal: Insights from titanite petrochronology. *Journal of Metamorphic Geology*, *35*(8), 897–917. https://doi.org/10.1111/jmg.12260

Weaver, B. L., & Tarney, J. (1984). Empirical approach to estimating the composition of the continental crust. *Nature*, *310*(5978), 575–577. https://doi.org/10.1038/310575a0

Weeraratne, D. S., Forsyth, D. W., Fischer, K. M., & Nyblade, A. A. (2003). Evidence for an upper mantle plume beneath the Tanzanian craton from Rayleigh wave tomography. *Journal of Geophysical Research: Solid Earth*, *108*(B9). https://doi.org/10.1029/2002jb002273

Wendt, I., & Carl, C. (1991). The statistical distribution of the mean squared weighted deviation. *Chemical Geology: Isotope Geoscience Section*, *86*(4), 275–285. https://doi.org/10.1016/0168-9622(91)90010-T

Whitehouse, M. J., & Platt, J. P. (2003). Dating high-grade metamorphism - Constraints from rare-earth elements in zircon and garnet. *Contributions to Mineralogy and Petrology*, *145*(1), 61–74. https://doi.org/10.1007/s00410-002-0432-z

Woodhead, J. D., & Hergt, J. M. (2001). Strontium, Neodymium and Lead Isotope Analyses of NIST Glass Certified Reference Materials: SRM 610, 612, 614. *Geostandards and Geoanalytical Research*, *25*(2–3), 261–266. https://doi.org/10.1111/j.1751-908X.2001.tb00601.x

Xu, Y., Tang, W., Hui, H., Rudnick, R. L., Shang, S., & Zhang, Z. (2019). Reconciling the discrepancy between the dehydration rates in mantle olivine and pyroxene during xenolith emplacement. *Geochimica et Cosmochimica Acta*, *267*, 179–195. https://doi.org/10.1016/j.gca.2019.09.023

Yakymchuk, C., & Brown, M. (2014). Behaviour of zircon and monazite during crustal melting. *Journal of the Geological Society*, *171*(4), 465–479. https://doi.org/10.1144/jgs2013-115

Yang, Y. H., Wu, F. Y., Yang, J. H., Chew, D. M., Xie, L. W., Chu, Z. Y., et al. (2014). Sr and Nd isotopic compositions of apatite reference materials used in U-Th-Pb

geochronology. *Chemical Geology*, *385*, 35–55. https://doi.org/10.1016/j.chemgeo.2014.07.012

Zack, T., Moraes, R., & Kronz, A. (2004). Temperature dependence of Zr in rutile: empirical calibration of a rutile thermometer. *Contributions to Mineralogy and Petrology*, *148*(4), 471–488. https://doi.org/10.1007/s00410-004-0617-8

Zack, Thomas, & Kooijman, E. (2017). Petrology and Geochronology of Rutile. *Reviews in Mineralogy and Geochemistry*, *83*(1), 443–467. https://doi.org/10.2138/rmg.2017.83.14

Zack, Thomas, Stockli, D. F., Luvizotto, G. L., Barth, M. G., Belousova, E., Wolfe, M. R., & Hinton, R. W. (2011). In situ U–Pb rutile dating by LA-ICP-MS: 208Pb correction and prospects for geological applications. *Contributions to Mineralogy and Petrology*, *162*(3), 515–530. https://doi.org/10.1007/s00410-011-0609-4

Appendix A

Four-dimensional thermal evolution of the East African Orogen: Accessory phase petrochronology of crustal profiles through the Tanzanian craton and Mozambique Belt, northeastern Tanzania – Supplementary Information

Supplementary text, figures, and tables can be found online at:

https://link.springer.com/article/10.1007/s00410-020-01737-6#Sec25

Appendix B

Supplementary information for **Heat transfer and production in cratonic continental crust: Constraints from U-Pb thermochronology of xenoliths from the Siberian craton**

Introduction

This document provides details of analytical procedures and models discussed in the main text. This includes: detailed sample descriptions, mineral compositions measured by EPMA, whole-rock compositions determined by XRF, zircon-rutile-apatite U-Pb and trace-element data, pseudosection models, and 1-D heat conduction geotherm models.

Sample descriptions

Sample 36-14 is a moderately-altered granoblastic felsic garnet granulite. Garnet in this sample is typically 0.5–1.5 mm wide and contains fine-grained oxide exsolutions (with high reflectivity). Orthopyroxene is peculiar in that it contains fine-grained exsolution along grain boundaries and along cracks that crosscut grans; in more extreme cases, orthopyroxene is almost entirely altered to a light brown color, with only a small orthopyroxene core remaining. Orthopyroxene also exhibits second-order interference colors, which may reflect the presence of these fine-grained exsolutions (Fig. S1). Matrix quartz, plagioclase, and alkali-feldspar show oscillatory extinction. Graphite is common and defines a weak foliation. Accessory rutile and apatite are present in the matrix; rutile is not observed as inclusions within garnet. Veins of very fine-grained crystalline material are pervasive in the sample and cross cut garnet, orthopyroxene, and other matrix minerals, and in some cases, rim garnet. Some of this fine-grained material is chlorite, which appear as clusters with green color in plane-polarized light and anomalous birefringence. Biotite also occurs, and is

interpreted to be entirely secondary based on its close association with fine-grained vein material.

Sample 74-53 is moderately-altered granoblastic mafic garnet granulite. Garnet is subhedral–euhedral, 0.5–1 mm wide, and free of exsolution; quartz (feldspar?) inclusions within garnet cores are observed. Clinopyroxene cores have fine-grained oxide exsolutions (high reflectivity). Matrix plagioclase is slightly sericitized and has faint oscillatory extinction. Accessory ilmenite is common in the matrix. Minor biotite is also observed, but this is exclusively associated with fine-grained grunge. Pockets of dark fine-grained crystalline material exists interstitial to plagioclase, pyroxene, and garnet. Crosscutting veins of the same material intersect the matrix. Some of this fine-grained material is actually very fine-grained plagioclase (intergrown lathes).

Sample 74-50 is moderately-altered granoblastic mafic garnet granulite. It is essentially identical to sample 74-53, except that sample 74-50 is coarser-grained (Fig. S1).

Sample 79-14 is moderately-altered granoblastic mafic garnet granulite. Unlike the previous samples, sample 79-14 contains modally subordinate plagioclase (Fig. S1). Garnet is 1.0–1.5 mm wide and networks of fine-grained oxide exsolutions (with high reflectivity) are common in its cores. Clinopyroxene cores also have fine-grained oxide exsolutions (high reflectivity). Accessory rutile and apatite are present in the matrix; rutile is not observed as inclusions within garnet. Accessory sulfide is also present. Blotches of very fine-grained crystalline material are pervasive in the sample and form rims around garnet, clinopyroxene, and other matrix minerals.

Laser ablation split-stream analyses

Coupled U-Pb and trace-element analyses of zircon, rutile, and apatite were carried out using laser ablation split stream inductively coupled plasma mass spectrometry (LASS) at UC Santa Barbara using a Cetac Teledyne 193 nm excimer Analyte laser with a HelEx ablation cell coupled to a Nu Instruments Plasma high-resolution multi-collector inductively couple plasma mass spectrometer (MC-ICPMS) for U-Pb isotopes and Agilent 7700S quadrupole ICPMS for trace-element abundances. For spot analyses on polished grain interiors, laser spot sizes and fluences varied depending on the analyzed phases: 25 μm, 4 Hz, 100% of 2 mJ for zircon; 35–40 μm, 4 Hz, 100% of 4 mJ for rutile; and 50 μm, 4 Hz, 100% of 2 mJ for apatite. The data were collected using standard-sample bracketing techniques and were calibrated against matrix-matched reference materials (RMs) for U-Pb analyses and glass standards for trace-element analyses, following the methods of Kylander-Clark et al. (2013) with modifications outlined in McKinney et al. (2015). Raw U-Pb ratios were baseline subtracted and corrected for laser- and plasma-induced element fractionation, and instrument drift using the Iolite software package (v. 2.5; Paton et al., 2011) in the Igor Pro interactive software environment.

The quoted uncertainties for all laser ablation data are 2σ and incorporate analytical uncertainty as well as additional uncertainties associated with reproducibility of secondary RMs (Horstwood et al., 2012). Zircon U-Pb analyses employed zircon 91500 (1065 Ma, ID-TIMS; Wiedenbeck et al., 1995) as the primary bracketing standard with zircons GJ1 (602 Ma, ID-TIMS; Jackson et al., 2004) and Plesovice (337 Ma, ID-TIMS; Sláma et al., 2008) analyzed as secondary standards. Rutile analyses employed rutile Kragero (1091 Ma, TIMS; Luvizotto et al., 2009) as the primary bracketing standard; rutiles Wodgina (2845 Ma, SIMS; Ewing et al., 2015), 9826J (382 Ma, TIMS; Kylander-Clark et al., 2008) and LJ04-08

(501 Ma, LASS-MC-ICP-MS; Apen et al., 2020) were analyzed as secondary standards. For apatite U-Pb analyses, apatite MAD-UCSB (467 Ma, ID-TIMS; Apen et al., 2021) as the primary bracketing standard with apatite RMs McClure (524 Ma, ID-TIMS; Schoene and Bowring, 2006) and OD306 (1597 Ma, ID-ICPMS age; 1545 Ma, LA-ICPMS age; Thompson et al., 2016) used as secondary standards. Trace-element concentrations were also calculated in Iolite using an internal element standard (Liu et al., 2008). Reported uncertainties for trace-element data are 2σ and only include analytical uncertainties. Repeat analyses of secondary RMs over the course of this study indicate that each 238U/206Pb and 207Pb/206Pb measurements require an additional 1.9 % and 0.9 % for zircon analyses, 3.1 % and 1.8 % for rutile analyses, and 2.8 % and 1.6 % for apatite analyses (all 2σ), to account for the long-term variability in laser ablation analyses; these values were added in quadrature to the internal error of each U-Pb datum and considered when calculating intercept ages (Horstwood et al., 2016). Final U-Pb ratios and associated uncertainties were plotted using IsoplotR (Vermeesch, 2018). The quoted U-Pb dates for apatite and rutile are common-Pb corrected assuming a Stacey and Kramers (1975) initial 207Pb/206Pb composition.

Rutile depth profiling analyses were preformed using the same instruments described above. Analyses used a 50-µm-diameter spot size, operating at a frequency of 2 Hz and 50 % of 5 mJ laser power. Each ablation sequence consisted of two cleaning shots, followed by 25 s of monitored washout, and 75 s of continuous ablation, equating to final pit depths of ~13 µm (pit depths measured by SEM). Rutile depth profiles were also processed in Iolite. The depth profile data were averaged at 1 s intervals rather than output at their natural 0.5 s

interval in order to reduce instrumental noise throughout each analysis while still maintaining a high-resolution sampling interval.

Whole profiles are exported from Iolite without formal uncertainties, so we approximated the uncertainty of each data point within a given profile based on the reproducibility of secondary reference rutiles (9826J and LJ04-08). A normal distribution was fitted to the U-Pb data from each reference rutile and the mean (μ) and standard deviation (σ) of the 238U/206Pb and 207Pb/206Pb distributions were examined. The 2σ associated with LJ04-08 was 6.7% (238U/206Pb) and 4.3% (207Pb/206Pb); the 2σ associated with 9826J was 3.5 % (238U/206Pb) and 2.6% (207Pb/206Pb). We adopted the more conservative 2σ associated with LJ04-08 as the 2σ for the unknowns.

Whole-rock geochemistry and pseudosection analyses

For newly analyzed samples, representative and unaltered rock chips were pulverized to a fine-powder using an alumina mill, and sent to Washington State University, Pullman (WSU) for major-element analyses by X-ray fluorescence (XRF).

For mafic garnet granulites 01-34, 01-95, and 79-14, we utilized the thermodynamic modeling program Perple_X (Connolly, 2009) to construct pseudosections. Pseudosections implemented major-element whole-rock composition from Moyen et al. (2017) and Table S2. We used the hp62ver thermodynamic data set of Holland and Powell (2011) and the metabasite set of a-x relations recommended by Palin et al. (2016) and Green et al. (2016). This includes: melt, augite, and hornblende (Green et al., 2016); garnet, orthopyroxene, and biotite (White et al., 2014); ilmenite (White et al., 2000); the feldspar solution model of Fuhrman and Lindsley (1988); and omphacite (Green et al., 2007). The rocks were modeled

as anhydrous (biotite in the xenoliths is likely to be wholly secondary and not representative of the stable mineral assemblage prior to eruption).

The observed mineral assemblage (garnet, clinopyroxene, plagioclase, and rutile) is stable >0.8 GPa and >700 °C, compatible with average P-T determined from mode 2 in THERMOCALC (Fig. S2). Mafic garnet granulite, which contains relict orthopyroxene, is consistent with a P-T path characterized by burial from <0.8 GPa to >1.2 GPa at 800 °C (Fig. S3).

Geotherm models

We computed one-dimensional, steady-state geotherms using methods outlined in Appendix A, with the exception that heat production values for the mantle lithosphere were set to values reported in McIntyre et al. (2021). We modeled three scenarios that assumed different crust heat production profiles (discussed in Chapter II).

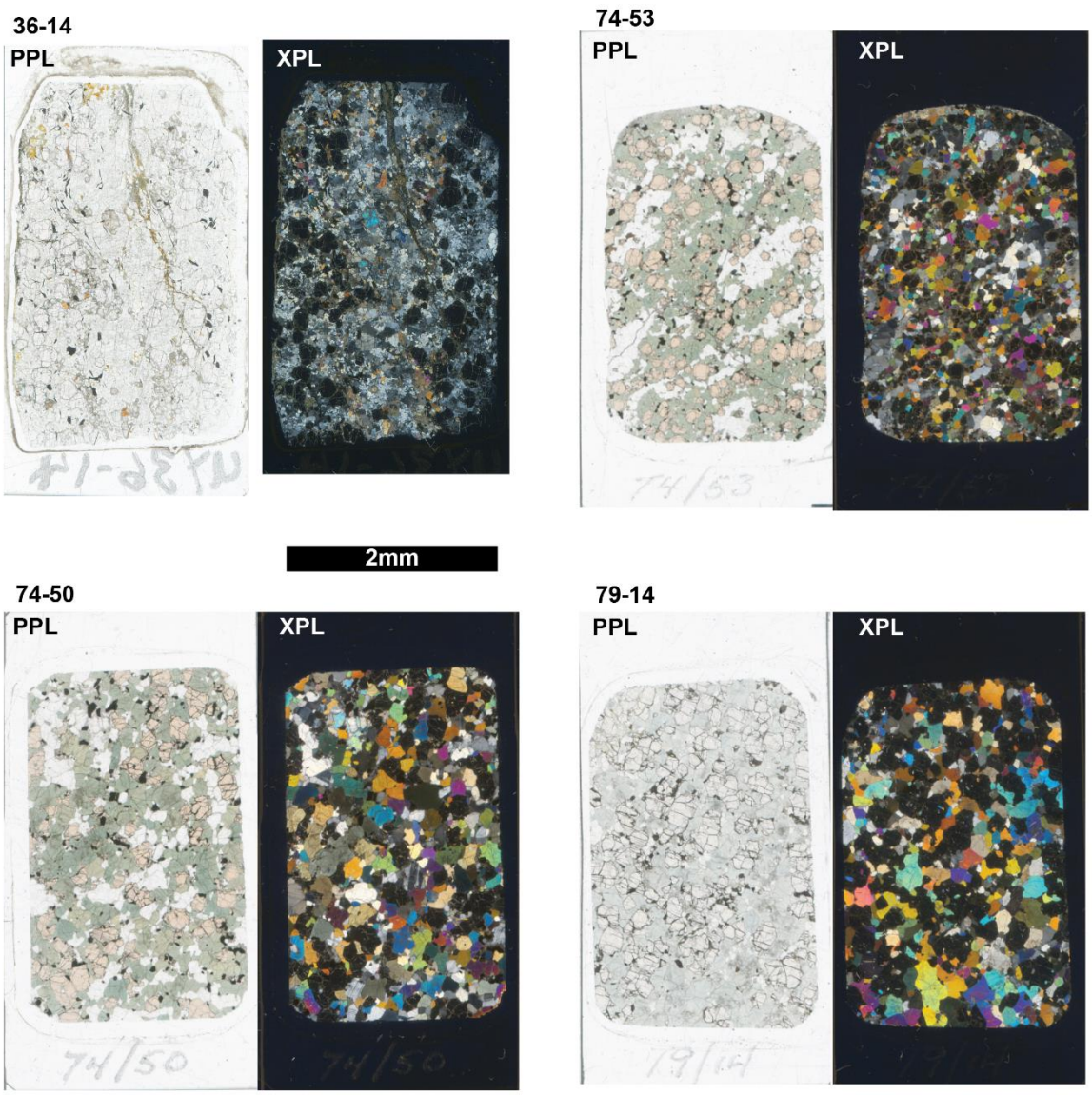

Figure B1. Thin section scans of newly reported xenoliths.

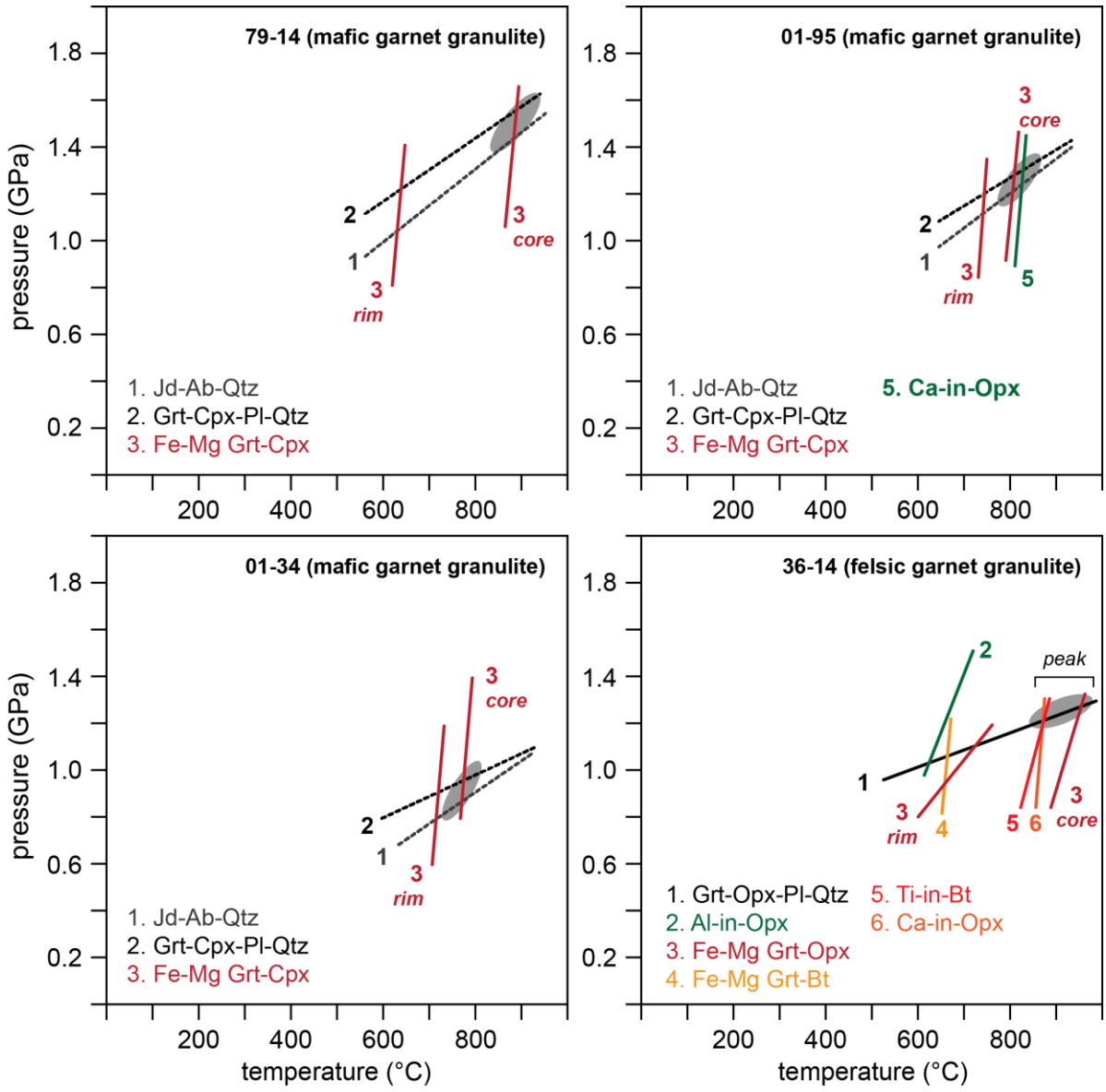

Figure B2. Positions and intersections of endmember equilibria from mode 2 of THERMOCALC

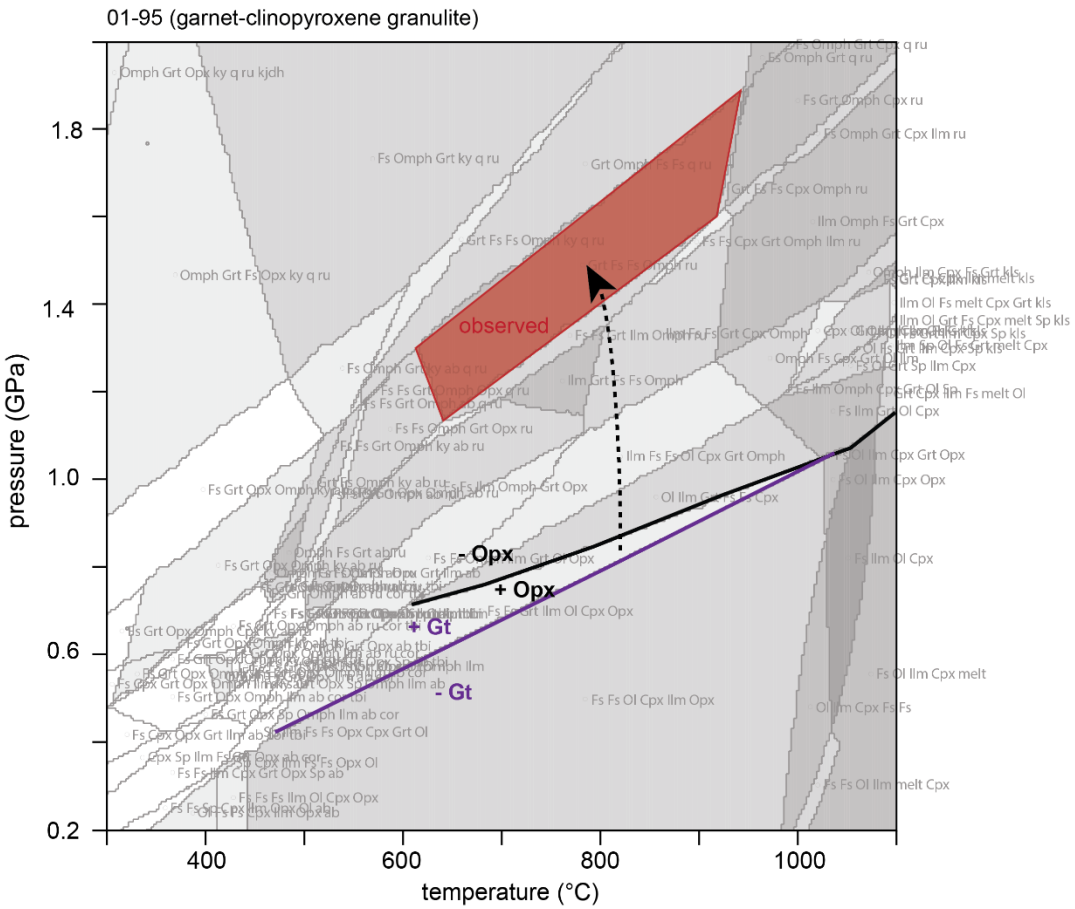

Figure B3. Results of pseudosection modeling of mafic garnet granulite 01-34. Red field corresponds to the stable mineral assemblage observed.

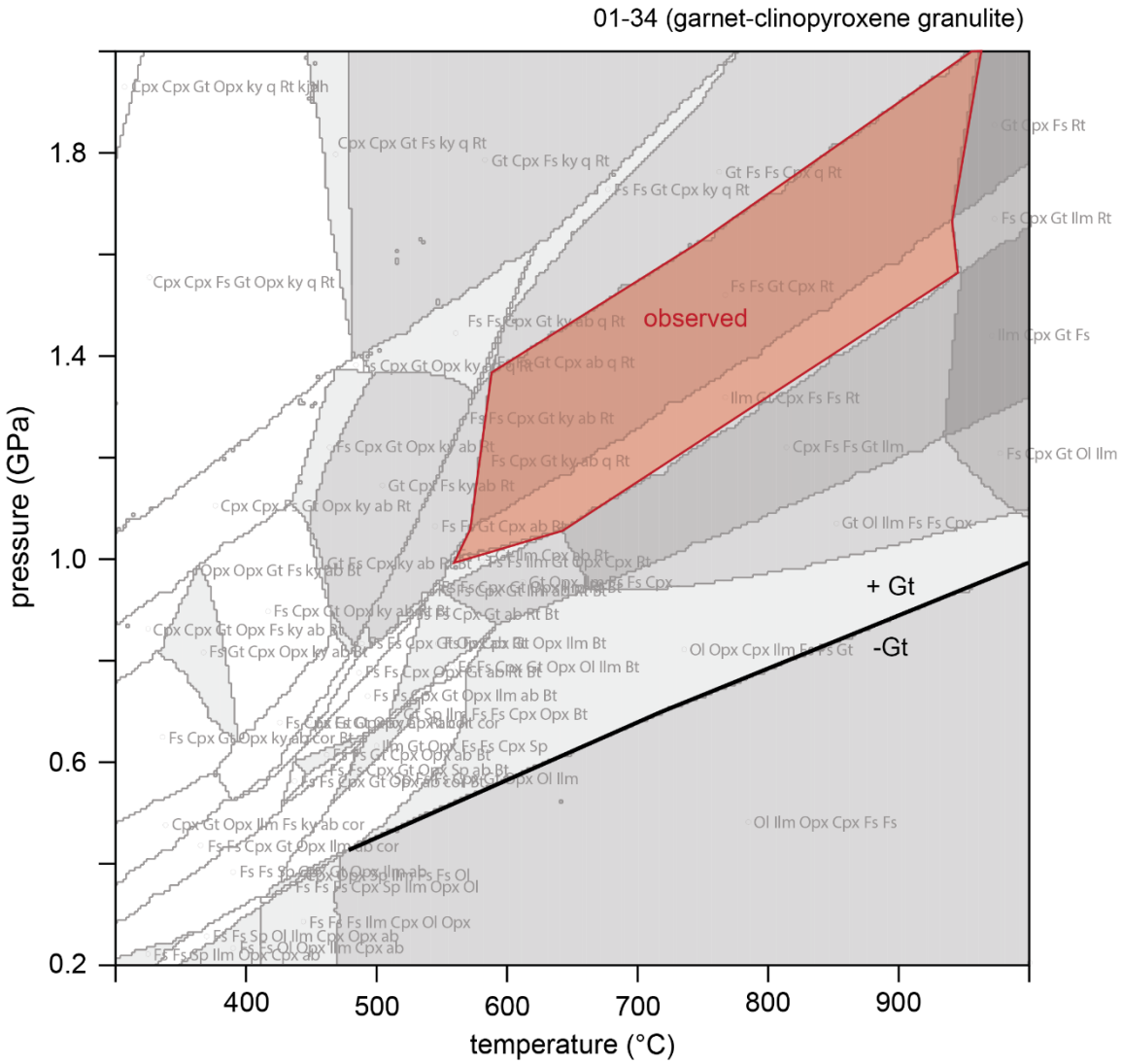

Figure B4. Results of pseudosection modeling of mafic garnet granulite 01-95. Red field corresponds to the stable mineral assemblage observed.

Appendix C

Supplementary information for **Apatites for destruction: Reference apatites from Morocco and Brazil for U-Pb petrochronology and Nd and Sr isotope geochemistry**

Supplementary tables can be found online at: https://ars.els-cdn.com/content/image/1-s2.0-S000925412100632X-mmc2.xlsx